Ollscoil na hÉireann, Corcaigh
National University of Ireland, Cork





Novel tools for *in vivo* fluorescence lifetime imaging using miniaturised SPAD arrays

Thesis presented by
Dario Angelone

ORCID: 0009-0003-6043-1224

for the degree of
Doctor of Philosophy

University College Cork

Tyndall National Institute

Head of Department: Fatima Gunning
Supervisor: Stefan Andersson-Engels
Co-supervisor: Sanathana Konugolu Venkata Sekar
Co-supervisor: Ray Burke

2026

Novel tools for *in vivo* fluorescence lifetime imaging using miniaturised SPAD arrays

© 2026 Dario Angelone
All rights reserved

Biophotonics, Tyndall National Institute
University College Cork, UCC
Ireland

Abstract

This thesis presents the development, validation, and application of novel tools for *in vivo* fluorescence lifetime imaging (FLIm) using miniaturised single-photon avalanche diode (SPAD) arrays. FLIm can enhance biochemical specificity by enabling discrimination between fluorophores with overlapping emission spectra but distinct fluorescence lifetimes (FLT). It is also sensitive to the local molecular environment, making it valuable for label-free diagnostics. The core technology applied in the thesis is the EndoCam, a compact 128 × 120 SPAD array with time-gated photon counting capability and a footprint of 2.0 mm × 1.4 mm, designed for integration into chip-on-tip endoscopic systems.

The thesis demonstrates the integration of the EndoCam into three distinct FLIm platforms: (i) a bench-top wide-field system for metabolic imaging of *ex vivo* tumour tissue using planar pH sensors (Paper **I**); (ii) a miniaturised imager for portable diagnostics, validated through measurement of polymer beads and imaging of stained porcine tissue (Paper **II**); and (iii) a chip-on-tip FLIm micro-camera with a 4 mm outer diameter – the first of its kind at a scale compatible with endoscopic deployment – capable of resolving features below 30 µm and benchmarked against a time-correlated single-photon counting (TCSPC) system (Paper **III**).

To support system benchmarking and clinical translation, a set of solid-state fluorescence lifetime standards using dyed epoxy resins was developed (Paper **IV**). These standards span lifetimes from sub-nanosecond to over 3.5 ns, and were evaluated for photostability, fabrication repeatability, and microstructural uniformity using a confocal microscope.

Together, these contributions establish a foundation for compact, disposable chip-on-tip FLIm systems suitable for clinical applications such as endoscopy and image-guided surgery; this helps advance the translation of FLIm from research to real-world diagnostics, paving the way for future clinical deployment.

List of Publications

This thesis is based in the following research papers, which will be referred to by their Roman numerals in the text.

I **Metabolic imaging of tumor tissue samples using planar fluorescence lifetime-based pH sensors and a SPAD array imager**
Dario Angelone, Liang Li, Ciaran Devoy, Andrew B. Matheson, Ahmet T. Erdogan, Robert K. Henderson, Mark Tangney, Dmitri B. Papkovsky, Stefan Andersson-Engels, and Sanathana Konugolu Venkata Sekar.
Sensors and Actuators B: Chemical **Vol. 431**, (2025).

II **Time resolved SPAD micro-camera probe for wide-field FLIm in microendoscopy**
Dario Angelone, Sanathana Konugolu Venkata Sekar, Walter Messina, Andrew B. Matheson, Ahmet T. Erdogan, Robert K. Henderson, Ray Burke, and Stefan Andersson-Engels.
Proc. SPIE 12368, Advanced Biomedical and Clinical Diagnostic and Surgical Guidance Systems XXI **1236807**, (2023).

III **Chip-on-tip fluorescence lifetime imaging micro-camera toward endoscopic applications**
Dario Angelone, Noreen Nudds, Andrew B. Matheson, Ahmet T. Erdogan, Walter Messina, Ray Burke, Robert K. Henderson, Stefan Andersson-Engels, and Sanathana Konugolu Venkata Sekar.
Optics Letters **Vol. 50, Issue 13**, pp. 4230-4233 (2025).

IV **Development of solid-state fluorescence lifetime standards for clinical applications using dyed epoxy resins**
Dario Angelone, Keela Hughes, Hasti Yavari, Sara Eugenia Garduño Gómez, Brian C. Wilson, Stefan Andersson-Engels, Katarzyna Komolibus, and Sanathana Konugolu Venkata Sekar.
Journal of Biomedical Optics **-**, (Accepted 30th December 2025).

Abbreviations

APD	Avalanche photodetector
DCF	Double-clad fibre
CMOS	Complementary metal-oxide-semiconductor
ENEPIG	Electroless nickel electroless palladium immersion gold
FAD	Flavin adenine dinucleotide
FD-FLIm	Frequency domain fluorescence lifetime imaging
FLIm	Fluorescence lifetime imaging
FLIM	Fluorescence lifetime imaging microscopy
FLImDAR	Fluorescence lifetime imaging with distance and ranging
FLT	Fluorescence lifetime
FoV	Field of view
FPGA	Field-programmable gate array
FRET	Förster resonance energy transfer
FWHM	Full width at half maximum
GBM	Glioblastoma multiforme
GI	Gastrointestinal
GRIN	Gradient index
GUI	Graphical user interface
HNSCC	Head and neck squamous cell carcinoma
ICCD	Intensified charge-coupled device
IRF	Instrument response function
LiDAR	Light detection and ranging
MPE	Maximum permissible exposure
NA	Numerical aperture
NADH	Nicotinamide adenine dinucleotide
ND	Neutral density
NIM	Nuclear Instrumentation Module
OCT	Optical coherence tomography
OEPK	Octaethylporphin-ketone
PCB	Printed circuit board
pHe	Extracellular pH
PMT	Photomultiplier tube
RLD	Rapid lifetime determination
RO	Ring oscillator
SiPMs	Silicon photomultipliers
SNR	signal-to-noise ratio
SPAD	Single-photon avalanche diode

TCSPC	Time-correlated single-photon counting
TDC	Time-to-digital converter
TP-FLIM	Two-photon fluorescence lifetime imaging microscopy
TTL	Transistor-transistor logic
ZnPc	Zinc phthalocyanine

Contents

Abstract iii

List of Publications v

Abbreviations vii

1 Introduction 1
- 1.1 Motivation . . . 1
- 1.2 Thesis Goals . . . 2
- 1.3 Structure of the thesis . . . 2

2 Background and theory 5
- 2.1 Fundamental principles of FLIm . . . 5
  - 2.1.1 Fluorescence . . . 5
  - 2.1.2 Fluorescence decay and lifetime . . . 5
- 2.2 Measurement techniques . . . 6
  - 2.2.1 Time-domain fluorescence measurements . . . 6
  - 2.2.2 Time-correlated single photon counting . . . 8
  - 2.2.3 Time-gating . . . 9
  - 2.2.4 Pulse sampling . . . 10
  - 2.2.5 Frequency domain fluorescence measurements . . . 10
- 2.3 Analysis Methods . . . 11
  - 2.3.1 Tail fitting . . . 12
  - 2.3.2 Reconvolution fitting . . . 14
  - 2.3.3 Fast lifetime estimation . . . 16
  - 2.3.4 Error analysis in lifetime estimation . . . 17
- 2.4 Phototoxicity and safe exposure considerations . . . 18
- 2.5 Summary . . . 18

3 *In vivo* FLIm 21
- 3.1 State of the art . . . 21
  - 3.1.1 Free-hand scanning . . . 22
  - 3.1.2 Helical scanning . . . 23
  - 3.1.3 Laser scanning . . . 24
  - 3.1.4 Wide-field . . . 27
- 3.2 SPAD arrays for wide-field FLIm . . . 29
- 3.3 Discussion . . . 30
- 3.4 Summary . . . 31

4 Instrumentation 33
- 4.1 The EndoCam . . . 33
  - 4.1.1 Overview . . . 33
  - 4.1.2 Time-gating implementation . . . 34
- 4.2 Modular FLIm system . . . 35
  - 4.2.1 Computer – EndoCam interface . . . 35
  - 4.2.2 Laser – EndoCam synchronisation . . . 36
  - 4.2.3 Time-bin calibration . . . 37
- 4.3 TCSPC system for bulk lifetime measurements . . . 38
- 4.4 Summary . . . 41

5 Bench-top wide-field FLIm systems 43
- 5.1 Wide-field FLIm system for lifetime-based metabolic imaging of *ex vivo* tissue samples . . . 43
  - 5.1.1 EndoCam connectivity challenges . . . 43
  - 5.1.2 Custom PCB design . . . 44
  - 5.1.3 Optical design . . . 45
  - 5.1.4 MPE calculations and evaluation . . . 47
  - 5.1.5 Summary . . . 48
- 5.2 Miniaturised FLIm imager . . . 49

5.2.1 Custom PCB design . . . 49
5.2.2 Optical design . . . 50
5.2.3 Animal tissue demonstration . . . 51
5.2.4 MPE evaluation . . . 51
5.2.5 Summary . . . 52
5.3 Discussion . . . 52
5.4 Conclusions . . . 53

6 Chip-on-tip FLIm micro-camera 55
6.1 Custom PCB . . . 55
6.2 Optical design . . . 56
6.2.1 Initial exploration . . . 56
6.2.2 Final design . . . 57
6.3 Mechanical design . . . 58
6.3.1 3D-printed mounts . . . 58
6.3.2 Assembly process . . . 59
6.3.3 Mid-assembly tests . . . 60
6.4 Excitation source integration . . . 60
6.4.1 Stray fluorescence . . . 60
6.4.2 Off-centre illumination . . . 61
6.4.3 Angled fibre tip for beam steering . . . 61
6.4.4 Final excitation profile . . . 63
6.5 Characterisation of the FLIm micro-camera . . . 63
6.6 MPE evaluation . . . 63
6.7 Discussion . . . 64
6.8 Summary . . . 65

7 Conclusions 67
7.1 Key contributions . . . 67
7.1.1 Integration of the EndoCam into bench-top and hand-held imaging systems . . . 67
7.1.2 Chip-on-tip FLIm micro-camera . . . 67
7.1.3 Solid-state FLT standards for system validation . . . 68
7.2 Future work . . . 68
7.2.1 Micro-camera packaging and clinical readiness . . . 68
7.2.2 Illumination design . . . 69
7.2.3 Excitation source development . . . 69
7.2.4 Connectivity and data transmission . . . 70
7.2.5 Advancing SPAD imagers for FLIm . . . 70
7.2.6 Standardisation and regulatory pathways . . . 71
7.3 Final remarks . . . 71

Comments on the Papers 73

Acknowledgements 75

References 77

Papers

I **Metabolic imaging of tumor tissue samples using planar fluorescence lifetime-based pH sensors and a SPAD array imager** **95**

II **Time resolved SPAD micro-camera probe for wide-field FLIm in microendoscopy** **107**

III **Chip-on-tip fluorescence lifetime imaging micro-camera toward endoscopic applications** **113**

IV **Development of solid-state fluorescence lifetime standards for clinical applications using dyed epoxy resins** **119**

Appendix **145**

Chapter 1

Introduction

1.1 Motivation

Fluorescence lifetime imaging (FLIm) is a powerful analytical tool with a wide range of potential applications. It can increase the biochemical specificity of fluorescence measurements by allowing differentiation between fluorophores with overlapping emission spectra but with different fluorescence lifetimes [1, 2]. Because the lifetime of a fluorophore is dependent on its environment, FLIm can also discriminate between different fractions of the *same* fluorophore under varying environmental conditions [3].

Fluorescence lifetime (FLT) measurements of endogenous fluorophores in tissue and cell cultures have provided insights into tissue metabolism [4], and lifetime-based exogenous fluorescent markers have been applied to measure parameters such as temperature, viscosity, pH, and ion concentration [3, 5]. Wider applications of FLT measurements reported in literature include diagnostic measurements of combustive fuels [6], the detection of explosive vapours emitted from landmines [7], and the monitoring of varnish removal in painting conservation [8].

In the analysis of *ex vivo* tissue samples, changes in FLT have been shown to be indicative of disease, enabling differentiation between healthy and diseased tissue [1, 9]. In recent years, FLIm[1] has shown promise for label-free intraoperative tumour margin assessment in *ex vivo* human tissue samples [10–12].

However, translating these capabilities to *in vivo* clinical settings remains challenging. Most existing *in vivo* FLIm systems rely on point-scanning or fibre-bundle-based architectures, which are limited by mechanical complexity, acquisition speed, and probe flexibility. Wide-field FLIm systems offer improved throughput and reduced motion artefacts, but current implementations are often bulky and not easily miniaturised for clinical use.

Concurrently, white-light endoscopy has seen a growing trend toward single-use, chip-on-tip devices. This shift is driven by the miniaturisation and cost reduction of CMOS camera technology, as well as the clinical advantages of disposability, such as avoiding sterilisation and reducing cross-contamination risks [13, 14]. Therefore, the development of chip-on-tip endoscopes with wide-field FLIm capability is of interest for the long term application of FLIm in surgery.

Recent advances in single-photon avalanche diode (SPAD) technology have enabled the development of compact, time-resolved SPAD ar-

[1] Throughout this thesis, the acronym FLIm is used broadly to refer to systems performing fluorescence lifetime imaging across various spatial scales. The term FLIM (fluorescence lifetime imaging microscopy) is reserved specifically for systems operating at the microscopic scale.

rays [15]. These detectors offer high temporal resolution, single-photon sensitivity, and the potential for scalable, low-cost production. Commercially available SPAD cameras have already demonstrated wide-field FLIm capability in bench-top systems [16, 17].

The miniaturisation of SPAD arrays, fabricated with standard CMOS processes, makes their use for a chip-on-tip FLIm endoscope feasible. An example of this is the EndoCam, a 128×120 SPAD array with dimensions $1.4\,\text{mm} \times 1.4\,\text{mm}$ presented in Erdogan et al. [18]. The EndoCam uses time-gated photon counting to enable wide-field, time-resolved imaging in a chip small enough for endoscopic integration. By leveraging the unique capabilities of miniaturised SPAD arrays such as the EndoCam, it becomes feasible to design chip-on-tip FLIm devices that combine time-resolved imaging with the practical advantages of disposability and integration. This thesis is motivated by the potential of such systems to bridge the gap between advanced fluorescence lifetime imaging and real-world clinical deployment.

1.2 Thesis Goals

The primary goal of this thesis is to evaluate the capability of miniaturised SPAD arrays for wide-field, chip-on-tip fluorescence lifetime imaging and to explore their potential for clinical translation. This is achieved by:

- Developing and validating bench-top and handheld wide-field FLIm systems using the EndoCam.
- Designing and assembling a chip-on-tip FLIm micro-camera with integrated imaging optics and excitation light delivery, at a size scale compatible with endoscopic deployment.
- Investigating the performance limits and imaging capabilities of these systems, and demonstrating their utility for biomedical applications, including metabolic imaging and tissue differentiation.
- Exploring the suitability of dyed epoxy resins as solid-state fluorescence lifetime standards for system benchmarking and calibration.

Together, these efforts aim to lay the groundwork for compact, disposable FLIm systems that could one day complement conventional white-light endoscopy in clinical diagnostics and image-guided surgery.

1.3 Structure of the thesis

The thesis is based on 4 papers which are appended at the end of the thesis and will be referred to by their Roman numerals as Papers **I**–**IV**, respectively, in the text. The primary scientific contribution of the work conducted as part of the PhD is contained within the papers. The main text of the thesis includes key background and theory; more in-depth details of the work carried out to produce the papers; and further work which is not captured in the papers. As much as possible, content from the papers has not been repeated in the main text. There are six main chapters, the content of which is outlined below.

Chapter 2 covers the basic theory of time-resolved fluorescence before introducing the prominent measurement techniques used to perform FLT measurements along with the typical instrumentation used. The fitting methods used for data analysis are also outlined.

Chapter 3 reviews the current state-of-the-art in FLIm systems developed for *in vivo* applications and discusses their respective advantages, limitations, and clinical relevance. The chapter also introduces the use of single-photon avalanche diode (SPAD) arrays for wide-field FLIm, highlighting their potential for miniaturisation and clinical translation. This further establishes the technological context and motivation for the development of compact, chip-on-tip FLIm systems.

Chapter 4 introduces EndoCam, the miniaturised 128 × 120 SPAD array detector that was used for the vast majority of the work in this thesis. The key characteristics and functionality of the detector are described. The different pulsed laser sources used are also described before an overview of the modular FLIm system developed is presented. The modular system facilitates the use of different excitation sources and interchangeable front-end imaging systems which use the EndoCam as a detector.

Chapter 5 provides details on the bench-top wide-field FLIm systems using the EndoCam which were developed. Firstly, the design of custom PCBs for the EndoCam are presented. These enabled the chip to be operated remotely from the control board and integrated into standard lens tube systems.

The first imaging system presented is the FLT macro-imager which was used in Paper **I**. This system was designed for imaging of *ex vivo* mouse tumour samples combined with lifetime-based solid-state pH sensors with a desired field of view of 1 cm × 1 cm.

The second system is the miniaturised FLIm imager which was used in Paper **II**. The motivation for this system was to demonstrate wide-field FLIm in a hand-held form factor which, if pursued further, could be applied for *in vivo* applications where portability and flexibility are beneficial but where size constraints are not extreme. Such as for lifetime imaging of skin lesions or of the oral cavity.

Chapter 6 sees the EndoCam integrated into the micro-camera system presented in Paper **III** which includes integrated imaging optics and excitation light delivery. With an external diameter of 4 mm, this is the first chip-on-tip FLIm micro-camera on a size scale compatible with endoscopic applications. The optical and mechanical designs are presented, and the assembly process is explained in detail. Finally, the challenges faced in the effective delivery of excitation light, and the methods implemented to overcome them, are presented.

In **Chapter 7**, the results of the thesis are then summarised and some future directions are discussed.

Chapter 2

Background and theory

In this chapter the necessary background and theory related to FLIm are covered. The fundamental principles of time-resolved fluorescence are outlined. Fluorescence lifetime measurement techniques are then described; TCSPC and time gating have both been applied in this thesis, therefore they are covered in some detail. Pulse sampling has not been applied here, however this technique is outlined briefly due to its application in many existing *in vivo* FLIm systems. Finally, the analysis methods for FLIm data applied in this thesis are then covered.

2.1 Fundamental principles of FLIm

2.1.1 Fluorescence

Fluorescence is a photo-luminescent phenomenon which occurs when a molecule, referred to as a fluorophore, undergoes optical excitation and relaxation. This process is illustrated in a Jablonski diagram in Figure 2.1. The fluorophore absorbs a photon at an excitation light wavelength λ_A, causing it to transition from the ground state S_0, to an excited electronic state (S_1, ..., S_n). In each of these electronic states, there are a number of vibrational energy levels the fluorophore can be excited to. Following excitation, the vast majority of excited molecules rapidly relax to the lowest vibrational level of S_1 in a process called internal conversion [19]. From S_1, the fluorophore can return to the ground state through non-radiative processes or through the emission of a photon with light wavelength λ_F. Because of the energy lost through internal conversion, the emitted light has a wavelength that is longer than that of the excitation light that was absorbed. The difference between λ_A and λ_F is known as the Stokes shift.

An important property of fluorophores is the fluorescent quantum yield, Φ_f; the quantum yield is the proportion of photons absorbed by a fluorophore which then result in the emission of a fluorescent photon, thereby influencing the brightness of a given fluorophore. The quantum yield of a fluorophore is determined by its rates of radiative and non radiative decay (k_r and k_{nr}, respectively) according to the following expression [19]:

$$\Phi_f = \frac{k_r}{k_r + k_{nr}}. \tag{2.1}$$

2.1.2 Fluorescence decay and lifetime

The radiative and non-radiative decay rates also define the fluorescence lifetime (τ) of a given fluorophore; the lifetime is inversely proportional

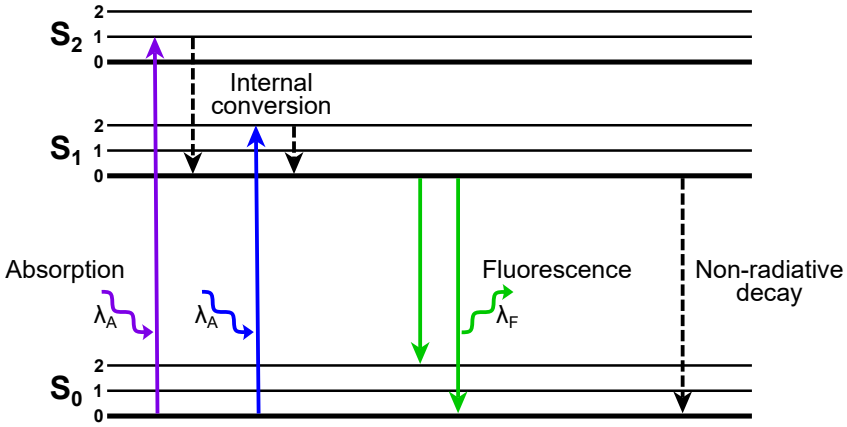


Figure 2.1: A Jablonski diagram illustrating the fluorescence process. An incident photon with wavelength λ_A is absorbed by the fluorophore, causing it to transition to an excited state. From this excited state it undergoes rapid non-radiative transition to the lowest vibrational level of S_1. From S_1 it returns to the ground state S_0 either through non-radiative processes or through the emission of a fluorescent photon with a longer wavelength λ_F.

to the sum of the radiative and non-radiative decay rates, as expressed by [19]:

$$\tau = \frac{1}{k_r + k_{nr}}. \tag{2.2}$$

Fluorescence emission is a stochastic process so the fluorescence lifetime is the average time a fluorophore remains in the excited state before returning to the ground state and emitting a photon [19, 20]. The lifetime is an intrinsic property of a fluorophore in a specific environment and, within reasonable limits, is independent of its concentration; this can be a key advantage over intensity-based measurements [3, 21]. It is sensitive to the environment of the fluorophore, including pH, temperature, viscosity, and binding state, meaning the measurement of a fluorophore's lifetime can provide important information about its environment [1, 20]. In reality, many samples exhibit complex decay patterns characterised by two or more lifetimes; this is due to the presence of populations of different fluorophores or subpopulations of the same fluorophore in different states [22].

2.2 Measurement techniques

2.2.1 Time-domain fluorescence measurements

Time-domain methods for measuring fluorescence lifetime directly measure the number of fluorescent photons emitted over time following a short excitation light pulse. If a sample is excited with an infinitely short pulse of excitation light, this creates a population of fluorophores in an excited state. These fluorophores then decay over time according to the decay rates, k_r and k_{nr}. The rate of change in the number of excited fluorophores is described by the differential equation:

$$\frac{dN^*(t)}{dt} = N^*(t).(k_r + k_{nr}) = \frac{N^*(t)}{\tau} \tag{2.3}$$

where $N^*(t)$ is the number of excited fluorophores at a time t following the excitation pulse. For a sample containing a single fluorophore in a homogenous environment, $N^*(t)$ is then given by:

$$N^*(t) = N_0^* e^{-\frac{t}{\tau}} \tag{2.4}$$

where N_0^* denotes the number of excited fluorophores at $t = 0$. The rate of fluorescent photon emission $I(t)$ is then found by multiplying the number of excited fluorophores by the radiative decay rate,

$$I(t) = k_r \cdot N^*(t). \tag{2.5}$$

We can substitute equation 2.4 for $N^*(t)$ giving

$$I(t) = k_r \cdot N_0^* e^{-\frac{t}{\tau}}. \tag{2.6}$$

N_0^* and k_r are both constants and multiplying them together gives the rate of fluorescent photon emission at $t = 0$ (denoted here as I_0). The time-resolved fluorescent emission can therefore be described by a mono-exponential decay with a decay constant equal to the fluorescence lifetime τ:

$$I(t) = I_0 e^{-\frac{t}{\tau}}. \tag{2.7}$$

As has been stated already, samples often exhibit two or more lifetimes due to the presence of multiple fluorophores in different states. In the general case of a sample with n lifetime components, the fluorescent emission can be described by a weighted sum of exponential decays,

$$I(t) = I_0 . \sum_{i=1}^{n} \alpha_i e^{-\frac{t}{\tau_i}}, \tag{2.8}$$

where α_i is the fractional contribution of lifetime component τ_i such that

$$\sum_{i=1}^{n} \alpha_i = 1. \tag{2.9}$$

After analysis, an average fluorescence lifetime for a sample is often reported; this may be the intensity average lifetime $\langle\tau\rangle_f$ or the amplitude average lifetime $\langle\tau\rangle_a$. The intensity average lifetime can be defined as the average time of a mixed population of fluorophores remain in an excited state. Each lifetime component is weighted by its relative contribution to the total fluorescence decay. $\langle\tau\rangle_f$ can be calculated using the following expression 2.10 [23]:

$$\langle\tau\rangle_f = \frac{\sum_{i=1}^{n} \alpha_i \tau_i^2}{\sum_{i=1}^{n} \alpha_i \tau_i}. \tag{2.10}$$

The amplitude average lifetime is instead calculated using the expression 2.11:

$$\langle\tau\rangle_a = \sum_{i=1}^{n} \alpha_i \tau_i, \tag{2.11}$$

where each lifetime component τ_i is weighted by its fractional contribution α_i. $\langle\tau\rangle_f$ is less stable than $\langle\tau\rangle_a$ as it requires lifetime components to be well resolved [24]. However, it can be useful for the analysis of heterogeneous biological systems with multi-exponential decay dynamics; it can be used to estimate the energy transfer efficiency in Förster resonance energy transfer (FRET) or to investigate quenching behaviours [25].

In practice, it is not possible to create an infinitely short pulse of excitation light, nor is it possible to take a perfectly precise measurement of photon emission times. The precision of a given FLT measurement system is defined by its instrument response function (IRF). The IRF

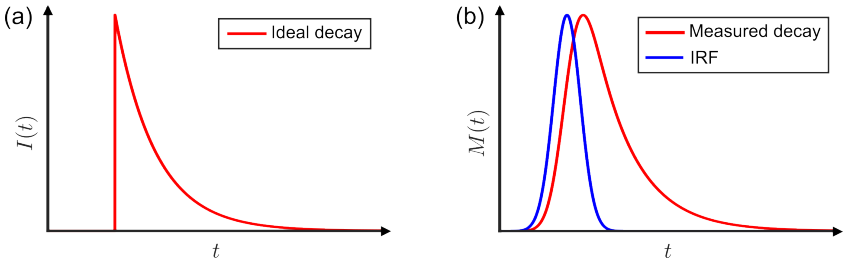


Figure 2.2: An illustration of the effect of the IRF on the measured fluorescence decay. The IRF is a representation of the instruments response to an infinitely short decay. It has the effect of smearing out the measured decay (right) when compared to the ideal decay model (left). The broader the IRF, the more pronounced the effect will be.

characterises how the system would respond to an ideal, infinitely short fluorescence decay, effectively describing the system's temporal resolution. The primary contributors to the IRF are the temporal response of the detector, timing jitter in the system electronics, the temporal shape of the excitation light pulse, and dispersion in the system optics. The fluorescence decay measured by a system, $M(t)$, is the convolution of the ideal fluorescent decay in equation 2.8 with the system IRF:

$$M(t) = \mathrm{IRF}(t) * I(t). \tag{2.12}$$

The effect of the IRF on the decay curve measured by a system is illustrated in Figure 2.2.

2.2.2 Time-correlated single photon counting

Time-correlated single photon counting, or TCSPC, involves repeated detection of single photons and recording of their arrival time relative to a periodic reference signal [19, 26], as illustrated schematically in Figure 2.3. For FLT measurements, the reference signal comes from the excitation source, typically a pulsed laser operating with a repetition rate in the MHz range. A single fluorescent photon is detected using a high-gain detector, such as a PMT or a SPAD. The arrival time of the photon relative to the reference signal is recorded and assigned to a discrete time bin. This process is repeated many times and a histogram of photon arrival times is gradually built up which reflects the fluorescence decay being measured as illustrated in Figure 2.4 [5, 26].

TCSPC is a widely used time-domain technique which is employed in many commercially available FLT spectrometers and confocal FLIM systems. It can have excellent time resolution as the system IRF width is dictated by the timing jitter in the rising edge of the detector's response, not by its temporal width [26]. The technique is sensitive to individual

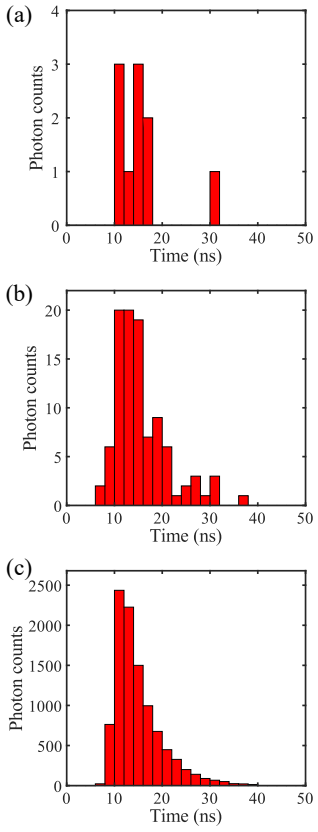


Figure 2.4: Simulated photon arrival-time histograms after detection of (a) 10, (b) 100, and (c) 10,000 photons. As the number of detected photons increases, the measured distribution more closely resembles the expected decay curve.

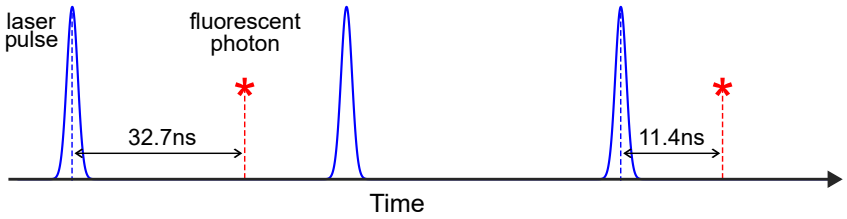


Figure 2.3: A schematic of the TCSPC method. The time delay between the excitation laser pulse and single detected photons are recorded. This is repeated many thousands or millions of times to build up a histogram of photon arrival times.

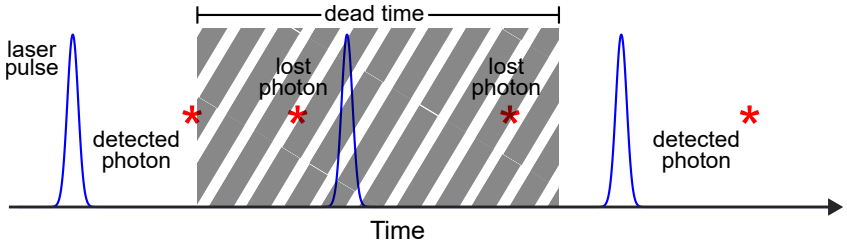


Figure 2.5: A schematic of the pileup effect that can occur with traditional TCSPC systems. After a photon is detected, the detector and electronics have a fixed dead time where the system cannot detect any photons. If a second photon arrives during this dead time then it is lost. If two photons are regularly arriving during a single laser cycle, it will distort the photon arrival time statistics, biasing photons that arrive early in the detection window.

photons making it suitable for measurement of weak fluorescence signals where analog measurements are not possible [27].

A limitation of TCSPC is that the acquisition speeds are limited by the maximum count rate achievable. Traditional TCSPC systems are designed to detect only one photon per excitation cycle. If a second photon arrives during one laser cycle then it will be lost; if this were to occur very often throughout a measurement then it would lead to a distortion of the measured signal which over represents early-arriving photons, an effect referred to as pile-up [26, 27]. In addition to this, both the detector and electronics have a dead time following the detection of a photon. At sufficiently high laser repetition rates this dead time can extend into subsequent laser cycles. Any photons arriving during this dead time are also lost. These two effects are illustrated in Figure 2.5.

Because of this, count rates in standard TCSPC systems are typically limited to approximately 1 % to 5 % of the laser repetition rate. For instance, with a 20 MHz laser, the detector count rate should be limited to 0.2 MHz to 1 MHz to avoid pile-up.

More modern detection systems using low dead time time-to-digital converters (TDC) have been reported which are capable of recording multiple photon arrival times from the same laser pulse, thereby increasing the maximum count rate [28]. The maximum count rate can also be increased by splitting the light collected into parallel detection channels with parallel TCSPC modules. Such systems have not been applied in this thesis, however.

2.2.3 Time-gating

In time-gating the detector is activated at specific time intervals after the excitation pulse, meaning the fluorescence emission is only detected during specific time windows (gates) [21]. The delay time can be shifted in steps to acquire photons at different delay times. This enables the fluorescence decay across the sample to be reconstructed as illustrated in Figure 2.6. The number of time gates acquired and their width can be tuned to trade off between temporal precision and acquisition speed. Acquiring photons over fewer gates with a larger width will be faster but will result in a coarser measurement of the fluorescence decay. This technique can be performed with gated image intensifiers or SPAD arrays [20].

This approach can provide fast FLIM acquisition, especially for wide-field imaging, allowing much higher count rates than TCSPC [5]. However, it is quite optically inefficient as any photons which arrive outside

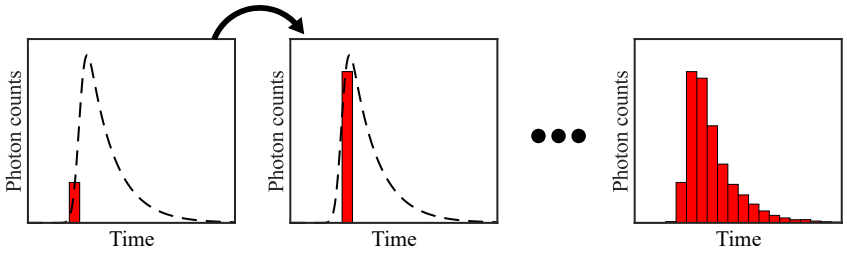


Figure 2.6: A schematic of the time-gating measurement technique. The decay curve is sampled in a short window (time gate). The position of this gate is then shifted over several measurements to recover the full decay curve.

the time gate are lost [28] and has a lower time resolution than TCSPC [5].

2.2.4 Pulse sampling

Pulse sampling refers to techniques where the entire fluorescence decay waveform after a pulsed excitation is directly recorded using fast-response detectors such as a photomultiplier tube (PMT) or an avalanche photodetector (APD) and digitisers with GHz bandwidth [1]. As seen in Section 3.1, this method is used in many clinical FLIm systems, often in combination with multispectral detection [1].

Data processing typically involves averaging waveforms to improve signal-to-noise ratio and correcting for background signals. Pulse sampling is less susceptible to interference from background illumination which is beneficial for integration into clinical procedures where bright room lights are desirable for clinicians [1, 29]. However, analog detection means high energy laser pulses are required for good signal-to-noise ratio (SNR); for *in vivo* applications this needs to be closely monitored to ensure safe exposure limits are not exceeded and to prevent thermal and photochemical tissue damage [28, 30]. The temporal resolution of pulse sampling is limited by the bandwidth of the digitiser used and by the temporal single-photon response of the detector; this limits the ability to resolve multi-exponential decays, especially those containing lifetime components faster than 300 ps [28].

2.2.5 Frequency domain fluorescence measurements

Although this thesis focuses on time-domain FLIm, frequency-domain FLIm (FD-FLIm) is briefly introduced here for completeness, as it represents an alternative approach widely used in fluorescence lifetime microscopy and macroscopic imaging. Because FD-FLIm was not applied in this work, only a high-level overview is provided, and the analysis methods described later in this chapter pertain exclusively to time-domain techniques.

FD-FLIm estimates fluorescence lifetimes by modulating the excitation light at a radio frequency and analysing the response of the emitted fluorescence. Due to the finite lifetime of the excited state, the emitted fluorescence is delayed relative to the excitation and its modulation amplitude is reduced. These effects can be quantified using either the phase delay or the modulation depth of the fluorescence signal.

The phase lifetime (τ_ϕ) is derived from the phase shift (ϕ) between the modulated excitation and the delayed fluorescence emission. It represents the average temporal delay of the fluorescence signal:

$$\tau_\phi = \frac{tan(\phi)}{\omega}, \tag{2.13}$$

where ω is the angular modulation frequency of the excitation source.

The modulation lifetime (τ_M) is instead derived from the reduction in modulation depth (M) of the fluorescence emission compared to the excitation:

$$\tau_M = \frac{1}{\omega}\sqrt{\frac{1}{M^2} - 1}. \tag{2.14}$$

Phase and modulation lifetimes are mathematically related to time-domain measurements through the Fourier transform [3, 21]. For a single-exponential decay, τ_ϕ and τ_M are identical, but for multi-exponential or complex decays they generally differ, with the phase lifetime weighting longer components more and the modulation lifetime more sensitive to shorter components.

One of the main advantages of FD-FLIm is its ability to achieve high-speed acquisition. Lifetime estimation is derived from phase and modulation, without reconstructing the full decay curve. This significantly reduces acquisition time, making the technique well-suited for real-time imaging. FD-FLIm also simplifies the electronics compared to time-correlated single-photon counting (TCSPC). Instead of requiring picosecond timing of individual photons and complex time-to-digital converters, FD-FLIm uses analog phase detection or on-chip demodulation. This reduces hardware complexity and data throughput because only two parameters, phase and modulation, are extracted per pixel [5]. Furthermore, FD-FLIm does not require single-photon sensitivity; detectors operate in linear mode, measuring the analog modulation of the fluorescence signal rather than discrete photon arrival times. This allows the use of conventional high-speed detectors rather than specialised single-photon devices.

Despite these advantages, FD-FLIm has some limitations. Accurate lifetime determination requires precise calibration to correct for phase errors and instrument response, which can introduce complexity in system setup. The technique is also less robust for samples exhibiting multi-exponential decays, where phase-based estimation becomes less reliable. Furthermore, while FD-FLIm offers excellent speed, its temporal resolution is generally lower than that achieved by TCSPC, making it less suitable for applications requiring precise characterisation of fast decay components.

2.3 Analysis Methods

Once fluorescence data has been acquired, appropriate analysis methods are required to extract the sample lifetimes. Since frequency-domain FLIm was not implemented in this thesis, the discussion here focuses exclusively on time-domain data processing. In this work, this has been done using curve fitting; the acquired data is fit to a model of fluorescence decay yielding lifetime values that best describe the observed data. The model applied can be an ideal exponential decay as in equations 2.7 and 2.8, this is herein referred to as tail fitting. Alternatively, the model can take into account the influence of the system's IRF as in equation 2.12, this is herein referred to as reconvolution fitting. Both of these fitting methods are explained below and implemented on the same example dataset for comparison.

The data used for fitting is example data provided with the operation software for the PicoQuant PicoHarp 300 TCSPC module. At the time of writing, the software (and the data within it) is freely available online [31]. The data is a fluorescence decay acquired from a sample of Coumarin 6 dye in ethanol using 440 nm laser excitation at a 10 MHz repetition rate, and 520 nm emission detection with a PMT.

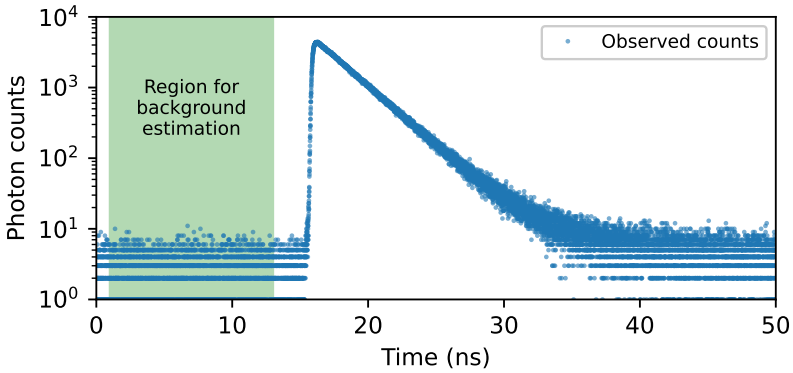


Figure 2.7: The example data set used here for demonstrating the fitting process. The data was acquired from a sample of Coumarin 6 fluorescent dye using 440 nm excitation and a TCSPC system with a PMT detector. The region from which the background counts can be estimated is also indicated on the plot.

2.3.1 Tail fitting

Tail fitting involves fitting an exponential decay model to the later part of the measured signal. This approach doesn't consider the influence of the system IRF on the measured signal, therefore it will not yield as accurate results as methods which do take this into account, especially for decay components of a similar size to the IRF width. However it can be useful when knowledge of the system IRF is not available.

Before fitting can be performed, there is some pre-processing on the data required, beginning with background correction. For real-world measurements, the photon counts observed will be offset from zero by a background offset; this can come from ambient light in the room or from the dark count rate of the detector. The background offset can be included as a fitting parameter if preferred, but it is often possible to select a region in the measurement where no visible fluorescence is detected; the photon counts over this region can be averaged to estimate the background and then subtracted from the signal to obtain the background-corrected count values. Care must be taken when using this approach for fluorophores with longer lifetimes; in these cases, the tail of the decay can be long enough that it wraps around and can be seen at the beginning of the measurement window. Any region including the tail for the decay should not be included for background estimation of course. This effect can be mitigated by using a lower laser repetition rate but this will lead to a corresponding increase in acquisition time. The observed background-corrected counts in time bin t_j is denoted c_j. The sample data is presented in Figure 2.7 and the region for background estimation indicated.

The next step is to select the region of the signal over which to perform fitting. For tail fitting this should begin enough beyond the peak of the curve that the influence of the IRF has mostly subsided. In this case we will fit from 80 % to 1 % of the maximum observed counts on the falling edge of the decay. Let a and b denote the time-bin indices after the peak where c_j first falls below 80 % and 1 % of the max value respectively. Fitting will then be performed over the time window t_a to t_b.

Next we determine the model for fitting. For this example a mono-exponential decay model is used, therefore the predicted counts is given by the expression 2.15:

$$\hat{c}_j = I_0 \exp -\frac{(t_j - t_0)}{\tau}. \tag{2.15}$$

Here t_0 is the time bin where the fluorescence decay "starts". With real data there is no exact moment the decay starts but t_0 can be estimated as the time bin with the maximum photon counts or alternatively the steepest point on the rising edge of the measured decay[1]. Either of these estimation methods are preferred to a user-defined t_0 as they are repeatable and can be applied consistently across multiple measurements.

I_0 is sometimes included as a fitting parameter but we can also constrain it according to equation 2.16:

$$\sum_{j=a}^{b} \hat{c}_j = \sum_{j=a}^{b} c_j. \tag{2.16}$$

This enforces the condition that, over the fitting range, the total predicted photon events is equal to the total observed photon events. The value of I_0 can then be found as follows by substituting the expression for $\hat{c}_j$ from equation 2.15 and moving I_0 outside of the summation:

$$I_0 \sum_{j=a}^{b} \exp -\frac{(t_j - t_0)}{\tau} = \sum_{j=a}^{b} c_j, \tag{2.17}$$

$$I_0 = \frac{\sum_{j=a}^{b} c_j}{\sum_{j=a}^{b} \exp -\frac{(t_j - t_0)}{\tau}}. \tag{2.18}$$

For the work in this thesis, fitting is performed through minimization of the sum of weighted squared residuals. Here this takes the form of a Pearson's chi squared, χ^2_P, in which squared residuals are weighted by dividing by the predicted counts and then summed over the fitting region [32], this is expressed as:

$$\chi^2_P = \sum_{j=a}^{b} \frac{(c_j - \hat{c}_j)^2}{\hat{c}_j}. \tag{2.19}$$

A value of τ which minimises the above expression is then found using an optimisation algorithm, typically the Levenberg-Marquardt algorithm. The fitting result is evaluated by calculating the reduced chi-squared value χ^2_{red} over the fitting range, this is found by dividing χ^2_P by the degrees of freedom such that

$$\chi^2_{red} = \frac{1}{b - a - p} \chi^2_P, \tag{2.20}$$

where $b - a$ gives the number of time bins used for fitting and p is the number of fitting parameters and constraints. In this case $p = 2$ as we have one fitting parameter τ and one constraint as imposed in equation 2.16. The closer the value of χ^2_{red} is to 1, the better the fit is considered.

The results of fitting can be visualised by plotting the observed and predicted counts as shown in Figure 2.8. The residuals (the difference between the observed and predicted counts) are also presented; residuals randomly distributed around zero are desirable within the fitting range. For this data, a lifetime value of 2.60 ns was obtained with a χ^2_{red} of 1.12 using tail fitting.

[1] In the case of a monoexponential decay model, the choice of t_0 does not affect the result. However, for a multiexponential model, it can influence the relative weightings of the lifetime components. For lifetime values within the range where tail-fitting is appropriate, this impact is likely to be small. Tail fitting with multiexponential models has not been applied in this thesis; therefore, a detailed discussion of this effect is not included.

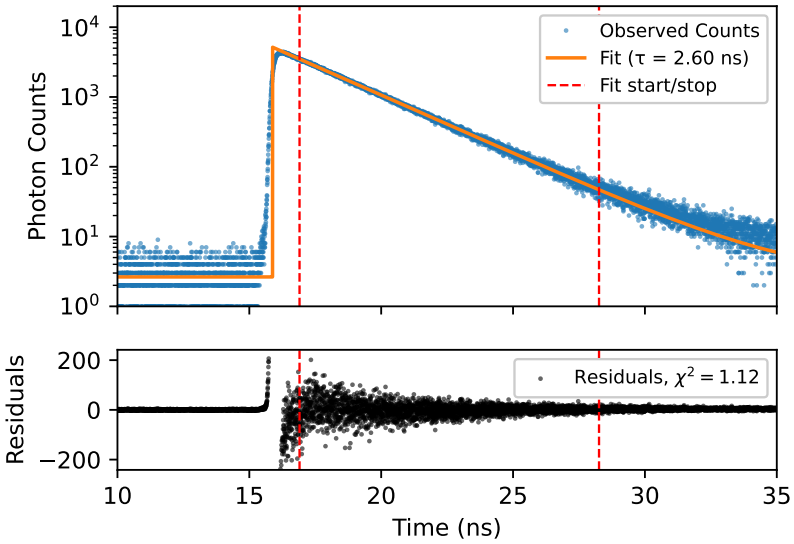


Figure 2.8: The results of tail fitting on a fluorescence decay measurement from Coumarin 6 dye. The measured photon counts and the fitted model are plotted in the upper axes while the residuals ($c_j - \hat{c}_j$) are shown in the lower graph. The fitting range (t_a to t_b) is indicated by the dashed red lines in both plots. An optimum τ value of 2.60 ns was obtained after fitting. The residuals appear randomly distributed either side of zero over the fitting range and a χ^2_{red} value of 1.12 indicates a good fit.

A better fit with measured data can often be achieved by increasing the number of lifetime components in a the model applied, and therefore the number of fitting parameters. The equation for $\hat{c}_j$ then takes the following form:

$$\hat{c_j} = I_0 \sum_{i=1}^{n} \alpha_i \exp - \frac{(t_j - t_0)}{\tau_i}. \tag{2.21}$$

However, the number of components should ideally be chosen based on knowledge of the expected photophysics of the sample. Without this, the inclusion of additional lifetime components can lack physical meaning.

2.3.2 Reconvolution fitting

If a measurement of the system IRF has been taken, we can incorporate this into out model for fitting by convolving the IRF with the exponential decay model as in equation 2.12. This allows compensation for the imperfection of the measurement system, thereby yielding more reliable lifetime measurements, especially at shorter lifetimes. The IRF can be measured by removing the filter from the detection path and directly measuring the laser pulse from a scattering, non-fluorescent sample. This sample is often LUDOX® silica beads or a piece of frosted glass. Alternatively, an IRF measurement can be obtained from a quenched fluorescent dye with a very fast decay, much shorter than the width of the laser pulse. This second option has the benefit of measuring the IRF at a similar wavelength range as the fluorescence of future samples; this can become significant for detectors with wavelength-dependent response times, such as SPADs.

For the example data used in the previous section, a measurement of the IRF has also been provided and is presented in Figure 2.9. Before applying the IRF in the fitting model, the background counts should be

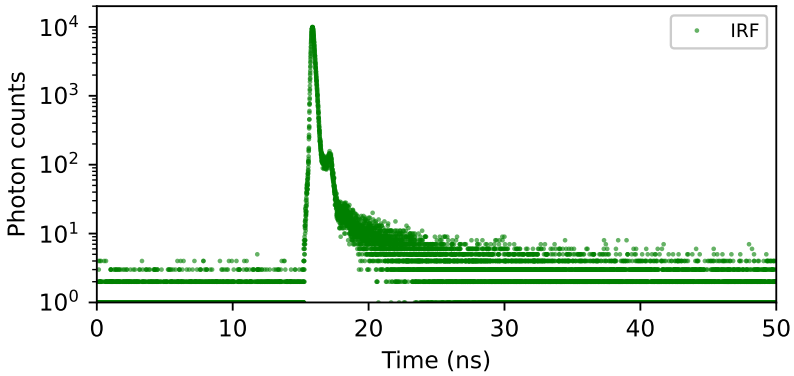


Figure 2.9: The measurement of the instrument response function (IRF) provided with the example decay data. Background subtraction should be performed before applying the IRF for reconvolution fitting.

estimated and subtracted; this can be done in the same way as was done previously with the data.

The predicted counts are now obtained from the discrete time convolution of an ideal exponential decay and the system IRF. For a monoexponential decay the predicted counts c_j for a given time bin j is found using equation 2.22,

$$\hat{c}_j = I_0 \sum_{k=-\infty}^{\infty} w_j \exp -\frac{(t_{k-j} - t_0)}{\tau}, \tag{2.22}$$

where w_j is the IRF value in the j^{th} time bin. In this instance, t_0 is now the temporal offset between the IRF measurement and the fluorescence decay and is included as a fitting parameter along with τ. This offset can arise from a few sources: if the IRF has been recorded at the excitation wavelength, it can be due to different propagation speeds through optical elements of the system compared to the fluorescence signal; or from different detector response times at the excitation wavelength; or in some systems, a different optical path is used for recording the IRF causing an offset in the arrival time.

Similarly as before, in the general case of a multiexponential model with n lifetime components, $\hat{c}_j$ is expressed as:

$$\hat{c}_j = I_0 \sum_{k=-\infty}^{\infty} w_j \sum_{i=1}^{n} \alpha_i \exp -\frac{(t_j - t_0)}{\tau_i}. \tag{2.23}$$

The same constraint on the total photon counts over the fitting range from equation 2.16 can be applied here; for a monoexponential decay I_0 is now obtained from equation 2.24:

$$I_0 = \frac{\sum_{j=a}^{b} c_j}{\sum_{j=a}^{b} \sum_{k=-\infty}^{\infty} w_j \exp -\frac{(t_{k-j} - t_0)}{\tau}}. \tag{2.24}$$

From this point, the fitting process can be carried out in the same way as with tail fitting over the same fitting range (t_a to t_b); optimum values of τ and t_0 are found which minimise equation 2.19, and the fit is evaluated by calculating χ^2_{red} using equation 2.20. In this case we have two parameters (τ and t_0) and one constraint from equation 2.16, so $p = 3$. The results of reconvolution fitting using the example data and IRF are shown in Figure 2.10 along with a plot of the residuals; a lifetime value of 2.47 ns was obtained with a χ^2_{red} of 1.12.

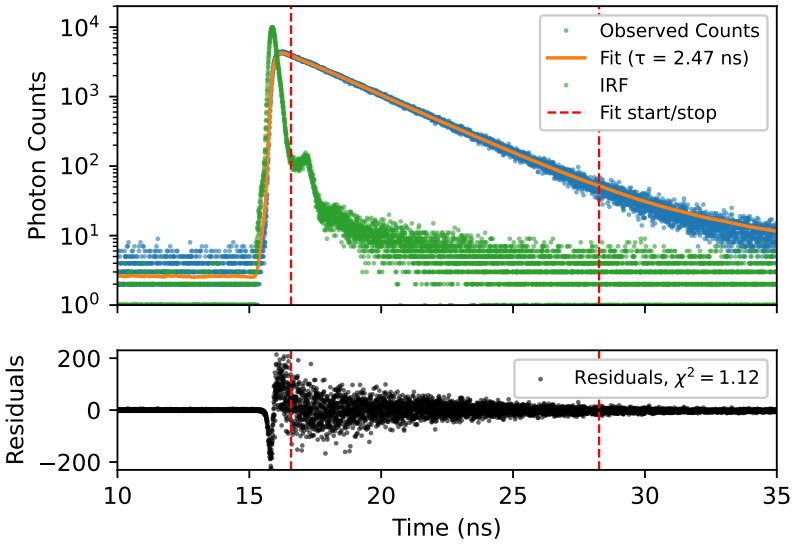


Figure 2.10: The results of reconvolution fitting on a fluorescence decay measurement from Coumarin 6 dye. The measured photon counts, IRF, and fitted model are shown in the upper plot. The residuals are shown in the lower plot. The fitting range is indicated by the dashed red lines. An optimum τ value of 2.47 ns was obtained after fitting. The residuals appear randomly distributed either side of zero over the fitting range and a χ^2_{red} value of 1.12 indicates a good fit.

Interestingly, the two fitting methods produce identical χ^2_{red} values indicating an equally good fit to the observed data. However, considering that reconvolution takes into account the response of the system (i.e. additional information about the measurement system), it is reasonable to accept this as a more accurate measurement of the sample photophysics. A lifetime value for Coumarin 6 of 2.5 ns is often used as a standard with 460 nm excitation for system calibration [33, 34], and Szlazak et al. [35] report a lifetime of 2.48 ns using 440 nm excitation, the same as was used for the example data presented here. This shows good agreement with the result obtained using reconvolution fitting.

Tail fitting can still be of use for detecting a lifetime contrast between different samples measured with the same system (or different locations on the same sample), though this contrast will be limited for lifetimes values approaching the IRF width. For an accurate absolute measurement of sample lifetimes, reconvolution fitting is preferred.

2.3.3 Fast lifetime estimation

In addition to the fitting-based methods described above, a fast estimation technique for fluorescence lifetimes was also applied in this thesis, herein referred to as FastLT. This method was used for the microscopic inspection of the solid-state FLT standards described in Paper **IV** using the Fast FLIM method[2] in PicoQuant's SymPhoTime fitting software.

The FastLT method estimates the average lifetime as the time difference between the barycentre (or centroid) of the IRF and the barycentre of the measured decay. This approach is computationally efficient and particularly useful for generating initial lifetime maps or for applications where speed is critical.

Mathematically, the barycentre of a decay curve $I(t)$ is given by:

[2] https://www.tcspc.com/doku.php/glossary:fast_lifetime

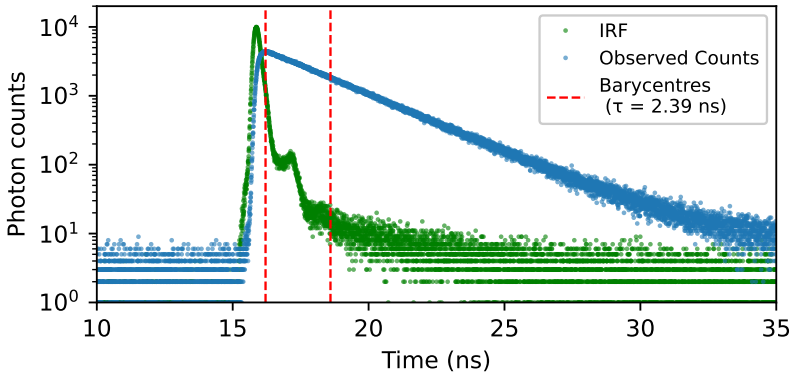


Figure 2.11: Application of the FastLT method to the Coumarin 6 decay dataset. The observed fluorescence decay and the instrument response function (IRF) are shown, along with their respective barycentres. The estimated average lifetime, calculated as the time difference between the two barycentres, is 2.39 ns.

$$\langle t \rangle = \frac{\sum_j t_j I(t_j)}{\sum_j I(t_j)}. \tag{2.25}$$

The estimated average lifetime τ_{FastLT} is then:

$$\tau_{\text{FastLT}} = \langle t \rangle_{\text{decay}} - \langle t \rangle_{\text{IRF}}. \tag{2.26}$$

If a measurement of the IRF is not available, a start time t_0 must be estimated by other means, such as were proposed in section 2.3.1. However, this can introduce a systematic offset in the estimated lifetimes. While this method does not resolve multiple exponential components, it is robust to low photon counts and provides a useful approximation of the average lifetime. This makes it well suited for rapid screening or for use in systems with limited computational resources.

By applying the FastFLT method to the same Coumarin 6 dataset used previously, the estimated average lifetime was found to be 2.39 ns as shown in Figure 2.11. This value is slightly lower than the values obtained using tail fitting (2.60 ns) and reconvolution fitting (2.47 ns). This small discrepancy is expected, given the simplicity of the estimation approach. Nonetheless, the method is useful for rapid and reasonably accurate lifetime estimation.

2.3.4 Error analysis in lifetime estimation

Error analysis is an important consideration in fluorescence lifetime imaging, as uncertainties arise from photon shot noise, background subtraction, and the non-linear fitting used to extract decay parameters. At the single-pixel level, the precision of a fitted mono-exponential lifetime can be estimated from the covariance matrix of the fit or by standard error-propagation methods. These confidence intervals reflect the variability expected from repeated measurements of the same pixel and depend strongly on photon statistics; higher photon counts yield lower statistical uncertainty, with the standard error approximately scaling as $1/\sqrt{N}$, where N is the number of detected photons [36]. Typical thresholds reported in the literature for reliable mono-exponential fitting lie in the range of 10^3–10^4 detected photons per pixel [36]. For multi-exponential models, the photon requirements are generally higher due to increased parameter correlation and fitting complexity; however, this is not explored

in detail here because only mono-exponential fitting was performed in this work.

Although pixel-level confidence intervals quantify measurement noise, they do not capture spatial or biological heterogeneity and therefore do not directly represent the uncertainty of a larger region or sample. For this reason, uncertainty is assessed at the image level by reporting the mean and standard deviation across groups of pixels. This approach, widely adopted in FLIm studies [37], provides a robust measure of variability while avoiding the instability of per-pixel error estimates in low-photon regimes.

2.4 Phototoxicity and safe exposure considerations

Optical excitation is an essential element of fluorescence lifetime imaging; in the context of in vivo applications where tissue is directly illuminated, this excitation must be carefully controlled to avoid photothermal or photochemical injury. Only certain tissues have well-established exposure limits; in particular, I.S. EN 60825-1 provides maximum permissible exposure (MPE) values for the skin and for ocular tissues (cornea, lens, and retina) [38], forming the regulatory basis for laser safety evaluations in biomedical systems. No specific exposure standards exist for deeper tissues or hollow organs, so these superficial tissue limits are the only formal references available. It is also important to recognise that accurate fluorescence lifetime estimation requires detecting sufficient photons (typically on the order of 10^3–10^4 per pixel for robust fitting), so the achievable measurement precision is fundamentally constrained by how many excitation photons can be delivered to the tissue while remaining below these MPE-defined safety limits.

Although all experiments were conducted on ex vivo specimens, comparing the delivered exposure to appropriate MPE values is important for understanding potential clinical translatability. In this context, ocular MPEs are substantially lower than those for the skin. This is primarily because the ocular media and pupil can collect and focus incident light onto a small retinal spot, greatly amplifying local irradiance and creating a more restrictive hazard condition. These more stringent limits therefore reflect a specific ocular risk rather than general tissue vulnerability. Because the imaging systems developed in this thesis are neither configured nor intended for ocular exposure, safety is assessed against the skin MPEs. These provide the most appropriate reference in the absence of standards for deeper tissues. For each system, the exposure from a single pulse and the time-averaged irradiance at the tissue plane are compared to the relevant skin MPE defined in I.S. EN 60825-1 [38]. All evaluations are performed using the standard's 3.5 mm skin-limiting aperture as defined in the standard [38], ensuring that irradiance or radiant exposure is averaged over a biologically meaningful area. The evaluation methodology is described in Section 5.1.4, with only the results stated for subsequent evaluations. The purpose of these assessments to provide an informed indication of the extent to which the operating conditions fall below recognised limits, providing evidence of their potential for future *in vivo* translation.

2.5 Summary

This chapter has outlined the fundamental principles and methodologies for FLIm which have been applied in this thesis. The fundamental principles of fluorescence and of fluorescence lifetimes were introduced, highlighting their sensitivity to the local molecular environment. Key time-domain measurement techniques have been described, including some

advantages and limitations in terms of temporal resolution, acquisition speed, and optical efficiency. Finally, the analytical approaches applied in this thesis to extract lifetime information have been detailed. Together, this forms the basis for understanding and interpreting FLIm data in the context of the experimental work that follows.

Chapter 3

In vivo FLIm

As was mentioned in Chapter 1, FLIm has demonstrated significant potential in biomedical diagnostics, particularly in *ex vivo* tissue analysis, particularly in *ex vivo* tissue analysis, where controlled conditions allow detailed characterisation of endogenous fluorophores [2, 9–11]. These studies showed that lifetime contrast can reveal biochemical differences between tissue types, motivating the development of *in vivo* FLIm systems to determine whether these contrasts can still be measured under physiological conditions. However, translating this capability to clinical settings introduces unique challenges and opportunities. Key challenges include tissue motion during imaging, restricted access to target sites, and the need for integration into existing clinical workflows.

A critical consideration is the variation in fluorescence lifetimes measured *in vivo* compared to those observed *ex vivo*, even for nominally similar tissues [1, 39]. This discrepancy arises from physiological changes following excision, such as loss of perfusion and oxygenation, altered pH, and temperature shifts, all of which influence the redox state of fluorophores like NADH and FAD. Additional factors, including differences in hydration and scattering, further contribute to lifetime shifts. These variations complicate the direct application of *ex vivo* calibration data to *in vivo* diagnostics and increase the risk of misclassification when diagnostic thresholds are derived from ex vivo studies. Consequently, robust strategies are required to account for these differences, including adaptive calibration methods and algorithms capable of handling dynamic physiological conditions. While these challenges add complexity, they also present opportunities: lifetime sensitivity to perfusion, metabolism, and micro-environmental changes may provide clinically valuable insights that are inaccessible in *ex vivo* measurements.

This chapter reviews the current state-of-the-art FLIm systems developed for *in vivo* applications. The systems are categorised based on their imaging modalities: free-hand scanning, helical scanning, laser scanning, and wide-field imaging; their respective advantages, limitations, and clinical relevance are then discussed. The chapter also introduces the use of single-photon avalanche diode (SPAD) arrays for wide-field FLIm, with a focus on their potential for miniaturisation and clinical translation. This review establishes the technological context and motivation for the development of compact, chip-on-tip FLIm systems.

3.1 State of the art

The efficacy of FLIm with thin *ex vivo* samples from patients raises the question of the potential clinical benefits that could be provided by such measurements performed on bulk tissue *in vivo*. Because of this, there

has been much research in the translation of these measurements into clinical applications, and in particular, the development of systems that can acquire lifetime information *in vivo* during surgical procedures. The systems developed already have opened vast research opportunities to explore the value of FLT measurements in a wide range of *in vivo* applications.

A recent review of FLIm for biomedical applications can be found in Datta et al. [20], an overview of the clinical translation of FLIm is found in Alfonso-Garcia et al. [1] and in an earlier article from Marcu [9]. Some illustrative examples are outlined here to inform the motivation for this thesis. The different FLIm systems are divided into categories based on how the lifetime image is acquired; free-hand scanning systems acquire an image by scanning the probe over the sample area (or by scanning a sample stage in some *ex vivo* examples); helical scanning systems are rotating point probes which are rotated and retracted at the same time to image the wall of a vessel; laser scanning probes scan a focussed excitation laser spot over the sample area to form an image, often using mirrors mounted on a galvanometer; and wide-field systems image lifetime information from an entire field of view in parallel. Examples of each system type from literature are described and some key performance metrics included for each.

3.1.1 Free-hand scanning

Most existing implementations of *in vivo* FLIm employ point scanning to recover lifetime images. In 2014, Yankelevich et al. [40] reported a clinically compatible fibre-optic based multispectral FLT system, a schematic of this system can be seen in Figure 3.1. The excitation source is a 355 nm pulsed UV laser while the detection module of the system separates the emission into four spectral channels; these channels are temporally delayed relative to one another using different lengths of optical fibre. This allows them to be detected with a single multichannel plate (MCP) gated intensified photomultiplier (PMT). The electronic pulses from the detector are then sampled using a high-speed digitiser with 125 ps temporal resolution. This method of directly sampling pulses for lifetime measurements is referred to as pulse-sampling FLIm (PS-FLIm).

A later PS-FLIm system, developed by the same research group, removed the requirement for temporal separation of the spectral channels

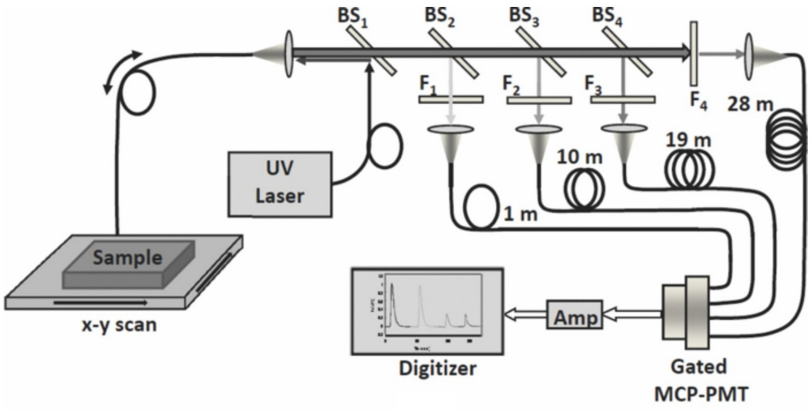


Figure 3.1: Reprinted from Yankelevich et al. [40], with the permission of AIP Publishing. A schematic of a fibre-optic based multispectral FLT system. F1–F4 are optical pass-band filters with center wavelength/bandwidth: 390/40, 452/45, 542/50, and 629/53 nm, respectively. BS1–BS4 are dichroic beam-splitters with >93% transmittance for wavelengths longer than 360, 420, 510, and 590 nm, respectively.

[41]; this was achieved by using three (and later four [42]) avalanche photodetectors, with pulse sampling performed using two 2-channel high-speed digitisers. Tissue autofluorescence is generated by many different components with often overlapping spectral emission (such as structural proteins, porphyrins and lipids) [41]. Therefore, resolving fluorescence lifetime decays into multiple spectral bands can improve the specificity of such measurements.

The front end of these systems, in many cases, simply uses a single optical fibre for both excitation light delivery, and for collection of the fluorescence emission. The fibre tip is scanned across the sample, often by hand, to acquire a lifetime image. Developments have been made to allow these lifetime measurements to be superimposed on a colour image from a surgical microscope; this is done by tracking the location of a visible "aiming beam" for co-registration of the lifetime measurement. This has enabled real-time visualisation of the lifetimes measured at different locations during surgical procedures as is illustrated in Figure 3.2 [30, 43].

Various iterations of the systems above have facilitated the acquisition of vast amounts of *in vivo* and *ex vivo* FLIm data. In particular, they have been used to investigate the efficacy of *in vivo* FLIm for tumour margin detection in the brain [44–46], the oral cavity [43, 47–49], and in resected breast tissue [50, 51].

While the systems above relied on pulse sampling with high-speed digitisers, an alternative approach was demonstrated by a different research group in Lagarto et al. [52]. Their system also performed spectrally-resolved lifetime measurements using multiple detectors, but instead of pulse sampling, it employed a single TCSPC card in combination with a router to serialise the outputs from three PMTs. This configuration enabled simultaneous multi-channel TCSPC. The system was applied *in vivo* to assess structural and metabolic changes in cardiac tissue in a rat model of heart failure, achieving high diagnostic accuracy.

Other free-hand FLIm probes include the system presented by Lagarto et al. [53] which uses 375 nm excitation delivered via a multimode fibre, with emission collected by seven other fibres. The emission is then filtered into a single spectral channel (470 ± 14 nm) and recorded using a hybrid detector and a TCSPC card. This system was demonstrated on bovine heart and lamb kidney samples with visualisation performed similarly to the previous example, where the lifetime measurements were superimposed on a white light image of the sample captured with a USB camera.

The same research group later replaced the TCSPC module in this system with a diffraction grating and a single-photon avalanche diode (SPAD) array, effectively configured as a time-resolved spectrometer [54]. This system was demonstrated for lifetime imaging of porcine articular cartilage *ex vivo* pre- and post-treatment with bacterial collagenase to mimic the degradation that occurs in osteoarthritis, finding a decrease in the fluorescence lifetimes, particularly in regions which had undergone digestion.

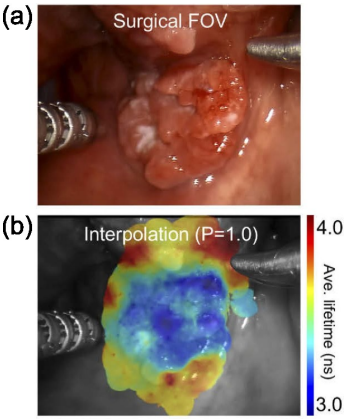


Figure 3.2: Adapted with permission from Marsden et al. [43] © 2020 Optical Society of America. (a) A white light image of a surgical field of view during a clinical head and neck surgery. (b) An overlay of the measured FLT in the same field of view. Sparse point-measurements are visualised using a custom interpolation method where P is a weighting exponent. The FLIm fibre probe is integrated with a da Vinci Si System and deployed using a fibre introducer seen in the left of the image.

3.1.2 Helical scanning

Free-hand point-scanning FLIm probes, like the ones mentioned above, have proved effective for applications which allow adequate space for a probe to be scanned in addition to a colour-imaging modality which can be used for co-registration of the lifetime measurements. Other fibre-based FLIm systems have been reported for more space-restrictive applications.

In Lee et al. [55] a hybrid rotating side-viewing probe uses a combination of FLIm and optical coherence tomography (OCT) to image intravascular plaques in a rabbit artery *in vivo*. The FLIm detection

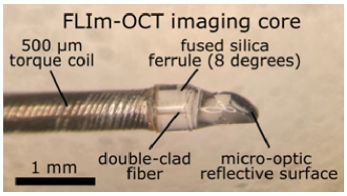


Figure 3.3: Adapted with permission from Bec et al. [59] © 2024 Optica Publishing Group. The FLIm-OCT catheter consisting of a double-clad fibre enclosed in a 500 µm diameter torque coil, a fused silica ferrule, and a side-viewing free-form reflective focusing micro-optic.

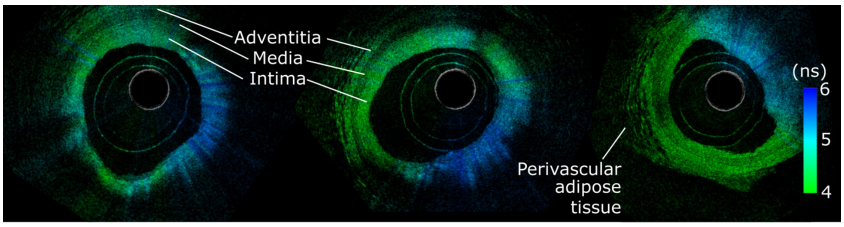


Figure 3.4: Adapted from Li et al. [58] under CC BY 4.0. FLIm-OCT images from three sections of a human coronary specimen. Pixel brightness corresponds to the OCT backscattered intensity whereas the hue corresponds to the FLIm averaged lifetime for the 390 nm spectral band. The OCT penetration depth enables the visualization of the full vessel wall in healthy regions, including some perivascular adipose tissue. Low FLT was found to be associated with healthy regions, whereas longer lifetimes was associated with pathological thickening of the intima and early plaque formation.

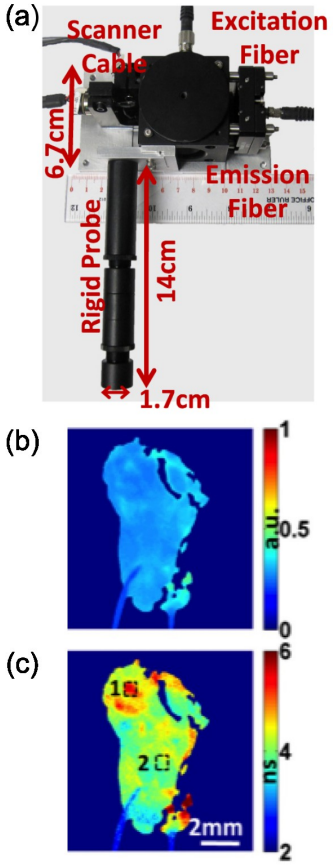


Figure 3.5: Adapted with permission from Cheng et al. [61] © 2014 Optical Society of America. (a) A photograph of the handheld rigid scanning endoscope. (b) Normalised fluorescence intensity map and (c) FLT map of an *ex vivo* human oral biopsy imaged with the rigid endoscope in the >500 nm emission channel. Region 1 in the FLT map was diagnosed as superficial invasive squamous cell carcinoma whereas region 2 which was diagnosed as dysplasia.

module for this system separates spectral channels temporally, similarly to the system described above. Side viewing was achieved by splicing a length of coreless fibre to the tip of a double-clad fibre (DCF) which is then polished at 41°, reflecting the beam to the side. A ball shape for light focusing was then formed on the side of the coreless fibre using a fusion splicer. The catheter is then rotated at up to 100 rotations per second for helical scanning of the vessel wall, achieving a spatial resolution of 80 µm for the lifetime measurements. The single-mode core of the DCF is used to perform OCT while the inner cladding is used for FLIm.

Bec et al. [56] have reported a free-form reflective focusing micro-optical element for side viewing fibre probes. The use of reflective optics can reduce chromatic aberrations, which is important for *in vivo* FLIm considering the broad autofluorescence emission spectrum. This micro-optical element has since been applied for intraluminal lifetime imaging of *ex vivo* murine colon samples [57]; for combined FLIm and OCT in an *ex vivo* human artery specimen [58]; and later for FLIm and polarization-sensitive OCT *in vivo* in a swine heart [59]. The side-viewing fibre probe assembly can be seen in Figure 3.3. A fluorescence excitation spot size of 50 µm was reported by Li et al. [58] using the free-form focusing optic; example FLIm-OCT images acquired with the system can be seen in Figure 3.4.

3.1.3 Laser scanning

The systems already described require mechanical motion at the distal end of the probe. For the free-hand examples the fibre tip is scanned across the sample area, and for the side-viewing catheter systems the tip of the catheter is rotated at high speeds. Other systems have been reported in which a focused excitation laser spot is scanned across the sample using mirrors to acquire a lifetime image. An early PS-FLIm system used galvanometer-mounted mirrors at the back focal plane of a microscope objective to image a cancerous legion in a hamster cheek pouch *in vivo* [60]. The same research group later reported a more compact, handheld, rigid probe with a similar imaging approach which can be seen in Figure 3.5 [61]. This consisted of a handheld box (dimensions: 7 cm × 13 cm × 5 cm, mass: 450 g) attached to a rigid scope (length: 14 cm, diameter: 1.7 cm). The capability of this system was initially demonstrated *in vivo* in a hamster cheek pouch and on *ex vivo* human oral cancer samples. This same system was later applied for discrimination of cancerous tissue *in vivo* in the oral cavity [62].

The same research group also developed a digitally modulated frequency domain FLIm (FD-FLIm) platform capable of simultaneous ultraviolet and visible excitation (375 nm and 445 nm), multispectral detection, and real-time FPGA-based phase and modulation processing [63]. The system supports sub-nanosecond to nanosecond lifetime estimation and was validated through *in vivo* FLIm of human skin and oral mucosa. Building on this engine, the same group implemented a rigid, handheld endoscope that integrates the FD–FLIm approach for imaging of the oral mucosa [64]. In that endoscopic implementation, the average optical power at the distal tip was on the order of 1 mW per excitation wavelength, and a 140 × 140 pixel image was typically acquired in ∼1.6 s at a pixel rate of 12.5 kHz. Together, these works demonstrate that frequency-domain architectures offer promising routes toward simplified, low-cost, and clinically translatable FLIm instrumentation, complementing the time-domain systems reviewed in this chapter.

For applications where smaller, flexible scopes are required, several fibre-bundle based scanning FLIm endomicroscopes have been reported; these systems use coherent fibre bundles for excitation light delivery and fluorescence emission collection with an imaging lens often mounted at the distal end of the probe. The excitation laser is scanned over the proximal end of the fibre bundle, thereby scanning the location of the focused laser spot at the distal end across the field of view. A schematic of a fibre-bundle based scanning FLIm endomicroscope can be seen in Figure 3.6.

Kennedy et al. [66] adapted a commercially available endomicroscope, which was already licensed for clinical use in the gastrointestinal (GI) tract and for bronchoscopy. The probe used a coherent fibre bundle consisting of 30,000 single-mode fibres, achieving a lateral resolution of

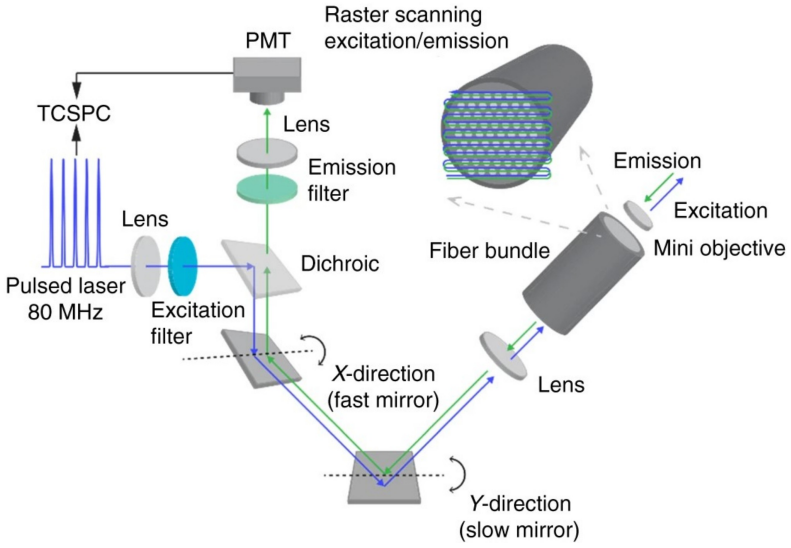


Figure 3.6: Reprinted from Sparks et al. [65] under CC BY 4.0. A schematic of the confocal FLIm endomicroscope system. A Ti:Sapphire laser operating at 80 MHz is frequency-doubled to generate excitation light at 488 nm. Two scanning mirrors scan the focused excitation beam, sequentially exciting the approximately 30,000 individual cores in a coherent fibre bundle. At the distal tip of the probe, a mini-objective lens focuses the excitation light onto a scanning spot on the sample plane. The same lens images the fluorescence signal from the sample back onto the same core of the fibre bundle. At the proximal end, the fluorescence signal is descanned and focused onto a confocal aperture in front of a PMT, with photon arrival times recorded via a TCSPC card.

1.4 µm and a field of view of 240 µm. Crucially, the probe had an external diameter of 2.6 mm, meaning it could be deployed using any endoscope with a working channel of at least 2.8 mm in diameter. 488 nm excitation was provided by a modelocked frequency-doubled Ti:Sapphire laser with a PMT and a TCSPC card used for detection. The system capability was demonstrated by imaging fixed COS-7 cells expressing green fluorescent protein with acquisition times down to almost 1 s. This system was later applied to quantify drug-target engagement *in vivo* in a mouse model of peritoneal metastasis of ovarian cancer, with an effective acquisition time of 10 s per lifetime image [65].

Pedretti et al. [67] developed a fibre-bundle based system which performed imaging in contact with the sample, thereby not requiring an objective at the distal end of the fibre-bundle. This system used a 32 × 32 SPAD array with TCSPC capability for time-resolved detection [68]. Dual-wavelength excitation at 480 and 640 nm was performed using two synchronised pulsed laser diodes driven at a 20 MHz repetition rate with a 25 ns delay between them. This enabled simultaneous lifetime measurements at the two different wavelengths. The system capability was demonstrated by lifetime imaging of *ex vivo* human lung tissue plus E.coli labelled with a fluorescent SmartProbe. Imaging was performed a rate of up to 1 Hz, imaging a circular area with a diameter of approximately 600 µm with resolution determined by the fibre core spacing of around 5 µm [69].

Another scanning fibre-bundle FLIm system using in-contact imaging was recently applied for label-free cancer detection in *ex vivo* human lung samples [70]. This system used a 488 nm excitation source and a 512 SPAD line array sensor capable of on-chip TCSPC and histogramming in each SPAD. The detector has previously been used in a bench-top full-spectral FLIM system [71]; for the endomicroscope, photon counts were binned into two spectral channels (500—580 and 610–760 nm) to increase signal-to-noise ratio and increase acquisition speed. The system was used to image *ex vivo* human lung tissue samples from cancerous and adjacent non-cancerous regions at a frame rate of 3 Hz. They found that the FLT in the 500—580 nm spectral channel was significantly reduced in the cancerous samples, allowing label-free differentiation between the sample types with a sensitivity of 81.0% and specificity of 71.4%.

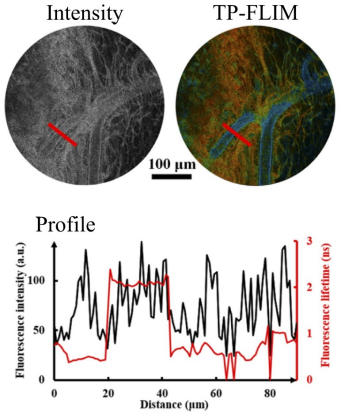


Figure 3.7: Adapted with permission from Lin et al. [72] © 2022 Optica Publishing Group. Two-photon fluorescence intensity and TP-FLIM images from the intestine of an anaesthetised mouse at 45 µm depth captured with the fibre bundle TP-FLIM microendoscope. The profiles plot the intensity and lifetime values along the red lines in the two images.

A fibre bundle system for *in vivo* two-photon FLIM (TP-FLIM) has also been reported by Lin et al. [72] with a 1.4 mm miniature objective mounted at the distal end of the fibre bundle. An 80 MHz femtosecond laser tuned to 840 nm was used for excitation and fluorescence was detected with a PMT and TCSPC module. The field of view had a diameter of approximately 390 µm and a lateral resolution of 1.55 µm. The system was used for *in vivo* TP-FLIM of the intestine of an anaesthetised mouse following injection of a squaraine dye that binds serum albumin and exhibits strong two-photon absorption. A Z-stack of images from 0 µm to 130 µm was acquired by changing the distance between the tissue surface and the mini objective, with each image acquired in under 4 s. The resulting lifetime maps showed strong contrast between blood vessels and surrounding connective tissue (Figure 3.7), attributed to different dye-binding states in the respective tissue types. The optical sectioning of TP-FLIM arises from the nonlinear nature of two-photon excitation: fluorescence is generated only at the focal point where photon density is highest, resulting in a very small excitation volume and eliminating out-of-focus background without the need for a pinhole [72, 73]. This provides sub-micron lateral resolution and excellent axial confinement

Another TP-FLIM endomicroscope reported in the literature employs resonant fibre scanning. In this design, the tip of a double-clad fibre (DCF) is driven in a spiral pattern by a piezoelectric actuator positioned behind a miniature objective that focuses the excitation spot onto the

sample [73]. Femtosecond 730 nm pulses from a Ti:sapphire laser are delivered through the single-mode core, while fluorescence is collected by the objective and coupled into the DCF's inner cladding. The probe tip has a diameter of approximately 2 mm, with all mechanical scanning confined within the probe head behind the objective (Figure 3.8). Emission is filtered to isolate autofluorescence from NADH in the 417 nm to 477 nm band and detected with a PMT–TCSPC system. This endomicroscope was demonstrated *in vivo* in mice to monitor NADH lifetime changes during renal ischaemia–reperfusion and to map metabolic alterations in subcutaneous tumour cells following induced apoptosis. It achieved a spatial resolution of ∼0.7 µm over a ∼100 µm to ∼130 µm field of view. Although capable of a 2 Hz frame rate, ten frames were averaged for *in vivo* imaging to improve signal, with motion correction applied to compensate for respiration-induced movement.

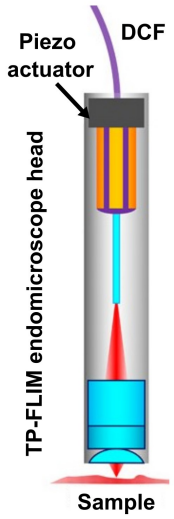


Figure 3.8: Adapted from Liang et al. [73] with permission. © 2022 American Chemical Society. Schematic of the resonant-scanning TP-FLIM endomicroscope head design. The tip of a DCF is driven in a spiral pattern by a piezoelectric actuator behind a miniature objective which focusses the excitation light and collects the two-photon fluorescent emission.

Beyond fibre-based probes, multiphoton FLIM has also been used for high-resolution metabolic imaging with benchtop systems, as demonstrated by Skala et al. [74] for *in vivo* imaging of hamster cheek pouch epithelium. In the clinical domain, JenLab's CE-certified multiphoton tomographs, DermaInspect® and MPTflex®, have enabled *in vivo* FLIM of human skin for dermatological and cosmetic research [75, 76]. These platforms provide label-free structural and metabolic contrast using integrated TCSPC-based FLIM. However, their reliance on high-power pulsed lasers, complex scanning optics, and precise alignment increases system cost and limits portability, highlighting the trade-off between clinical capability and engineering complexity.

3.1.4 Wide-field

Wide-field FLIm has the benefit of capturing lifetime information from the entire field of view (FoV) at the same time, reducing motion artefacts and potentially increasing system throughput and effective pixel rate [17]. Wide-field *in vivo* FLIm has been demonstrated with probes using a gradient index (GRIN) lens to image onto a fibre bundle at the distal end of the probe, and a gated intensified charge-coupled device (ICCD) camera for detection at the proximal end. Despite these advantages, wide-field FLIm inherently lacks optical sectioning. As a result, fluorescence from out-of-focus planes contributes to the detected signal, which can reduce spatial resolution, blur fine structural features, and lead to lifetimes that represent depth-averaged values rather than the local biochemical environment. This makes it difficult to isolate signals from thin epithelial layers, weakly fluorescent lesions, or small subsurface structures; these limitations can become significant for diagnostic applications where depth specificity is important.

In 2009 Sun et al. [77] reported a wide-field FLIm system with this configuration, itself an improvement on a previously published prototype [78]. The system delivered 337 nm excitation pulses via a multimode fibre positioned adjacent to a 0.5 mm diameter imaging lens cemented onto a fibre bundle with 10,000 individual fibres. Emission was filtered at the proximal end of the fibre bundle using a bandpass filter centred at 450 nm to target NADH autofluorescence. The system had a field of view with a diameter of 4 mm and a spatial resolution of 35 µm. Typical acquisition time for tissue measurements was 120 s. The system was validated by *in vivo* imaging of cancerous lesions in a hamster cheek with; the cancerous tissue was found to have a shorter lifetime than the surrounding normal tissue. The same system was later used in human patients to explore FLIm-based intraoperative diagnosis of glioblastoma multiforme (GBM) [79] and head and neck squamous cell carcinoma (HNSCC) [80]. GBM was found to have weaker florescence intensity and a longer lifetime than normal cortex tissue while HNSCC also had a weaker florescence intensity

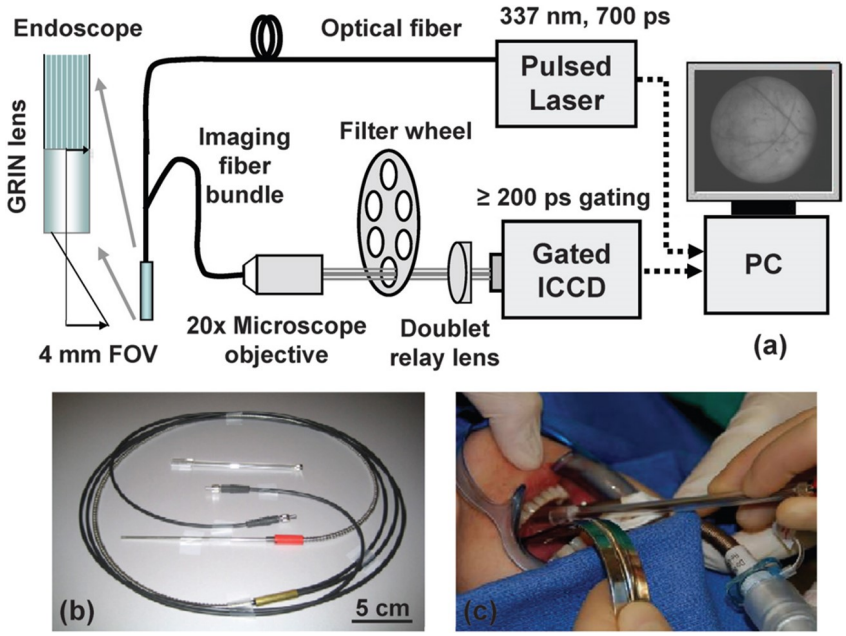


Figure 3.9: Reprinted from Sun et al. [80] with permission from Oxford University Press. (a) A schematic of the wide-field *in vivo* FLIm system for intraoperative diagnosis of oral carcinoma. (b) Picture of the semi-flexible integrated endoscope used in patient studies. (c) Picture of the FLIm probe during *in vivo* imaging of the oral cavity.

but a shorter lifetime when compared to surrounding normal tissue. A schematic of this system and a photograph of it being applied *in vivo* for oral cavity imaging can be seen in Figure 3.9. The tip of the probe used in Sun et al. [80] was packaged in a stainless steel rigid tip with a diameter of 2.4 mm, while the outer probe diameter is not specified in the other applications.

In Sparks et al. [81] a wide-field FLIm endoscope with an external diameter of ∼2.3 mm is presented. This system used 440 nm excitation with fluorescence emission with wavelength >488 nm detected. The system was validated on *ex vivo* human larynx samples imaged immediately following resection with an acquisition time of 8 s. An example of images captured with the system is presented in Figure 3.10. Measurements were also demonstrated with a higher power laser used on *ex vivo* normal and neoplastic mouse bowel samples to image at 2.5 Hz. Neoplastic bowel samples were observed to have a longer lifetime than the normal samples.

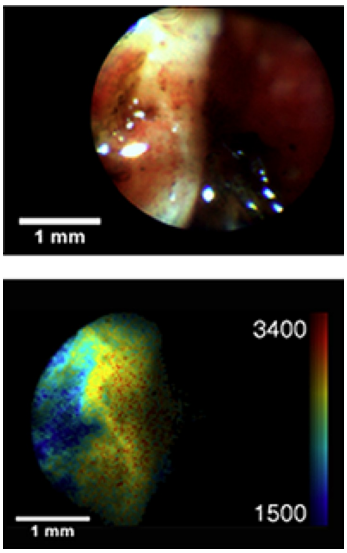


Figure 3.10: Adapted from Sparks et al. [81] under CC BY 4.0. A white light image (top) and a lifetime image (bottom) of the same location on a diseased human larynx sample, captured *ex vivo* with the wide-field fibre-bundle FLIm endoscope.

Cheng et al. [82] have reported another wide-field FLIm endoscope system, this time with excitation delivered in-line with collection through the imaging fibre bundle. The emitted fluorescence signal was then split into three spectral channels and imaged onto different regions of the ICCD detector, enabling the three channels to be imaged in parallel. The system had a field of view of 2.25 mm in diameter and an estimated spatial resolution of ∼35 µm. An imaging speed of 2 Hz was achieved by only acquiring counts for two gates and using a rapid lifetime determination (RLD) algorithm for lifetime estimation. *In vivo* system validation was again performed on a lesion diagnosed by histopathology as dysplasia in a hamster cheek. They found that the lesion had a longer lifetime than the surrounding tissue in the 450 nm spectral channel, in agreement with the example mentioned above from Sun et al. [77].

3.2 SPAD arrays for wide-field FLIm

Single-photon avalanche diodes (SPADs), as their name suggests, have excellent single-photon detection and time-stamping capability. Commercially, they are most commonly available in the form of silicon photomultipliers (SiPMs), arrays of individual SPADs which are read in parallel to increase dynamic range. In research, their use has been explored for a range of biophotonics applications including FLIm, super-resolution microscopy and time-resolved Raman spectroscopy [15]. The use of SPAD cameras for wide-field FLIm has previously been demonstrated using a 0.5 MP time-gated SPAD camera [83] and there are now commercially available SPAD cameras with FLIm capability.

In 2014 Burri et al. [84] presented a gated 512 × 128 SPAD image sensor termed SwissSPAD, demonstrating FLT measurements of various fluorescent dyes. Since then, the SwissSPAD2 (with 512 × 512 pixels) [85] and SwissSPAD3 (with 500 × 500 pixels) [86] have been applied in bench-top systems for macro-FLIm of fluorescent dyes in well plates [87, 88] and for *in vivo* FLIm-FRET to study target-drug engagement in tumour xenografts in mice [88]. A successor to these cameras is now commercially available as the SPAD512^2 from Pi Imaging Technology [89]; this camera has 512 × 512 pixels each with an active area of 6 µm × 6 µm, though has the option to add microlenses with a quoted efficiency of 50 % with collimated light. The SPAD512^2 uses a sliding time gate to perform lifetime measurements with a minimum gate width of 6 ns and a minimum step size of ∼17 ps, and has been shown capable of wide-field FLIm of cells stained with Alexa Fluor 546 and 555 dyes with an acquisition time of 0.27 s using 0.4 mW of 532 nm excitation in the field of view [16].

SPAD cameras with in-pixel TCSPC capability have also been developed. In 2019 Henderson et al. [90] reported a 192 × 128 TCSPC SPAD image sensor with a 33 ps temporal resolution. The camera's capabilities have been demonstrated through light-sheet FLIM of algae samples with only 180 nW of laser power irradiating the visible part of the sample and an acquisition time of ∼1 s per image [91]. The camera has since been commercialised and is available from HORIBA as FLIMera [92]. The sensor has a fill-factor of 13 % and each 18.4 µm × 9.2 µm pixel contains it's own TDC which sorts photon arrival times into up to 4096 time bins of 50 ps. This commercially available SPAD camera has also been applied for light-sheet FLIM, this time *in vivo* in a zebra fish tail (as seen in Figure 3.11) and to monitor changes in NAD(P)H lifetimes in PANC-1 cells following cyanide treatment [17].

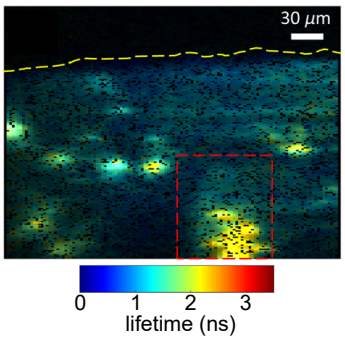


Figure 3.11: Adapted from Samimi et al. [17] under CC BY 4.0. Wide-field light-sheet mean lifetime image of a zebrafish caudal fin wound model *in vivo*. Captured using 375 nm excitation at 0.4 mW average power and the FLIMera SPAD camera with 10 s integration time. The transection wound is indicated but the yellow dashed line) and the tip of the notochord (the midline structure in the zebrafish tail) by the red dashed box.

The vTau camera from Lambert Instruments is a SPAD-powered, frequency-domain FLIm camera designed for high-speed wide-field imaging. It delivers up to 100 lifetime images per second with a 512 × 512 pixel format (16 µm pixel pitch). The specified lifetime operating range spans approximately 0.2 ns to 300 ns, enabled by an ultra-high-sensitivity SPAD detector with microlens enhancement for improved light collection [93]. The commercial availability of SPAD cameras for wide-field FLIm demonstrates their potential in this area. However, the detectors described above are designed for use with bench-top microscopes and are therefore too large for endoscopic applications.

As an aside, although not SPAD-based, the pco.flim X (Excelitas) illustrates the continued potential of modulated CMOS sensors for FD-FLIm and their possible future relevance to miniaturised wide-field instrumentation. The camera employs a rapidly modulatable CMOS sensor with two readout taps per pixel and provides 1008 × 1008 pixels at up to 45 double images per second. It supports lifetime measurements from 1 ns to 100 µs. Thermoelectric cooling is used to reduce the readout noise to below 15 e^- and extends usable exposure times to 4 s [94]. These active cooling requirements would pose a substantial engineering

challenge for chip-on-tip miniaturisation, where distal heat dissipation, available volume, sterilisable packaging, and power budgets are all tightly constrained.

The miniaturisation of SPAD arrays makes their application for a chip-on-tip FLIm endoscope feasible. Such detectors can be fabricated with standard CMOS processes, meaning they could be, in principle, fabricated at scale at a similar cost to microcamera chips currently used in disposable white light endoscopes. In fact, low-cost SPAD detectors for LiDAR applications are already widely available; with sufficient market demand, SPAD imagers could follow a similar trend. A miniaturised 128×120 SPAD array with time-gated photon counting and dimensions of $1.4\,\text{mm} \times 1.4\,\text{mm}$ was presented by Erdogan et al. [18]. This SPAD array, named EndoCam, is described in more detail in Chapter 4. The integration and application of this detector in a bench-top system, a hand-held system, and finally in a chip-on-tip FLIm micro-camera are described in Chapters 5 and 6.

3.3 Discussion

The literature reviewed here demonstrates both the potential and complexity of translating FLIm to *in vivo* use. A consistent observation across studies is that lifetimes measured *in vivo* differ from those obtained *ex vivo* for nominally similar tissues due to rapid physiological changes such as loss of perfusion, altered oxygenation and pH, temperature shifts, and differences in hydration. While this limits direct transfer of *ex vivo* calibration data, it also highlights that fluorescence lifetime is intrinsically sensitive to metabolic and micro-environmental conditions, offering contrast mechanisms that complement those of intensity-based imaging [1, 39].

Across the existing imaging modalities, clear and consistent trade-offs emerge. Free-hand point-scanning systems offer flexibility and have generated substantial clinical datasets [43, 44], but their acquisition speed is inherently slow, and they are poorly suited to confined or restricted spaces. Helical scanning probes address certain access constraints by enabling circumferential imaging in tight spaces [55], yet their rotating mechanics add complexity and limit compatibility to specific applications such as vascular imaging. Laser-scanning approaches deliver higher spatial precision [60, 61], but require mechanical motion, careful optical alignment, and image reconstruction, all of which increase system overhead and reduce robustness. Wide-field FLIm mitigates motion artefacts by capturing an entire field of view simultaneously [77, 81], but its lack of optical sectioning imposes limits on resolution; additional challenges include significant photon loss through fibre bundles and reliance on expensive, bulky intensified cameras. Together, these modality-specific limitations emphasise the need for wide-field, mechanically simple, miniaturised architectures capable of maintaining useful biochemical contrast in clinically constrained environments.

Recent developments in SPAD arrays suggest a practical route to miniaturised wide-field FLIm. Commercial bench-top SPAD cameras demonstrate strong performance but are too large for endoscopic use [16, 85, 86, 90], whereas miniaturised arrays such as the EndoCam [18] enable chip-on-tip architectures that also avoid fibre-bundle autofluorescence, dispersion, and signal attenuation. Fabrication in standard CMOS makes SPAD arrays uniquely suited to mass production, aligning with the broader clinical trend toward chip-on-tip architectures already established in white-light endoscopy, where CMOS miniaturisation has enabled low-cost, single-use devices. This raises the prospect of scalable, potentially disposable FLIm devices compatible with clinical workflows

It is important to recognise that current miniaturised SPAD imagers still involve engineering compromises. Fill factor, photon detection efficiency, and temporal precision remain below the levels achievable with larger gated-intensified or TCSPC systems. These limitations highlight areas for continued development, and it is reasonable to expect further improvements in noise performance, timing jitter, microlens integration, and per-pixel processing in line with broader advances in CMOS detector technology.

Looking ahead, a natural extension of this trajectory is the possibility of chip-on-tip frequency-domain FLIm using miniaturised, modulated CMOS detectors. Frequency-domain lifetime estimation requires only phase and modulation measurements, reducing data bandwidth and simplifying on-sensor electronics. Although no endoscope-scale FD-FLIm detectors are currently available, ongoing progress in compact, high-speed CMOS imaging sensors indicates that chip-integrated FD-FLIm may become feasible in the future [63, 64]. Such devices would complement time-domain SPAD approaches and could enable real-time lifetime imaging in constrained clinical environments.

Together, these considerations reinforce the motivation for the work that follows: to evaluate whether miniaturised SPAD arrays can provide a clinically compatible path toward wide-field, chip-on-tip FLIm, and to explore how current performance aligns with the long-term vision of scalable, integrated lifetime imaging systems.

3.4 Summary

In this chapter, a review of the current state-of-the-art in *in vivo* FLIm systems has been presented, categorizing them by imaging modality and highlighting their respective advantages, limitations, and clinical relevance. The diversity of systems explored reflects the breadth of innovation in the field, while also underscoring persistent challenges in miniaturisation, acquisition speed, and clinical integration.

Building on this, common trade-offs across existing approaches have been discussed and the broader technological trend toward compact, chip-on-tip architectures. Within this context, the chapter also introduced the technological development of SPAD detectors, with a focus on their potential to overcome these limitations in wide-field FLIm. In particular, the emergence of miniaturised SPAD arrays, such as the EndoCam, offers a promising route toward compact, time-resolved imaging systems suitable for endoscopic deployment.

The following chapters detail the instrumentation and system architectures developed to evaluate the EndoCam's capability to address the unmet needs identified in current *in vivo* FLIm technologies.

Chapter 4

Instrumentation

In this chapter the main instrumentation applied for the thesis is described. First, the EndoCam, the miniaturised SPAD array for wide-field FLIm, is covered. The physical dimensions of the chip are described as well as the modes of operation. The laser sources used throughout the thesis are then listed and briefly described. Then the modular system configuration developed for operation of the EndoCam integrated into different imaging systems and with the different laser sources is explained. Finally, the in-house TCSPC system for bulk measurement of sample lifetimes is described.

4.1 The EndoCam

The EndoCam is the product of the Proteus Project funded by the Engineering and Physical Sciences Research Council (grant number EP/R005257/1). Proteus was a cross-disciplinary project spread across multiple universities, with the primary aim of advancing technology for the diagnosis of pulmonary diseases [95]. As part of this project, Dr Tarek Al Abbas (then a PhD student at the University of Edinburgh) developed a compact time-resolved SPAD image sensor capable of wide-field fluorescence lifetime imaging, named the EndoCam [96, 97].

Aside from the work presented in this thesis, the EndoCam has been used for FLIm of biological samples in bench-top [18] as well as handheld systems [98], and used for FLIm based explosive detection [7]. A handheld system (23 mm × 23 mm × 28 mm) incorporating the detector has also been used for combined lifetime and distance measurements (FLIm-DAR) [99].

The physical layout of the sensor, its key characteristics, and main modes of operation are described here. A more comprehensive description of the detector can be found in the PhD thesis of Dr Al Abbas [96], in the conference proceeding where it was first presented [97], and in the journal article from Erdogan et al. [18].

4.1.1 Overview

The EndoCam was designed with a footprint of 1.4 mm × 1.4 mm and has 128 × 120 pixels. Each pixel has an individual SPAD with independent time-resolved photon-counting circuitry. The chip is implemented in an STMicroelectronics 3-D-stacked CMOS (complementary metal-oxide-semiconductor) process and has an 8 µm pixel pitch, giving an active area of ∼1 mm × 1 mm. The layout of the top tier of the EndoCam is presented in Figure 4.1.

The chip has many pads along two edges of the top surface but many of these are for test purposes. For normal operation, only five electronic

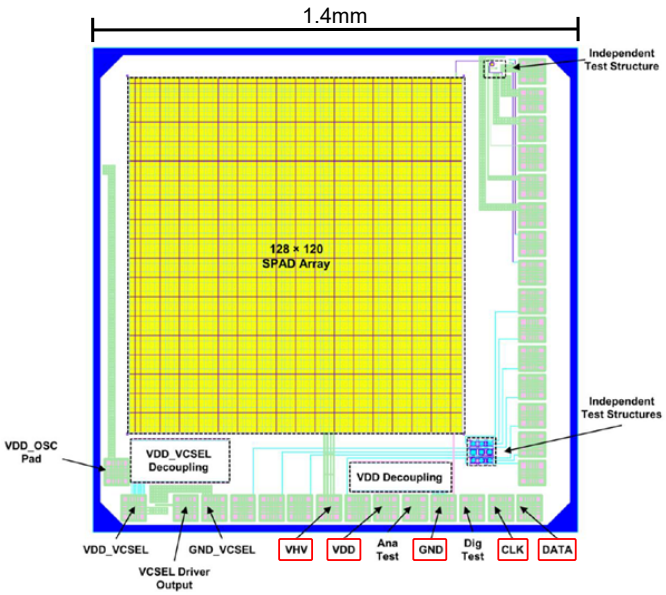


Figure 4.1: A schematic of the top layer of the EndoCam chip design. As can be seen, there are many pads along two edges of the chip but only five are required for operation: VHV, VDD, GND, DATA, and CLK.

connections are required; 1) the SPAD bias voltage (VHV), 2) 2.8 V power supply (VDD), 3) Ground (GND), 4) a bidirectional data signal, and 5) a clock signal. Electronic connections are made to each of these pads with wire bonds. Unless stated otherwise, VHV was set at 17.5 V. The clock frequency for all work presented in this thesis was 20 MHz. The EndoCam is controlled using a MATLAB graphical user interface (GUI) initially developed by Dr Andrew Matheson from The University of Edinburgh and further modified by myself.

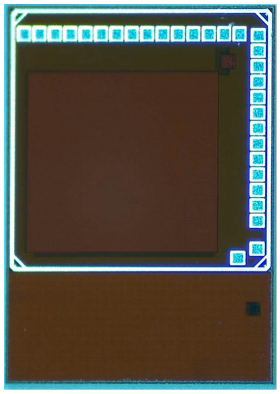


Figure 4.2: A microscope image of the EndoCam chip showing the extra silicon region in the bottom. This led to the chip having a physical footprint of 1.4 mm × 2.0 mm.

Although the EndoCam was designed to have a functional footprint of 1.4 mm × 1.4 mm, unfortunately the physical devices after dicing are approximately 1.4 mm × 2.0 mm. A microscope image of the chip with the extra dead space can be seen in Figure 4.2. This is due to layout and dicing constraints as the chip was fabricated on a wafer shard with multiple other projects.

The detector also has a defective pixel region in one corner. This defect is caused by a race condition between the read and reset signals for these pixels and has previously been reported in Al Abbas [96] and Erdogan et al. [18]. Nevertheless, the vast majority of the detector area remains useable. In spite of these two drawbacks, the EndoCam represents a significant step forward in the miniaturisation of time-resolved image sensors and is still suitable for application in proof-of-concept miniaturised wide-field FLIm systems.

4.1.2 Time-gating implementation

Time-resolved photon counting is achieved in the EndoCam through time-gating the on-pixel counting electronics. When a photon is absorbed in the active region of the SPAD it creates a rapid voltage pulse. Following this, the SPAD is passively quenched; until this process is complete, it is unable to detect more photons. The time taken for quenching is the pixel dead-time, this is ∼3.5 ns for the EndoCam [18].

When a photon is detected, the voltage pulse generated by the SPAD is digitised and sent to a counter. Each pixel has independent counting circuitry which is rapidly enabled and disabled using a reference clock generated on-chip by a ring oscillator (RO). The period during which the

counting circuitry is enabled therefore defines the time gate. The width and position of each time gate are in multiples of the RO period, and can be controlled through the GUI by the user. For the EndoCam, the RO period is in the range of 370 ps to 390 ps[1]. The number of laser cycles integrated for each gate is also set via the GUI to effectively control the exposure time. For a single time gate, photon counts are summed on-chip with 14-bit depth.

In order to perform a gate sweep and recover a fluorescence decay, multiple cycles of programming and readout from the chip are required. For each gate in a sweep, the time gate position and width are programmed, the measurement is performed, and then the data is read out. This means the acquisition time scales linearly with the number of gates acquired.

It is important to stress that the SPADs on the EndoCam operate in free-running mode, meaning they are constantly active, even if the counting circuitry is disabled. This is in contrast to other time-gating techniques where the detector itself is only active during the time gate. In order to make this distinction clearer, the term time-gated photon counting is preferred when describing the EndoCam operation.

4.2 Modular FLIm system

A modular system configuration was implemented for operation of the EndoCam. The system is considered modular in the sense that the laser source and the optical imaging subsystem could be changed in a relatively straightforward manner. This allowed operation and evaluation of multiple imaging system designs using the EndoCam with interchangeable light sources.

The evaluation of multiple imaging systems was important as the development of such systems for different applications is a primary activity for this thesis. The laser sources used for the work in this thesis are shared across more than one project within the research group, therefore easy interchangeability of these laser sources was a necessity. Aside from this, it was also beneficial for the laser source to be interchangeable to allow the use of different excitation wavelengths depending on the sample of interest.

A schematic of the modular system is presented in Figure 4.3. The system design and functionality is described in the following sections.

4.2.1 Computer – EndoCam interface

As mentioned previously, the EndoCam is controlled using a custom MATLAB GUI; this is done via a field programmable gate array (FPGA) module connected to a custom motherboard provided by our collaborators at the University of Edinburgh. Over the course of the project, two FPGA modules were used, the Opal Kelly XEM6310 and later the Opal Kelly XEM7310-A200. The firmware for EndoCam operation with both FPGA modules was developed by Dr Ahmet T. Erdogan based at the University of Edinburgh. In terms of the high-level operation of the EndoCam, these two modules provide the same functionality.

The FPGA module is connected to the EndoCam via the motherboard providing the five electronic connections required for operation listed in section 4.1.1, and connected to the MATLAB GUI via USB. The FPGA module thereby provides an interface between the EndoCam and the rest of the system. The voltage for the VHV connection is supplied to the motherboard by an external power supply while the 2.8 V for the VDD connection is generated on the motherboard.

[1]See Section 4.2.3 for the time-bin calibration method applied.

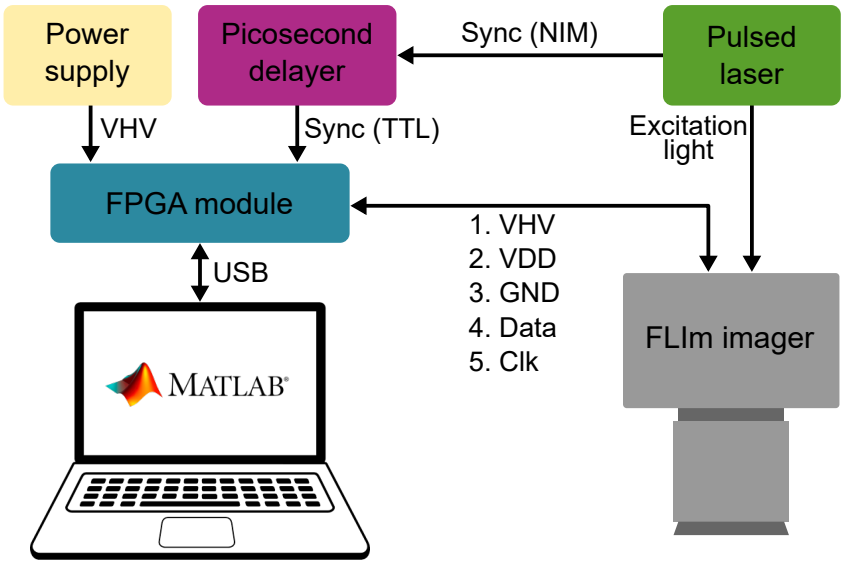


Figure 4.3: Block diagram of the modular FLIm system developed for use with the EndoCam. The system architecture enables flexible integration of different laser sources and optical imaging subsystems, allowing rapid reconfiguration for a variety of experimental setups. This modularity supports the evaluation of multiple imaging platforms using the same core components, facilitating efficient testing and development across bench-top and miniaturised FLIm systems.

In the original system setup, the EndoCam is packaged into a ceramic chip carrier which is then plugged directly into a socket on the motherboard. A photograph of this arrangement can be seen in Figure 4.4. For bench-top systems it would be possible to maintain this configuration and construct the system optics around the motherboard. For translation to handheld systems or smaller, it is instead required to operate the chip at the end of a cable. In addition, there were only two motherboards available, so being able to operate even bench-top imaging systems over a short length of cable would mean the same board could be used for different systems and very easily changed over. Different strategies for this have been implemented for the different imaging systems; details of this as well as the challenges faced are covered in Chapters 5 and 6.

4.2.2 Laser – EndoCam synchronisation

For time domain measurements, the detection system used must be synchronised with the excitation light pulses. With the EndoCam, this is achieved by synchronising the system clock for the FPGA module and chip with the laser source, using the laser clock as a master. Therefore, the laser repetition rate and the EndoCam clock frequency are the same.

Three different pulsed laser sources were used for the work in this thesis: a 375 nm pulsed laser diode (LDH-D-C-375, PicoQuant), a 405 nm pulsed laser diode (BDL-405-SMN-F, Becker&Hickl), and a pulsed supercontinuum laser (SuperK FIANIUM FIR-20 PP, NKT Photonics). All three sources have a pulse width of <100 ps. The supercontinuum laser was used in combination with a monochromator as described in [100], designed and constructed by Dr Sanathana Konugolu Venkata Sekar. These three sources enabled pulsed excitation at different wavelengths and the supercontinuum source was also applied for measurement of the system response to a short pulse of light in the fluorescence emission wavelength range in Paper **III**.

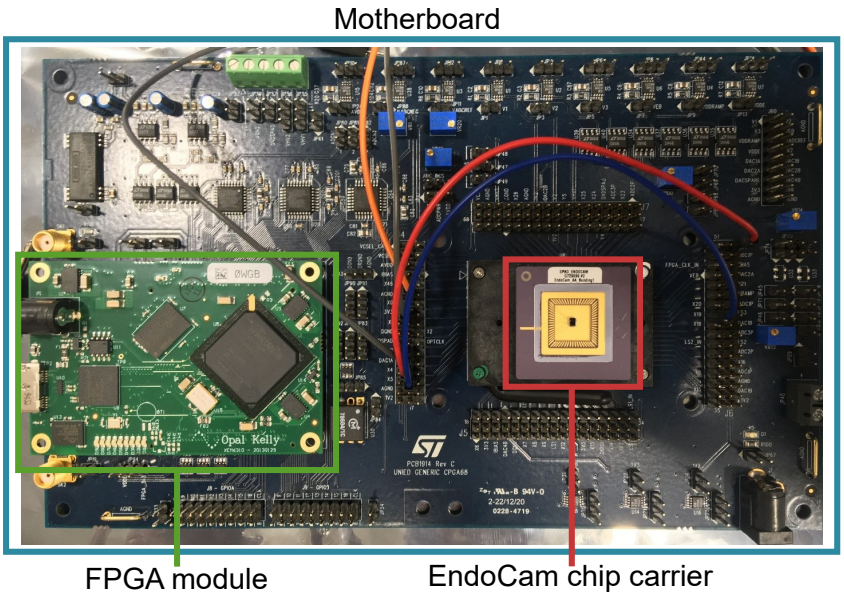


Figure 4.4: The motherboard and FPGA module used for EndoCam operation. In this configuration the EndoCam is packaged into a ceramic chip carrier and plugged directly into a socket on the motherboard. For the imaging systems described in Chapters 5 and 6, the chip is instead connected over a cable.

All three laser sources provide a similar NIM (nuclear instrumentation module) sync signal which is used for synchronisation with the EndoCam. Before connection to the motherboard, the NIM signal is converted to a TTL (transistor-transistor logic) signal using a picosecond delayer (Micro Photon Devices). The picosecond delayer also allows an adjustable delay to be added, which enables tuning of the laser pulse arrival time relative to the system clock. This feature was particularly useful, as different iterations of imaging systems employed different lengths of electronic cable and optical fibre, as well as different optical paths.

For earlier versions of the system, a pulse generator (8112A, Hewlett Packard) was used in place of the picosecond delayer, serving the same purpose and in practice providing equivalent functionality. This was the case for the work carried out for Paper **I** and Paper **II**.

4.2.3 Time-bin calibration

As mentioned in Section 4.1.2, the minimum time-bin width on the EndoCam is in the range of 370 ps to 390 ps, as determined by the ring oscillator (RO) period. It is stated as 390 ps in Erdogan et al. [18] and Al Abbas et al. [97], 379 ps in Matheson et al. [98], and 370 ps in Al Abbas [96]. This fluctuation may be due to minute variations in the fabrication process or may arise from some other cause. An investigation into the factors influencing this is beyond the scope of this thesis. However, it is still important that the minimum bin-width is calibrated to maintain the accuracy of the time-resolved measurements.

This calibration can be performed for a given system by measuring a short pulse of light with the EndoCam, delaying the pulse by a known amount of time, then measuring it again. The EndoCam time-bin width Δt_{EC} can then be calculated from equation 4.1,

$$\Delta t_{EC} = \frac{t_{shift}}{i_1 - i_0}, \tag{4.1}$$

where t_{shift} is the known time the laser pulse is shifted by, and i_0 and i_1 are the time-bin indices with the highest photon counts in each measure-

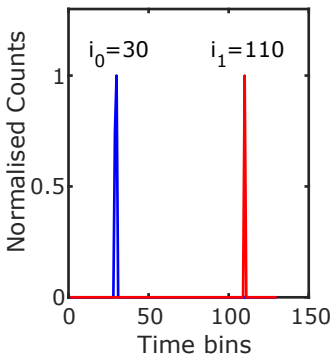


Figure 4.5: A short pulse of light from the SuperK laser source measured with the EndoCam (pixel $x = 34$, $y = 71$) before and after being delayed by 30 ns using the picosecond delayer. The number of time-bins shifted can be used to calibrate the bin width of the system.

ment. This known time shift can be achieved optically, by using different lengths of fibre or some other method to increase the optical path. For the work in this thesis this has instead been done electronically, by changing the delay between the laser sync and the EndoCam clock using the picosecond delayer or the pulse generator.

An example of this calibration measurement from an individual pixel is shown in Figure 4.5. A short pulse of light from the pulsed supercontinuum laser is measured with the system. The pulse is then shifted by 30 ns and measured again. The time-bin shift for the pixel shown in Figure 4.5 was $i_1 - i_0 = 80$, corresponding to a time-bin width of 375 ps using equation 4.1. As the time-bins for all pixels are controlled by the same RO, the mean bin width across all pixels is calculated and taken as the global value across the detector. For the measurement in this example that yields a time-bin width Δt_{EC} of 370 ps.

4.3 TCSPC system for bulk lifetime measurements

As part of the evaluation of different imaging systems constructed using the EndoCam and incorporated into the modular setup described above, there was a need for a reliable lifetime measurement system against which the imaging systems can be benchmarked. Within the last year of the project, access to a confocal FLIM system in Dublin City University was possible, but comparable measurements of the same samples with imaging systems in different cities is time-consuming and impractical[2]. There were also no pre-existing systems in the lab for this purpose.

In order to meet this requirement, a TCSPC-based system for bulk lifetime measurements was designed and assembled. This system uses a hybrid photomultiplier detector (PMA Hybrid 50, PicoQuant) and a PicoHarp 300 TCSPC module (PicoQuant). In principle, any of the three pulsed lasers mentioned in Section 4.2.2 can be used for excitation but, for all the measurements described in this thesis, only the 405 nm pulsed laser diode is used. The system was operated at a laser repetition rate of 20 MHz with a photon count rate of <200 kHz. This ensured operation within the single-photon regime and avoided pile-up effects, as discussed in Chapter 2.

A schematic of the system is presented in Figure 4.6. The optomechanical design of the system is based around a cuvette holder with four light ports (CVH100/M, Thorlabs). The system can be used for measurement of liquid samples in a 25 mm × 25 mm quartz glass cuvette or of planar samples (provided they are narrow enough) placed at a 45° angle.

Light from the laser is coupled into an optical fibre. The other end of the fibre is connected to a fibre collimator (F950FC-A, Thorlabs) generating a collimated beam with a diameter of approximately 4.5 mm. The collimated excitation beam is directed towards the sample through one of the ports on the cuvette holder.

A variable reflective neutral density (ND) filter wheel (NDM4/M, Thorlabs) is placed in the path of the beam before the light port, allowing the excitation light power to be adjusted. The laser power could also be adjusted directly on the laser diode switch box by changing the voltage supplied to one of the SMA connectors. However, this will affect the laser pulse shape requiring a delay for laser stabilisation and remeasurement of the system instrument response function (IRF). For a given set of measurements, setting this to a fixed value then attenuating the light as

[2]The confocal FLIM system was used as part of the characterisation of the FLT standards as described in Paper **IV**. Given further development of the modular FLIm system and proper planning, transportation of the system to Dublin for a robust comparison may be feasible in the future.

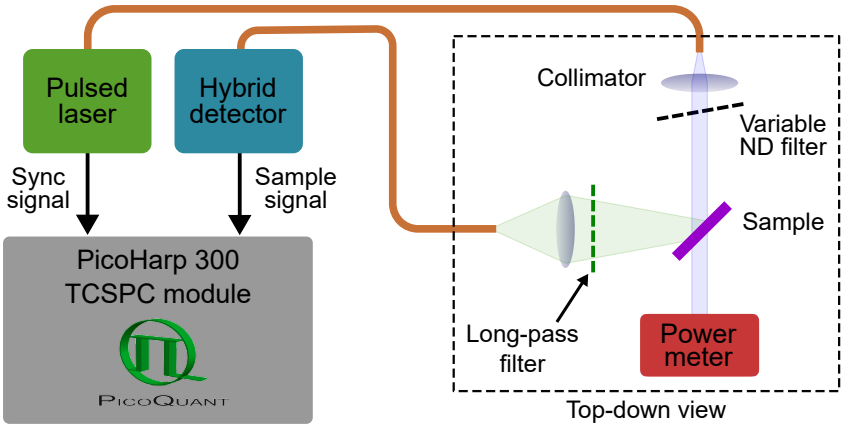


Figure 4.6: The time-correlated single-photon counting (TCSPC) system developed for bulk fluorescence lifetime measurements. The setup includes a pulsed laser source, optical filtering, and a hybrid photomultiplier detector connected to a TCSPC module. The system enables reliable benchmarking of FLIm platforms using both liquid and planar samples.

required with the ND filter removes this as a variable. The ND filter is also mounted at a slight angle to reduce back-reflections in the system.

Fluorescent emission from the sample is collected through a port perpendicular to the one through which excitation was delivered. The light is first filtered, then coupled into a second optical fibre using a plano-convex lens mounted in an SMA fibre adapter (LA1074 and CVH100-COL, Thorlabs). This second fibre is then connected to the hybrid detector. The cuvette holder has a slot for a filter holder (CVH100-FH, Thorlabs) which allows filters to be quickly removed or changed. For all measurements included in this thesis, a long-pass filter with a cut-on wavelength of 500 nm is used (FELH0500, Thorlabs).

For monitoring of the excitation laser power, a photodiode connected to a power meter (S120VC and PM100D, Thorlabs) can be mounted on the port opposite the excitation beam. Samples of course scatter and attenuate the excitation beam; therefore, samples are first measured with the TCSPC system, then removed from the holder, and finally the power of the excitation beam is recorded on the power meter. A photograph of the front-end of the TCSPC FLT system can be seen in Figure 4.6.

The IRF of the system is recorded by removing the long-pass filter and placing a piece of frosted glass in the sample holder at a 45° angle; this is recorded for each set of measurements and used in a reconvolution fitting model for analysis. An example IRF recorded with this system is shown in Figure 4.8 having a width (FWHM) of approximately 180 ps. It is likely that a narrower IRF could be achieved by removing the two optical fibres from the system and instead mounting the laser and detector directly in front of the ports on the cuvette holder. However, similarly to the modular FLIm system already described, both the detector and laser sources are shared across multiple projects within the lab. Therefore, having these elements remain quickly interchangeable in a plug-and-play style was a necessity. In any case, for the range of lifetimes measured with the system and given the use of reconvolution fitting, this IRF width is sufficiently narrow.

This system hardware was designed and assembled by myself in late 2024. In early 2025 I co-supervised (along with Dr Sanathana Konugolu Venkata Sekar and Dr Katarzyna Komolibus) an undergraduate student, Keela Hughes, in carrying out her final year project in our lab. As part of her project she developed a Python-based app for automated data

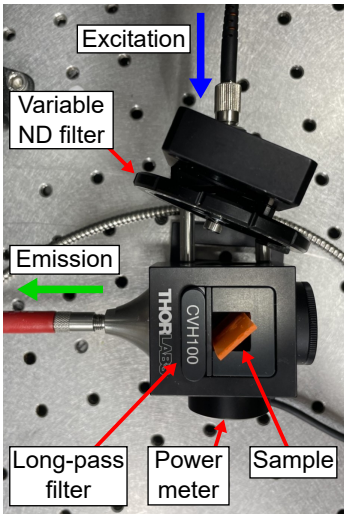


Figure 4.7: A photograph of the system built for bulk measurements of sample fluorescence lifetimes. The system has a light-tight lid which has been removed for the photograph. The sample being measured here is one of the orange FLT standards developed as part of the work in Paper **IV**.

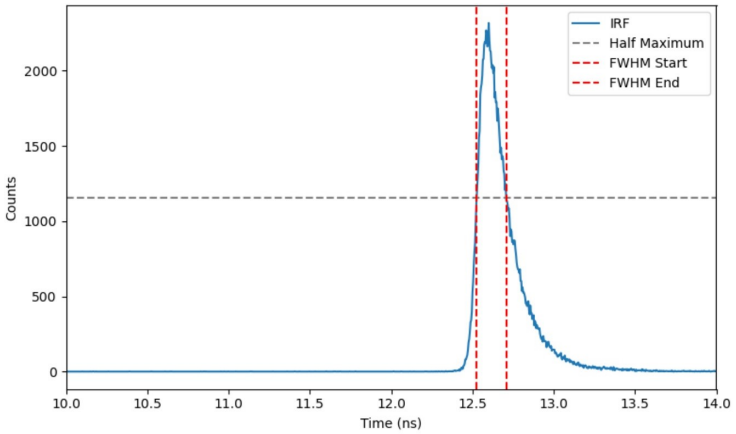


Figure 4.8: An IRF measurement for the TCSPC system acquired by removing the long-pass filter and measuring a laser pulse directly scattered off a piece of frosted glass. This IRF has a FWHM value of 180 ps.

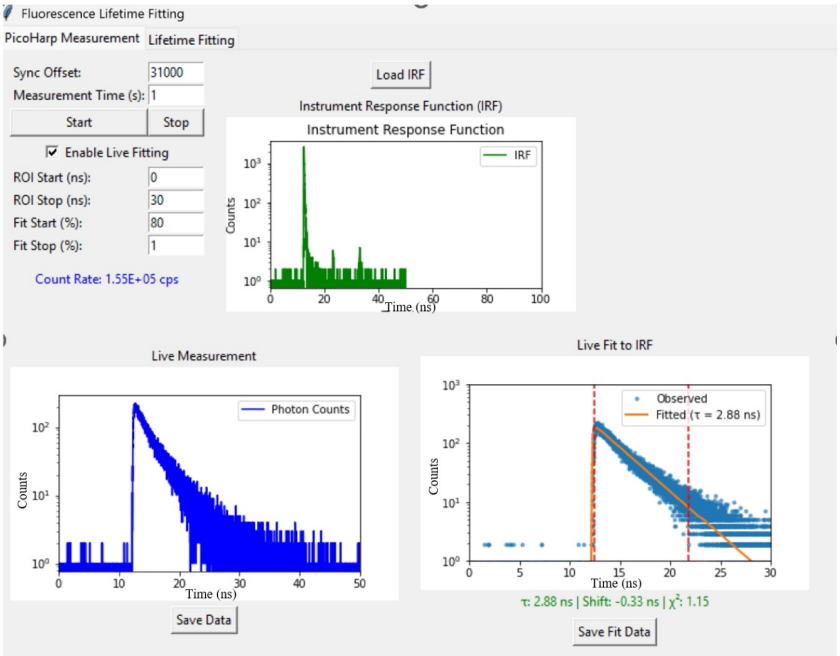


Figure 4.9: A screenshot from the Python-based app (developed by Keela Hughes under the supervision of Dr Sanathana Konugolu Venkata Sekar, Dr Katarzyna Komolibus, and myself) for automation of data acquisition and analysis with the TCSPC system. This system and app have been applied for much of the work presented in Paper **IV**.

acquisition from the PicoHarp 300 and for monoexponential lifetime-fitting using reconvolution fitting as described in Section 2.3.2; the code for this app is available on GitHub [101]. A screenshot from the app after acquiring and fitting sample data is shown in Figure 4.9.

This system has been applied for benchmarking of the FLIm micro-camera system as described in Paper **III**, and for the characterisation of dyed epoxy resins, laying the foundations for the work presented in Paper **IV**. Outside of the work included in this thesis, the system has also been used as part of the characterisation of fluorescent carbon dots developed for anticounterfeiting applications [102].

4.4 Summary

This chapter has presented the core instrumentation applied throughout this thesis. The key characteristics of the EndoCam, a compact SPAD array designed for wide-field fluorescence lifetime imaging, have been described. The modular FLIm system developed to support the testing of multiple systems using the EndoCam as well as interchangeable excitation laser sources has also been described in detail. A custom-built TCSPC system was also assembled for bulk fluorescence lifetime measurements, providing a reliable reference for benchmarking and validation. This system has been applied extensively in support of the work presented in later chapters. Together, these instrumentation components support the development, validation, and benchmarking of both benchtop and miniaturised FLIm systems described throughout this thesis.

Chapter 5

Bench-top wide-field FLIm systems

This chapter presents the development of two wide-field FLIm systems based on the EndoCam: a bench-top system designed for metabolic imaging using fluorescent pH sensors, and a miniaturised handheld system aimed at demonstrating the EndoCam's potential for portable tissue imaging. The engineering challenges, optical design, and imaging performance of both systems are described.

5.1 Wide-field FLIm system for lifetime-based metabolic imaging of *ex vivo* tissue samples

Extracellular pH (pHe) is an important indicator of homeostatic condition of mammalian tissue and its pathophysiological state such as tumor development and tissue acidosis. Optochemical sensors with internal referencing capabilities can perform dynamic quantitative imaging of pHe in live tissue samples [103].

In 2022, researchers based at the School of Biochemistry and Cell Biology, University College Cork reported the development of advanced planar solid-state pH sensors based on a fluorescent octaethylporphinketone (OEPK) [104]. A photograph of one of these sensors while under 405 nm excitation can be seen in Figure 5.1. For measurements, the sensor material is placed in contact with the sample of interest, then the fluorescence of the sensor is measured optically. In the initial publication on these sensors both intensity-based and lifetime-based detection methods were explored. These sensors were successfully applied for analysis of cultured cells and 3D spheroid models.

Following on from this work, there was an interest in applying these sensors for metabolic analysis of *ex vivo* tissue samples, and in examining if these sensors could be used to resolve sample pH spatially, specifically using the lifetime detection method. In order to explore this, a custom wide-field FLIm imager was designed and built using the EndoCam as a detector. This system was then applied for lifetime-based metabolic imaging of *ex vivo* mouse tissue samples. This work has since been published [105] and is presented in Paper **I**.

In this section, the work carried out in the development of this imager is outlined; this includes the design of a custom PCB for remote operation of the EndoCam over a cable, and the optical design of the system for imaging the tissue samples.

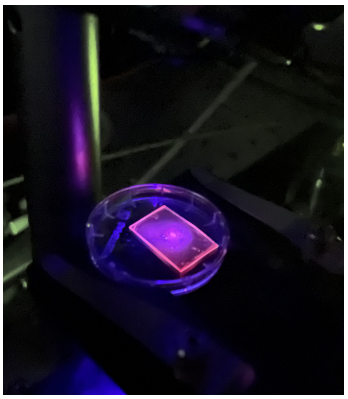


Figure 5.1: One of the planar solid-state pH sensors fluorescing under 405 nm excitation.

5.1.1 EndoCam connectivity challenges

As mentioned in Section 4.2, the EndoCam was initially configured for operation plugged directly into a socket on the motherboard. However, for

use in benchtop imaging systems and eventual integration into a micro-camera device, it is required to operate the chip over a length of cable.

Unfortunately this proved much more challenging than initially hoped. Initial efforts to operate the EndoCam at the end of a cable resulted in the sensor failing the initialisation tests. It was suspected that degradation of the digital signal quality over the cable was a potential cause of this. In order to test this, the clock signal was probed directly on the motherboard, and then at the end of a 50 cm five-wire screened cable (6305 SL005, Alpha Wire). For the tests with the cable, the cable was connected to the motherboard using five pin-headers providing the necessary connections. The other end of the cable was connected to the necessary pins on the ceramic chip package containing the EndoCam using an adapter (SSW-107-02-G-D-RA, Samtec); this can be seen in Figure 5.2.

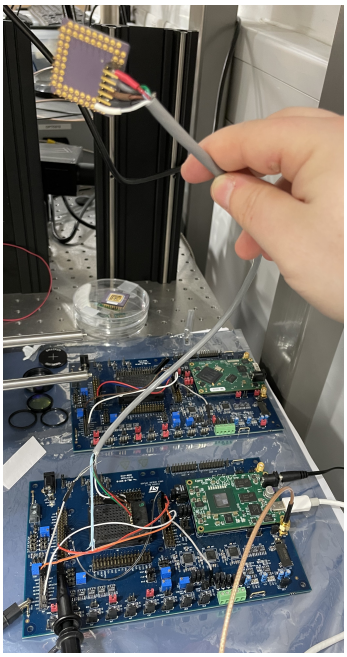


Figure 5.2: The EndoCam was connected to the board over a 50 cm-long screened cable for initial testing of the connectivity.

Oscilloscope traces of a 20 MHz clock signal on the motherboard and at the end of the cable can be seen in Figures 5.3a and 5.3b respectively. Clearly there is significant degradation of the signal quality and it is not at all surprising that the chip is unable to operate at the end of the cable. It is noteworthy that even directly on the board, the clock signal is far from ideal, suggesting that the clock signal quality from the FPGA module might not be adequate for operation of the chip remotely. This is especially true when considering that the 50 cm cable used here is still far too short for use in an endoscope, where a cable length of ∼2 m may be required.

The signal quality can be improved by operating at a slower clock frequency; as can be seen in Figures 5.3c and 5.3d which show a 10 MHz clock signal measured on the motherboard and at the end of the cable respectively. Significant ringing still remains in the signal both on the board and at the end of the cable, but at this frequency the chip is able to pass the initialisation tests and operate at the end of the cable. While operating at a slower clock frequency is acceptable for initial tests and ultimately would allow the system to function, it has an inversely proportional effect on the acquisition time; if the clock frequency is halved from 20 MHz to 10 MHz, then the acquisition time for each measurement will be doubled.

5.1.2 Custom PCB design

In order to address the connectivity challenges outlined in the previous section, a custom PCB was designed for remote operation of the Endo-

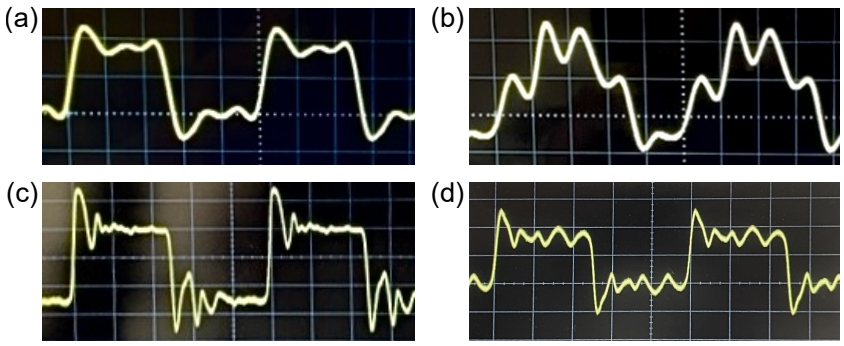


Figure 5.3: Oscilloscope traces of the EndoCam clock signal. (a) A 20 MHz clock signal probed at a pin on the motherboard and (b) probed at the end of a 50 cm long screened cable. (c) A 10 MHz clock signal on the motherboard and (d) at the end of the same cable. The scale on the x-axis is 10 ns/div for the 20 MHz signals and 20 ns/div for the 10 MHz signals.

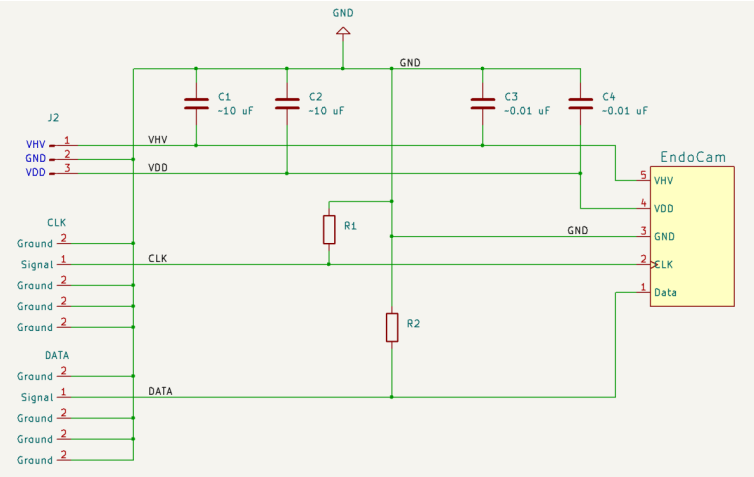


Figure 5.4: The electronic circuit schematic used for the custom PCB design for the EndoCam.

Cam away from the motherboard. The electronic circuit diagram for the PCB is presented in Figure 5.4. Two capacitors to ground (one low frequency and one high frequency) have been placed on both the VHV and VDD connections; this is in an effort to ensure these signals are as stable as possible as supplied to the EndoCam. In the circuit schematic there have also been resistors to ground added to both the CLK and DATA signals; this was initially considered as an option to reduce the ringing observed in these signals but ultimately this was not pursued further. Pads for these resistors are included on the PCB layout but have been left unconnected after assembly.

Schematics of the PCB layout and photographs of the PCB after assembly are presented in Figure 5.5. The main goal of the PCB design was to ensure a reliable connection between the EndoCam and the motherboard which might preserve the CLK and DATA signal integrity as much as possible. For this purpose, the PCB was designed with SMA connectors for both these signals. These connectors enable the use of coaxial cables which provide good signal shielding and are screwed onto the board, establishing a reliable electrical and mechanical connection. The other three signals are connected using pin headers on the PCB. All five connections are made on the opposite side of the PCB to where the EndoCam chip is mounted.

In addition to addressing the connectivity challenges, the PCB was designed with a 25 mm-diameter circular footprint. This enables the EndoCam, mounted on the PCB, to be inserted into standard lens tubes and easily integrated into optical imaging systems. The assembled PCB, including the EndoCam and inserted into a Thorlabs SM1 lens tube, can be seen in Figures 5.5c and 5.5d.

When mounted on the PCB, the chip can now successfully operate remotely with a 20 MHz clock signal frequency. In the interest of reliability, cables of 30 cm to 50 cm in length were used for operation.

5.1.3 Optical design

The tumours used in this study were induced in female Balb/C mice using murine colorectal carcinoma CT26 cells. Cells were injected subcutaneously into the flank of the mice and allowed to grow for at least 12 days; after this time they were typically between 0.5 cm and 1 cm in diameter. For the pH measurements, it was desirable to image the whole tissue sample in the same image. This meant that the target field of view for the system was approximately 1 cm × 1 cm.

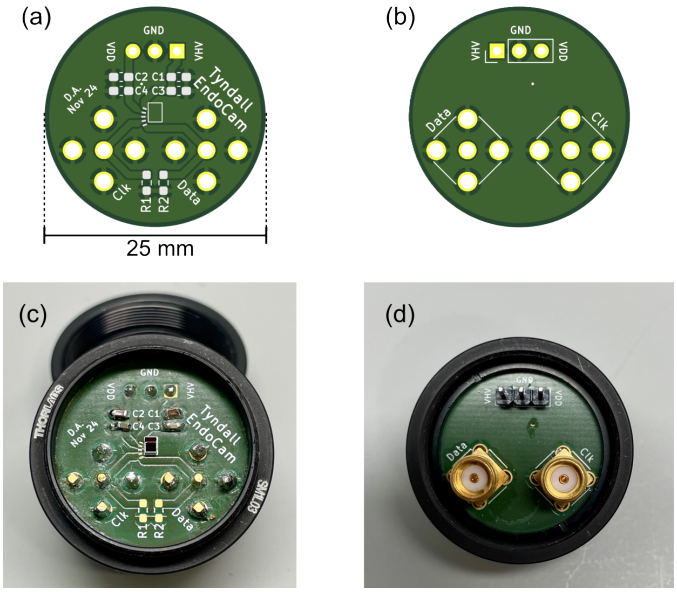


Figure 5.5: Schematics showing the (a) front and (b) back sides of the custom PCB layout. Photographs of the (c) front and (d) back of the PCB housed in a Thorlabs SM1 lens tube after soldering of all components and connection of the EndoCam.

Given that the active area of the EndoCam is ∼1 mm × 1 mm, this required a ten-fold demagnification from the sample plane to the detector plane. This is achieved by using something akin to a reversal of a traditional microscope optical design. Fluorescence emission from the planar sensor is collected using an achromatic doublet with a focal length of 100 mm (AC254–100-B-ML, Thorlabs) and then imaged onto the detector using a microscope objective (LU Plan Fluor 20×, Nikon).

It was mentioned above that a ten-fold demagnification was required, but a 20× microscope objective has been used. This is because the objective is designed for use with a tube lens with a focal length of 200 mm; by instead using the achromatic doublet with half the focal length, the effective magnification (or demagnification as implemented here) is also halved to the desired amount. This also has the benefit of giving the system a working distance of 100 mm as opposed to 200 mm, thereby increasing the amount of fluorescence emission collected. An image of a ruler captured with the system is presented in Figure 5.6, verifying that in practice the system has a field of view slightly larger than 1 cm × 1 cm.

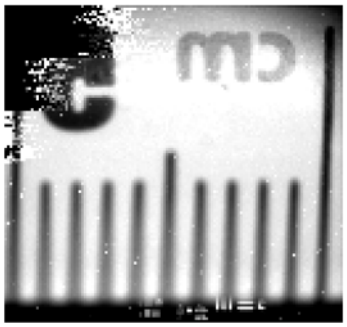


Figure 5.6: An intensity image of a ruler captured with the benchtop system to verify that the field of view meets the target requirements.

The 405 nm pulsed laser diode operated at a repetition rate of 20 MHz is used for excitation with the system; this was the excitation wavelength used in the initial development of the planar sensors [104]. The optical setup has an epi-fluorescence configuration. The pulsed laser source delivers a collimated beam which is focused using an aspheric lens (part number) and directed towards the sample using a dichroic mirror (FF506-Di03–25×36, Semrock) through the same achromatic doublet used for fluorescence emission collection. The position of the spheric lens is adjusted such that the excitation beam is focussed to the back focal plane of the achromatic doublet. This results in a collimated excitation beam reaching the sample. A 600 nm long-pass emission filter (FEL0600, Thorlabs) is placed before the microscope objective to remove the excitation light and isolate the fluorescent emission from the OEPK sensor which is almost entirely in the 600 nm to 700 nm range [104]. A schematic and photograph of the imaging system are presented in Figure 5.7 including the addition of a hot plate used for regulation of the tissue sample temperature during measurements. A list of the optical elements used in the

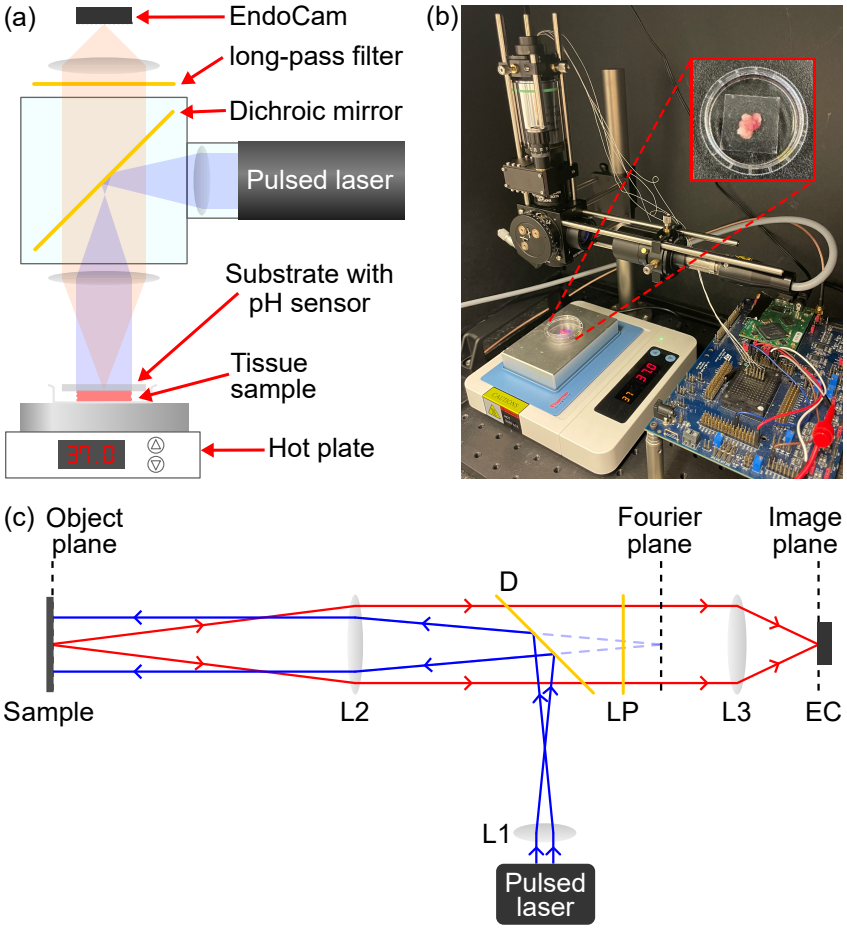


Figure 5.7: (a) Schematic of the measurement setup applied in Paper **I** including the wide-field bench-top FLIm system, the tissue sample in a Petri dish covered with the pH sensor and placed on a hot plate for temperature control. (b) Photograph of this setup, including a top-down image of a tissue sample and pH sensor in a Petri dish. (c) An optical diagram of the imaging system. The key for the part labels can be seen in Table 5.1 below.

Key	Part	Supplier	Part No.
EC	EndoCam	-	-
L1	Aspheric lens, f =20.1 mm	Thorlabs	ACL2520U-A
L2	Achromatic doublet, f =100 mm	Thorlabs	AC254–100-B-ML
L3	Infinity-corrected objective, 20×	Nikon	LU Plan Fluor 20×
D	Dichroic mirror, 506 nm long-pass	Semrock	FF506-Di03–25×36
LP	Emission filter, 600 nm long-pass	Thorlabs	FEL0600

Table 5.1: Optical elements used in the bench-top imaging system for lifetime-based metabolic imaging shown in Figure 5.7.

system is shown in Table 5.1.

5.1.4 MPE calculations and evaluation

To evaluate suitability for potential *in vivo* applications, the delivered exposure from the bench-top system is compared with the maximum permissible exposure (MPE) values provided in I.S. EN 60825-1 [38]. The 405 nm laser is operated at a repetition rate (f_{rep}) of 20 MHz, with an average excitation power (P_{ave}) of 1.3 mW, and has a typical pulse width (t_{pulse}) of 100 ps. The excitation is delivered to the sample as a

10 mm diameter collimated beam.

First, we consider the exposure from a single laser pulse; the peak power during a pulse is found from equation 5.1:

$$P_{peak} = \frac{P_{ave}}{f_{rep} \cdot t_{pulse}}, \tag{5.1}$$

yielding a peak power of 0.65 W[1]. The standard states that the exposure must be averaged over a 3.5 mm diameter aperture; to do this we assume the beam profile is Gaussian and find the laser power that would pass through the limiting aperture when the beam and aperture are aligned i.e. when the brightest portion of the beam passes through the aperture. This approach is more conservative than assuming a top-hat profile as a greater portion of the beam passes through the aperture with this approach. The power which passes through the aperture (P_{acc}) can be found from equation 5.2:

$$P_{acc} = P_{beam}\left(1 - \exp\left(-\frac{2\alpha^2}{\omega^2}\right)\right), \tag{5.2}$$

where P_{beam} is the total power in the beam(here equal to P_{peak}), α is the aperture radius of 1.75 mm and ω is the beam radius of 5 mm. In this case this translates to 21.7% of the beam passing through the aperture, 0.142 W. Averaged over the limiting aperture area this gives an intensity of $1.48 \times 10^4\,\mathrm{W\,m^{-2}}$ for a single pulse. At this time scale the skin MPE stated in the standard is $2 \times 10^{11}\,\mathrm{W\,m^{-2}}$, therefore the system is well below the skin MPE for a single pulse.

For prolonged exposure we can again use equation 5.2, this time using the average power value of 1.3 mW for P_{beam}. Doing this we get an average intensity of $29\,\mathrm{W\,m^{-2}}$. The skin MPE for exposures up to 30 000 s is $2000\,\mathrm{W\,m^{-2}}$, nearly two orders of magnitude higher than the exposure delivered by the system. This analysis demonstrates that, under the conditions used here, the system cannot approach the skin MPE during any plausible imaging sequence.

5.1.5 Summary

Here the EndoCam has been successfully integrated into a bench-top imaging system and applied for lifetime-based metabolic imaging of *ex vivo* tissue samples using fluorescent planar pH sensors as presented in Paper **I**. This has been achieved through the design of a custom PCB for remote operation of the EndoCam, and through the design and construction of a custom wide-field FLIm system which meets the requirements for imaging the tissue samples under examination.

Measurement of tumour acidosis *in vivo* is of interest to deepen understanding of tumour metabolism [106] and has shown potential for surgical guidance [107]. Translation of the technology applied in Paper **I** to *in vivo* measurements could be achieved through the deposition of the sensor on to the tissue area of interest, followed by imaging of the sensor with a system similar to the one developed here but with increased portability. This may find use in application areas with adequate space for sensor deposition to be carried out, such as examination of lesions on the skin or in the oral cavity.

The integration and application of the EndoCam as described here and in Paper **I** is a good example of the utility of SPAD arrays applied for

[1] Equation 5.1 assumes the pulse has a square shape. In reality, the temporal pulse shape is closer to Gaussian with a FWHM of 100 ps. Assuming a square pulse is simpler and, crucially, it overestimates the peak power, leading to a more conservative estimate for safety considerations.

wide-field FLIm in biomedical research. It also demonstrates the effectiveness of the EndoCam specifically in performing such measurements. However, the bench-top system developed here does not take advantage of the miniature form factor of the EndoCam. The next steps in the project focus on the validation of the EndoCam with a more miniaturised system as described in Section 5.2, and the integration of the detector into a chip-on-tip FLIm micro-camera small enough for endoscopic applications as described in Chapter 6 and Paper **III**.

5.2 Miniaturised FLIm imager

As mentioned in the previous section, a more portable system using the EndoCam could be applied for examination of lesions on the skin or in the oral cavity. This could be done in combination with exogenous probes such as the ones applied in Paper **I** or through measurement of endogenous fluorescence lifetimes. Therefore there was an interest, at an early stage in the project, in integrating the EndoCam into a handheld imaging system. This would allow the detector to be tested and validated in a more miniaturised system.

In this section, the work carried out in the development of this smaller imager with a handheld form factor is outlined; this includes the design of an additional custom PCB for integration into smaller lens tubes, and the optical design of the system. The development of this system commenced at the same time as for the system described in Section 5.1. The system was presented at Photonics West 2023 [108] as can be seen in Paper **II** which includes a characterisation of the spatial and temporal performance and example images of plant samples captured with the system.

5.2.1 Custom PCB design

In order to integrate the EndoCam into a more miniaturised system, a second custom PCB layout was designed. Schematics of the PCB layout and photographs of the assembled PCB can be seen in Figure 5.8. This smaller PCB has a diameter of 12.5 mm allowing it to be inserted into

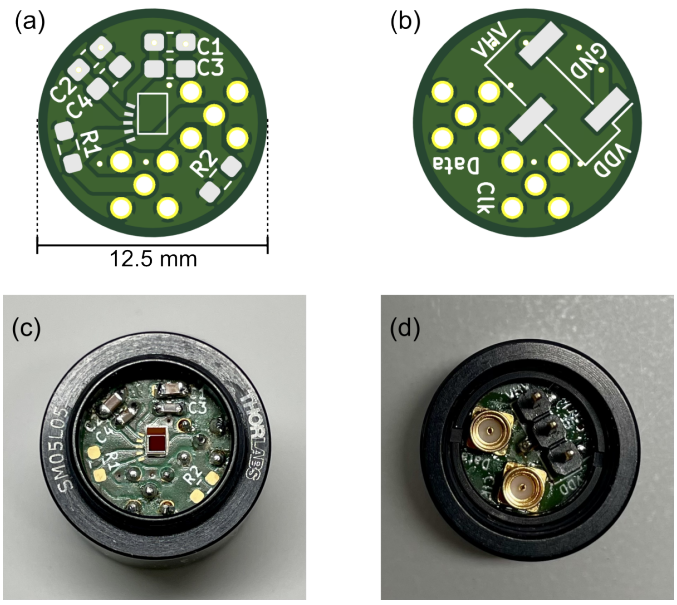


Figure 5.8: Schematics of the (a) front and (b) back sides of the miniaturised custom PCB layout. Photographs of the (c) front and (d) back of the PCB housed in a Thorlabs SM05 lens tube after soldering of all components and connection of the EndoCam.

standard SM05 lens tubes which can be purchased from suppliers such as Thorlabs and Edmund Optics; these type of lens tubes are the ones used in the handheld rigid scanning FLIm endoscope presented in Cheng et al. [61] which was later applied for *in vivo* FLIm in the oral cavity [62].

This PCB uses the same electronic design as shown before in Figure 5.4; a more compact layout was achieved through careful positioning of the components and by replacing the SMA connectors with MMCX connectors (1-1634009-0, TE Connectivity); these connectors have a smaller footprint but still enable the use of coaxial cables and provide a reliable electrical and mechanical connection.

5.2.2 Optical design

The optical design uses an epi-illumination scheme with a very similar layout to the system described in Section 5.1. A schematic and photograph of this miniaturised system are presented in Figure 5.9. A list of the optical elements used is shown in Table 5.2.

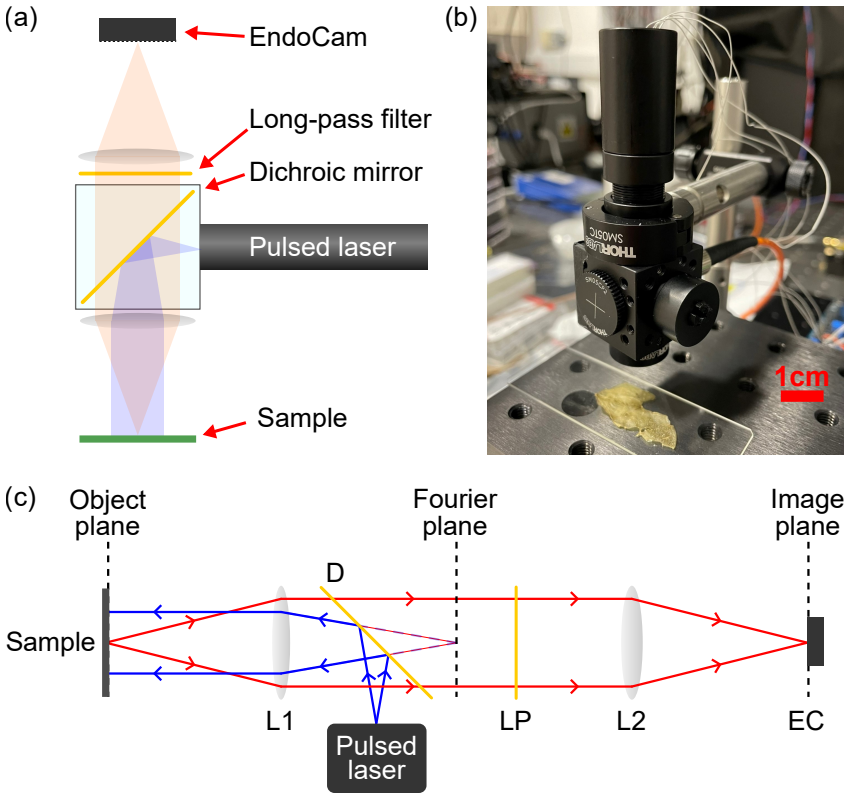


Figure 5.9: A basic schematic (a) and a photograph (b) of the miniaturised wide-field FLIm system. (c) An optical diagram of the imaging system. The key for the part labels can be seen in Table 5.2.

Key	Part	Supplier	Part No.
EC	EndoCam	-	-
L1	Achromatic doublet, f =19 mm	Thorlabs	AC127-019-AB-ML
L2	Achromatic doublet, f =19 mm	Thorlabs	AC127-019-AB-ML
D	Dichroic mirror, 506 nm long-pass	Semrock	FF506-Di03–25×36
LP	Emission filter, 515 nm long-pass	Semrock	FF01-515/LP-25

Table 5.2: Optical elements used in the handheld wide-field FLIm system shown in Figure 5.9.

For this system, two achromatic doublets with a focal length of 19 mm are used (AC127-019-AB-ML, Thorlabs); one to collect the light from the sample, the second to re-focus it onto the sensor. This means the system has a magnification of approximately one, therefore imaging an area of $\sim$1 mm $\times$ 1 mm.

The excitation light is coupled into an optical fibre which is connected to the side of the system. A long-pass dichroic mirror and filter (FF506-DI03-25X36, Semrock) was cut to approximately 12 mm $\times$ 15 mm, and used to direct the excitation light towards the sample. The distance between the fibre tip and the first achromatic doublet was adjusted such that the excitation beam reaching the sample was approximately collimated. A long-pass filter (FF01-515/LP-25, Semrock) was also used for removal of elastically scattered light before the second lens.

5.2.3 Animal tissue demonstration

In addition to the measurements presented in Paper **II**, images were also captured of *ex vivo* animal tissue samples to demonstrate tissue lifetime imaging with the system. Two samples cut from a porcine heart were used for these measurements. One sample was cut from the myocardium, the muscular layer of the heart, and the other was cut primarily from the pericardium, the fibrous tissue which encloses the heart. The two samples were soaked in 1M Zinc phthalocyanine (ZnPc) solution for 10 minutes. ZnPc is a common photosensitiser used in photodynamic therapy and was used here to increase the fluorescence signal for tissue imaging. The 405 nm pulsed laser diode was used for excitation at a repetition rate of 20 MHz and an average power of 0.33 mW. Photon counts were acquired over 20 time bins with an acquisition time of $\sim$15 s. Pixels were binned into groups of four to improve photon statistics, and tail fitting with a mono-exponential decay model was performed between 90 % and 20 % of the peak value.

Fluorescence intensity and lifetime images of the samples are presented in Figure 5.10 along with the lifetime distributions. The lifetime images have been upscaled to the original image dimensions and pixel values interpolated (bilinear) for display purposes only. The brightness of each pixel in the lifetime images is scaled by the intensity to highlight regions with a strong fluorescence signal. The field of view has been cropped to exclude the defective pixel region.

There is a clear lifetime contrast measured between the two samples; the myocardium sample has a mean lifetime of 1.84 ns with a standard deviation of 1.20 ns while the pericardium sample has a lifetime of 3.20 ns and a standard deviation 0.56 ns. The observed difference in fluorescence lifetimes between the two samples may be due to the difference in composition of the two tissue types. The pericardium is connective tissue rich in collagen while the myocardium is composed primarily of metabolically active cardiac muscle, with a higher content of endogenous fluorophores, such as NADH and FAD (flavin adenine dinucleotide), which are involved in metabolic processes.

5.2.4 MPE evaluation

Using the same methodology described in Section 5.1.4, the exposure from the miniaturised FLIm imager is assessed and compared with MPE values in I.S. EN 60825-1. The peak irradiance from a single excitation pulse, averaged over the limiting aperture, was found to be $4.8 \times 10^3\,\mathrm{W\,m^{-2}}$, while the corresponding time averaged irradiance was $9.7\,\mathrm{W\,m^{-2}}$. For this wavelength, the relevant skin MPEs are $2 \times 10^{11}\,\mathrm{W\,m^{-2}}$ for nanosecond scale pulsed exposure and $2 \times 10^3\,\mathrm{W\,m^{-2}}$ for prolonged exposure up to 30 000 s. Both the single pulse and average

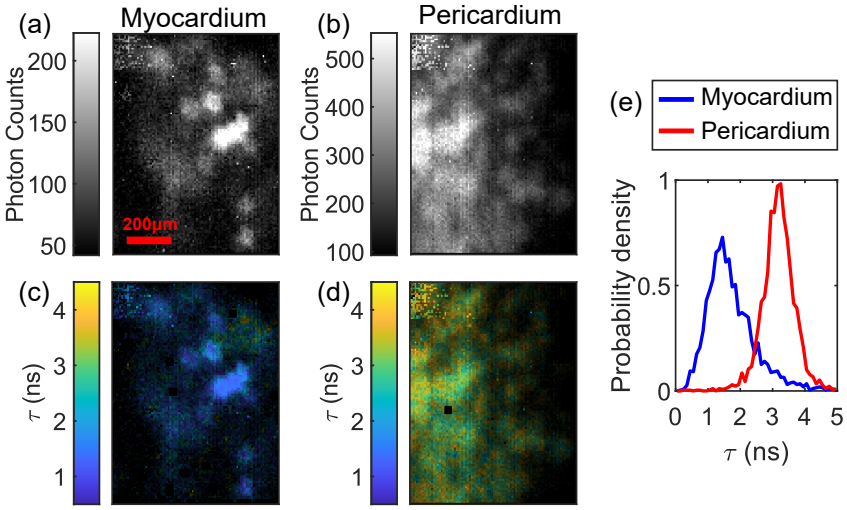


Figure 5.10: Example fluorescence intensity (a and b) and lifetime (c and d) images of *ex vivo* porcine heart samples captured with the miniature wide-field FLIm system. The samples were excited using the 405 nm laser at a repetition rate of 20 MHz and an average power of 0.33 mW. Photon counts were acquired over 20 time bins with an acquisition time of ∼15 s. (e) Lifetime distributions for the two samples. The myocardium sample had a mean lifetime of 1.84 ± 1.20 ns (standard deviation) and the pericardium sample had a mean lifetime of 3.20 ± 0.56 ns.

irradiance values are therefore well below the applicable skin MPEs. As with the bench-top configuration, these results indicate that the excitation levels used in the miniaturised FLIm imager are comfortably within recognised safety limits when assessed against skin exposure criteria.

5.2.5 Summary

In this section the EndoCam has been integrated into a handheld wide-field FLIm system. This system has been characterised and validated as presented in Paper **II**; the presented system has a spatial resolution of 12.4 µm and has been shown to successfully differentiate polymer bead samples with a range of fluorescence lifetimes. In addition, the FLIm capability of the system with tissue samples has been demonstrated here on stained porcine tissue samples.

With further development and refinement of the system described here, the EndoCam could be applied for a thorough study of *in vivo* fluorescence lifetimes in the oral cavity, on the skin, or in the brain, where there is sufficient space for use of a handheld probe. It could also be deployed as a compact system for intraoperative FLIm of freshly excised tissue samples. For this project, a primary goal was to integrate the EndoCam into a micro-camera system for endoscopic applications; therefore, the application of a handheld system has not been further explored here. Other researchers have however had success in the further development of handheld systems using the EndoCam for wide-field FLIm of tissue samples [98, 99].

5.3 Discussion

The two wide-field FLIm systems presented in this chapter were developed with distinct goals but ultimately serve a common purpose: to evaluate the suitability of the EndoCam SPAD array for wide-field, time-resolved imaging under conditions representative of future clinical deployment. Together, they illustrate both the capabilities of the detector

and the engineering constraints that arise when moving from bench-top experimentation toward miniaturised instrumentation.

The bench-top system demonstrates that robust wide-field lifetime imaging can be achieved using the EndoCam. Its application to planar pH sensors and *ex vivo* tumour samples, as seen in Paper **I**, shows that the detector can support biologically meaningful measurements, even when fluorescence contrast arises from subtle lifetime shifts. This system benefits from the comparatively strong fluorescence of the optochemical sensors, a stable optical geometry, and the freedom to use large optics without space constraints. These advantages allow high-precision lifetime estimation and provide a controlled environment in which to validate the detector and imaging workflow. At the same time, the system's physical footprint, demagnification optics, and mechanical complexity make it impractical for endoscopic use, highlighting the gap between laboratory performance and the realities of clinical translation.

The handheld system provides a complementary evaluation by prioritising compactness and mechanical simplicity. Its ability to differentiate beads with known lifetimes and to image *ex vivo* porcine tissue demonstrates that useful lifetime contrast can be extracted even with a greatly reduced footprint and a restricted photon budget. This shows that the EndoCam can deliver meaningful lifetime contrast under conditions much closer to those expected of a deployable instrument.

A significant finding common to both systems is that they were able to operate safely within established exposure limits [38]. The bench-top configuration, despite using relatively high excitation power for metabolic imaging, delivered irradiances far below the relevant MPE thresholds. Likewise, the handheld system, operating at substantially reduced optical throughput, also remained comfortably within these limits. This demonstrates that lifetime imaging with the EndoCam can be performed safely at excitation levels compatible with biological samples, an essential requirement for future *in vivo* studies.

Viewed together, the two imaging platforms provide a valuable comparative perspective on how the EndoCam performs across a spectrum of operating conditions, from large bench-top designs to more space-limited, miniaturised systems. This perspective is essential for understanding how the detector behaves when scaled toward endoscopic dimensions. The bench-top system maximises performance and validates the sensor technology, while the handheld system demonstrates practical feasibility in a compact form factor and clarifies the engineering trade-offs required for portability.

Finally, these results emphasise the broader theme of this thesis: that the miniaturisation of SPAD arrays opens a pathway toward compact, wide-field lifetime imaging devices. The systems developed in this chapter validate the feasibility of such devices and clarify the optical, electronic, and safety-related considerations that must be addressed as the detector is further scaled and integrated. These insights directly inform the system architecture and design choices made in the chip-on-tip FLIm micro-camera presented in the following chapter.

5.4 Conclusions

This chapter has evaluated the EndoCam SPAD array through the development of two wide-field FLIm systems: a bench-top platform for lifetime-based metabolic imaging and a compact handheld system for portable tissue imaging. Both systems demonstrated the detector's ability to capture meaningful fluorescence lifetime contrast while operating well within recognised exposure limits. The engineering solutions developed here, particularly for remote operation and compact optical design,

provide a foundation for further miniaturisation. These findings motivate and inform the design of the chip-on-tip FLIm micro-camera presented in the next chapter.

Chapter 6

Chip-on-tip FLIm micro-camera

This chapter details the design, development, and integration of a compact chip-on-tip fluorescence lifetime imaging (FLIm) micro-camera system using the EndoCam as the detector. A primary objective of this work was to develop a system with dimensions suitable for endoscopic applications. As such, the developed micro-camera has an external diameter of 4 mm and a rigid length of 10 mm. To the best of the author's knowledge, this represents the first chip-on-tip FLIm micro-camera on a size scale compatible with endoscopic applications. This development is a significant step towards evaluating the capability of miniaturised SPAD arrays for wide-field chip-on-tip endoscopic FLIm, which is a core goal of this thesis.

In this chapter the design process for the FLIm micro-camera is explained including the custom flexible printed circuit board (PCB); the optical design considerations and simulations undertaken; the mechanical design of the housing and mounting components; and the assembly process. Finally, the integration of the excitation light source is presented, highlighting challenges such as stray fluorescence and off-centre illumination encountered during development, and the solutions implemented to overcome them.

The implementation of the FLIm micro-camera led directly to the work published in Paper **III**, which includes a comprehensive characterisation of the spatial and temporal performance of the micro-camera. The device has been further characterised as part of the work for Paper **IV**, where novel solid-state fluorescence lifetime standard tools were applied for system validation. The results of the FLIm micro-camera characterisation from both of these are summarised briefly at the end of this chapter.

6.1 Custom PCB

For integration of the EndoCam into the chip-on-tip micro-camera system, a custom flex PCB was designed by Dr. Walter Messina. This PCB design is shown in Figure 6.1. The PCB thickness is 150 µm, the material is polyamide with ENEPIG (Electroless Nickel Electroless Palladium Immersion Gold) finish, fabricated by Genesis Circuits. The PCB has a width of 2 mm and a length of 13 mm (though the length is not critical) with five traces running the length of the PCB. It was designed such that the EndoCam chip can be placed at one end, wire bond connections made from the pads on the chip to the five PCB traces, then micro-coaxial cables (9442 WH033, Alpha Wire) soldered to the other end of the PCB to be connected back to the motherboard. The traces are 0.2 mm wide and the pads for soldering are 0.275 mm wide.

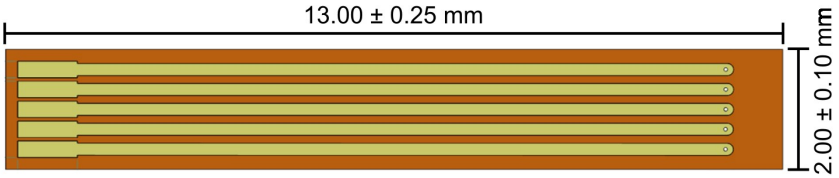


Figure 6.1: Custom flexible PCB designed for the FLIm micro-camera. The PCB enables wire bonding of the EndoCam sensor on the right as imaged here and connection to the system via micro-coaxial cables soldered to the pads on the left.

Given the size constraints, there were no additional components such as decoupling capacitors included in this design. Also, considering the connectivity challenges already faced with the EndoCam, a conservative cable length of 30 cm was used for the FLIm micro-camera.

6.2 Optical design

For the optical design, the main considerations were the spatial resolution, field of view, and the light collection efficiency of the system. Commercial white-light endoscopes are typically designed with a very large field of view for navigation, and to maximise throughput in terms of the total area of tissue imaged. However, this would likely result in a longer working distance, thereby reducing the amount of light collected. For FLIm, the signal level is typically weak (especially with endogenous fluorescence), so maximising the amount of light collected is critical. In the end, it was decided to target a field of view similar to the wide-field fibre-bundle FLIm probes reported by Sparks et al. [81] and Cheng et al. [82] of ∼2.3 mm.

6.2.1 Initial exploration

For the two fibre bundle probes mentioned previously, the lens is glued directly onto the fibre bundle. Similarly for the NanEye, a commercially available CMOS micro-camera from ams, the lens is integrated with the sensor at the wafer level into a single device. In the case of the EndoCam however, wafer-level integration was not an option as the devices had already been diced. The bond pads are also positioned on the same side of the device as the active area, immediately adjacent to it. Therefore if a lens were to be glued directly to the camera, it must be small enough not to cover these pads required for operation.

This option was explored at an early stage using a 1 mm diameter GRIN lens with a focal length of 10 mm. The lens was glued directly to the active area on the detector and black paint was added to the outside of the lens in an effort to block stray light. A photograph of the EndoCam with this lens glued onto it can be seen in Figure 6.2 along with example images captured with this configuration.

This approach was not pursued beyond this initial test but the potential benefit of integrating the lens with the detector in one solid piece merits further consideration. One drawback apparent in this configuration is that the pixels in the corner of the detector are not utilised; they are also saturated by ambient light in the room directly hitting the detector, though this could be eliminated if the device were packaged fully. Interestingly, though the lens has a nominal focal length of 10 mm, the image remains near in focus for distances much greater than this as can be seen in Figure 6.2b. This large depth of focus could be of practical use in surgical applications if the detector was to be used for navigation imaging, similar to a standard endoscope, prior to FLIm measurements.

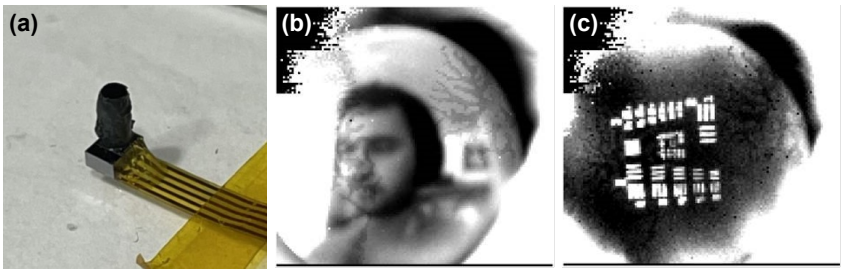


Figure 6.2: (a) Photograph of the EndoCam with a 1 mm GRIN lens glued directly to the sensor surface. (b) An example image of myself captured with this configuration, showing extended depth of field and artefacts from epoxy thickness variation. (c) An image of a USAF resolution test target captured at a working distance of 10 mm.

There is also a strange pattern visible across the images, most prominently seen in the top-right hand region of Figure 6.2b. It is suspected that this is due to variation in thickness of the epoxy between the lens and the detector or perhaps small air gaps. It is likely that this effect could be eliminated with further development of the lens integration process.

Following this early exploration, it was decided to instead use a lens with a larger diameter, mounted a small distance away from the detector surface. The strategy employed for mounting the lens is described in Section 6.3. This would allow utilisation of the full detector area and avoid the patterning effects mentioned previously.

6.2.2 Final design

For the final design, a 2 mm diameter GRIN lens (Grintech) was used with a length of 5.1 mm. An aperture window with a 1.8 mm diameter opening and a thickness of 0.3 mm was glued directly to the front of the lens, this step was performed by Grintech prior to shipping the lens. A 0.3 mm thick long-pass filter with a cut-on wavelength of 500 nm was chosen for use in the micro-camera. A ray-tracing simulation of this design and the spot diagrams at different distances from the optical axis on the image plane are presented in Figure 6.3. The distance between the

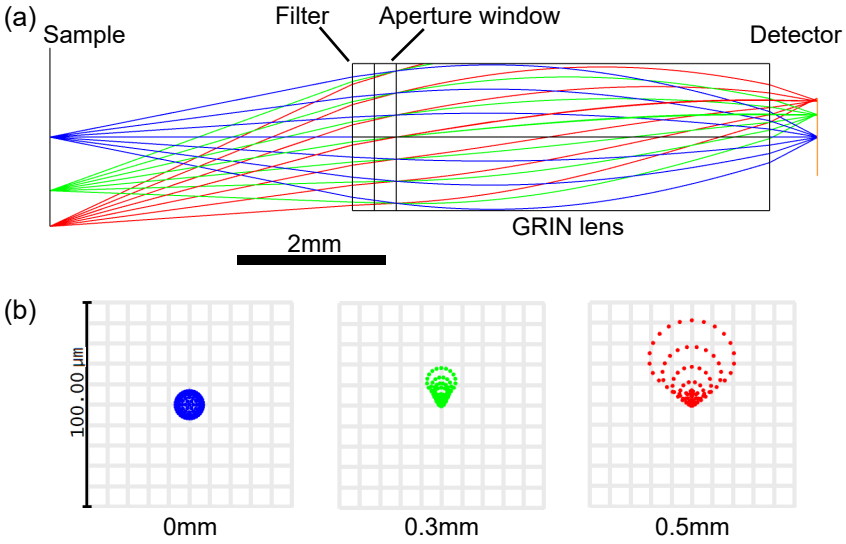


Figure 6.3: (a) A Zemax ray-tracing simulation of the final FLIm micro-camera optical design. (b) Spot diagrams from this simulation at various distances from the optical axis at the image plane.

back of the lens and the detector is 0.65 mm and the distance between the sample and the filter (the working distance) is 4.1 mm.

The distance between the sample and the 1.8 mm diameter aperture is therefore 4.7 mm, from this we can give a rough estimate for the numerical aperture of the microcamera as 0.19. The real value may be marginally larger than this given the higher refractive index of the filter and aperture window which are in between the sample and the aperture itself.

From the simulation, the RMS spot radius is 5.9 µm at the optical axis, 5.5 µm at 0.3 mm from the optical axis, and 14.1 µm at 0.5 mm from the optical axis. The EndoCam has a pixel pitch of 8 µm so a spot diameter close to this value is desirable. The EndoCam has an active area of ∼1 mm × 1 mm so a distance of 0.5 mm from the optical axis is at the very edge of the detector and the corners. The decreased performance at the image edges was considered tolerable for this demonstrator system, but is an area to be improved on in future designs.

6.3 Mechanical design

In this section, the design of the mechanical parts used to house the different components of the FLIm micro-camera is described along with the assembly process. The design and the assembly process presented here are the result of approximately four iterations. A design would be developed and the parts fabricated, then the assembly carried out by myself and Noreen Nudds from the Photonics Packaging Group at Tyndall National Institute. During and after assembly, Noreen and myself would discuss areas for improvement and adjustment. Based on this feedback, the designs were further iterated.

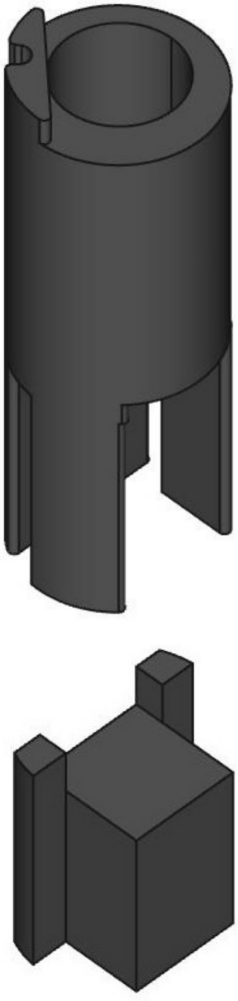


Figure 6.4: 3D CAD models of the custom 3D-printed components used in the FLIm micro-camera: (bottom) chip mount, (top) lens mount with groove for fibre placement.

6.3.1 3D-printed mounts

For the mechanical design of the FLIm micro-camera, custom 3D-printed parts were developed. These parts were fabricated by Proto Labs Ltd. using stereolithography with Accura ABS Black (SL 7820) as the material. The design consists of three separate custom parts: a chip mount to hold the EndoCam, a lens mount to hold the GRIN lens, and an outer casing to house the system. The chip mount and lens mount were designed to have interlocking teeth which helped increase mechanical stability between the two pieces and maintain alignment between the lens and the detector.

The lens mount has a 2.1 mm diameter hole for insertion of the 2 mm diameter lens. There is a 1.9 mm diameter lip at the bottom of the hole which holds the lens, keeping it the correct distance (0.65 mm) from the detector. Along the edge of the lens mount there is a groove for holding an optical fibre to deliver excitation light. At the top of the lens there is a space left for the long-pass filter to be glued in place. 3D CAD models of the chip and lens mounts can be seen in Figure 6.4. When the two parts are put together there is an opening left at one side for the flex PCB to exit.

The outer casing is simply a hollow tube which slides over the top of the other two parts to house them along with the optical fibre. The case has a wall thickness of 0.3 mm, the minimum supported by the 3D printing process, giving an outer diameter of 4 mm for the micro-camera design. This outer casing could be replaced by an appropriately-sized metal tube, which is more suitable for medical applications and may marginally decrease the outer diameter of the micro-camera.

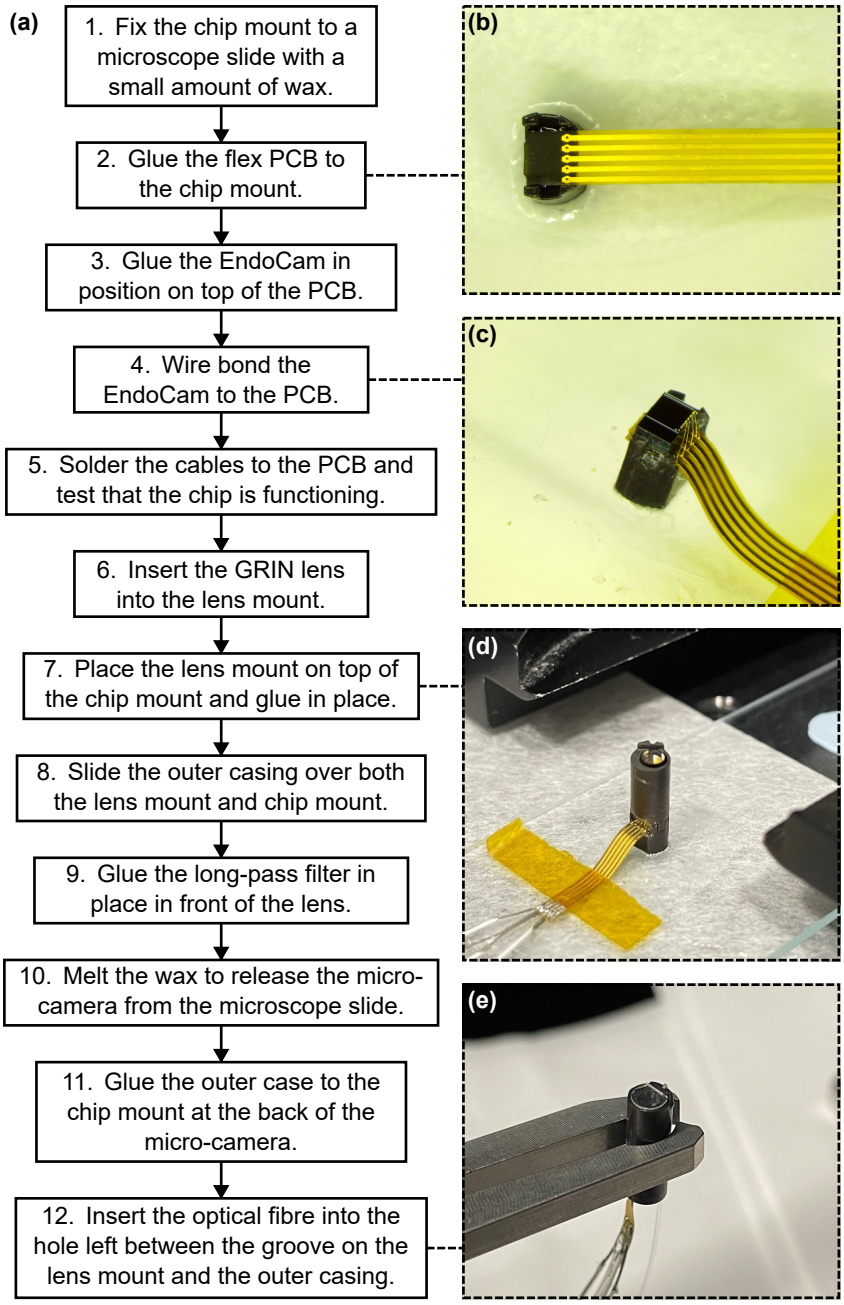


Figure 6.5: (a) The assembly process for the FLIm micro-camera. (b) A top-down photograph of the chip mount with the flex PCB glued in place after step 2. (c) The EndoCam glued in place and wire bonded to the PCB after step 5. (d) The FLIm micro-camera with the chip and lens mounts assembled and the lens inserted after step 7. (e) The fully assembled FLIm micro-camera including the EndoCam, imaging optics, long-pass filter, and an optical fibre for excitation light delivery.

6.3.2 Assembly process

The assembly of the FLIm micro-camera was carried out in a stepwise manner, as illustrated in Figure 6.5 which also includes photographs of key stages in the assembly process. It is worth noting that the cables are connected to the PCB midway through the system assembly. This was necessary as a failure rate of approximately 50 % was observed with the EndoCam, meaning the chip would not power up; this was observed both by ourselves and by the research group in Edinburgh who developed

the chip. The exact cause of these failures is unknown, it may be due to fabrication variations leading to internal failures, or due to electrostatic discharge at any point in the chip handling. Care was of course taken to avoid this second case where possible. Therefore, by attaching the cable and testing the chip midway through assembly, parts were not lost unnecessarily by integrating them with a non-functioning chip.

6.3.3 Mid-assembly tests

Connecting the cables and testing the chip mid-way through the assembly also allowed for an initial validation of the micro-camera's optical design. This was carried out following step 7 in the assembly process when the lens has been added but the casing, filter and optical fibre had not. At this point, the device is still fixed to the microscope slide as seen in Figure 6.5d.

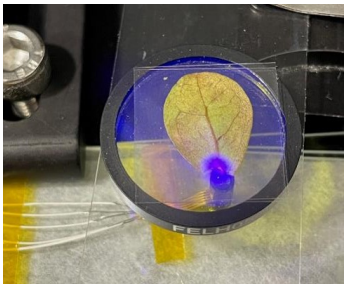


Figure 6.7: The configuration used to capture the lifetime image of the leaf sample shown in Figure 6.6b. The micro-camera was positioned under the sample with the long-pass filter in between. 405 nm excitation was provided from above.

An intensity image of the millimetre lines on a ruler was captured, showing that the device has a field of view of approximately 2 mm × 2 mm as seen in Figure 6.6a[1]. A fluorescence lifetime image was also captured of a leaf sample. In order to perform this measurement the leaf sample was mounted on a microscope cover-slip on top of a long-pass filter (FELH0500, Thorlabs), with the micro-camera positioned below both the sample and the filter as seen in Figure 6.7. A collimated beam of 405 nm excitation light was aimed from above at the leaf sample. The resulting lifetime image from this measurement can be seen in Figure 6.6b. Having performed this initial validation of the optical design, the rest of the assembly process was carried out.

6.4 Excitation source integration

6.4.1 Stray fluorescence

Initially, a standard multimode fibre (FP400URT, Thorlabs) was used to deliver the excitation light to the sample. However, during early testing, significant stray fluorescence was observed originating from the micro-camera mount, as shown in Figure 6.8a. This fluorescence was attributed to the excitation light leaking from the fibre and interacting with the surrounding 3D-printed plastic components. This effect was observed with both the 405 nm and 375 nm laser sources. A silica-coated fibre (FG400UEA, Thorlabs) was also tested but the issue remained.

[1] A more precise measurement of the field of view was later performed with the fully assembled micro-camera using a stage micrometer with 50 µm divisions (R1L3S1P, Thorlabs).

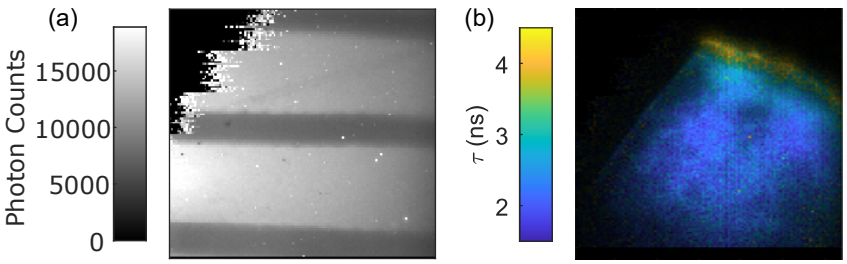


Figure 6.6: (a) Intensity image of a ruler captured mid-assembly with the FLIm micro-camera, showing a field of view of approximately 2 mm × 2 mm. (b) Fluorescence lifetime image of a leaf sample acquired using the same configuration. For the lifetime image 405 nm excitation was used at a repetition rate of 20 MHz and an average power of 1.3 mW. Photon counts were acquired over 40 time-bins with an acquisition time of ∼24 s.

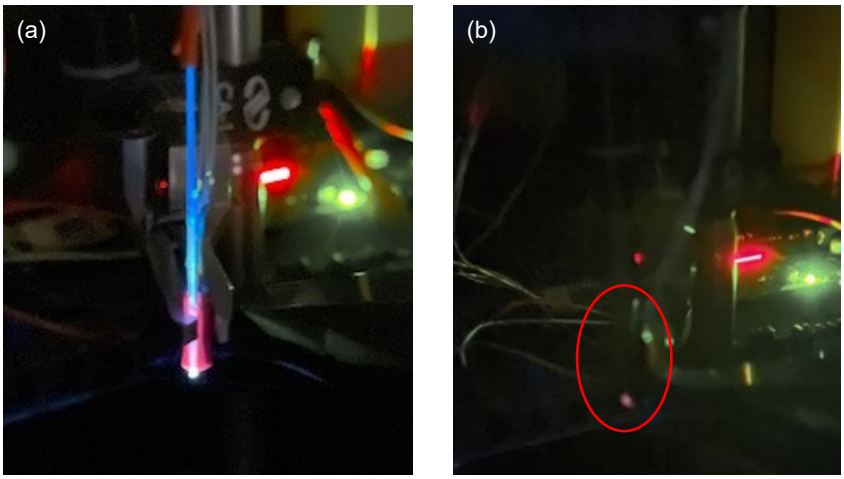


Figure 6.8: (a) Stray fluorescence observed when using a standard multimode fibre for excitation light delivery. Bright scattered light is visible around the micro-camera mount and the 3D printed parts appear to be strongly fluorescing. (b) Equivalent photo when using an aluminium-coated multimode fibre. The red circle indicates the location of the micro-camera. Almost no stray fluorescence is observed.

To address this challenge, an aluminium-coated multimode fibre with a 300 µm (AS300/330 USMA 430, Heracle GmbH) was used instead. This provided much-improved confinement of the excitation light and prevented leakage through the cladding. This change significantly reduced the observed stray fluorescence, as shown in Figure 6.8b. The red circle in the image indicates the location of the micro-camera, where no significant fluorescence is now visible.

6.4.2 Off-centre illumination

During initial testing of the excitation light delivery, it was observed that the illumination profile at the sample plane was not centred with respect to the field of view of the micro-camera. This misalignment is illustrated in Figure 6.9, which shows an intensity image of a uniform fluorescent card captured with the micro-camera. The excitation beam is almost entirely localised to the bottom left corner of the image.

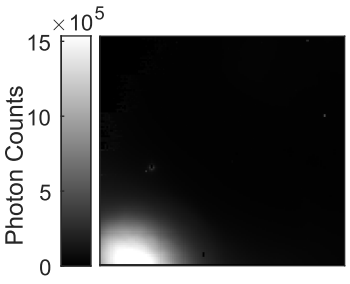


Figure 6.9: Excitation light profile at the sample plane showing off-centre illumination. The photon count heatmap reveals that the excitation spot is not aligned with the centre of the field of view.

The off-centre nature of the excitation profile is not surprising given that the fibre is positioned adjacent to the imaging optics. A similar effect was observed in Sparks et al. [81] though much less extreme in that case. One challenge is that the aluminium-coated fibre has a limited numerical aperture (NA) of only 0.22. If a fibre with a larger NA could be used, then the beam exiting the fibre would disperse more widely and the non-uniformity of the excitation profile would be less extreme. Metal-coated fibre with a larger NA was unfortunately not sourced in time for integration with this system, therefore an alternative solution was implemented as described below.

6.4.3 Angled fibre tip for beam steering

To solve the challenge outlined in the previous section, the use of angled fibre tips to steer the excitation beam toward the optical axis of the micro-camera was explored. A series of tests were conducted using 400 µm core multimode fibres (FG400UEA, Thorlabs). Three fibres were cleaved and then the ends of each fibre polished at different angles: 0°, 30°, and 45°. The fibre polishing was done using a NOVA™ bare fibre polishing system (KrellTech).

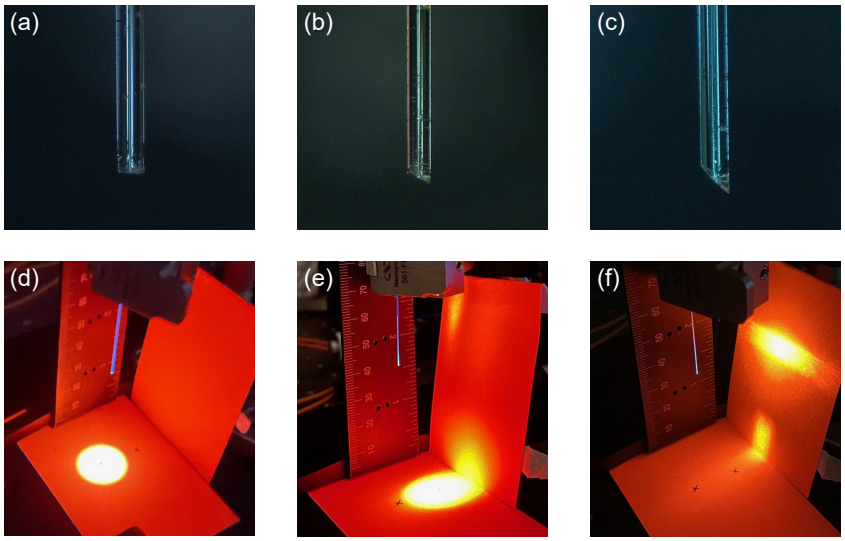


Figure 6.10: Effect of fibre polishing angle on beam direction. (a–c) Fibre tips polished at 0°, 30°, and 45°, respectively. (d–f) Corresponding beam profiles projected onto a surface. Increasing the polishing angle results in greater lateral deflection of the beam.

After polishing, the fibre was mounted above a fluorescent sheet at a distance of ∼4.6 cm. The 405 nm laser was coupled to the other end of the fibre and the emitted beam profile was observed. Figure 6.10 shows the fibre tips (a – c) and the corresponding beam profiles projected onto a surface (d – f) for each polishing angle. As expected, increasing the polishing angle resulted in a more pronounced lateral shift of the emitted beam. The 0° tip produced a beam aligned with the fibre axis, while the 30° and 45° tips progressively deflected the beam away from the axis.

At a polishing angle of 45°, most of the light appears to be internally reflected at the fibre face and emitted from the side of the fibre. This kind of side emission has been reported previously in literature and even utilised for side-viewing fibre probes [109, 110]. For this application however, this side emission is undesirable and could potentially lead to stray light within the micro-camera housing. Therefore, while angled polishing offers a useful method for beam steering, it also introduces additional considerations for optical isolation and integration.

For the fibres polished at 0° and 30°, the distance between the beam profiles was measured manually by marking the centre of each beam spot on the sheet. While approximate, this method was sufficient for the purpose of this exploration. The deflection distance was 16 mm, based on the distance from the fibre tips to the screen of 46 mm, corresponding to an estimated beam deflection angle of 19°. In the micro-camera design, the distance between the centre of the lens and the fibre is 1.5 mm. At a working distance of 4.1 mm, we can estimate the beam deflection angle required to be 20.1°.

Based on these results, the aluminium fibre was polished at a 30° angle and tested with the micro-camera. The polishing angle was incrementally increased up to 35°, where the excitation profile was considered optimal. This angle provided sufficient beam steering to centre the excitation profile while minimizing side emission and internal reflections.

This solution was arrived at empirically, primarily through trial an error. The use of angled fibre tips has been somewhat explored in the literature [109–112], but a more systematic investigation of their potential in an application such as this one could be of interest in the future. With further development, this approach could be generalised to other miniature optical systems where beam steering is required within tight

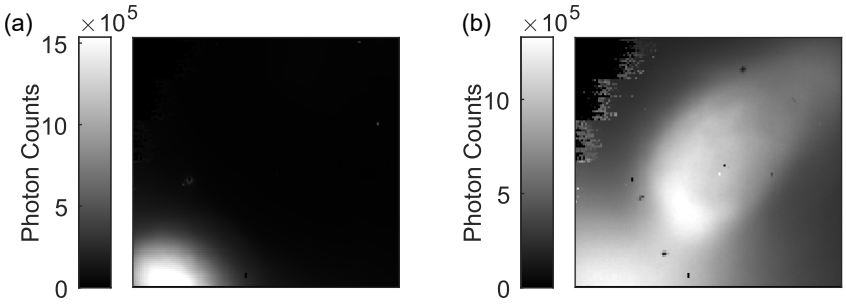


Figure 6.11: Excitation profile at the sample plane. (a) Before using the 35° angled fibre, showing off-centre illumination. (b) After using the 35° fibre, showing much-improved alignment. The excitation profile was measured by imaging a piece of uniform fluorescent card.

spatial constraints

6.4.4 Final excitation profile

Figure 6.11 shows the excitation profile before and after implementing the 35° angled fibre. In the initial configuration (a), the excitation spot is localised to one corner. After switching to the 35° fibre (b), the excitation is more centrally aligned and more widely spread. The resulting profile is far from perfect and this would be a key area of focus for future designs. However, this adjustment is a clear improvement and was critical for ensuring sufficient excitation across the field of view.

6.5 Characterisation of the FLIm micro-camera

The fully assembled FLIm micro-camera system is shown in Figure 6.12. To evaluate the performance system, a comprehensive characterisation was carried out, focusing on both spatial and temporal performance and demonstrating FLIm of unlabelled *ex vivo* animal tissue samples. This characterisation is presented in detail in Paper **III** and is further supported by the case study described in Paper **IV**.

Spatial resolution was assessed using a USAF resolution test target, with the system resolving features down to 27.8 µm. Temporal performance was characterised by measuring the system impulse response function (IRF), which was found to be >1 ns, enabling accurate fluorescence lifetime measurements.

Benchmarking against a TCSPC system using commercial lifetime standards also showed good agreement. Additional validation using solid-state FLT standards confirmed the system's ability to resolve multiple lifetimes within a single field of view. These results demonstrate that the micro-camera meets the requirements for miniaturised FLIm and supports its potential for clinical translation.

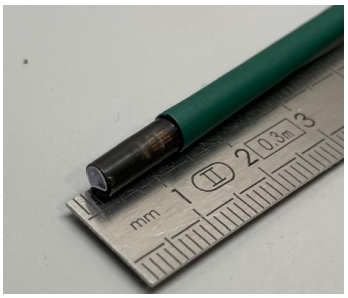


Figure 6.12: The fully assembled chip-on-tip FLIm micro-camera, including the EndoCam SPAD array, GRIN-lens, long-pass emission filter, and angled excitation fibre. The device has a 4 mm outer diameter and 10 mm rigid length.

6.6 MPE evaluation

Using the same methodology as for the previous systems described in Section 5.1.4, the exposure from the chip-on-tip FLIm micro camera is assessed and compared with MPE values. In this instance, the excitation light is delivered to the sample from a 0.22 NA optical fibre. At the working distance of 5 mm, >99 % of the beam passes through the limiting aperture diameter of 3.5 mm; therefore, the full laser power is used as a conservative approximation. Averaged over the limiting aperture, the peak irradiance from a single excitation pulse is $1.45 \times 10^4\,\mathrm{W\,m^{-2}}$, and the time averaged irradiance is $30\,\mathrm{W\,m^{-2}}$. For 375 nm, the applicable

skin limits are of $3 \times 10^{10}\,\mathrm{W\,m^{-2}}$ for nanosecond time scales, and a cumulative radiant exposure limit of $10^4\,\mathrm{J\,m^{-2}}$ for long term exposure. The single pulse irradiance delivered by the system is several orders of magnitude below the corresponding limit. For cumulative radiant exposure at $30\,\mathrm{W\,m^{-2}}$, the limit of $10^4\,\mathrm{J\,m^{-2}}$ would be exceeded after approximately 330 s of continuous illumination of the same tissue region. The images of *ex vivo* tissue acquired with this system presented in Paper **III** used an integration time of ∼30 s per image, less than one tenth of the time required to exceed the MPE assuming the beam and sample are stationary. Therefore, the exposure delivered during a typical acquisition remains well within conservative safety margins.

6.7 Discussion

Compared to the state-of-the-art FLIm systems reviewed in Chapter 3, the chip-on-tip FLIm micro-camera represents a significant advancement in system integration and simplification. The system requires no mechanical motion for imaging, offering a more robust and simplified approach compared to point-scanning systems.

Existing fibre-bundle-based systems have smaller outer diameters (2.3 mm in [81], 2.4 mm in [80], and 2.6 mm in [66]), but these require external detection modules and more complex optical paths. In contrast, the 4 mm diameter of the micro-camera includes fully integrated detection and imaging optics, representing a more compact and self-contained solution overall. Furthermore, the current outer diameter is partly constrained by the physical footprint of the EndoCam chip, which, although designed with a functional footprint of 1.4 mm × 1.4 mm, has a diced size of approximately 1.4 mm × 2.0 mm due to layout and fabrication constraints as mentioned in Chapter 4. Future iterations using a dedicated wafer could reduce this footprint, offering a clear path towards even more compact designs. In addition, future designs could explore the use of smaller diameter lenses to further reduce the system profile.

The spatial resolution of the micro-camera, measured at 27.8 µm, is not as high as that achieved by scanning endomicroscopes, which can reach sub-micron resolution (e.g., 0.7 µm in [73] and 1.4 µm in [66]). These systems are typically designed for cellular-level imaging and often have very small fields of view, making them well-suited for microscopic interrogation but less practical for imaging larger areas or for navigational imaging. However, the micro-camera's spatial performance is comparable to other wide-field FLIm systems, such as those reported by Sun et al. [77] and Cheng et al. [82], which achieved resolutions of approximately 35 µm, and by Sparks et al. [81] which achieved a resolution of approximately 20 µm.[2]

The system's temporal resolution, with an IRF width of less than 1 ns, is sufficient for resolving nanosecond-scale fluorescence lifetimes. This enables accurate lifetime measurements across a range of biological fluorophores and supports the system's suitability for FLIm applications.

In the characterisations presented in Paper **III** and Paper **IV**, the acquisition time per image was relatively long (30 s to 75 s), due to the use of full gate sweeps and high photon count integration for accurate benchmarking. However, faster imaging with the same detector has been demonstrated in other studies. For example, in Matheson et al. [98], a handheld system using the EndoCam demonstrated FLIm at a frame rate of approximately 1 Hz using rapid lifetime determination (RLD) with only two time-gates. This highlights a key area for future optimisation. In the EndoCam, the acquisition time scales linearly with the number

[2] The reported resolution for this device was 25 lp/mm which corresponds to a line width of ∼20 µm.

of gates measured; therefore, reducing the number of gates represents a straightforward and effective way to improve the achievable frame rate. The main drawback with this approach is a reduction in temporal sampling, which will generally lead to a decrease in lifetime precision. Further work will be required to determine the minimum number of gates necessary for different clinical use cases, balancing acquisition speed with the level of precision needed to maintain meaningful contrast. Such improvements would be essential for real-time clinical applications, including intraoperative guidance and dynamic tissue monitoring.

Beyond acquisition speed, system safety is another critical requirement for translation. Notably, the chip-on-tip FLIm micro-camera (as with the bench-top and handheld systems presented in Chapter 5) performed lifetime imaging while remaining comfortably within maximum permissible exposure limits. This confirms that time-domain FLIm using miniaturised SPAD arrays can be performed safely at powers suitable for biological tissue, further supporting the feasibility of future *in vivo* studies using similar architectures.

Overall, the chip-on-tip FLIm micro-camera closes a key gap identified in Chapter 3; it demonstrates that wide-field, time-resolved imaging can be achieved in a compact form factor without the need for fibre bundles or distal scanning. There remain clear avenues for optimisation including excitation uniformity and alignment, acquisition speed, and further miniaturisation. However, these results support the idea that miniaturised SPAD arrays provide a promising platform for endoscope-scale wide-field FLIm. These insights directly inform future refinement and pave the way for clinically deployable devices.

6.8 Summary

In this chapter the design and development of a compact chip-on-tip FLIm micro-camera system based on the EndoCam SPAD array has been presented. With an external diameter of 4 mm and a rigid length of 10 mm, the system is the first of its kind at a scale compatible with endoscopic applications.

Key engineering challenges were addressed, including sensor interfacing, optical design, mechanical packaging, and excitation light delivery. A custom flexible PCB, GRIN lens-based optics, and 3D-printed housing were developed to meet the constraints of miniaturisation. Issues such as stray fluorescence and off-centre illumination were mitigated through the use of aluminium-coated fibres and angled fibre tips.

The system was validated through spatial and temporal characterisation, benchmarking against a TCSPC system, and testing with solid-state FLT standards. These results collectively demonstrate that chip-on-tip SPAD-based FLIm is technically feasible, and they establish a practical foundation for future optimisation and eventual in vivo translation.

Chapter 7

Conclusions

This chapter summarises the key contributions of the thesis and outlines potential directions for future work. The aim of this thesis was to develop and validate novel tools for *in vivo* fluorescence lifetime imaging (FLIm) using miniaturised SPAD arrays, with a particular focus on enabling chip-on-tip FLIm for endoscopic applications. The work presented here spans the design, integration, and validation of multiple FLIm systems, culminating in the first demonstration of a chip-on-tip FLIm micro-camera which is small enough for endoscopic applications.

7.1 Key contributions

7.1.1 Integration of the EndoCam into bench-top and hand-held imaging systems

To explore the potential of SPAD arrays for wide-field *in vivo* FLIm, the EndoCam was integrated into two distinct imaging platforms: a bench-top system for metabolic imaging and a handheld system for portable diagnostics. The bench-top system was developed to enable lifetime-based pH imaging of tumour tissue in combination with solid-state planar fluorescent sensors. This required custom PCB design for remote EndoCam operation, and a tailored optical setup optimised for spatial and spectral performance. The system was successfully applied for metabolic imaging of *ex vivo* mouse tissue samples as presented in Paper **I**, demonstrating its potential for future *in vivo* applications in accessible sites such as the skin or oral cavity.

To address the need for portability in clinical and intraoperative settings, a miniaturised handheld system was also developed. It was validated through measurement of polymer beads having different lifetimes and through imaging of stained porcine tissue, achieving a spatial resolution of 12.4 µm and demonstrating wide-field FLIm capability in a compact format. While not the primary focus of this thesis, the handheld system illustrates the broader applicability of the EndoCam platform, which has since been further developed by other researchers [7, 98, 99].

Together, these systems demonstrate the versatility of SPAD arrays for wide-field FLIm and establish the EndoCam's effectiveness in both research and potential clinical contexts. They also laid the foundation for the development of a chip-on-tip FLIm micro-camera for endoscopic use.

7.1.2 Chip-on-tip FLIm micro-camera

To support the clinical translation of FLIm, this work aimed to demonstrate that wide-field lifetime imaging could be achieved using a com-

pact, chip-on-tip device. This work contributes toward the broader goal of translating fluorescence lifetime imaging from a specialist, research-grade technique into a technology suitable for routine use in clinical and diagnostic settings.

The resulting micro-camera, based on the EndoCam SPAD array, has a diameter of 4 mm and a rigid length of 10 mm making it the first demonstration of wide-field chip-on-tip FLIm at a scale compatible with endoscopic applications. Key engineering challenges, including sensor interfacing, optical alignment, mechanical packaging, and excitation light delivery, were addressed through the development of a custom flexible PCB and 3D-printed housing. These elements enabled the integration of the EndoCam, along with miniature imaging optics and excitation light delivery, into the compact device. Stray fluorescence and illumination misalignment were mitigated using aluminium-coated fibres and angled fibre tips.

The system was validated through spatial and temporal characterisation, benchmarking against a TCSPC reference (Paper **III**), and testing with solid-state FLT standards (Paper **IV**). These results confirmed its suitability for wide-field FLIm and its potential for clinical translation. This work demonstrates the feasibility of integrating SPAD-based lifetime imaging into ultra-compact formats for clinical applications.

7.1.3 Solid-state FLT standards for system validation

To address the lack of robust, reproducible tools for validating FLIm systems, this thesis introduced a set of solid-state fluorescence lifetime (FLT) standards using dyed epoxy resins. These were developed to support consistent benchmarking and facilitate clinical translation. The standards span lifetimes from sub-nanosecond to over 3.5 ns and were shown to be photostable and fabrication-repeatable.

Their application in validating the chip-on-tip FLIm micro-camera demonstrated strong agreement with bench-top TCSPC measurements and revealed platform-dependent lifetime biases, highlighting the importance of cross-platform benchmarking. By enabling simultaneous assessment of spatial and temporal resolution, these standards provide a practical, scalable tool for system calibration. They help address a key barrier to clinical adoption of FLIm and offer a foundation for standardisation, regulatory alignment, and widespread use in both research and diagnostic imaging workflows.

7.2 Future work

7.2.1 Micro-camera packaging and clinical readiness

Translating the FLIm micro-camera into a clinically deployable device will require further refinement of its physical design. Waterproof packaging, sterilisable materials, and robust mechanical integration are essential for safe and practical use in clinical environments. Additionally, the imaging optics must be optimised for consistent performance across manufacturing batches and use cases.

Beyond engineering, clinical validation is another critical next step. This includes pilot studies in relevant clinical settings, such as intraoperative imaging or point-of-care diagnostics, to assess usability, workflow integration, and diagnostic value. Feedback from clinicians and end-users will be vital in guiding design iterations and ensuring the system meets real-world needs.

An alternative system architecture is to position the EndoCam at the proximal end of an optical fibre bundle endoscope rather than at the distal tip. However, this configuration would forfeit many of the benefits

that motivated the chip on tip approach. One of the principal advantages of using a distal end detector is the avoidance of fibre bundle autofluorescence, wavelength dependent dispersion, and inter core variability, all of which degrade the temporal precision and signal strength in FLIm measurements. Relocating the EndoCam to the proximal end would reintroduce these limitations and undermine the fundamental rationale for using a miniaturised SPAD array.

At the same time, using the EndoCam proximally offers no clear advantage in environments where size is not constrained. The EndoCam was deliberately designed with substantial compromises in temporal resolution and readout architecture to achieve such a small footprint. If the detector is placed at the proximal end, where space is ample, it would be more appropriate to use a larger, high performance SPAD camera, such as the commercial systems discussed in Chapter 3, which provide significantly higher photon throughput and temporal resolution. For these reasons, using the EndoCam proximally is unlikely to provide practical or performance advantages in endoscopic applications. However, a systematic comparison of future chip on tip FLIm micro cameras with fibre bundle based systems that use state of the art proximal end SPAD cameras would be of significant interest. Such studies would help quantify the trade-offs between distal and proximal detection and further clarify the most suitable system design for clinical deployment.

7.2.2 Illumination design

Efficient and uniform excitation light delivery remains a key challenge in miniaturised wide-field FLIm systems. FLIm measurements are less sensitive to intensity variations, as lifetime measurements are independent of absolute signal strength. This allows for some relaxation in illumination uniformity requirements, provided that sufficient photon counts are achieved across the field of view. Nonetheless, improving excitation efficiency remains important for reducing acquisition time and enhancing signal-to-noise ratio, especially in low-fluorescence environments.

In this work, an angled fibre tip was used to direct light across the field of view. This approach was effective and enabled functional imaging performance; however, there remains room for improvement in both efficiency and integration.

A key limitation arose from the use of a metal-coated fibre, which was necessary to suppress stray light due to the use of 3D-printed plastic components in the housing. However, the metal-coated fibre used here has a limited numerical aperture (NA), reducing the divergence of excitation light delivered to the sample leading to regions in the image with inadequate excitation power. Future iterations using machined metal components, in place of the plastic 3D-printed parts, could eliminate the need for metal-coated fibres and allow the use of higher-NA fibres; this would improve the uniformity of the excitation profile.

Intensity-based micro-camera systems have used multiple illumination fibres to achieve homogeneity [13, 113]. The use of multiple fibres is worth exploration but may introduce an offset in the excitation pulse arrival times from each fibre. In fact, Sparks et al. [81] observed a spatially non-uniform IRF with their wide-field fibre-bundle FLIm system due to different modal propagation speeds in a single multi-mode fibre. These effects would need to be carefully monitored and compensated for if multiple fibres are to be used.

7.2.3 Excitation source development

Further to the points above, in many commercial white-light endoscopes, illumination is provided by a white LED with a very wide illumination an-

gle mounted at the distal end of the endoscope. Pulsed excitation sources suitable for distal mounting are not yet available at the wavelength range required for FLIm. The laser sources used in this work, while effective, remain bulky and expensive, limiting the portability of the overall system. Although these sources are not required to be single-use, their size and cost are barriers to broader deployment.

Compact pulsed sources in the NIR range have already been developed for use in LiDAR and time-domain diffuse optics applications [114, 115]. If similar sources can be developed in the UV range, they would significantly enhance the portability of FLIm systems, supporting their use in outpatient clinics, operating theatres, and other space-constrained environments.

7.2.4 Connectivity and data transmission

Stable data transmission over long cable lengths is a known challenge in endoscopic systems. In this work, signal integrity was a limiting factor, particularly at higher clock speeds. Commercial solutions for micro-camera devices, such as the ams NanEye, demonstrate stable operation over 3 m of cable at 30 MHz to 40 MHz. At these cable lengths, signal propagation time between the board and the chip can lead to a loss of synchronisation. In the case of the NanEye, the data sent from the micro-camera to the board is sampled at 750 MHz ($>10\times$ the clock frequency); this enables detection of the signal transitions and reliable extraction of the data [116]. Future chip-on-tip FLIm systems will require similarly robust connectivity solutions.

This is increasingly important as endoscopic systems become more data-intensive; the implementation of more sophisticated imaging techniques, such as FLIm, requires faster data rates to maintain adequate imaging speeds. At Tyndall, there is active research into using optical communication with chip-on-tip endoscope systems to address this challenge [117, 118]. Additional efforts are also underway to achieve optical powering of chip-on-tip micro-cameras [119]. Together, these developments could increase data transmission rates and eliminate the need for direct electronic connections to the distal end of chip-on-tip endoscopes.

7.2.5 Advancing SPAD imagers for FLIm

The EndoCam SPAD array has proven effective for wide field FLIm in a chip on tip micro camera device. However, the development of the EndoCam began nearly a decade ago, and SPAD technology has progressed significantly since then. Modern SPAD imagers benefit from markedly improved fill factors, reduced timing jitter, lower dark count rates, and substantially higher photon detection efficiencies. These enhancements directly influence the photon budget and therefore the minimum integration time required to achieve reliable lifetime estimates. Increased detection efficiency reduces the number of excitation cycles needed to accumulate the required photon counts, enabling either shorter acquisition times and higher frame rates, or alternatively improved lifetime precision within the same measurement duration. A next generation miniaturised sensor incorporating these advances would therefore deliver better sensitivity, finer spatial performance, and substantially improved imaging speed.

In parallel, the integration of on chip lifetime extraction represents another promising route for future FLIm systems. By performing the lifetime estimation directly on the sensor, rather than transmitting full decay curves, data bandwidth requirements can be reduced by orders of magnitude. This approach has already been demonstrated in larger SPAD arrays by Li et al. [120], where hardware level processing provided

fast and resource efficient lifetime estimation. Incorporating similar functionality into a chip on tip FLIm micro camera would significantly reduce the volume of data that must be transmitted along the endoscopic cable, mitigating a major bottleneck and enabling higher frame rates. Such architectures could also open the possibility of dynamic or adaptive acquisition, with gate timing or exposure adjusted in real time based on photon statistics at each pixel.

A further promising direction is the development of SPAD imagers that support on chip frequency domain demodulation for FLIm. Frequency domain lifetime estimation requires only the extraction of phase and modulation information, and therefore inherently demands much lower data throughput than time domain methods. While FD FLIm cannot resolve complex multi exponential decay profiles as robustly as time domain approaches, it may still provide adequate contrast for many diagnostic applications. For clinical tasks such as real time margin assessment, tissue classification, or metabolic monitoring—where a single effective lifetime parameter is often sufficient, frequency domain SPAD imagers offer a compelling combination of speed, simplicity, and bandwidth efficiency.

Together, these directions in SPAD imager development represent complementary ways in which the performance of future chip on tip FLIm systems could be substantially enhanced. Their integration into next generation devices may help support the high frame rates, sensitivity, and robustness required for translation of wide field FLIm into routine clinical workflows.

7.2.6 Standardisation and regulatory pathways

As FLIm systems move closer to clinical adoption, standardisation and regulatory alignment will become increasingly important [121, 122]. The solid-state FLT standards developed in this work and described in Paper **IV** contribute to addressing this, but more work is still required to provide a foundation for consistent benchmarking and cross-platform validation. Tools such as the solid state FLT standards can support the development of quality assurance protocols and facilitate engagement with regulatory bodies.

Future work should focus on expanding the range of available standards, improving material homogeneity at the microscopic level, and contributing to broader efforts in defining performance metrics and validation procedures for clinical FLIm instrumentation.

In addition to technical benchmarking, future work should consider alignment with international regulatory frameworks. For example, ISO 13485 outlines quality management systems for medical devices, while ISO 10993 addresses biocompatibility testing. For clinical deployment in Europe, compliance with the Medical Device Regulation (MDR 2017/745) is required, and in the United States, FDA approval may be necessary depending on the intended use. Early engagement with these standards can streamline the translation of FLIm systems from research prototypes to approved clinical tools.

7.3 Final remarks

The work presented in this thesis demonstrates the feasibility of integrating SPAD based fluorescence lifetime imaging into compact, application ready systems. By addressing key engineering challenges and validating performance across multiple platforms, this research lays the groundwork for the clinical translation of FLIm technology. A central motivation throughout this work has been the broader goal of translating fluorescence lifetime imaging from a specialist, research grade technique into a

technology suitable for routine use in clinical and diagnostic settings. The development of miniaturised, chip on tip FLIm systems and robust solid state lifetime standards represents a significant step toward this vision, enabling practical deployment in real world healthcare environments.

Although the systems developed here achieve functional wide field lifetime imaging in a form factor compatible with endoscopic use, it is important to acknowledge that their performance does not yet surpass that of established technologies. Techniques based on TCSPC, gated image intensifiers, and frequency domain detection continue to provide superior temporal resolution, photon efficiency, and multi exponential fitting capability. The compromises inherent to miniaturisation, such as reduced fill factor, reduced temporal resolution, and lower photon throughput, mean that considerable innovation will be required before a chip scale system can match the absolute performance of these laboratory grade instruments. In the near term, the value of this work lies not in outperforming the state of the art, but in demonstrating a viable technological pathway toward compact, clinically integrated FLIm.

Importantly, the innovation presented in this thesis is not incremental improvement over existing high-performance systems but the demonstration of a platform with fundamentally different long term advantages. Because SPAD arrays can be fabricated using standard CMOS processes, future devices have the potential to be manufactured at wafer scale, enabling low cost, disposable, chip on tip FLIm endoscopes. Such scalability is simply not achievable with conventional FLIm technologies that rely on bulky detectors and complex optomechanics. As SPAD technology continues to develop, the performance gap is likely to narrow, bringing miniaturised devices closer to the required levels of performance while retaining their advantages of size, integration, and manufacturability.

The solid state FLT standards developed here further support this transition, offering a scalable route to standardisation and regulatory alignment. As SPAD technology advances, and as clinical interest in label free optical diagnostics grows, the tools and systems developed in this thesis are well positioned to contribute to the next generation of biomedical imaging

This work builds on the prior efforts in translational FLIm outlined in Chapter 3 by leveraging miniaturised SPAD array technology for wide-field chip-on-tip FLIm. Hopefully this provides a platform upon which subsequent systems can be developed to realise the full potential of FLIm in diagnostics and surgical guidance.

Comments on the Papers

I **Metabolic imaging of tumor tissue samples using planar fluorescence lifetime-based pH sensors and a SPAD array imager**
In this paper the bench-top wide-field FLIm system using the EndoCam is applied in combination with planar solid-state pH sensors for metabolic imaging of *ex vivo* mouse tumour and muscle tissue. The system enabled spatially resolved pH mapping and revealed differences in extracellular pH between the different sample types. The data and analysis code used for this publication have been made publicly available on Zenodo [123].

I contributed significantly to the initial project ideation. I designed and constructed the FLIm imaging system to meet the desired specification. I led the planning of all measurements which were performed by myself, *Liang Li* who developed and fabricated the solid-state pH sensors, and *Ciaran Devoy* who managed the mice used for the tissue study and prepared all tissue samples. I performed all data analysis and co-wrote the manuscript.

II **Time resolved SPAD micro-camera probe for wide-field FLIm in microendoscopy**
This conference paper introduces a miniaturised, handheld wide-field FLIm system using the same SPAD array. The system was validated through imaging of resolution targets, lifetime-encoded beads, and biological samples, demonstrating its potential for portable diagnostics.

I designed and assembled the miniaturised optical system and custom PCB, performed all experimental measurements and data analysis, and led the manuscript preparation.

III **Chip-on-tip fluorescence lifetime imaging micro-camera toward endoscopic applications**
This paper presents the first chip-on-tip FLIm micro-camera with a 4 mm diameter, integrating a miniaturised SPAD array, imaging optics, and excitation light delivery. The system was characterised for spatial and temporal performance and demonstrated through imaging of unlabelled *ex vivo* animal tissue. The data and analysis code used for this publication have been made publicly available on Zenodo [124].

I led the design of the micro-camera including the development of the optical and mechanical integration strategy. *Walter Messina* designed the custom flexible PCB in collaboration with *Ray Burke*. The micro-camera assembly and design iteration was carried out by myself and *Noreen Nudds*. I performed all measurements and data analysis and led the writing of the manuscript.

IV **Development of solid-state fluorescence lifetime standards for clinical applications using dyed epoxy resins**
This manuscript introduces a set of solid-state FLT standards for system validation, fabricated using dyed epoxy resins. The standards were characterised for lifetime, intensity, stability, and uniformity, and applied to benchmark the chip-on-tip FLIm micro-camera. The data and analysis code used for this publication have been made publicly available on Zenodo [125].

The idea was conceived by *Sanathana Konugolu Venkata Sekar* and further developed by myself, *Stefan Andersson-Engels*, and *Katarzyna Komolibus*. I designed and constructed the TCSPC-based system used for lifetime measurements. I co-supervised *Keela Hughes* who fabricated and tested initial versions of the FLT standards with the assistance of *Sara Eugenia Garduño Gómez*, and automated the data acquisition and lifetime fitting with the TCSPC system. The FLT standards measured for the manuscript were fabricated by *Sanathana Konugolu Venkata Sekar* and *Katarzyna Komolibus*. Confocal FLIM measurements were performed by *Hasti Yavari*. All other measurements and additional analysis presented in the manuscript were performed by myself, and I led the writing of the manuscript.

Acknowledgements

This research was made possible through funding provided by the EU H2020 MSCA-ITN project Photonics for Healthcare: Multiscale Cancer Diagnosis and Therapy (PHAST-ETN), grant agreement no. 86018; Taighde Éireann – Research Ireland (15/RP/2828, 22/RP-2TF/10293, and 12/RC/2276 P2); and the PROTEUS project, Grant no. EP/K03197X/1.

I would like to express my gratitude to all those who have supported me throughout the course of my PhD. Firstly to my supervisors, Stefan, Sana, and Ray. Stefan, your experience and guidance have been invaluable in shaping this project. Thank you for your generosity with your time and support. Sana, when I began my PhD, I barely knew how to use an oscilloscope, let alone assemble and test optical systems. Your mentorship has helped me grow immensely in confidence and skill in the lab, thank you. To all the researchers in the Biophotonics research group, thank you for your help and for fostering such a positive and stimulating environment for learning and research.

I would also like to thank our collaborators at the University of Edinburgh. Robert, your leadership and the technology developed by your team were foundational to this project. Andrew and Ahmet, thank you for your patience and support in helping us use the EndoCam at Tyndall, your time and expertise were greatly appreciated.

Noreen, there is no thesis without you and certainly no publication on the FLIm micro-camera. It was an absolute joy to spend time in the packaging lab with you. Thank you.

To our UCC collaborators, particularly Dmitri and Liang, thank you for a positive collaboration that brought real-world relevance to our research and led to my first first-author journal article. I hope we can collaborate again in the future.

To all the other ESRs in the PHAST project, especially Daniyal, Vamshi, Aybüke, Edoardo, Matteo, Stefan, and Arno; the PHAST project meetings have been a real highlight of the past four years. I always looked forward to seeing you all, hearing about your work, and catching up over dinner and drinks. I feel so lucky to have met you and hope that we can stay in touch.

Thank you to my friends in Cork: John, Jack, Megan, Kevin, Colum, Michael, and Louise; you welcomed me so readily when I moved to Cork and made it feel like home. To Eoin, Julie, Kamille, Salam, and Conor (and John again), you've made me feel part of a real friend group at Tyndall that I can rely on.

To my family, especially Mum and Dad, thank you for everything, I wouldn't be here without you.

Finally, to Louise, your love, support, understanding, and care have meant everything to me, thank you.

References

[1] Alba Alfonso-Garcia, Julien Bec, Brent Weyers, Mark Marsden, Xiangnan Zhou, Cai Li, and Laura Marcu. Mesoscopic fluorescence lifetime imaging: Fundamental principles, clinical applications and future directions. *Journal of Biophotonics*, 14(6): e202000472, June 2021. ISSN 1864-0648. doi: 10.1002/JBIO.202000472. URL https://onlinelibrary.wiley.com/doi/full/10.1002/jbio.202000472. Publisher: John Wiley & Sons, Ltd.

[2] R. Cubeddu, D. Comelli, C. D'Andrea, P. Taroni, and G. Valentini. Time-resolved fluorescence imaging in biology and medicine. *Journal of Physics D: Applied Physics*, 35(9):61–76, May 2002. ISSN 00223727. doi: 10.1088/0022-3727/35/9/201. URL https://iopscience.iop.org/article/10.1088/0022-3727/35/9/201. Publisher: Institute of Physics Publishing.

[3] W. Becker. Fluorescence lifetime imaging – techniques and applications. *Journal of Microscopy*, 247(2):119–136, 2012. ISSN 1365-2818. doi: 10.1111/j.1365-2818.2012.03618.x. URL https://onlinelibrary.wiley.com/doi/abs/10.1111/j.1365-2818.2012.03618.x. _eprint: https://onlinelibrary.wiley.com/doi/pdf/10.1111/j.1365-2818.2012.03618.x.

[4] Olivia I. Kolenc and Kyle P. Quinn. Evaluating cell metabolism through autofluorescence imaging of NAD(P)H and FAD. *Antioxidants and Redox Signaling*, 30(6):875–889, 2019. ISSN 15577716. doi: 10.1089/ars.2017.7451. URL https://doi.org/10.1089/ars.2017.7451. Publisher: Mary Ann Liebert Inc.

[5] Rupsa Datta, Tiffany M. Heaster, Joe T. Sharick, Amani A. Gillette, and Melissa C. Skala. Fluorescence lifetime imaging microscopy: fundamentals and advances in instrumentation, analysis, and applications. *Journal of Biomedical Optics*, 25(07):1, May 2020. ISSN 1560-2281. doi: 10.1117/1.jbo.25.7.071203. URL https://www.spiedigitallibrary.org/terms-of-use. Publisher: SPIE-Intl Soc Optical Eng.

[6] Tuqiang Ni and Lynn A. Melton. Two-Dimensional Gas-Phase Temperature Measurements Using Fluorescence Lifetime Imaging. *Applied Spectroscopy*, 50(9):1112–1116, September 1996. URL https://opg.optica.org/as/abstract.cfm?uri=as-50-9-1112. Publisher: Society for Applied Spectroscopy.

[7] Andrew B. Matheson, Robert Henderson, Ross N. Gillanders, Graham A. Turnbull, and Edward B. Ogugu. Fluorescence lifetime imaging for explosive detection. *Optics Letters, Vol. 48, Issue 22, pp. 6015-6018*, 48(22):6015–6018, November 2023. ISSN 1539-4794. doi: 10.1364/OL.498123. URL https://opg.optica.org/

viewmedia.cfm?uri=ol-48-22-6015&seq=0&html=true. Publisher: Optica Publishing Group.

[8] Christine B. Wilda, Aviva Burnstock, Klaus Suhling, Francesco Mattioli Della Rocca, Robert K. Henderson, and Jakub Nedbal. Visualising varnish removal for conservation of paintings by fluorescence lifetime imaging (FLIM). *Heritage Science*, 11(1):1–21, June 2023. ISSN 2050-7445. doi: 10.1186/s40494-023-00957-w. URL https://www.nature.com/articles/s40494-023-00957-w. Publisher: Nature Publishing Group.

[9] Laura Marcu. Fluorescence Lifetime Techniques in Medical Applications. *Annals of Biomedical Engineering*, 40(2):304–331, February 2012. ISSN 1573-9686. doi: 10.1007/s10439-011-0495-y. URL https://doi.org/10.1007/s10439-011-0495-y.

[10] Elvis Duran-Sierra, Shuna Cheng, Rodrigo Cuenca-Martinez, Bilal Malik, Kristen C. Maitland, Y. S. Lisa Cheng, John Wright, Beena Ahmed, Jim Ji, Mathias Martinez, Moustafa Al-Khalil, Hussain Al-Enazi, and Javier A. Jo. Clinical label-free biochemical and metabolic fluorescence lifetime endoscopic imaging of precancerous and cancerous oral lesions. *Oral Oncology*, 105:104635, June 2020. ISSN 1368-8375. doi: 10.1016/J.ORALONCOLOGY.2020.104635. URL https://doi.org/10.1016/j.oraloncology.2020.104635. Publisher: Pergamon.

[11] Mengyan Wang, Feng Tang, Xiaobo Pan, Longfang Yao, Xinyi Wang, Yueyue Jing, Jiong Ma, Guifang Wang, and Lan Mi. Rapid diagnosis and intraoperative margin assessment of human lung cancer with fluorescence lifetime imaging microscopy. *BBA Clinical*, 8:7–13, December 2017. ISSN 22146474. doi: 10.1016/j.bbacli.2017.04.002. URL https://pubmed.ncbi.nlm.nih.gov/28567338/. Publisher: Elsevier B.V.

[12] Rakesh Patalay, Clifford Talbot, Yuriy Alexandrov, Martin O. Lenz, Sunil Kumar, Sean Warren, Ian Munro, Mark A. A. Neil, Karsten König, Paul M. W. French, Anthony Chu, Gordon W. H. Stamp, and Chris Dunsby. Multiphoton Multispectral Fluorescence Lifetime Tomography for the Evaluation of Basal Cell Carcinomas. *PLoS ONE*, 7(9):e43460, September 2012. ISSN 1932-6203. doi: 10.1371/journal.pone.0043460. URL https://www.ncbi.nlm.nih.gov/pmc/articles/PMC3439453/.

[13] Simon T. Sørensen, Walter Messina, Lorenzo Niemitz, Claire O'Dowling, Claire O'Dowling, Piotr Buszman, Stefan Andersson-Engels, Stefan Andersson-Engels, and Ray Burke. Camera-on-tip endoscope for in vivo cardiovascular diagnostics and surgical guidance. *Biomedical Optics Express, Vol. 16, Issue 1, pp. 12-27*, 16(1):12–27, January 2025. ISSN 2156-7085. doi: 10.1364/BOE.543373. URL https://opg.optica.org/viewmedia.cfm?uri=boe-16-1-12&seq=0&html=true. Publisher: Optica Publishing Group.

[14] Michael R. Gaab. Instrumentation: Endoscopes and Equipment. *World Neurosurgery*, 79(2):S14.e11–S14.e21, February 2013. ISSN 1878-8750. doi: 10.1016/J.WNEU.2012.02.032. URL https://doi.org/10.1016/j.wneu.2012.02.032. Publisher: Elsevier.

[15] Claudio Bruschini, Harald Homulle, Ivan Michel Antolovic, Samuel Burri, and Edoardo Charbon. Single-photon avalanche diode imagers in biophotonics: review and outlook. *Light: Science & Applications*, 8(1):87, September 2019. ISSN 2047-7538. doi: 10.1038/

s41377-019-0191-5. URL https://www.nature.com/articles/s41377-019-0191-5. Publisher: Nature Publishing Group.

[16] Max Tillmann, Johan Hummert, Felix Koberling, Rainer Erdmann, Cyril Saudan, Harald Homulle, and Ivan Michel Antolovic. Next generation SPAD image sensors and lasers for widefield time domain FLIM. In *Single Molecule Spectroscopy and Superresolution Imaging XVI*, volume PC12386, page PC123860O. SPIE, March 2023. doi: 10.1117/12.2666381. URL https://doi.org/10.1117/12.2666381.

[17] Kayvan Samimi, Danielle E. Desa, Wei Lin, Kurt Weiss, Joe Li, Jan Huisken, Veronika Miskolci, Anna Huttenlocher, Jenu V. Chacko, Andreas Velten, Jeremy D. Rogers, Kevin W. Eliceiri, and Melissa C. Skala. Light-sheet autofluorescence lifetime imaging with a single-photon avalanche diode array. *Journal of Biomedical Optics*, 28(6):066502, June 2023. ISSN 1083-3668. doi: 10.1117/1.JBO.28.6.066502. URL https://doi.org/10.1117/1.JBO.28.6.066502. Publisher: SPIE.

[18] Ahmet T. Erdogan, Tarek Al Abbas, Neil Finlayson, Charlotte Hopkinson, Istvan Gyongy, Oscar Almer, Neale A.W. Dutton, and Robert K. Henderson. A High Dynamic Range 128 x 120 3-D Stacked CMOS SPAD Image Sensor SoC for Fluorescence Microendoscopy. *IEEE Journal of Solid-State Circuits*, 2022. ISSN 1558173X. doi: 10.1109/JSSC.2022.3150721. URL https://doi.org/10.1109/JSSC.2022.3150721. Publisher: Institute of Electrical and Electronics Engineers Inc.

[19] Joseph R. Lakowicz. *Principles of Fluorescence Spectroscopy*. Springer, 3rd edition, January 2006. ISBN 978-0-387-31278-1. URL https://link.springer.com/book/10.1007/978-0-387-46312-4.

[20] Rupsa Datta, Amani Gillette, Matthew Stefely, and Melissa C. Skala. Recent innovations in fluorescence lifetime imaging microscopy for biology and medicine. *https://doi.org/10.1117/1.JBO.26.7.070603*, 26(7):070603, July 2021. ISSN 1083-3668. doi: 10.1117/1.JBO.26.7.070603. URL https://doi.org/10.1117/1.JBO.26.7.070603. Publisher: SPIE.

[21] Jongchan Park and Liang Gao. Advancements in fluorescence lifetime imaging microscopy Instrumentation: Towards high speed and 3D. *Current Opinion in Solid State and Materials Science*, 30:101147, June 2024. ISSN 1359-0286. doi: 10.1016/j.cossms.2024.101147. URL https://www.sciencedirect.com/science/article/pii/S1359028624000135.

[22] David P Millar. Time-resolved fluorescence spectroscopy. *Current Opinion in Structural Biology*, 6(5):637–642, October 1996. ISSN 0959-440X. doi: 10.1016/S0959-440X(96)80030-3. URL https://www.sciencedirect.com/science/article/pii/S0959440X96800303.

[23] Alain Sillen and Yves Engelborghs. The Correct Use of "Average" Fluorescence Parameters. *Photochemistry and Photobiology*, 67(5):475–486, May 1998. ISSN 1751-1097. doi: 10.1111/J.1751-1097.1998.TB09082.X. URL https://onlinelibrary.wiley.com/doi/full/10.1111/j.1751-1097.1998.tb09082.x. Publisher: John Wiley & Sons, Ltd.

[24] Eva Fišerová and Martin Kubala. Mean fluorescence lifetime and its error. *Journal of Luminescence*, 132(8):2059–2064, August 2012. ISSN 0022-2313. doi: 10.1016/j.jlumin.2012.03.038. URL https://www.sciencedirect.com/science/article/pii/S0022231312001718.

[25] Yahui Li, Sapermsap Natakorn, Yu Chen, Mohammed Safar, Margaret Cunningham, Jinshou Tian, and David Day-Uei Li. Investigations on Average Fluorescence Lifetimes for Visualizing Multi-Exponential Decays. *Frontiers in Physics*, 8, October 2020. ISSN 2296-424X. doi: 10.3389/fphy.2020.576862. URL https://www.frontiersin.orghttps://www.frontiersin.org/journals/physics/articles/10.3389/fphy.2020.576862/full. Publisher: Frontiers.

[26] W. Becker. The bh TCSPC Handbook 10th edition, 2023. URL https://www.becker-hickl.com/literature/documents/flim/the-bh-tcspc-handbook/.

[27] Michael Wahl. Time-Correlated Single Photon Counting. Technical note, PicoQuant GmbH, 2014. URL https://www.picoquant.com/images/uploads/page/files/14528/technote_tttr.pdf.

[28] Xiongbo Liu, Danying Lin, Wolfgang Becker, Jingjing Niu, Bin Yu, Liwei Liu, and Junle Qu. Fast fluorescence lifetime imaging techniques: A review on challenge and development. *Journal of Innovative Optical Health Sciences*, 12(5):12, September 2019. ISSN 17937205. doi: 10.1142/S1793545819300039/ASSET/IMAGES/LARGE/S1793545819300039FIGF8.JPEG. URL www.worldscientific.com. Publisher: World Scientific Publishing Co. Pte Ltd.

[29] Xiangnan Zhou, Julien Bec, Katjana Ehrlich, Alba Alfonso Garcia, and Laura Marcu. Pulse-sampling fluorescence lifetime imaging: evaluation of photon economy. *Optics Letters*, 48(17):4578–4581, September 2023. ISSN 1539-4794. doi: 10.1364/OL.490096. URL https://opg.optica.org/ol/abstract.cfm?uri=ol-48-17-4578. Publisher: Optica Publishing Group.

[30] D. Gorpas, J. Phipps, J. Bec, D. Ma, S. Dochow, D. Yankelevich, J. Sorger, J. Popp, A. Bewley, R. Gandour-Edwards, L. Marcu, and D. G. Farwell. Autofluorescence lifetime augmented reality as a means for real-time robotic surgery guidance in human patients. *Scientific Reports*, 9(1):1187, February 2019. ISSN 2045-2322. doi: 10.1038/s41598-018-37237-8. URL https://doi.org/10.1038/s41598-018-37237-8. Publisher: Nature Publishing Group.

[31] Downloads | PicoQuant, . URL https://www.picoquant.com/downloads.

[32] Kalyan Santra, Jinchun Zhan, Xueyu Song, Emily A. Smith, Namrata Vaswani, and Jacob W. Petrich. What Is the Best Method to Fit Time-Resolved Data? A Comparison of the Residual Minimization and the Maximum Likelihood Techniques As Applied to Experimental Time-Correlated, Single-Photon Counting Data. *The Journal of Physical Chemistry B*, 120(9):2484–2490, March 2016. ISSN 1520-6106. doi: 10.1021/acs.jpcb.6b00154. URL https://doi.org/10.1021/acs.jpcb.6b00154. Publisher: American Chemical Society.

[33] P.M. Conn. *Imaging and Spectroscopic Analysis of Living Cells: Optical and Spectroscopic Techniques*. Methods in Enzymology.

Academic Press, 2012. ISBN 978-0-12-391869-7. URL https://books.google.ie/books?id=G_kev1ePUn4C.

[34] References | ISS, . URL https://iss.com/resources#lifetime-data-of-selected-fluorophores.

[35] Radoslaw Szlazak, Krzysztof Tutaj, Wojciech Grudzinski, Wieslaw I. Gruszecki, and Rafal Luchowski. Plasmonic-based instrument response function for time-resolved fluorescence: toward proper lifetime analysis. *Journal of Nanoparticle Research*, 15(6): 1677, May 2013. ISSN 1572-896X. doi: 10.1007/s11051-013-1677-3. URL https://doi.org/10.1007/s11051-013-1677-3.

[36] Malte Köllner and Jürgen Wolfrum. How many photons are necessary for fluorescence-lifetime measurements? *Chemical Physics Letters*, 200(1):199–204, November 1992. ISSN 0009-2614. doi: 10.1016/0009-2614(92)87068-Z. URL https://www.sciencedirect.com/science/article/pii/000926149287068Z.

[37] H. C. Gerritsen, M. a. H. Asselbergs, A. V. Agronskaia, and W. G. J. H. M. Van Sark. Fluorescence lifetime imaging in scanning microscopes: acquisition speed, photon economy and lifetime resolution. *Journal of Microscopy*, 206(3):218–224, 2002. ISSN 1365-2818. doi: 10.1046/j.1365-2818.2002.01031.x. URL https://onlinelibrary.wiley.com/doi/abs/10.1046/j.1365-2818.2002.01031.x. _eprint: https://onlinelibrary.wiley.com/doi/pdf/10.1046/j.1365-2818.2002.01031.x.

[38] I.S. EN 60825-1:2014 SAFETY OF LASER PRODUCTS - PART 1: EQUIPMENT CLA, January 2014. URL https://shop.standards.ie/en-ie/standards/.

[39] Moinuddin Hassan, Jason Riley, Victor Chernomordik, Paul Smith, Randall Pursley, Sang Bong Lee, Jacek Capala, and Gandjbakhche Amir H. Fluorescence Lifetime Imaging System for in Vivo Studies. *Molecular Imaging*, 6(4):7290.2007.00019, July 2007. ISSN 1535-3508. doi: 10.2310/7290.2007.00019. URL https://doi.org/10.2310/7290.2007.00019. Publisher: SAGE Publications Inc.

[40] Diego R. Yankelevich, Dinglong Ma, Jing Liu, Yang Sun, Yinghua Sun, Julien Bec, Daniel S. Elson, and Laura Marcu. Design and evaluation of a device for fast multispectral time-resolved fluorescence spectroscopy and imaging. *Review of Scientific Instruments*, 85(3):034303, March 2014. ISSN 0034-6748. doi: 10.1063/1.4869037. URL https://doi.org/10.1063/1.4869037.

[41] Xiangnan Zhou, Julien Bec, Diego Yankelevich, and Laura Marcu. Multispectral fluorescence lifetime imaging device with a silicon avalanche photodetector. *Optics Express*, 29(13): 20105–20120, June 2021. ISSN 1094-4087. doi: 10.1364/OE.425632. URL https://opg.optica.org/oe/abstract.cfm?uri=oe-29-13-20105. Publisher: Optica Publishing Group.

[42] Xuhui Liu, Julien Bec, Xiangnan Zhou, Alba Alfonso Garcia, and Laura Marcu. Multispectral laser-scanning pulse-sampling fluorescence lifetime system for large-scale tissue imaging. *Optics Letters*, 50(3):900–903, February 2025. ISSN 1539-4794. doi: 10.1364/OL.547582. URL https://opg.optica.org/ol/abstract.cfm?uri=ol-50-3-900. Publisher: Optica Publishing Group.

[43] Mark Marsden, Takanori Fukazawa, Yu-Cheng Deng, Brent W. Weyers, Julien Bec, D. Gregory Farwell, and Laura Marcu. FLIm-Brush: dynamic visualization of intraoperative free-hand fiber-based fluorescence lifetime imaging. *Biomedical Optics Express*, 11 (9):5166–5180, September 2020. ISSN 2156-7085. doi: 10.1364/BOE.398357. URL https://opg.optica.org/boe/abstract.cfm?uri=boe-11-9-5166. Publisher: Optica Publishing Group.

[44] Alba Alfonso-Garcia, Julien Bec, Shamira Sridharan Weaver, Brad Hartl, Jakob Unger, Matthew Bobinski, Mirna Lechpammer, Fady Girgis, James Boggan, and Laura Marcu. Real-time augmented reality for delineation of surgical margins during neurosurgery using autofluorescence lifetime contrast. *Journal of Biophotonics*, 13(1): e201900108, 2020. ISSN 1864-0648. doi: 10.1002/jbio.201900108. URL https://doi.org/10.1002/jbio.201900108. _eprint: https://onlinelibrary.wiley.com/doi/pdf/10.1002/jbio.201900108.

[45] Silvia Noble Anbunesan, Alba Alfonso-Garcia, Xiangnan Zhou, Julien Bec, Han Sung Lee, Lee-Way Jin, Orin Bloch, and Laura Marcu. Intraoperative detection of IDH-mutant glioma using fluorescence lifetime imaging. *Journal of Biophotonics*, 16(4):e202200291, 2023. ISSN 1864-0648. doi: 10.1002/jbio.202200291. URL https://onlinelibrary.wiley.com/doi/abs/10.1002/jbio.202200291. _eprint: https://onlinelibrary.wiley.com/doi/pdf/10.1002/jbio.202200291.

[46] Alba Alfonso-Garcia, Silvia Noble Anbunesan, Julien Bec, Han Sung Lee, Lee-Way Jin, Orin Bloch, and Laura Marcu. In vivo characterization of the human glioblastoma infiltrative edge with label-free intraoperative fluorescence lifetime imaging. *Biomedical Optics Express*, 14(5):2196–2208, May 2023. ISSN 2156-7085. doi: 10.1364/BOE.481304. URL https://opg.optica.org/boe/abstract.cfm?uri=boe-14-5-2196. Publisher: Optica Publishing Group.

[47] Brent W. Weyers, Mark Marsden, Tianchen Sun, Julien Bec, Arnaud F. Bewley, Regina F. Gandour-Edwards, Michael G. Moore, D. Gregory Farwell, and Laura Marcu. Fluorescence lifetime imaging for intraoperative cancer delineation in transoral robotic surgery. *Translational Biophotonics*, 1(1-2):e201900017, 2019. ISSN 2627-1850. doi: 10.1002/tbio.201900017. URL https://onlinelibrary.wiley.com/doi/abs/10.1002/tbio.201900017. _eprint: https://onlinelibrary.wiley.com/doi/pdf/10.1002/tbio.201900017.

[48] Brent W. Weyers, Andrew C. Birkeland, Mark A. Marsden, Athena Tam, Julien Bec, Roberto P. Frusciante, Dorina Gui, Arnaud F. Bewley, Marianne Abouyared, Laura Marcu, and Donald Gregory Farwell. Intraoperative delineation of p16+ oropharyngeal carcinoma of unknown primary origin with fluorescence lifetime imaging: Preliminary report. *Head & Neck*, 44(8):1765–1776, 2022. ISSN 1097-0347. doi: 10.1002/hed.27078. URL https://onlinelibrary.wiley.com/doi/abs/10.1002/hed.27078. _eprint: https://onlinelibrary.wiley.com/doi/pdf/10.1002/hed.27078.

[49] Mark Marsden, Brent W. Weyers, Julien Bec, Tianchen Sun, Regina F. Gandour-Edwards, Andrew C. Birkeland, Marianne Abouyared, Arnaud F. Bewley, D. Gregory Farwell, and Laura Marcu. Intraoperative Margin Assessment in Oral and Oropharyngeal Cancer Using Label-Free Fluorescence Lifetime Imaging

and Machine Learning. *IEEE Transactions on Biomedical Engineering*, 68(3):857–868, March 2021. ISSN 1558-2531. doi: 10.1109/TBME.2020.3010480. URL https://ieeexplore.ieee.org/document/9144381. Conference Name: IEEE Transactions on Biomedical Engineering.

[50] Jennifer E Phipps, Dimitris Gorpas, Jakob Unger, Morgan Darrow, Richard J Bold, and Laura Marcu. Automated detection of breast cancer in resected specimens with fluorescence lifetime imaging. *Physics in Medicine & Biology*, 63(1):015003, December 2017. ISSN 0031-9155. doi: 10.1088/1361-6560/aa983a. URL https://dx.doi.org/10.1088/1361-6560/aa983a. Publisher: IOP Publishing.

[51] Jakob Unger, Christoph Hebisch, Jennifer E. Phipps, João L. Lagarto, Hanna Kim, Morgan A. Darrow, Richard J. Bold, and Laura Marcu. Real-time diagnosis and visualization of tumor margins in excised breast specimens using fluorescence lifetime imaging and machine learning. *Biomedical Optics Express*, 11 (3):1216–1230, March 2020. ISSN 2156-7085. doi: 10.1364/BOE.381358. URL https://opg.optica.org/boe/abstract.cfm?uri=boe-11-3-1216. Publisher: Optica Publishing Group.

[52] João Lagarto, Benjamin T. Dyer, Clifford Talbot, Markus B. Sikkel, Nicholas S. Peters, Paul M. W. French, Alexander R. Lyon, and Chris Dunsby. Application of time-resolved autofluorescence to label-free in vivo optical mapping of changes in tissue matrix and metabolism associated with myocardial infarction and heart failure. *Biomedical Optics Express*, 6(2):324–346, February 2015. ISSN 2156-7085. doi: 10.1364/BOE.6.000324. URL https://opg.optica.org/boe/abstract.cfm?uri=boe-6-2-324. Publisher: Optica Publishing Group.

[53] João L. Lagarto, Vladislav Shcheslavskiy, Francesco S. Pavone, and Riccardo Cicchi. Real-time fiber-based fluorescence lifetime imaging with synchronous external illumination: A new path for clinical translation. *Journal of Biophotonics*, 13(3):e201960119, 2020. ISSN 1864-0648. doi: 10.1002/jbio.201960119. URL https://onlinelibrary.wiley.com/doi/abs/10.1002/jbio.201960119.

[54] João L. Lagarto, Federica Villa, Simone Tisa, Franco Zappa, Vladislav Shcheslavskiy, Francesco S. Pavone, and Riccardo Cicchi. Real-time multispectral fluorescence lifetime imaging using Single Photon Avalanche Diode arrays. *Scientific Reports*, 10(1):8116, May 2020. ISSN 2045-2322. doi: 10.1038/s41598-020-65218-3. URL https://www.nature.com/articles/s41598-020-65218-3. Publisher: Nature Publishing Group.

[55] Min Woo Lee, Joon Woo Song, Woo Jae Kang, Hyeong Soo Nam, Tae Shik Kim, Sunwon Kim, Wang-Yuhl Oh, Jin Won Kim, and Hongki Yoo. Comprehensive intravascular imaging of atherosclerotic plaque in vivo using optical coherence tomography and fluorescence lifetime imaging. *Scientific Reports*, 8:14561, 2018. doi: 10.1038/s41598-018-32951-9. URL https://www.nature.com/articles/s41598-018-32951-9.

[56] Julien Bec, Cai Li, and Laura Marcu. Broadband, freeform focusing micro-optics for a side-viewing imaging catheter. *Optics Letters*, 44(20):4961–4964, October 2019. ISSN 1539-4794. doi: 10.1364/OL.44.004961. URL https://opg.optica.org/ol/abstract.cfm?uri=ol-44-20-4961. Publisher: Optica Publishing Group.

[57] Alba Alfonso-Garcia, Stephanie A. Cevallos, Jee-Yon Lee, Cai Li, Julien Bec, Andreas J. Bäumler, and Laura Marcu. Assessment of Murine Colon Inflammation Using Intraluminal Fluorescence Lifetime Imaging. *Molecules*, 27(4):1317, January 2022. ISSN 1420-3049. doi: 10.3390/molecules27041317. URL https://www.mdpi.com/1420-3049/27/4/1317. Number: 4 Publisher: Multidisciplinary Digital Publishing Institute.

[58] Cai Li, Julien Bec, Xiangnan Zhou, and Laura Marcu. Dual-modality fluorescence lifetime imaging-optical coherence tomography intravascular catheter system with freeform catheter optics. *Journal of Biomedical Optics*, 27(7):076005, July 2022. ISSN 1083-3668, 1560-2281. doi: 10.1117/1.JBO.27.7.076005. URL https://doi.org/10.1117/1.JBO.27.7.076005. Publisher: SPIE.

[59] Julien Bec, Xiangnan Zhou, Martin Villiger, Jeffrey A. Southard, Brett Bouma, and Laura Marcu. Dual modality intravascular catheter system combining pulse-sampling fluorescence lifetime imaging and polarization-sensitive optical coherence tomography. *Biomedical Optics Express*, 15(4):2114–2132, April 2024. ISSN 2156-7085. doi: 10.1364/BOE.516515. URL https://opg.optica.org/boe/abstract.cfm?uri=boe-15-4-2114. Publisher: Optica Publishing Group.

[60] Sebina Shrestha, Brian E. Applegate, Jesung Park, Xudong Xiao, Paritosh Pande, and Javier A. Jo. High-speed multispectral fluorescence lifetime imaging implementation for *in vivo* applications. *Optics Letters*, 35(15):2558–2560, August 2010. ISSN 1539-4794. doi: 10.1364/OL.35.002558. URL https://opg.optica.org/ol/abstract.cfm?uri=ol-35-15-2558. Publisher: Optica Publishing Group.

[61] Shuna Cheng, Rodrigo M. Cuenca, Boang Liu, Bilal H. Malik, Joey M. Jabbour, Kristen C. Maitland, John Wright, Yi-Shing Lisa Cheng, and Javier A. Jo. Handheld multispectral fluorescence lifetime imaging system for in vivo applications. *Biomedical Optics Express*, 5(3):921–931, March 2014. ISSN 2156-7085. doi: 10.1364/BOE.5.000921. URL https://opg.optica.org/boe/abstract.cfm?uri=boe-5-3-921. Publisher: Optica Publishing Group.

[62] Elvis Duran-Sierra, Shuna Cheng, Rodrigo Cuenca, Beena Ahmed, Jim Ji, Vladislav V. Yakovlev, Mathias Martinez, Moustafa Al-Khalil, Hussain Al-Enazi, Yi-Shing Lisa Cheng, John Wright, Carlos Busso, and Javier A. Jo. Machine-Learning Assisted Discrimination of Precancerous and Cancerous from Healthy Oral Tissue Based on Multispectral Autofluorescence Lifetime Imaging Endoscopy. *Cancers*, 13(19):4751, January 2021. ISSN 2072-6694. doi: 10.3390/cancers13194751. URL https://www.mdpi.com/2072-6694/13/19/4751. Number: 19 Publisher: Multidisciplinary Digital Publishing Institute.

[63] Michael J. Serafino and Javier A. Jo. Direct frequency domain fluorescence lifetime imaging using simultaneous ultraviolet and visible excitation. *Biomedical Optics Express*, 14(4):1608–1625, April 2023. ISSN 2156-7085. doi: 10.1364/BOE.480287. URL https://opg.optica.org/boe/abstract.cfm?uri=boe-14-4-1608. Publisher: Optica Publishing Group.

[64] Gabriel Tortorelli, Rodrigo Cuenca, Michael J. Serafino, Kayla Caughlin, Carlos Busso, Victoria L. Woo, Jacqueline Plemons, Yi-Shing L. Cheng, Celeste Abraham, Ying S. Wang, Rashmi

Hegde, and Javier A. Jo. Dual-excitation multispectral fluorescence lifetime imaging handheld endoscope for label-free metabolic and biochemical imaging of the oral mucosa. *Optics Letters*, 50 (12):3966–3969, June 2025. ISSN 1539-4794. doi: 10.1364/OL.561483. URL https://opg.optica.org/ol/abstract.cfm?uri=ol-50-12-3966. Publisher: Optica Publishing Group.

[65] Hugh Sparks, Hiroshi Kondo, Steven Hooper, Ian Munro, Gordon Kennedy, Christopher Dunsby, Paul French, and Erik Sahai. Heterogeneity in tumor chromatin-doxorubicin binding revealed by in vivo fluorescence lifetime imaging confocal endomicroscopy. *Nature Communications*, 9(1):2662, July 2018. ISSN 2041-1723. doi: 10.1038/s41467-018-04820-6. URL https://www.nature.com/articles/s41467-018-04820-6. Publisher: Nature Publishing Group.

[66] Gordon T. Kennedy, Hugh B. Manning, Daniel S. Elson, Mark A.A. Neil, Gordon W. Stamp, Bertrand Viellerobe, François Lacombe, Chris Dunsby, and Paul M.W. French. A fluorescence lifetime imaging scanning confocal endomicroscope. *Journal of Biophotonics*, 3(1-2):103–107, January 2010. ISSN 1864-0648. doi: 10.1002/JBIO.200910065. URL https://onlinelibrary.wiley.com/doi/full/10.1002/jbio.200910065. Publisher: John Wiley & Sons, Ltd.

[67] Ettore Pedretti, Michael G. Tanner, Tushar R. Choudhary, Nikola Krstajić, Alicia Megia-Fernandez, Robert K. Henderson, Mark Bradley, Robert R. Thomson, John M. Girkin, Kevin Dhaliwal, and Paul A. Dalgarno. High-speed dual color fluorescence lifetime endomicroscopy for highly-multiplexed pulmonary diagnostic applications and detection of labeled bacteria. *Biomedical Optics Express*, 10(1):181–195, January 2019. ISSN 2156-7085. doi: 10.1364/BOE.10.000181. URL https://opg.optica.org/boe/abstract.cfm?uri=boe-10-1-181. Publisher: Optica Publishing Group.

[68] Simon P. Poland, Ahmet T. Erdogan, Nikola Krstajić, James Levitt, Viviane Devauges, Richard J. Walker, David Day-Uei Li, Simon M. Ameer-Beg, and Robert K. Henderson. New high-speed centre of mass method incorporating background subtraction for accurate determination of fluorescence lifetime. *Optics Express*, 24 (7):6899–6915, April 2016. ISSN 1094-4087. doi: 10.1364/OE.24.006899. URL https://opg.optica.org/oe/abstract.cfm?uri=oe-24-7-6899. Publisher: Optica Publishing Group.

[69] Nikola Krstajić, Ahsan R. Akram M.d, Tushar R. Choudhary, Neil McDonald, Michael G. Tanner, Ettore Pedretti, Paul A. Dalgarno, Emma Scholefield, John M. Girkin, Anne Moore, Mark Bradley, and Kevin Dhaliwal M.d. Two-color widefield fluorescence microendoscopy enables multiplexed molecular imaging in the alveolar space of human lung tissue. *Journal of Biomedical Optics*, 21(4):046009, April 2016. ISSN 1083-3668, 1560-2281. doi: 10.1117/1.JBO.21.4.046009. URL https://doi.org/10.1117/1.JBO.21.4.046009. Publisher: SPIE.

[70] Susan Fernandes, Elvira Williams, Neil Finlayson, Hazel Stewart, Catharine Dhaliwal, David A. Dorward, William A. Wallace, Ahsan R. Akram, James Stone, Kevin Dhaliwal, and Gareth O.S. Williams. Fibre-based fluorescence-lifetime imaging microscopy: a real-time biopsy guidance tool for suspected lung cancer. *Translational Lung Cancer Research*, 13(2):355–361, February 2024. ISSN

22264477. doi: 10.21037/TLCR-23-638/COIF. URL https://tlcr.amegroups.org/article/view/83599/html. Publisher: AME Publishing Company.

[71] Gareth O. S. Williams, Elvira Williams, Neil Finlayson, Ahmet T. Erdogan, Qiang Wang, Susan Fernandes, Ahsan R. Akram, Kev Dhaliwal, Robert K. Henderson, John M. Girkin, and Mark Bradley. Full spectrum fluorescence lifetime imaging with 0.5 nm spectral and 50 ps temporal resolution. *Nature Communications*, 12(1):6616, November 2021. ISSN 2041-1723. doi: 10.1038/s41467-021-26837-0. URL https://www.nature.com/articles/s41467-021-26837-0. Publisher: Nature Publishing Group.

[72] Fangrui Lin, Chenshuang Zhang, Yihua Zhao, Binglin Shen, Rui Hu, Liwei Liu, and Junle Qu. In vivo two-photon fluorescence lifetime imaging microendoscopy based on fiber-bundle. *Optics Letters*, 47(9):2137–2140, May 2022. ISSN 1539-4794. doi: 10.1364/OL.453102. URL https://opg.optica.org/ol/abstract.cfm?uri=ol-47-9-2137. Publisher: Optica Publishing Group.

[73] Wenxuan Liang, Defu Chen, Honghua Guan, Hyeon-Cheol Park, Kaiyan Li, Ang Li, Ming-Jun Li, Israel Gannot, and Xingde Li. Label-Free Metabolic Imaging In Vivo by Two-Photon Fluorescence Lifetime Endomicroscopy. *ACS Photonics*, 9(12):4017–4029, December 2022. doi: 10.1021/acsphotonics.2c01493. URL https://doi.org/10.1021/acsphotonics.2c01493. Publisher: American Chemical Society.

[74] Melissa C. Skala, Kristin M. Riching, Annette Gendron-Fitzpatrick, Jens Eickhoff, Kevin W. Eliceiri, John G. White, and Nirmala Ramanujam. In vivo multiphoton microscopy of NADH and FAD redox states, fluorescence lifetimes, and cellular morphology in precancerous epithelia. *Proceedings of the National Academy of Sciences of the United States of America*, 104(49):19494–19499, December 2007. ISSN 00278424. doi: 10.1073/pnas.0708425104. URL www.pnas.orgcgidoi10.1073pnas.0708425104. Publisher: National Academy of Sciences.

[75] Karsten König, Ana Batista, Michael Zieger, Martin Kaatz, Holger Hänssle, Christine Fink, and Hans Georg Breunig. Clinical multimodal multiphoton tomography of pigmented skin lesions with an ultracompact femtosecond fiber laser. In *Photonics in Dermatology and Plastic Surgery 2020*, volume 11211, pages 29–36. SPIE, February 2020. doi: 10.1117/12.2542322. URL https://doi.org/10.1117/12.2542322.

[76] Elisa Benati, Valerio Bellini, Stefania Borsari, Christopher Dunsby, Chiara Ferrari, Paul French, Mario Guanti, Davide Guardoli, Karsten Koenig, Giovanni Pellacani, Giovanni Ponti, Simona Schianchi, Clifford Talbot, and Stefania Seidenari. Quantitative evaluation of healthy epidermis by means of multiphoton microscopy and fluorescence lifetime imaging microscopy. *Skin Research and Technology*, 17(3):295–303, 2011. ISSN 1600-0846. doi: 10.1111/j.1600-0846.2011.00496.x. URL https://onlinelibrary.wiley.com/doi/abs/10.1111/j.1600-0846.2011.00496.x. _eprint: https://onlinelibrary.wiley.com/doi/pdf/10.1111/j.1600-0846.2011.00496.x.

[77] Yinghua Sun, Jennifer Phipps, Daniel S. Elson, Heather Stoy, Steven Tinling, Jeremy Meier, Brian Poirier, Frank S. Chuang, D. Gregory Farwell, and Laura Marcu. Fluorescence lifetime imaging microscopy: *in vivo* application to diagnosis of oral carcinoma.

Optics Letters, 34(13):2081–2083, July 2009. ISSN 1539-4794. doi: 10.1364/OL.34.002081. URL https://opg.optica.org/ol/abstract.cfm?uri=ol-34-13-2081. Publisher: Optica Publishing Group.

[78] D S Elson, J A Jo, and L Marcu. Miniaturized side-viewing imaging probe for fluorescence lifetime imaging (FLIM): validation with fluorescence dyes, tissue structural proteins and tissue specimens. *New Journal of Physics*, 9(5):127, May 2007. ISSN 1367-2630. doi: 10.1088/1367-2630/9/5/127. URL https://dx.doi.org/10.1088/1367-2630/9/5/127.

[79] Yinghua H. Sun, Nisa Hatami, Matthew Yee, Jennifer E. Phipps, Daniel S. Elson, Fredric Gorin, Rudolph J. Schrot, and Laura Marcu. Fluorescence lifetime imaging microscopy for brain tumor image-guided surgery. *Journal of Biomedical Optics*, 15 (5):056022, September 2010. ISSN 1083-3668, 1560-2281. doi: 10.1117/1.3486612. URL https://doi.org/10.1117/1.3486612. Publisher: SPIE.

[80] Yinghua Sun, Jennifer E Phipps, Jeremy Meier, Nisa Hatami, Brian Poirier, Daniel S Elson, D Gregory Farwell, and Laura Marcu. Endoscopic Fluorescence Lifetime Imaging for In Vivo Intraoperative Diagnosis of Oral Carcinoma. *Microscopy and Microanalysis*, 19(4):791–798, August 2013. ISSN 1431-9276. doi: 10.1017/S1431927613001530. URL https://doi.org/10.1017/S1431927613001530.

[81] Hugh Sparks, Sean Warren, Joana Guedes, Nagisa Yoshida, Tze Choong Charn, Nadia Guerra, Taranjit Tatla, Christopher Dunsby, and Paul French. A flexible wide-field FLIM endoscope utilising blue excitation light for label-free contrast of tissue. *Journal of Biophotonics*, 8(1-2):168–178, January 2015. ISSN 1864-0648. doi: 10.1002/JBIO.201300203. URL https://onlinelibrary.wiley.com/doi/full/10.1002/jbio.201300203. Publisher: John Wiley & Sons, Ltd.

[82] Shuna Cheng, J. Jesus Rico-Jimenez, Joey Jabbour, Bilal Malik, Kristen C. Maitland, John Wright, Yi-Shing Lisa Cheng, and Javier A. Jo. Flexible endoscope for continuous in vivo multispectral fluorescence lifetime imaging. *Optics Letters*, 38(9): 1515–1517, May 2013. ISSN 1539-4794. doi: 10.1364/OL.38.001515. URL https://opg.optica.org/ol/abstract.cfm?uri=ol-38-9-1515. Publisher: Optica Publishing Group.

[83] Vytautas Zickus, Ming Lo Wu, Kazuhiro Morimoto, Valentin Kapitany, Areeba Fatima, Alex Turpin, Robert Insall, Jamie Whitelaw, Laura Machesky, Claudio Bruschini, Daniele Faccio, and Edoardo Charbon. Fluorescence lifetime imaging with a megapixel SPAD camera and neural network lifetime estimation. *Scientific Reports 2020 10:1*, 10(1):1–10, December 2020. ISSN 2045-2322. doi: 10.1038/s41598-020-77737-0. URL https://www.nature.com/articles/s41598-020-77737-0. Publisher: Nature Publishing Group ISBN: 0123456789.

[84] Samuel Burri, Yuki Maruyama, Xavier Michalet, Francesco Regazzoni, Claudio Bruschini, and Edoardo Charbon. Architecture and applications of a high resolution gated SPAD image sensor. *Optics Express*, 22(14):17573–17589, July 2014. ISSN 1094-4087. doi: 10.1364/OE.22.017573. URL https://opg.optica.org/oe/abstract.cfm?uri=oe-22-14-17573. Publisher: Optica Publishing Group.

[85] Arin Can Ulku, Claudio Bruschini, Ivan Michel Antolović, Yung Kuo, Rinat Ankri, Shimon Weiss, Xavier Michalet, and Edoardo Charbon. A 512 × 512 SPAD Image Sensor With Integrated Gating for Widefield FLIM. *IEEE Journal of Selected Topics in Quantum Electronics*, 25(1):1–12, January 2019. ISSN 1558-4542. doi: 10.1109/JSTQE.2018.2867439. URL https://ieeexplore.ieee.org/abstract/document/8449092. Conference Name: IEEE Journal of Selected Topics in Quantum Electronics.

[86] Michael Wayne, Arin Ulku, Andrei Ardelean, Paul Mos, Claudio Bruschini, and Edoardo Charbon. A 500 × 500 Dual-Gate SPAD Imager With 100% Temporal Aperture and 1 ns Minimum Gate Length for FLIM and Phasor Imaging Applications. *IEEE Transactions on Electron Devices*, 69(6):2865–2872, June 2022. ISSN 1557-9646. doi: 10.1109/TED.2022.3168249. URL https://ieeexplore.ieee.org/abstract/document/9775113. Conference Name: IEEE Transactions on Electron Devices.

[87] Xavier Michalet, Arin C. Ulku, Michael A. Wayne, Shimon Weiss, Claudio Bruschini, and Edoardo Charbon. NIR Fluorescence lifetime macroscopic imaging with a novel time-gated SPAD camera. *Proceedings of SPIE–the International Society for Optical Engineering*, 12384:1238409, 2023. ISSN 0277-786X. doi: 10.1117/12.2649227. URL https://www.ncbi.nlm.nih.gov/pmc/articles/PMC10586139/.

[88] Jason T. Smith, Alena Rudkouskaya, Shan Gao, Juhi M. Gupta, Arin Ulku, Claudio Bruschini, Edoardo Charbon, Shimon Weiss, Margarida Barroso, Xavier Intes, and Xavier Michalet. In vitro and in vivo NIR fluorescence lifetime imaging with a time-gated SPAD camera. *Optica*, 9(5):532–544, May 2022. ISSN 2334-2536. doi: 10.1364/OPTICA.454790. URL https://opg.optica.org/optica/abstract.cfm?uri=optica-9-5-532. Publisher: Optica Publishing Group.

[89] SPAD512^2 single-photon (SPAD) camera | Pi Imaging, . URL https://piimaging.com/product-spad512s.

[90] Robert K. Henderson, Nick Johnston, Francescopaolo Mattioli Della Rocca, Haochang Chen, David Day-Uei Li, Graham Hungerford, Richard Hirsch, David Mcloskey, Philip Yip, and David J. S. Birch. A 192\times128 Time Correlated SPAD Image Sensor in 40-nm CMOS Technology. *IEEE Journal of Solid-State Circuits*, 54(7):1907–1916, July 2019. ISSN 1558-173X. doi: 10.1109/JSSC.2019.2905163. URL https://ieeexplore.ieee.org/document/8681087. Conference Name: IEEE Journal of Solid-State Circuits.

[91] Jakub Nedbal, Francesco Mattioli Della Rocca, Iveta T. Ivanova, Andrew Allan, Jeremy Graham, Richard Walker, Robert K. Henderson, and Klaus Suhling. A time-correlated single photon counting SPAD array camera with a bespoke data-processing algorithm for lightsheet fluorescence lifetime imaging (FLIM) and FLIM videos. *Scientific Reports*, 14(1):7247, March 2024. ISSN 2045-2322. doi: 10.1038/s41598-024-56122-1. URL https://www.nature.com/articles/s41598-024-56122-1. Publisher: Nature Publishing Group.

[92] FLIMera SPAD array imaging camera for dynamic FLIM studies at real time video rates - HORIBA, . URL https://www.horiba.com/int/scientific/products/detail/action/show/Product/flimera-1989/.

[93] LiFA-FLIM: Versatile FLIM System with SPAD Camera - Lambert, . URL https://lambertinstruments.com/products/lifa-flim.

[94] pco.flim X | Excelitas, . URL https://www.excelitas.com/product/pcoflim-x.

[95] Lighting up the Lung to treat infection - the Proteus Project, August 2024. URL https://edinburgh-infectious-diseases.ed.ac.uk/our-research/research-themes/clinical-and-translational-research/lighting-lung-treat-infection.

[96] Tarek Al Abbas. *Miniature High Dynamic Range Time-Resolved CMOS SPAD Image Sensors*. PhD thesis, University of Edinburgh, July 2019. URL https://era.ed.ac.uk/handle/1842/35970. Accepted: 2019-08-06T10:50:08Z Publisher: The University of Edinburgh.

[97] Tarek Al Abbas, Oscar Almer, Sam W. Hutchings, Ahmet T. Erdogan, Istvan Gyongy, A. W.Dutton Neale, and Robert K. Henderson. A 128×120 5-Wire 1.96mm2 40nm/90nm 3D Stacked SPAD Time Resolved Image Sensor SoC for Microendoscopy. *IEEE Symposium on VLSI Circuits, Digest of Technical Papers*, 2019-June:C260–C261, June 2019. doi: 10.23919/VLSIC.2019.8777979. URL https://doi.org/10.23919/VLSIC.2019.8777979. Publisher: Institute of Electrical and Electronics Engineers Inc. ISBN: 9784863487185.

[98] Andrew B. Matheson, Ahmet T. Erdogan, Sam Borrowman, Michael G. Tanner, Charlotte Hopkinson, Robert K. Henderson, and Gary J. Loake. Handheld wide-field fluorescence lifetime imaging system based on a distally mounted SPAD array. *Optics Express, Vol. 31, Issue 14, pp. 22766-22775*, 31(14): 22766–22775, July 2023. ISSN 1094-4087. doi: 10.1364/OE.482273. URL https://opg.optica.org/viewmedia.cfm?uri=oe-31-14-22766&seq=0&html=true. Publisher: Optica Publishing Group.

[99] Andrew B. Matheson, Charlotte Hopkinson, Michael G. Tanner, and Robert K. Henderson. Fluorescence lifetime imaging with distance and ranging using a miniaturised SPAD system. *Scientific Reports 2024 14:1*, 14(1):1–9, June 2024. ISSN 2045-2322. doi: 10.1038/s41598-024-63409-w. URL https://www.nature.com/articles/s41598-024-63409-w. Publisher: Nature Publishing Group ISBN: 0123456789.

[100] Sanathana Konugolu Venkata Sekar, Alberto Dalla Mora, Ilaria Bargigia, Edoardo Martinenghi, Claus Lindner, Parisa Farzam, Marco Pagliazzi, Turgut Durduran, Paola Taroni, Antonio Pifferi, and Andrea Farina. Broadband (600–1350 nm) Time-Resolved Diffuse Optical Spectrometer for Clinical Use. *IEEE Journal of Selected Topics in Quantum Electronics*, 22(3):406–414, May 2016. ISSN 1558-4542. doi: 10.1109/JSTQE.2015.2506613. URL https://ieeexplore.ieee.org/document/7349112.

[101] Keela Hughes. konugolu/FLIM_keela, April 2025. URL https://github.com/konugolu/FLIM_Keela.

[102] Martina Piletti, Themis Krasoudaki, Andrea Matulac, Labrini Sygellou, Dario Angelone, Sanathana Konugolu Venkata Sekar, Rodorico Giorgi, Aidan Quinn, and Daniela Iacopino. Electrochemical Synthesis of Nitrogen-doped Carbon Dot Inks and Evaluation of their Use for Anticounterfeiting Applications. *Journal*

of Materials Chemistry C, May 2025. ISSN 2050-7534. doi: 10.1039/D5TC00939A. URL https://pubs.rsc.org/en/content/articlelanding/2025/tc/d5tc00939a. Publisher: The Royal Society of Chemistry.

[103] Ruslan I. Dmitriev and Dmitri B. Papkovsky. Optical probes and techniques for O2 measurement in live cells and tissue. *Cellular and Molecular Life Sciences*, 69(12):2025–2039, June 2012. ISSN 1420-9071. doi: 10.1007/s00018-011-0914-0. URL https://doi.org/10.1007/s00018-011-0914-0.

[104] Liang Li, Alexander V. Zhdanov, and Dmitri B. Papkovsky. Advanced multimodal solid-state optochemical pH and dual pH/O2 sensors for cell analysis. *Sensors and Actuators B: Chemical*, 371:132486, November 2022. ISSN 0925-4005. doi: 10.1016/j.snb.2022.132486. URL https://www.sciencedirect.com/science/article/pii/S0925400522011285.

[105] Dario Angelone, Liang Li, Ciaran Devoy, Andrew B. Matheson, Ahmet T. Erdogan, Robert K. Henderson, Mark Tangney, Dmitri B. Papkovsky, Stefan Andersson-Engels, and Sanathana Konugolu Venkata Sekar. Metabolic imaging of tumor tissue samples using planar fluorescence lifetime-based pH sensors and a SPAD array imager. *Sensors and Actuators B: Chemical*, 431:137441, May 2025. ISSN 0925-4005. doi: 10.1016/J.SNB.2025.137441. URL https://doi.org/10.1016/j.snb.2025.137441. Publisher: Elsevier.

[106] Xiaomeng Zhang, Yuxiang Lin, and Robert J. Gillies. Tumor pH and Its Measurement. *Journal of Nuclear Medicine*, 51(8):1167–1170, August 2010. ISSN 0161-5505, 2159-662X. doi: 10.2967/jnumed.109.068981. URL https://jnm.snmjournals.org/content/51/8/1167. Publisher: Society of Nuclear Medicine Section: Focus on Molecular Imaging.

[107] F. J. Voskuil, P. J. Steinkamp, T. Zhao, B. van der Vegt, M. Koller, J. J. Doff, Y. Jayalakshmi, J. P. Hartung, J. Gao, B. D. Sumer, M. J. H. Witjes, and G. M. van Dam. Exploiting metabolic acidosis in solid cancers using a tumor-agnostic pH-activatable nanoprobe for fluorescence-guided surgery. *Nature Communications*, 11(1):3257, June 2020. ISSN 2041-1723. doi: 10.1038/s41467-020-16814-4. URL https://www.nature.com/articles/s41467-020-16814-4. Publisher: Nature Publishing Group.

[108] Dario Angelone, Sanathana Konugolu Venkata Sekar, Walter Messina, Andrew Matheson, Ahmet T. Erdogan, Robert K. Henderson, Ray Burke, and Stefan Andersson-Engels. Time resolved SPAD micro-camera probe for wide-field FLIm in microendoscopy. In *Advanced Biomedical and Clinical Diagnostic and Surgical Guidance Systems XXI*, volume 12368, pages 34–37. SPIE, March 2023. doi: 10.1117/12.2648340. URL https://doi.org/10.1117/12.2648340.

[109] Heng Li, Beau A. Standish, Adrian Mariampillai, Nigel R. Munce, Youxin Mao, Stephanie Chiu, Norman E. Marcon, Brian C. Wilson, Alex Vitkin, and Victor X.D. Yang. Feasibility of interstitial Doppler optical coherence tomography for in vivo detection of microvascular changes during photodynamic therapy. *Lasers in Surgery and Medicine*, 38(8):754–761, 2006. ISSN 1096-9101. doi: 10.1002/lsm.20387. URL https://onlinelibrary.wiley.com/doi/abs/10.1002/lsm.20387. _eprint: https://onlinelibrary.wiley.com/doi/pdf/10.1002/lsm.20387.

[110] Gerd Keiser, Fei Xiong, Ying Cui, and Perry Ping Shum. Review of diverse optical fibers used in biomedical research and clinical practice. *Journal of Biomedical Optics*, 19(8):080902, August 2014. ISSN 1083-3668, 1560-2281. doi: 10.1117/1.JBO.19.8.080902. URL https://doi.org/10.1117/1.JBO.19.8.080902. Publisher: SPIE.

[111] John J. Davenport, Michelle Hickey, Justin P. Phillips, and Panicos A. Kyriacou. Method for producing angled optical fiber tips in the laboratory. *Optical Engineering*, 55(2):026120, February 2016. ISSN 0091-3286. doi: 10.1117/1.OE.55.2.026120. URL https://doi.org/10.1117/1.OE.55.2.026120. Publisher: SPIE-Intl Soc Optical Eng.

[112] A. Sakamoto and T. Saito. Computational analysis of responses of a wedge-shaped-tip optical fiber probe in bubble measurement. *Review of Scientific Instruments*, 83(7):075107, July 2012. ISSN 0034-6748. doi: 10.1063/1.4732819. URL https://doi.org/10.1063/1.4732819.

[113] Walter Messina, Lorenzo Niemitz, Simon Sorensen, Claire O'Dowling, Piotr Buszman, Stefan Andersson-Engels, and Ray Burke. Design and Assembly of a Miniature Catheter Imaging System for In Vivo Heart Endoscopic Imaging. *Sensors*, 24(19): 6216, January 2024. ISSN 1424-8220. doi: 10.3390/s24196216. URL https://www.mdpi.com/1424-8220/24/19/6216. Number: 19 Publisher: Multidisciplinary Digital Publishing Institute.

[114] Laura Di Sieno, Giulia Maffeis, Alberto Dalla Mora, Edoardo Ferocino, Alberto Tosi, Enrico Conca, Alessandro Ruggeri, Simone Tisa, Alexander Flocke, Antonio Pifferi, and Paola Taroni. Smart Optode for 8-Wavelength Time-Gated Diffuse Optics. *IEEE Journal of Selected Topics in Quantum Electronics*, 30(1: Single-Photon Technologies and Applications):1–9, January 2024. ISSN 1558-4542. doi: 10.1109/JSTQE.2023.3321436. URL https://ieeexplore.ieee.org/document/10268981.

[115] Laura Di Sieno, Alberto Dalla Mora, Alessandro Torricelli, Giulia Maffeis, Alessandro Ruggeri, Simone Tisa, Alberto Tosi, Enrico Conca, Alexander Flocke, Antonio Pifferi, and Paola Taroni. First In-Vivo Diffuse Optics Application of a Time-Domain Multiwavelength Wearable Optode. In *Biophotonics Congress: Biomedical Optics 2022 (Translational, Microscopy, OCT, OTS, BRAIN) (2022), paper OTu4D.3*, page OTu4D.3. Optica Publishing Group, April 2022. doi: 10.1364/OTS.2022.OTu4D.3. URL https://opg.optica.org/abstract.cfm?uri=OTS-2022-OTu4D.3.

[116] ams NanEye2D Miniature Camera Module CMOS Image Sensors - ams-osram - ams, . URL https://ams-osram.com/products/sensor-solutions/cmos-image-sensors/ams-naneye2d-miniature-camera-module.

[117] Asif Newaz Khan, Cleitus Antony, Meena Baskaran, Brian Corbett, Sanathana Konugolu Venkata Sekar, Ray Burke, Stefan Andersson-Engels, and Paul D. Townsend. Optical communication for next generation chip on tip surgical endoscopes. In *Diagnostic and Therapeutic Applications of Light in Cardiology 2024*, volume 12819, page 128190G. SPIE, March 2024. doi: 10.1117/12.3002842. URL https://doi.org/10.1117/12.3002842.

[118] Asif Khan, Meena Baskaran, Owen Moynihan, Cleitus Antony, James O'Callaghan, Brendan Roycroft, Kevin Thomas, Emanuele

Pelucchi, Sanathana Konugolu Venkata Sekar, Stefan Andersson-Engels, Paul Townsend, and Brian Corbett. Half duplex transmission with asymmetric surface normal electro absorption modulator-based optical transceiver for camera-on-tip surgical endoscopes. *Optics Express*, 33(15):31181–31194, July 2025. ISSN 1094-4087. doi: 10.1364/OE.566896. URL https://opg.optica.org/oe/abstract.cfm?uri=oe-33-15-31181. Publisher: Optica Publishing Group.

[119] Sanathana Konugolu Venkata Sekar, Meena Baskaran, Hui Ma, Marc Rensing, Kamil Gradkowski, Asif Khan, Cleitus Antony, Paul D. Townsend, Brian Corbett, and Stefan Andersson-engels. All optically powered chip-on-tip microcamera for surgical guidance. In *Frontiers in Optics + Laser Science 2023 (FiO, LS) (2023), paper JTu5A.83*, page JTu5A.83. Optica Publishing Group, October 2023. doi: 10.1364/FIO.2023.JTu5A.83. URL https://opg.optica.org/abstract.cfm?uri=FiO-2023-JTu5A.83.

[120] Day-Uei Li, Eleanor Bonnist, David Renshaw, and Robert Henderson. On-chip, time-correlated, fluorescence lifetime extraction algorithms and error analysis. *JOSA A*, 25(5):1190–1198, May 2008. ISSN 1520-8532. doi: 10.1364/JOSAA.25.001190. URL https://opg.optica.org/josaa/abstract.cfm?uri=josaa-25-5-1190. Publisher: Optica Publishing Group.

[121] Noël Boens, Wenwu Qin, Nikola Basarić, Johan Hofkens, Marcel Ameloot, Jacques Pouget, Jean-Pierre Lefèvre, Bernard Valeur, Enrico Gratton, Martin vandeVen, Norberto D. Silva, Yves Engelborghs, Katrien Willaert, Alain Sillen, Garry Rumbles, David Phillips, Antonie J. W. G. Visser, Arie van Hoek, Joseph R. Lakowicz, Henryk Malak, Ignacy Gryczynski, Arthur G. Szabo, Don T. Krajcarski, Naoto Tamai, and Atsushi Miura. Fluorescence Lifetime Standards for Time and Frequency Domain Fluorescence Spectroscopy. *Analytical Chemistry*, 79(5):2137–2149, March 2007. ISSN 0003-2700. doi: 10.1021/ac062160k. URL https://doi.org/10.1021/ac062160k. Publisher: American Chemical Society.

[122] Anca Margineanu. Calibration approaches for fluorescence lifetime applications using time-domain measurements. *Methods in Microscopy*, 2(1):61–71, April 2025. ISSN 2942-3899. doi: 10.1515/mim-2024-0031. URL https://doi.org/10.1515/mim-2024-0031.

[123] Dario Angelone and Sanathana Konugolu Venkata Sekar. Dataset: Metabolic imaging of tumor tissue samples using planar fluorescence lifetime-based pH sensors and a SPAD array imager, November 2024. URL https://zenodo.org/records/14024767.

[124] Dario Angelone and Sanathana Konugolu Venkata Sekar. Dataset: Chip-on-tip fluorescence lifetime imaging micro-camera toward endoscopic applications, May 2025. URL https://zenodo.org/records/15375005.

[125] Dario Angelone and Sanathana Konugolu Venkata Sekar. Dataset: Development of solid-state fluorescence lifetime standards for clinical applications using dyed epoxy resins, December 2025. URL https://zenodo.org/records/17952539.

Papers

Paper I

Metabolic imaging of tumor tissue samples using planar fluorescence lifetime-based pH sensors and a SPAD array imager

Dario Angelone, Liang Li, Ciaran Devoy, Andrew B. Matheson, Ahmet T. Erdogan, Robert K. Henderson, Mark Tangney, Dmitri B. Papkovsky, Stefan Andersson-Engels, and Sanathana Konugolu Venkata Sekar.

Sensors and Actuators B: Chemical **Vol. 431**, (2025).

Sensors & Actuators: B. Chemical 431 (2025) 137441

Contents lists available at ScienceDirect

Sensors and Actuators: B. Chemical

journal homepage: www.elsevier.com/locate/snb

Metabolic imaging of tumor tissue samples using planar fluorescence lifetime-based pH sensors and a SPAD array imager

Dario Angelone [a,*], Liang Li [b], Ciaran Devoy [c], Andrew B. Matheson [d], Ahmet T. Erdogan [d], Robert K. Henderson [d], Mark Tangney [c], Dmitri B. Papkovsky [b], Stefan Andersson-Engels [a,e], Sanathana Konugolu Venkata Sekar [a,*]

[a] Biophotonics@Tyndall, Tyndall National Institute, Lee Maltings Complex, Cork T12 R5CP, Ireland
[b] School of Biochemistry and Cell Biology, University College Cork, Pharmacy Building, College Road, Cork, Ireland
[c] Cancer Research @UCC, University College Cork, Cork, Ireland
[d] Institute for Integrated Micro and Nano Systems, School of Engineering, University of Edinburgh, Edinburgh, United Kingdom
[e] Department of Physics, University College Cork, College Road, Cork, Ireland

ARTICLE INFO

Keywords:
Acidosis of tumor tissue
Planar optochemical pH sensor
Fluorescence lifetime-based sensing
SPAD array imager
FLIM detection

ABSTRACT

Extracellular pH (pHe) is an important indicator of the homeostatic condition of mammalian tissue and its pathophysiological state such as tumor development and tissue acidosis. Optochemical sensors with internal referencing capabilities can perform dynamic quantitative imaging of pHe in live tissue samples. Here we have used planar solid-state pH sensors based on a fluorescent octaethylporphin-ketone (OEPK) dye in plasticized PVC matrix, which produce robust fluorescence lifetime response in the physiological pH range and stable lifetime calibration. A custom-built fluorescence lifetime imager, with a 405 nm picosecond diode laser excitation and a photon counting SPAD array detector (120 ×128 pixels) with wide-field Fluorescence Lifetime Imaging (FLIM) capability, was used to image the planar pH sensor brought in contact with freshly excised normal and tumor tissue. The FLIM based sensor system has demonstrated good analytical performance and suitability for *in vivo* use. Producing detailed maps of tissue pHe, such sensors can facilitate a deeper understanding of tissue metabolism and physiology, and can find use in fluorescence guided surgery of solid tumors.

1. Introduction

Different tissues and cells of the human body are set to function under specific metabolic conditions, which correspond to their physiological roles. Maintenance of the physiological homeostasis in all tissues is therefore critical for the normal functioning of the organism, while significant deviations from the norm can impair the organism and even cause death.

The metabolic networks of human and animal cells involve a number of pathways, the major ones being oxidative phosphorylation (OxPhos), glycolysis and tricarboxylic acid (TCA) cycle, complemented by the pentose phosphate, glutaminolysis and fatty acid oxidation pathways [1–3]. The different energy-generating pathways are interlinked and cross-regulated, so they can respond to altered energy demand (e.g. exercise for muscle tissue), substrate availability (e.g. hypoxia in cancer), and stress condition (e.g. oxidative stress or drug treatment) [3,4]. This feature allows the cells to compensate for dysfunctional pathways and mitigate stress. Because of this, many common disease states have characteristic metabolic signatures and adaptive or mal-adaptive responses in the affected cells and tissues [5–7]; knowledge of these characteristics can be useful in the development of efficient therapeutic interventions and pharmacological treatments.

A number of analytical techniques and biomarkers are currently used to probe tissue metabolism, in either *in vitro* or *in vivo* settings [3,8,9]. Thus, the OxPhos flux can be assessed by measuring oxygen consumption rate (OCR) of host cells in vitro. Similarly, glycolytic flux and TCA cycle activity can be assessed by measuring the release of the acidic species (lactate/H^+ and CO_2, respectively) from the cells, i.e. extracellular acidification rate (ECAR) [3]. The use of optochemical sensors has greatly facilitated these tasks. Thus, the MitoXpress platform [3], operating with a pair of soluble O_2 and pH sensitive probes, and the XF Analyzer platform [10], which uses solid-state O_2 and pH sensors [11],

* Corresponding authors.
E-mail addresses: dario.angelone@tyndall.ie (D. Angelone), sanathana.konugolu@tyndall.ie (S. Konugolu Venkata Sekar).

https://doi.org/10.1016/j.snb.2025.137441
Received 21 November 2024; Received in revised form 5 February 2025; Accepted 12 February 2025
Available online 12 February 2025
0925-4005/© 2025 The Authors. Published by Elsevier B.V. This is an open access article under the CC BY license (http://creativecommons.org/licenses/by/4.0/).

and the corresponding assay settings, provide simple and accurate measurement of the OCR and ECAR, by means of a phosphorescent O_2 sensor and a fluorescent pH sensor, respectively. They allow rapid, high-throughput, multi-parametric metabolic assessment of cells under different conditions generating their characteristic metabolic signatures.

Metabolic assessment of live tissue by imaging techniques in *in vivo* or *ex vivo* settings is also of high interest [12]. Here, photoluminescence lifetime based sensing systems are particularly advantageous, as this detection mode with internal referencing capabilities allows the use of disposable, calibration-free (batch calibrated), low-cost sensor probes for the relevant analytes [13,14]. Thus, advanced quenched-phosphorescence O_2 imaging systems operating with intravascular cell-impermeable O_2 probes [15–17], cell-permeable probes injected into tissue [18], or planar O_2 sensing foils applied onto skin or tissue [19], coupled with Phosphorescence Lifetime IMaging (PLIM) detection [13,16,20], have been described.

On the other hand, optical sensor-based imaging systems for other key markers of tissue metabolism are less developed and rarely used in clinical settings. Thus, monitoring of tissue acid-base homeostasis is important, especially in tumors which have enhanced glucose catabolism and production of acid (lactate and H^+) [21]. Although tumor cells can maintain a normal or alkaline intracellular pH (pHi), their major acid load is transported outside where it cannot be removed due to poor perfusion and disorganized vasculature. This reduces extracellular pH (pHe) leading to acidosis of tumor tissue [21,22], also known as Warburg effect [23,24]. Low pHe in solid tumors promotes cell proliferation (maximized at pHe 6.8 vs 7.3 for normal cells) and metastases, and contributes to cancer aggressiveness and the outcomes of anti-cancer therapy [25].

Techniques currently explored for imaging tumor pHe, which include Magnetic Resonance Imaging and Spectroscopy (MRS-^{32}P, MRS-^{19}F, MRS-^{1}H), Positron Emission Tomography, Electron Paramagnetic Resonance, Optical Imaging and Photoacoustic Imaging [22,24], suffer from inadequate sensitivity, selectivity (cross-sensitivity with pHi), accuracy and spatial resolution, invasiveness, toxicity and hazard of the contrast agents, etc.; these factors limit their adoption for diagnostics and treatment of cancer and solid tumors in humans [24]. From the above prospectives, optical sensor based Imaging techniques, particularly fluorescence lifetime imaging (FLIM) of tissues [26], hold promise.

Photoluminescence lifetime detection modality is becoming increasingly popular in optochemical sensing and bio-imaging [13,15,16,20,26]. This internally referenced (i.e. independent of the luminophore concentration) readout helps reduce measurement artefacts and achieve accurate quantification of the analyte without tedious re-calibrations and control measurements [20]. It is particularly efficient in quenched-phosphorescence sensing of O_2 in PLIM mode, where microsecond lifetimes are measured [16,18], whereas the measurement of fluorescence lifetimes in the low nanosecond time range and FLIM based sensing have been challenging so far. This is due to a low availability of sensor materials with robust ns lifetime response to analytes of interest, and affordable and sensitive imaging detectors (2D array chips) with time-correlated single photon counting (TCSPC), ns lifetime measurement capabilities, and fast readout electronics.

Nowadays, this is beginning to change. Thus, sensing materials based on fluorescent porphyrin dyes with useful spectral characteristics and large lifetime response to pH in the physiological range, measured on standard laser-scanning confocal FLIM-TCSPC microscopes equipped with fast photon-counting PMT detectors, were recently described [27]. Furthermore, photon counting imaging detectors comprising 2D array chips with accessory readout electronics, that can perform TCSPC and lifetime measurements simultaneously in all pixels, are also coming to the fore. One example is the TpxCam family of optical cameras [28], in which the CMOS chip comprising a 256 × 256 pixel detector array with time-stamping capabilities is integrated with fast readout electronics and coupled with an image intensifier and pulsed LED or laser excitation [29]. While the system has single photon sensitivity and a high level of integration, its temporal resolution (1.6 ns for Tpx4Cam cameras and 32 ns for the imager setup IRF [29]) is still inadequate for the majority of common fluorophores with lifetimes of 1–5 ns, and the system requires an image intensifier and is prohibitively expensive (>$50k). On the other hand, 2-dimentional single photon avalanche diode (SPAD) array detectors [30], which have single photon sensitivity and time stamping functions with sub-nanosecond temporal resolution, look promising. Such devices are produced with an increasing number of pixels - currently up to 1 M [31].

Here we describe a new FLIM system for wide-field imaging of tissue pHe, which uses a time-resolved SPAD detector with a minimum time bin-width of 390 ps [32], and planar solid-state fluorescent sensors that change their lifetime characteristic in response to pH [27]. The system is demonstrated with a model of grafted tumors in mice, in which live tissue excised from the animals is brought in contact with the pH sensor and imaged *ex vivo* at different time points. Normal tissue samples are also measured for comparison. The results produced are then discussed from the physiological viewpoint.

The animal trial and FLIM experiments were designed to generate initial sets of data of mean values and 2D maps of pHe for samples of normal and tumor tissue imaged *ex vivo*. Specifically, with the aim of answering the following questions: i) how does the pHe in tumor tissue samples compare with that of normal muscle tissue; ii) are there any detectable gradients of pHe within cross-sections of the imaged tissue; and iii) is there a dependence between the tumor size/age (or the time it was allowed to grow) and pHe?

2. Materials and methods

2.1. Preparation of disposable fluorescent pH sensors

A comprehensive description of the sensor preparation can be found in [27] along with a demonstration of their ability to perform accurate pH measurements with pH standard solutions over a range of 5.5 – 7.5. Briefly, the pH sensing material comprised a protonable fluorescent dye, octaethylporphin-ketone (OEPK), embedded in a plasticized PVC matrix containing a proton transfer agent tetrakis-[3,5-bis(trifluoromethyl) phenyl]borate (TFMPB) [27]. 4 ml of a sensor precursor cocktail containing 2 % w/w PVC, 4 % w/w dioctyl sebacate 3 μM TFMPB and 0.08 mM OEPK in chloroform were prepared and applied in 200 μL aliquots onto 22 × 22 mm pieces of Mylar film, fixed in the sample holder of a spin coater SCS 6800 (Kisco, Indianapolis, USA) rotating at 1000 rpm. The sensor coatings were allowed to dry inside the spin coater (5 s ramp and 55 s spin cycle), and then in an oven (1 h at 60°C). Batches of thus produced disposable planar sensors (10–20 pieces in each batch) were stored in a fridge at 4 °C until further use as solid-state sensors for imaging pHe in tissue samples. A drawing of the chemical structure of OEPK is presented in Figure S1.

In such pH sensors, the ionization mechanism for the OEPK porphyrin dyes involves the addition of two protons to the nitrogen atoms of the tetrapyrrole macrocycle. Thus, the OEPK dye can exist in two spectral forms, the unprotonated free base, and the protonated dication [33,34], which have different spectral and lifetime characteristics. When protons from the sample move into the pH sensor, the balance of the two lifetime components responds to the sample's proton concentration. The two forms are excitable with one light source (a 405 nm laser) and have sharp fluorescence bands at 600–700 nm. Based on a calibration curve of lifetime and pH, the measured sensor lifetime can be converted to its corresponding pH value.

2.2. Design of the FLIM imager and measurement setup

A schematic of the SPAD array FLIM system for imaging live (post-mortem) tissue samples with fluorescence lifetime based planar pH sensors, and a photograph of the system, including an inset image of a

tissue sample covered in the solid-state pH sensor, are shown in Fig. 1.

The FLIM imager consisted of a 405 nm picosecond laser diode with a pulse width of < 300 ps (BDL-405-SMN-F, Becker&Hickl) as an excitation source pulsed at a repetition rate of 20 MHz; and a 1.4 × 1.4 mm time-resolved SPAD array chip with 128 × 120 pixels as the imaging detector. The chip utilizes free-running SPADs along with on-chip time-gated photon counting for each pixel independently to enable widefield FLIM. This detector has been previously used in a range of biomedical and sensing applications [32,35–37]. The optical setup had an epi-fluorescence configuration, the excitation beam was directed towards the samples using a dichroic mirror (Semrock FF506-Di03–25 ×36) and collimated using an achromatic doublet (Thorlabs AC254–100-B-ML, f = 100 mm). The fluorescence emission was collected using the same lens, passed through a long-pass emission filter (>600 nm, Thorlabs FEL0600) to remove the excitation light, and imaged onto the detector using a microscope objective (Nikon LU Plan Fluor 20x).

The imager had a working distance of ~100 mm, and imaged an area of 10 × 10 mm. The imager is controlled using custom MATLAB code via an FPGA board and the data analysis was also carried out using MATLAB. For fluorescence lifetime measurements, photon counts were acquired sequentially over 50 time-bins, each with a width of 390 ps. All measurements were done under dark conditions to minimize noise. A mono-exponential fit was performed for each pixel independently; the range over which fitting was performed was from the first time-bin with less than 90 percent of the peak photon counts to the first time-bin with less than 20 percent.

2.3. Sensor calibration and stability tests

To allow translation from fluorescence lifetime to pH, a set of calibration measurements with a range of pH standard solutions was performed. Solutions of phosphate-buffered saline (PBS) at a range of pH values from 4.5 to 7.5 at intervals of 0.5 were prepared. The disposable pH sensors were placed in contact with the solution. The response time of these sensors has been found previously to be ~1.5 min [27]; therefore, to ensure they had stabilized, the sensors were left in contact with each solution for 3 min before the fluorescence lifetime (FLT) of the sensor was measured using the FLIM imager. This process was carried out using two clean, unused fluorescent sensors. The mean FLT at each pH was then calculated, and a linear fit was performed over a relevant range (5.5 – 7.0 pH).

Calibration measurements with PBS solutions were also repeated with four sensors that had been in contact with *ex vivo* animal tissue; this was done to assess the stability of the sensor response before and after use with tissue samples. Two of these sensors were pre-treated by soaking in fetal bovine serum (FBS) before contact with the tissue samples, while the remaining two did not undergo any pre-treatment. The tissue used for this process was muscle tissue taken from mice immediately following euthanasia; this process is described in more detail below.

2.4. Imaging test with pH standard solutions

For an initial assessment of the sensor's pH imaging capabilities, measurements were performed on a sensor with drops of two pH standard solutions (pH 5.5 and 6.5) placed on the sensor. A drop of each solution was deposited on top of the sensor such that they could be captured in one image by the FLIM imager, with the rest of the sensor remaining dry. The sensor was then allowed to stabilize for 3 minutes before being imaged as described in 2.2. A photograph of the optochemical sensor with drops of pH standard solutions deposited on its surface is shown in Figure S2.

2.5. Culturing of the cells and animal experiments

All animal procedures were performed according to the European Union Directive 2010/63/EU amended by Regulation (EU)2019/1010, as well as the national ethical guidelines of the Health Products Regulatory Authority (HPRA), under project authorization AE19130/I285. Health statuses of all mice were monitored daily for the duration of the experiments. There were no deaths outside humane euthanasia. Mice were humanely euthanized by cervical dislocation after tumors reached a size of 1.5 × 1.5 cm in diameter.

The female Balb/C mice (Envigo, UK) used in the experiments were in good condition, disease free and weighed 16–22 g at 6–8 weeks of age. They were kept in a conventional animal unit at a constant temperature (22℃) with a natural day/night light cycle. Standard laboratory food and water were provided *ad libitum*. Before experiments, the animals were given an adaptation period of at least 7 days.

Murine colorectal carcinoma CT26 cells (the American Collections of Cell Cultures) were maintained in high glucose Dulbecco's Modified Eagle Medium (DMEM) supplemented with 10 % FBS, 2 mM L-glutamine, 100 U/ml penicillin /100 µg/ml streptomycin, and 10 mM 4-(2-hydroxyethyl)-1-piperazineethanesulfonic acid, pH 7.2 (complete DMEM), in a humidified atmosphere of 95 % air and 5 % CO_2 at 37°C.

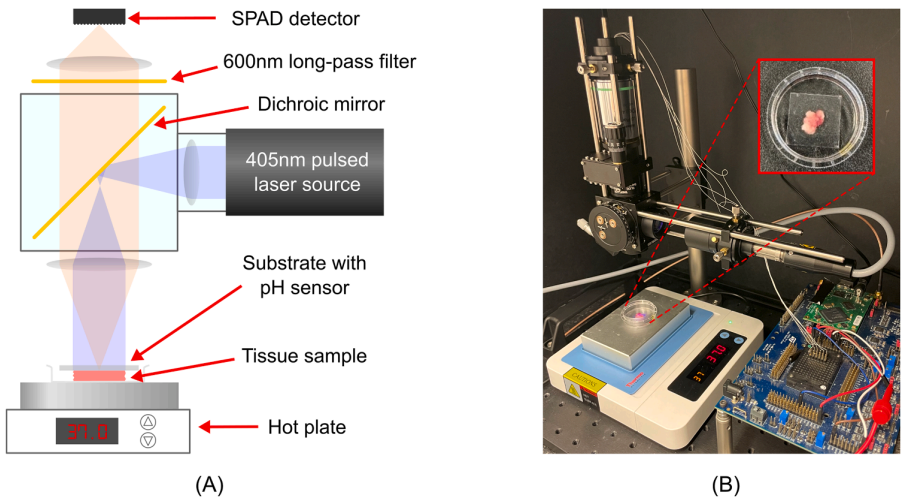


Fig. 1. A schematic of the measurement setup including the wide-field benchtop FLIM imager, the tissue sample in a petri dish covered with the pH sensor and placed on a hot plate for temperature control (A) and a photograph of the measurement setup, including a vertical image of a tissue sample and pH sensor in a petri dish (B).

For tumor induction, minimal tumorigenic doses of CT26 cells (1×10^5 cells in 200 µl of serum-free DMEM) were prepared and injected subcutaneously into the animals, in the right flank. Following injection, the tumors were allowed to grow and develop in the animals, and were monitored daily. Tumor volume was measured and calculated according to the formula: $V = (L \times W^2)/2$, where L is the longest diameter of the tumor (length) and W is the longest diameter perpendicular to diameter L (width).

2.6. Imaging of ex vivo tissue samples

At four defined time points after the injection of CT26 cells (on days 12, 15, 18 and 20), groups of five mice were taken from the animal facility for biological and imaging experiments. The measurement procedure for each animal was as follows. The animal was euthanized by cervical dislocation, tumor tissue was excised immediately, cut across and placed with its cross-section facing up on a standard Petri dish (Sarstedt) on a heated plate (Grant, UK) set at 37 °C. The tissue sample was covered with a planar pH sensor, such that the OEPK sensor coating was in immersion contact with the wet tissue surface, incubated for 3 min to allow T-equilibration, and then fluorescence intensity and lifetime images of the sensor were acquired. This procedure was repeated for each animal in the group.

On day 18 a group of five untreated mice which had not been injected with tumor cells were used for measurements as a control group. In this instance a tissue sample primarily consisting of muscle from the upper leg was excised and measured as described above. The timeline for these measurements is summarized in Fig. 2.

The time between animal euthanasia and the completion of the measurement was approximately 8 minutes, though this was influenced by the time taken to excise the samples. The temperature of the tissue samples was monitored during the imaging sessions with an infrared thermometer DT8803 (Duratool) to confirm that tissue temperature was stable during FLIM measurements. A plot of the sample temperature over time is presented in Figure S3.

Mean fluorescence intensity and lifetime values were calculated for each sample. The mean values from the two tissue types were then compared. The mean sample FLTs were then translated into a mean sample pH value, using the linear equation obtained from the sensor calibration process. A linear regression was then performed for tumor development time and sample pH to investigate the relationship between these two parameters.

3. Results and discussion

3.1. Calibration results and sensor stability

The results of these experiments are summarized in Fig. 3. Fig. 3A shows the FLT distributions of the new, unused sensors at different pH values. From these results, it can be seen that there is a clear change in the sensor FLT with pH over the measured range.

Fig. 3B is a plot of the mean sensor FLT at each pH value; there are three line-plots showing the results for the new sensors, the used sensors which underwent no pre-treatment, and the used sensors which were soaked in FBS solution before use. From these line plots it can be seen that there is very little difference in the mean values obtained in each case. There was also very little change in the width of the lifetime distributions for each calibration which are presented in Figure S4. These results show that the sensor response to pH remained stable before and after direct contact with tissue samples. From this it can be concluded that the sensors perform adequately in biological media and with tissue samples. Hence, the sensors can be used in the trial on a disposable basis and without re-calibration.

By re-plotting the linear part of the calibration for the unused sensors (pH range 5.5 – 7.0), inverting the plot axes (i.e. pHe vs LT) and fitting it with a trendline (Fig. 3C), the following linear calibration equation was obtained

$$\mathrm{pHe} = 0.69\tau + 3.27 \quad (1)$$

where pHe is the extracellular pH of the tissue sample and τ is the FLT in ns ($R^2 = 0.98$). This linear equation allows simple conversion of measured lifetimes of the sensor into pHe values and 2D maps of the imaged tissue samples.

3.2. pH standard solutions imaging

The lifetime image of the sensor with drops of different pH standard solutions was translated to a pH map using Eq. 1; this pH map is shown in Fig. 4 A. The two drops are easily identifiable in the pH maps within the two regions outlined. Region 1 indicates the pH 6.5 drop and has an area of 15.8 mm^2 while region 2 indicates the pH 5.5 drop and has an area of 13.5 mm^2. Histograms for the measured pH in these two regions are shown in Fig. 4B. The mean measured pH for each of the regions are pH 6.56 for region 1 and pH 5.47 for region 2. As with the calibration measurements, there is a distribution of pH values for each drop; the standard deviations are 0.16 for region 1 and 0.06 for region 2. When averaged over the regions of interest the pH has been measured with an error of > 0.1 compared to the true value of the pH standard solutions deposited. This result demonstrates the capability of the sensor to respond to spatial changes in pH, allowing the generation of pH maps when imaged with the widefield FLIM imager.

3.3. Imaging of mouse tumor and muscle tissue samples

As the imager is a widefield system, fluorescent signals from the non-focal planes are not explicitly eliminated or filtered. This configuration is advantageous as it simplifies the imaging process but may also lead to increased noise or interference. The fluorescence lifetime of interest is that of the planar pH sensors, which are positioned at the focal plane of the imager, while, for tissue imaging, the endogenous fluorescence of the mouse tissue samples is the main potential source of interference. To assess the significance of this interference, a preliminary measurement was done of a mouse tumor sample both with and without the pH sensor

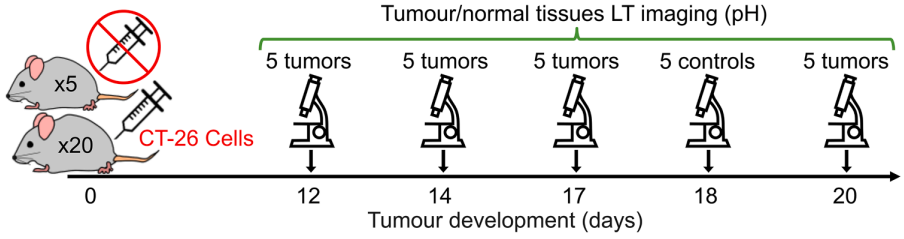


Fig. 2. Scheme of the animal study with sensor-based imaging of pHe in *ex vivo* tissue samples by FLIM. The day of tumor cell injection is referred to as day zero. On days 12, 14, 17, and 20, five mice were euthanized, a tumor sample was excised from each, and analyzed. On day 18 five mice which had not been injected with tumors were euthanized, a muscle tissue sample was excised from each and analyzed as a control group.

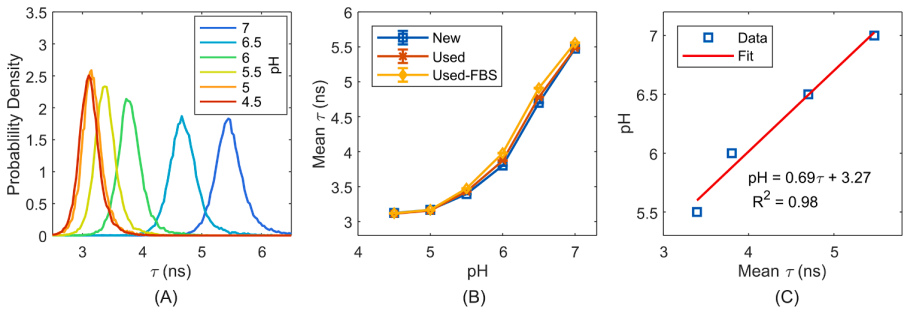


Fig. 3. The fluorescence lifetime distributions of the unused OEPK based planar sensors exposed to the different pH standards (A), and the mean lifetimes from the calibrations of the unused and used disposable sensors in fluorescence lifetime scale, N = 2 for each (B). The linear part of graph (B) with inverted axes and four calibration points (pH 5.5 – 7.0) of the unused sensors fitted with trendline (C). The resulting calibration equation for pHe and R^2 value of the fitting are also shown in (C).

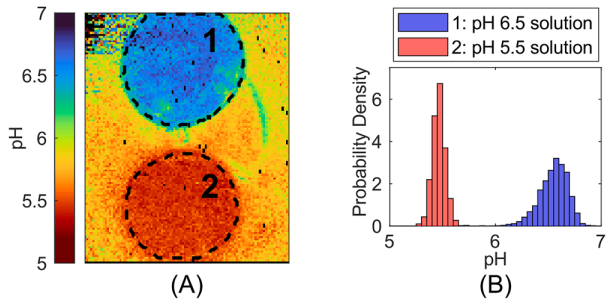


Fig. 4. (A) The pH map of the optochemical sensor with drops of different pH standard solutions deposited. Region 1 indicates the location of the drop with pH 6.5 while region 2 indicates the location of the drop with pH 5.5. Histograms of the two regions are shown in (B). The mean measured pH for region 1 was pH 6.56 and for region 2 was pH 5.47, with a standard deviation of 0.16 and 0.06 respectively. The areas of regions 1 and 2 are 15.8 mm^2 and 13.5 mm^2 respectively.

deposited on top; fluorescence intensity images of this measurement are presented in S5. The fluorescent signal from the sensor was observed to be significantly greater than that of the tissue itself (>50 ×). Therefore, the contribution of the tissue fluorescence was considered negligible, thereby simplifying the measurement procedure and analysis for the main animal study.

As presented in Fig. 2, a total of 25 animals were used in this trial: 5 mice represented a control group, from which normal muscle tissue was taken, while 20 mice were used for the injection of CT26 cancer cells and development of grafted tumors, from which tumor samples were taken and analyzed 12, 14, 17, and 20 days after injection.

In Fig. 5, the fluorescence intensity (5 A and 5B) and lifetime (5D and 5E) images for one muscle sample and one tumor sample are presented as representative examples. Two examples of photon decay curves measured by individual pixels on the SPAD array are presented in Figure S6 along with a plot of the fits obtained, and their residuals. The decay curves presented are from the data used to generate Fig. 5E.

The intensity and lifetime images are cropped to only include the sample under analysis. The black dots on all images correspond to defective SPADs in the array. Such defects are rare and do not prevent the use of these imaging detectors. Pixel line plots along row 76 (indicated by the blue and red dashed lines) for the two intensity images are shown in Fig. 5C and for the two lifetime images in Fig. 5F. The FLT distributions for these two samples are also presented in Fig. 5G. From Figs. 5A and 5B there is a clear pattern that can be seen in both images; this pattern is caused by a non-uniformity in the sensor thickness from the deposition process. This pattern is also observed from the large fluctuations in both line plots in Fig. 5C. There is also no clear difference observed between these two samples based on fluorescence intensity.

Despite this non-uniformity in the sensor fluorescence intensity, the sensor FLT for both samples appear stable across the sample area; this also indicates there are no significant pH gradients observed within

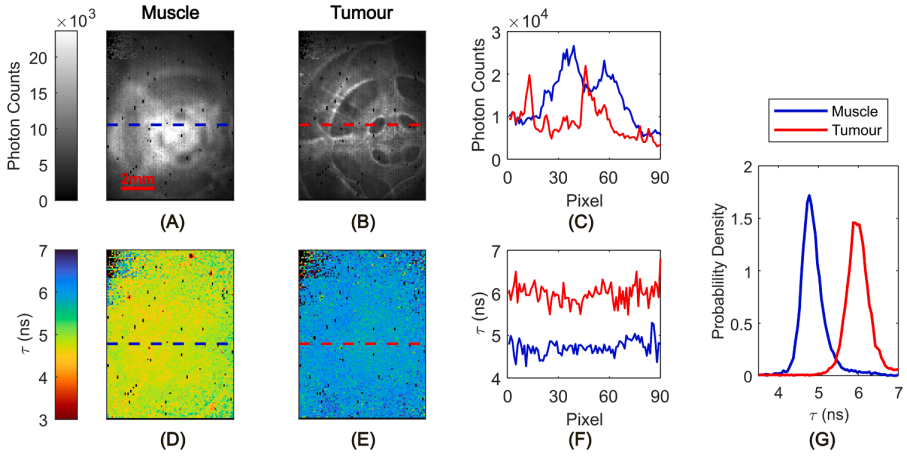


Fig. 5. Example fluorescence intensity (A and B) and lifetime (D and E) images of a control muscle tissue sample and a tumor sample taken on day 14. Cross-section plots along pixel row 76 for both the samples' intensity and lifetime images (as indicated with the blue and red dashed lines) are also presented (C and F) along with the lifetime distributions for both samples (G).

these two samples. However, while the FLT is stable within each sample, there is a clear difference between the two samples. This is seen immediately from the FLT images in Figs. 5D and 5E, and is confirmed by the consistent difference between the two line plots in Fig. 5F and the FLT distributions shown in Fig. 5G. The mean FLT for these two samples was 4.83 ± 0.01 ns (95 % confidence interval of the mean) for the muscle sample and 5.85 ± 0.01 ns for the tumor sample with a standard deviation of 0.46 ns and 0.58 ns respectively. Using the calibration equation obtained previously, this translates to a mean pHe value of 6.62 ± 0.01 and 7.36 ± 0.01 for the muscle and tumor samples respectively.

Across all samples, there were no significant pH gradients observed. This is likely due to the high homogeneity of each individual sample. During the excision of the muscle samples, effort was made to use only muscle tissue to maintain consistency. For the tumor samples, these tended to grow in a self-contained manner, subcutaneously; therefore, there was no mixing of tumor and healthy tissue or boundary regions in the samples imaged in this study. In addition, none of the tumor samples were observed to contain necrotic regions. The ethical approval for this study prevented tumors from being developed for longer, but it is possible that longer tumor development times would lead to the development of necrotic regions within the samples, and therefore a more heterogeneous pHe profile. For future work, it would be of interest to image such heterogeneous samples with this platform to test if the observation of significant pH gradients within such samples is possible.

3.4. Comparison of muscle and tumor samples

A one-way ANOVA test was applied to compare the mean fluorescence intensities and lifetimes for all 25 samples based on sample type. A statistically significant difference was found in both cases ($p = 0.04$ and $p < 0.001$ for the fluorescence intensities and lifetimes respectively). The mean sensor fluorescence lifetime was 5.60 ± 0.08 ns for the tumor samples and 5.07 ± 0.20 ns for the muscle samples from the control mice. By applying the calibration equation, this translates to a mean pH value of 7.17 ± 0.06 for the tumor samples and 6.78 ± 0.15 for the muscle samples. Box plots of the mean sensor fluorescence intensities and lifetimes are presented in Fig. 6.

While there is a statistically significant difference observed in both intensity and lifetime, the differentiation between the mean lifetimes for the two sample types is much clearer in the FLT measurements, as can be seen by the much smaller p value which is obtained. Therefore, the measurement system has successfully differentiated the tumor and muscle samples.

3.5. Longitudinal tumor pH measurements

Imaging the tumor tissue samples having different sizes and ages (days 12, 15, 17, 20) revealed only minor differences in their lifetimes. The tumor volume increased significantly over the measurement period; the mean tumor volume for each measurement day is plotted in Figure S7. A scatter plot of each sample's mean pH against the tumor age in days along with a trendline for this data is presented in Fig. 7. The trendline included has an R^2 value of 0.25 and a Pearson correlation coefficient calculated as −0.50. Mean pHe values on days 12 and 14 were 7.25 ± 0.12 and 7.3 ± 0.12, while on days 17 and 20 the mean pHe values were 7.15 ± 0.12 and 7.14 ± 0.12 respectively.

This result reveals a slight decrease in the mean lifetimes towards the end of tumor growth period although the R^2 and Pearson correlation coefficient values indicate a moderate negative correlation between tumor age and pHe. There is significant variation between the different samples measured on each day, so the lack of a strong correlation is not surprising. It is also important to consider that there are only five samples for each date. As mentioned above, the ethical approval for the study prevented the development of tumors for longer, a repeated study with an increased number of samples over longer tumor development times would help to further investigate the relationship between tumor age and pHe.

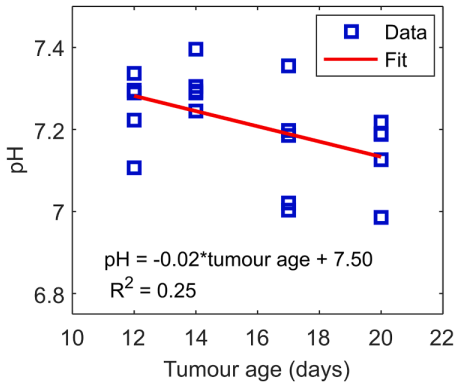


Fig. 7. A scatter plot of the tumor pH against the number of days after tumor injection for all tumor samples measured in the study. The resulting equation and trendline from a linear fit are also presented, indicating a moderate negative correlation between tumor pH and age.

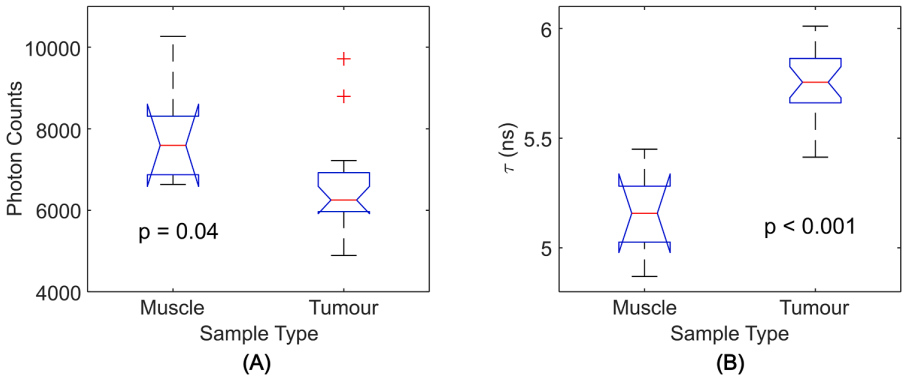


Fig. 6. Box plots of the mean fluorescence intensities (A) and lifetimes (B) for the muscle and tumor samples. On each box, the central red line indicates the median and the bottom and top edges of the box indicate the 25th and 75th percentiles, respectively. The notches on each box indicate the 95 % confidence interval of the median, and outliers are plotted individually with red markers. There was a significant difference found between the mean intensities ($p = 0.04$) and the mean lifetimes ($p < 0.001$) for the different sample types.

3.6. Comparison with literature data on tissue pH measurements

Surprisingly, the pHe values produced for the normal muscle tissue samples were consistently lower than those of the tumor tissue. This is seen from the example samples shown in Fig. 4 and is shown to be persistent across the samples as a whole when the lifetime measurements for all tumor and muscle samples are aggregated as shown in Fig. 5. Thus, the pHe values produced in this study differ significantly from those produced by the other methods and are widely accepted by clinicians [24] (~7.3 in normal tissues and 7.0–6.5 in various tumors).

Such discrepancies in pHe values may be explained by i) the highly invasive procedure of tissue excision and preparation: cutting tumor across may release the more alkaline intracellular fluid which then mixes with extracellular and shifts the measured pHe; ii) normal muscle tissue being an inadequate control, or iii) a real lack of acidification in grafted tumors produced by CT26 cells. However, another plausible physiological explanation is the fact that the measurements were performed *ex vivo*. For *in vivo* settings [38,39], tissue is perfused with blood which constantly supplies key nutrients, particularly glucose and O_2, and removes biological waste such as CO_2 and lactate, so natural homeostatic conditions are preserved. In contrast, in our *ex vivo* settings, the animals were sacrificed, and post-mortem tissue samples were dissected and then analyzed. Such tissue samples lack natural perfusion and metabolic homeostasis and, while cells are still alive, consume the available nutrients and accumulate waste. The pH of blood samples from humans, rats and pigs have previously been found to decrease significantly post-mortem [40]. While tumor tissue is hypoxic and metabolically more active, normal tissue has higher O_2 and glucose capacity. Therefore, after cutting off the glucose and O_2 supply from the blood, normal tissue can produce more lactate and H^+, and thus become more acidic than the tumor tissue. In our view, such physiological theory can explain the 'inversion' of the extracellular pH values for the grafted tumors derived from CT26 cells and normal muscle tissue samples, when analyzed under *ex vivo* settings. This effect is compatible with what is observed *in vivo* - acidosis in tumors, due to increased anaerobic respiration of their cells. Further investigation is required to fully understand the cause of the pH differences observed here.

Nevertheless, all this does not undermine the high analytical performance and practical utility of the FLIM based planar pH sensors and the SPAD array based FLIM platform. They are well-suited for *in vivo* use, particularly for fluorescence guided surgery [41,42] of live animal models (and potentially humans), in which the sensor and the imager can aid to visualize the borderline between malignant tumor and normal tissue. And combined with parallel measurements of tissue pHe with a pH microelectrode, the FLIM platform can help to answer the important questions on cancer tissue physiology that are formulated above. However, such experiments are outside the scope of the current study, being the subject of a separate investigation.

4. Conclusions

Fluorescence-lifetime based planar solid-state optochemical pH sensors based on OEPK dye have been applied for *ex vivo* analysis of extracellular pH in mammalian tumors. The sensors were calibrated over the range of relevant pH values using buffer solutions. The sensor response to the different pH buffer solutions was found to be stable before and after prolonged contact with tissue samples. This was the case both with and without pre-treatment with FBS solution. Therefore, there is no need for re-calibration of the sensors post tissue contact.

Tumor samples, freshly excised from animals and imaged on a FLIM imager with a SPAD array detector, were found to have a higher pH after excision than muscle tissue samples. This is thought to be caused by the invasive tissue preparation procedure and higher levels of glucose in normal muscle tissue at the time of excision which in turn lead to the production of higher quantities of lactate once the tissue oxygen supply is removed.

No gradients in the pH distribution across tumor samples were observed. This is primarily due to the homogeneity of the tissue samples used in this study. The measurement of different pH standard solutions presented here demonstrates the ability of the sensor to respond to spatial change in pH and generate a pH map. Future work could include the analysis of tissue samples containing different tissue types together (tumor, healthy tissue and a boundary region) to investigate if these regions can be resolved spatially with a measurement system similar to the one described here.

The observation of tumors over time has shown a moderate negative correlation between tumor pH and age but with significant variation between the samples on each day. A future study with increased sample numbers over a longer time would be required to investigate this relationship further.

CRediT authorship contribution statement

Devoy Ciaran: Writing – original draft, Resources, Investigation. **Matheson Andrew B:** Writing – review & editing, Software, Resources. **Erdogan Ahmet T:** Writing – review & editing, Software, Resources. **Tangney Mark:** Supervision, Resources, Funding acquisition. **Henderson Robert K:** Supervision, Resources, Funding acquisition. **Papkovsky Dmitri B:** Writing – review & editing, Writing – original draft, Supervision, Resources, Project administration, Methodology, Funding acquisition, Conceptualization. **Andersson-Engels Stefan:** Writing – review & editing, Supervision, Funding acquisition, Conceptualization. **Konugolu Sanathana:** Writing – review & editing, Writing – original draft, Supervision, Project administration, Methodology, Conceptualization. **Angelone Dario:** Writing – review & editing, Writing – original draft, Visualization, Software, Methodology, Investigation, Formal analysis, Data curation, Conceptualization. **Li Liang:** Writing – review & editing, Writing – original draft, Visualization, Resources, Methodology, Investigation, Conceptualization.

Declaration of Competing Interest

The authors declare that they have no known competing financial interests or personal relationships that could have appeared to influence the work reported in this paper.

Acknowledgements

We gratefully acknowledge funding from the EU H2020 MSCA-ITN project "Photonics for Healthcare: multiscale cancer diagnosis and therapy" (PHAST-ETN), grant agreement no. 86018; Taighde Éireann – Research Ireland (22/RP-2TF/10293, 15/RP/2828 and 12/RC/2276 P2); Breakthrough Cancer Research (Precision Oncology Ireland); and the PROTEUS project (http://proteus.ac.uk), Grant no: EP/K03197X/1. For the purpose of Open Access, the authors have applied a CC BY public copyright licence to any Author Accepted Manuscript version arising from this submission.

Appendix A. Supporting information

Supplementary data associated with this article can be found in the online version at doi:10.1016/j.snb.2025.137441.

Data availability

All of the data and code for analysis used for this manuscript are publicly available on Zenodo (10.5281/zenodo.14024766).

References

[1] R. Chaudhry, M. Varacallo, Treasure Island (FL). PMID. Biochemistry, Glycolysis, StatPearls Publishing, 2023, 29493928.

[2] D.L. Nelsen, M.M. Cox, Lehninger principles of biochemistry, Macmillan Learning, 2021. ISBN:9781319322342.
[3] D.B. Papkovsky, A.V. Zhdanov, Cell energy budget platform for multiparametric assessment of cell and tissue metabolism. Mitochondrial Medicine: Volume 2: Assessing Mitochondria, Springer, 2021, pp. 305–324.
[4] B. Alberts, et al., Essential cell biology, Garland Science, 2015. ISBN: 9781315815015.
[5] G. Soto-Heredero, et al., Glycolysis a key player in the inflammatory response, FEBS J. 287 (16) (2020) 3350–3369, https://doi.org/10.1111/febs.15327.
[6] S. Paul, S. Ghosh, S. Kumar, Tumor glycolysis, an essential sweet tooth of tumor cells, Semin. Cancer Biol. 86 (2022) 1216–1230, https://doi.org/10.1016/j.semcancer.2022.09.007.
[7] I. Martínez-Reyes, N.S. Chandel, Mitochondrial TCA cycle metabolites control physiology and disease, Nat. Commun. 11 (1) (2020) 102.2, https://doi.org/10.1038/s41467-019-13668-3.
[8] C.A. Schmidt, K.H. Fisher-Wellman, P.D. Neufer, From OCR and ECAR to energy: Perspectives on the design and interpretation of bioenergetics studies, J. Biol. Chem. 297 (4) (2021), https://doi.org/10.1016/j.jbc.2021.101140.
[9] W. Ji, et al., Optical/electrochemical methods for detecting mitochondrial energy metabolism, Chem. Soc. Rev. 51 (1) (2022) 71–127, https://doi.org/10.1039/D0CS01610A.
[10] D.A. Ferrick, A. Neilson, C. Beeson, Advances in measuring cellular bioenergetics using extracellular flux, Drug Discov. Today 13 (5-6) (2008) 268–274, https://doi.org/10.1016/j.drudis.2007.12.008.
[11] D.B. Papkovsky, Optochemical sensor-based systems for the analysis of cell metabolism and bioenergetics: an overview, Opt. Sens. 2023 12572 (2023) 90–95, https://doi.org/10.1117/12.2669076.
[12] X. Sun, et al., Tumor hypoxia imaging, Mol. Imaging Biol. 13 (2011) 399–410, https://doi.org/10.1007/s11307-010-0420-z.
[13] X.-d Wang, O.S. Wolfbeis, Optical methods for sensing and imaging oxygen: materials, spectroscopies and applications, Chem. Soc. Rev. 43 (10) (2014) 3666–3761, https://doi.org/10.1039/C4CS00039K.
[14] A. Steinegger, O.S. Wolfbeis, S.M. Borisov, Optical sensing and imaging of pH values: Spectroscopies, materials, and applications, Chem. Rev. 120 (22) (2020) 12357–12489, https://doi.org/10.1021/acs.chemrev.0c00451.
[15] Wilson, D.F., et al., Oxygen distributions in tissue measured by phosphorescence quenching. Oxygen Transport To Tissue XXIII: Oxygen Measurements in the 21st Century: Basic Techniques and Clinical Relevance, 2003: p. 181-185..
[16] S. Sakadžić, et al., Two-photon high-resolution measurement of partial pressure of oxygen in cerebral vasculature and tissue, Nat. Methods 7 (9) (2010) 755–759.
[17] Esipova, T.V., et al., Oxyphor 2P: a high-performance probe for deep-tissue longitudinal oxygen imaging. Cell Metabolism, 2019. 29(3): p. 736-744. e7. DOI: 10.1038/nmeth.1490.
[18] A.V. Zhdanov, et al., Analysis of tumour oxygenation in model animals on a phosphorescence lifetime based macro-imager, Sci. Rep. 13 (1) (2023) 18732, https://doi.org/10.1038/s41598-023-46224-7.
[19] P. Babilas, et al., In Vivo Phosphorescence Imaging of p O 2 Using Planar Oxygen Sensors, Microcirculation 12 (6) (2005) 477–487, https://doi.org/10.1080/10739680591003314.
[20] R.I. Dmitriev, D.B. Papkovsky, Optical probes and techniques for O 2 measurement in live cells and tissue, Cell. Mol. life Sci. 69 (2012) 2025–2039. DOI 10.1007/s00018-011-0914-0.
[21] R.A. Gatenby, R.J. Gillies, Why do cancers have high aerobic glycolysis? Nat. Rev. Cancer 4 (11) (2004) 891–899. DOI:10.1038/nrc1478.
[22] X. Zhang, Y. Lin, R.J. Gillies, Tumor pH and its measurement, J. Nucl. Med. 51 (8) (2010) 1167–1170, https://doi.org/10.2967/jnumed.109.068981.
[23] O. Warburg, On the origin of cancer cells, Science 123 (3191) (1956) 309–314, https://doi.org/10.1126/science.123.3191.309.
[24] A. Anemone, et al., Imaging tumor acidosis: a survey of the available techniques for mapping in vivo tumor pH, Cancer Metastas-.-. Rev. 38 (2019) 25–49, https://doi.org/10.1007/s10555-019-09782-9.
[25] A. Anemone, et al., Tumour acidosis evaluated in vivo by MRI-CEST pH imaging reveals breast cancer metastatic potential, Br. J. Cancer 124 (1) (2021) 207–216, https://doi.org/10.1038/s41416-020-01173-0.
[26] S. Rodimova, et al., Mapping metabolism of liver tissue using two-photon FLIM, Biomed. Opt. Express 11 (8) (2020) 4458–4470, https://doi.org/10.1364/BOE.398020.
[27] L. Li, A.V. Zhdanov, D.B. Papkovsky, Advanced multimodal solid-state optochemical pH and dual pH/O2 sensors for cell analysis, Sens. Actuators B: Chem. 371 (2022) 132486, https://doi.org/10.1016/j.snb.2022.132486.
[28] L.M. Hirvonen, et al., Photon counting phosphorescence lifetime imaging with TimepixCam, Rev. Sci. Instrum. 88 (1) (2017), https://doi.org/10.1063/1.4973717.
[29] R. Sen, et al., New luminescence lifetime macro-imager based on a Tpx3Cam optical camera, Biomed. Opt. Express 11 (1) (2020) 77–88, https://doi.org/10.1364/BOE.11.000077.
[30] I. Cusini, et al., Historical perspectives, state of art and research trends of SPAD arrays and their applications (Part II: SPAD arrays), Front. Phys. 10 (2022) 906671, https://doi.org/10.3389/fphy.2022.906671.
[31] I. Gyongy, et al., A $256\times256 $, 100-kfps, 61% fill-factor SPAD image sensor for time-resolved microscopy applications, IEEE Trans. Electron Devices 65 (2) (2017) 547–554, https://doi.org/10.1109/TED.2017.2779790.
[32] A.T. Erdogan, et al., A high dynamic range 128 × 120 3-D stacked CMOS SPAD image sensor SoC for fluorescence microendoscopy, IEEE J. Solid-State Circuits 57 (6) (2022) 1649–1660, https://doi.org/10.1109/JSSC.2022.3150721.
[33] D.B. Papkovsky, G.V. Ponomarev, O.S. Wolfbeis, Protonation of porphyrins in liquid PVC membranes: effects of anionic additives and application to pH-sensing, J. Photochem. Photobiol. A: Chem. 104 (1) (1997) 151–158, https://doi.org/10.1016/S1010-6030(97)04592-9.
[34] D.B. Papkovsky, G.V. Ponomarev, O.S. Wolfbeis, Longwave luminescent porphyrin probes, Spectrochim. Acta Part A: Mol. Biomol. Spectrosc. 52 (12) (1996) 1629–1638, https://doi.org/10.1016/0584-8539(96)01731-X.
[35] A.B. Matheson, et al., Fluoresc. Lifetime Imaging Explos. Detect. 48 (22) (2023) 6015–6018, https://doi.org/10.1364/OL.498123.
[36] A.B. Matheson, et al., Handheld wide-field fluorescence lifetime imaging system based on a distally mounted spad array, Opt. Express 31 (14) (2023) 22766–22775, https://doi.org/10.1364/OE.482273.
[37] A.B. Matheson, et al., Fluorescence lifetime imaging with distance and ranging using a miniaturised SPAD system, Sci. Rep. 14 (1) (2024) 13285, https://doi.org/10.1038/s41598-024-63409-w.
[38] S.R. Pillai, et al., Causes, consequences, and therapy of tumors acidosis, Cancer Metastas-.-. Rev. 38 (2019) 205–222, https://doi.org/10.1007/s10555-019-09792-7.
[39] A. Ibrahim-Hashim, V. Estrella, Acidosis and cancer: from mechanism to neutralization, Cancer Metastas-.-. Rev. 38 (2019) 149–155, https://doi.org/10.1007/s10555-019-09787-4.
[40] A.E. Donaldson, I.L. Lamont, Biochemistry changes that occur after death: potential markers for determining post-mortem interval, PloS One 8 (11) (2013) e82011, https://doi.org/10.1371/journal.pone.0082011.
[41] P.A. Sutton, et al., Fluorescence-guided surgery: comprehensive review, BJS Open 7 (3) (2023), https://doi.org/10.1093/bjsopen/zrad049.
[42] F.J. Voskuil, et al., Exploiting metabolic acidosis in solid cancers using a tumor-agnostic pH-activatable nanoprobe for fluorescence-guided surgery, Nat. Commun. 11 (1) (2020) 3257, https://doi.org/10.1038/s41467-020-16814-4.

Dario Angelone is a PhD student in the Biophotonics group at Tyndall National Institute, Cork, Ireland. His current work focuses on Fluorescence Lifetime Imaging (FLIM) for biomedical applications and is part of the PHAST project funded by the EU under the Horizon 2020 programme. Dario received his bachelor's degree in Physics from the University of Aberdeen before being awarded an Erasmus Mundus scholarship for the European Joint Master's Degree in Smart Systems Integration, carried out at Heriot-Watt University Edinburgh, the University of South-Eastern Norway, and the Budapest University of Technology and Economics.

Liang Li graduated from Jinan University, Guangzhou, in 2017 and obtained his Ph.D. in Biochemistry & Cell Biology in 2024 from University College Cork. His research interest includes optical chemical pH/O_2 sensing and their biological applications, living cells imaging, and cellular bioenergetics analysis.

Ciaran Devoy graduated from University College Cork with BScs in Zoology, Genetics, an MSc in Molecular Cell Biology, and a PhD in Cancer Research. Ciarán is a postdoctoral researcher working with Professor Mark Tangney in the Microbes and Cancer group in Cancer Research @UCC. His research is focused on how the microbiome affects treatment outcomes in cancer patients.

Andrew B. Matheson graduated with an MPhys from the University of Edinburgh, before receiving a PhD from the University of St. Andrews. Following this, he has worked on a range of topics at the University of Edinburgh and Heriot Watt University, mostly related to the use of spectroscopy and imaging to better understand soft matter and biological systems. His current work is on the development of optical instrumentation for trace gas monitoring.

Ahmet T. Erdogan received the B.Sc. degree in electronics engineering from Dokuz Eylul University, Izmir, Turkey, in 1990, and the M.Sc. and Ph.D. degrees in electronics engineering from Cardiff University, Cardiff, U.K., in 1995 and 1999, respectively. Since 1999, he has been working on several research projects at The University of Edinburgh, Edinburgh, U.K., where he is currently a Research Associate with the CMOS Sensors and Systems Group, School of Engineering. His research interests include low-power VLSI design, reconfigurable computing, and CMOS image sensors.

Robert K. Henderson received his Ph.D. in electronics and electrical engineering from the University of Glasgow, Glasgow, U.K., in 1990. From 1991–1996, he was a Research Engineer with the Swiss Centre for Microelectronics, Neuchâtel, Switzerland. In 1996, he was appointed as a Senior VLSI Engineer at VLSI Vision Ltd., Edinburgh, U.K., where he worked on world's first single-chip video camera. From 2000–2005, as a Principal VLSI Engineer with the Imaging Division, STMicroelectronics, Edinburgh, he developed image sensors for mobile phone applications. In 2005, he joined The University of Edinburgh, Edinburgh, designing the first single-photon avalanche diode image sensors in nanometer CMOS technologies in MegaFrame and SPADnet EU projects. He is currently a Professor with the School of Engineering, The University of Edinburgh. Dr. Henderson was awarded the prestigious ERC Advanced Fellowship in 2014.

Mark Tangney is Professor in Education for Enterprise at UCC, a Principal Investigator at Cancer Research @UCC, Funded Investigator at APC Microbiome Ireland, and Head of the iEd Hub. Mark has previously worked at various international institutions (Los Angeles, Boston, Copenhagen) and published extensively in the fields of cancer, gene & cell therapy and microbiology. Mark's interests include associations between bacteria and cancer, development of microbes as cancer therapeutics and diagnostics; Synthetic Biology; and

entrepreneurship. Mark serves as a member of the editorial board of several international journals.

Dmitri B. Papkovsky graduated from the Chemistry Department of Moscow State University in 1982 and received his Ph.D. in 1986 from the Institute of Biochemistry, Russian Academy of Science, Moscow. In 1997 he joined Biochemistry Department of University College Cork, where he is currently Professor at the School of Biochemistry and Cell Biology, Head of Biophysics and Bioanalysis Lab. Research interests of Prof. Papkovsky include quenched-luminescence oxygen sensing and its applications, new fluorescence and phosphorescence based probes and (bio)analytical techniques.

Stefan Andersson-Engels is head of Biophotonics at IPIC (Irish Photonic Integration Ctr.) since 2016. He graduated in Engineering Physics from Lund University in 1985, and received his PhD in Physics from Lund University in 1990. He was then a postdoc at McMaster University in Ontario, Canada, from 1990 to 1991. After a few years as lecturer he was appointed professor in 1999 at Lund University. He has published extensively in the area of biomedical optics. His main interest is optical spectroscopy and photodynamic therapy, while he also is active in improving the understanding in fundamental aspects of light propagation in turbid media. He is a senior advisory editor for the Journal of Biomedical Optics.

Sanathana Konugolu Venkata Sekar is a leading scientist and entrepreneur with over a decade of experience in biophotonics. He serves as the Biomedical Theme Coordinator at IPIC, overseeing research conducted by a multidisciplinary team of nine principal investigators and more than 25 PhD students and postdoctoral researchers. He is also an Associate Professor (Senior Lecturer B) at the School of Physics, University College Cork, and a distinguished recipient of the prestigious European Research Council (ERC) award. He leads the Integrated Fast Biophotonics Group at Tyndall, where he co-supervises a team of eight PhD students and two postdoctoral researchers. Additionally, he co-founded BioPixS Ltd, a spinoff based on his research. His key areas of interest include phantoms and standardization, time-domain diffuse optics, pulse oximeters, FLIM, endoscopes, multimodal microscopy, and probes. His vision is to translate cutting-edge photonics into miniaturized solutions for healthcare applications.

Paper II

Time resolved SPAD micro-camera probe for wide-field FLIm in microendoscopy

Dario Angelone, Sanathana Konugolu Venkata Sekar, Walter Messina, Andrew B. Matheson, Ahmet T. Erdogan, Robert K. Henderson, Ray Burke, and Stefan Andersson-Engels.

Proc. SPIE 12368, Advanced Biomedical and Clinical Diagnostic and Surgical Guidance Systems XXI **1236807**, (2023).

Time resolved SPAD micro-camera probe for wide-field FLIm in microendoscopy

Dario Angelone[a], Sanathana Konugolu Venkata Sekar[a], Walter Messina[a], Andrew B. Matheson[b], Ahmet T. Erdogan[b], Robert K. Henderson[b], Ray Burke[a], and Stefan Andersson-Engels[a,c]

[a]Biophotonics@Tyndall, IPIC, Tyndall National Institute, University College Cork, Cork, Ireland
[b]School of Engineering, Institute of Integrated Micro and Nano Systems, The University of Edinburgh, Edinburgh, United Kingdom
[c]Department of Physics, University College Cork, Cork, Ireland

ABSTRACT

We propose a handheld single photon avalanche diode (SPAD) micro-camera probe for wide-field *in-vivo* fluorescence lifetime imaging (FLIm) applications. The presented probe includes a novel 3D stacked 1.4 mm × 1.4 mm SPAD array, an integrated excitation light source, and imaging optics. The spatial and temporal performance of the integrated system was characterised using a USAF test target and range of fluorescence lifetime beads.

Keywords: fluorescence lifetime imaging, FLIm, SPAD, micro-camera

1. INTRODUCTION

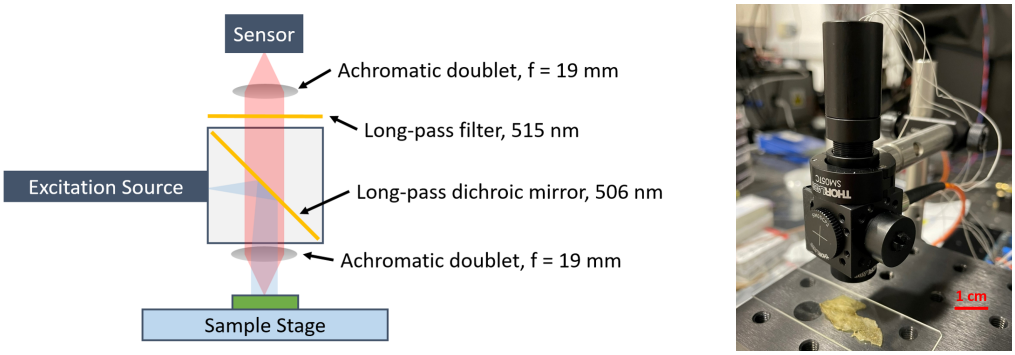
Recently, FLIm has proved to be an effective method for label-free intraoperative tumour margin assessment both *ex vivo*[1,2] and *in vivo*.[3] *In vivo* FLIm probes typically employ point scanning to recover lifetime images and thus far, there are few examples of wide-field *in vivo* FLIm and even fewer where sensing occurs at the distal end of the probe.[4,5] Wide-field *in vivo* FLIm would have the benefit of capturing lifetime information from the entire field of view at the same time. Developments in the miniaturisation of SPAD arrays with time resolving capability make their use in wide-field *in vivo* FLIm feasible. Here a probe using a miniaturised SPAD array with half-inch diameter optics and an integrated excitation source is presented. The system is characterised in terms of spatial resolution and temporal performance.

2. MATERIALS AND METHODS

The probe design uses an epi-illumination scheme as illustrated in Fig. 1a with the excitation light coupled into an optical fibre which is connected to the probe. A long-pass dichroic mirror and filter (Semrock FF506-DI03-25X36 and FF01-515/LP-25) are used to direct the excitation light towards the sample and filter out elastically scattered light, respectively. Two achromatic doublets with f =19 mm are used, one to collect the light from the sample, the second to re-focus it onto the sensor. The sensor for the probe is a 128 × 120 SPAD array with dimensions of 1.4 mm × 1.4 mm implemented in STMicroelectronics 40 nm/90 nm 3D-stacked BSI CMOS process with 8 µm pixels and a 45% fill factor. This sensor is described in detail by Erdogan et al.,[6] in which its *ex vivo* FLIm capability with biological samples was demonstrated using a 10X objective mounted on a fluorescence microscope system.

The spatial resolution was quantified by imaging a USAF resolution target. The temporal system performance was evaluated by measuring the instrument response function (IRF) and through measurements of lifetime-encoded fluorescent polymer beads (PolyAn GmbH). The beads were measured suspended in a solution in a well plate; therefore there was no spatial variation in lifetime to be resolved so all pixel values were binned for the fitting process. Intensity and lifetime images of a plant sample were also captured. Lifetime fitting was carried

Further author information: Send correspondence to Dario Angelone (dario.angelone@tyndall.ie)



(a) (b)

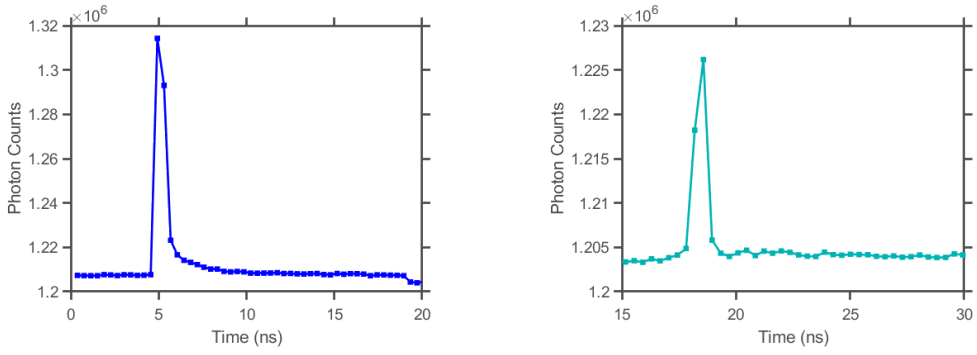
Figure 1: A basic schematic (a) and a photograph (b) of the miniaturised wide-field FLIm microscope.

out using eight time bins with a width of 390 ps each. The fluorescent beads were excited at 488 nm using a Fianium SC450 supercontinuum source and a monochromator and the plant sample was excited at 405 nm using a Becker and Hickl pulsed laser diode. Both sources were operated at a repetition rate of 20 MHz. The IRF was measured with both sources by placing a non-fluorescent white standard in the sample plane.

3. RESULTS

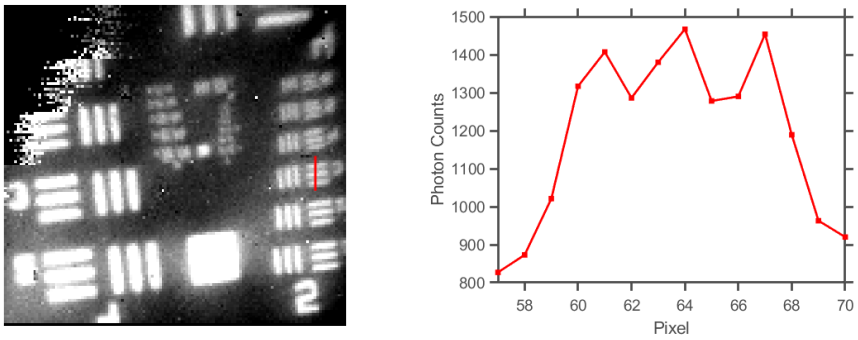
The IRF at 405 nm and 488 nm are show in Fig. 2 and are found to have a full width half maximum (FWHM) of 0.74 ns and 0.62 ns, respectively. An intensity image of a USAF resolution target captured with white light illumination is shown in Fig. 3a. The smallest resolved feature is Group 5 element 3 which has a line width of 12.4 µm; the pixels along this element are indicated by the red line in Fig. 3a and the pixel values are plotted in Fig. 3b. A race condition between pixel read and reset signals has caused a corner of the array to be insensitive to light[6] as can be seen in Fig. 3a; the images presented in Fig. 5 have been cropped to exclude this area.

The fluorescence decay curves from the lifetime-encoded bead measurements are presented in Fig. 4 with the quoted and measured lifetimes indicated in the legend. The different types of beads are clearly differentiated though there is a slight underestimation of the lifetime compared to the quoted value. Intensity and lifetime images of a leaf sample are shown in Fig. 5 demonstrating the capability of the miniaturised microscope to capture wide-field lifetime images of autofluorescence from biological samples.



(a) (b)

Figure 2: IRF measured with a 405 nm Becker and Hickl pulsed diode laser (a) and a Fianium supercontinuum laser at 488nm (b) found to have a FWHM of 0.74 ns and 0.62 ns, respectively.



(a) (b)

Figure 3: (a) Intensity image of a USAF resolution target captured with white light illumination to characterise the system imaging performance. (b) Plot of pixel values along the red line indicated in the intensity image left. Group 5 element 3 on the resolution target has been resolved and has a line width of 12.4 µm.

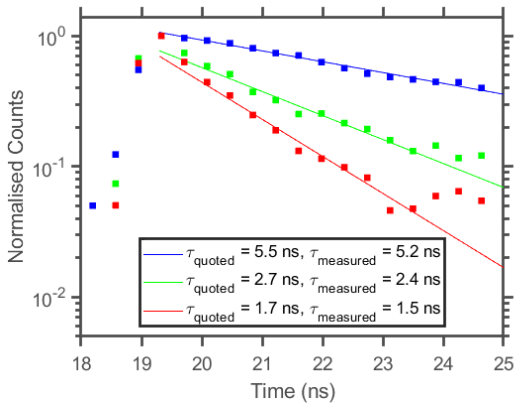
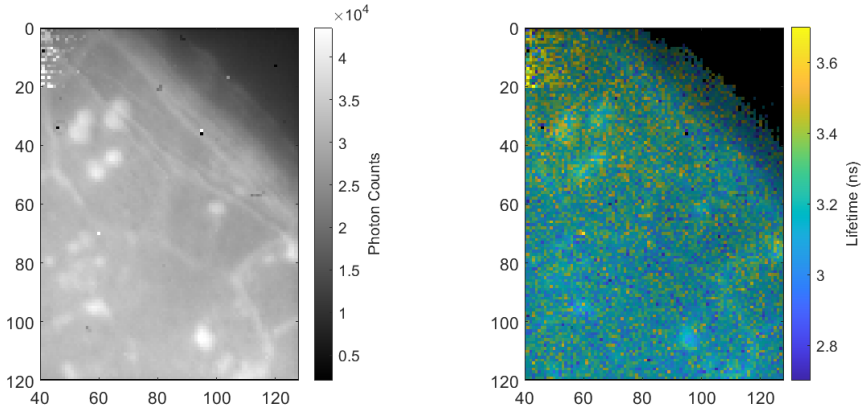


Figure 4: Scatter plot of the measured fluorescence decay for the different lifetime encoded beads with the fit indicated by the line plots. Fitting for all beads was carried out using 8 time bins with a width of 390 ps each.



(a) (b)

Figure 5: Fluorescence intensity (a) and lifetime (b) images of a leaf sample captured with excitation at 405 nm.

4. CONCLUSION

A handheld SPAD micro-camera probe for wide-field *in-vivo* FLIm applications including a novel 3D stacked 1.4 mm × 1.4 mm SPAD array, an integrated excitation light source, and imaging optics has been presented. The presented probe has a spatial resolution of 12.4 µm and has been shown to successfully differentiate polymer bead samples with a range of fluorescence lifetimes. An intensity and lifetime image of a plant sample has also been presented.

ACKNOWLEDGMENTS

We gratefully acknowledge funding from the EU H2020 MSCA-ITN project "Photonics for Healthcare: multiscale cancer diagnosis and therapy" (PHAST-ETN), grant agreement no. 86018; Science Foundation Ireland (SFI/15/RP/2828 and SFI-12/RC/2276_P2); and the PROTEUS project (http://proteus.ac.uk), Grant no: EP/K03197X/1.

REFERENCES

[1] Duran-Sierra, E., Cheng, S., Cuenca-Martinez, R., Malik, B., Maitland, K. C., Cheng, Y. S. L., Wright, J., Ahmed, B., Ji, J., Martinez, M., Al-Khalil, M., Al-Enazi, H., and Jo, J. A., "Clinical label-free biochemical and metabolic fluorescence lifetime endoscopic imaging of precancerous and cancerous oral lesions," *Oral Oncology* **105**, 104635 (6 2020).

[2] Wang, M., Tang, F., Pan, X., Yao, L., Wang, X., Jing, Y., Ma, J., Wang, G., and Mi, L., "Rapid diagnosis and intraoperative margin assessment of human lung cancer with fluorescence lifetime imaging microscopy," *BBA Clinical* **8**, 7–13 (12 2017).

[3] Weyers, B. W., Marsden, M., Sun, T., Bec, J., Bewley, A. F., Gandour-Edwards, R. F., Moore, M. G., Farwell, D. G., and Marcu, L., "Fluorescence lifetime imaging for intraoperative cancer delineation in transoral robotic surgery," *Translational Biophotonics* **1** (dec 2019).

[4] Alfonso-Garcia, A., Bec, J., Weyers, B., Marsden, M., Zhou, X., Li, C., and Marcu, L., "Mesoscopic fluorescence lifetime imaging: Fundamental principles, clinical applications and future directions," *Journal of Biophotonics* **14**, e202000472 (6 2021).

[5] Marcu, L., "Fluorescence lifetime techniques in medical applications," *Annals of Biomedical Engineering* **40**, 304–331 (2 2012).

[6] Erdogan, A. T., Abbas, T. A., Finlayson, N., Hopkinson, C., Gyongy, I., Almer, O., Dutton, N. A., and Henderson, R. K., "A High Dynamic Range 128 x 120 3-D Stacked CMOS SPAD Image Sensor SoC for Fluorescence Microendoscopy," *IEEE Journal of Solid-State Circuits* (2022).

Paper III

Chip-on-tip fluorescence lifetime imaging micro-camera toward endoscopic applications

Dario Angelone, Noreen Nudds, Andrew B. Matheson, Ahmet T. Erdogan, Walter Messina, Ray Burke, Robert K. Henderson, Stefan Andersson-Engels, and Sanathana Konugolu Venkata Sekar.

Optics Letters **Vol. 50, Issue 13**, pp. 4230-4233 (2025).

4230 Vol. 50, No. 13 / 1 July 2025 / Optics Letters Letter

Optics Letters

Chip-on-tip fluorescence lifetime imaging micro-camera toward endoscopic applications

Dario Angelone,[1,*] Noreen Nudds,[2] Andrew B. Matheson,[3] Ahmet T. Erdogan,[3] Walter Messina,[1] Ray Burke,[1] Robert K. Henderson,[3] Stefan Andersson-Engels,[1,4] and Sanathana Konugolu Venkata Sekar[1,4]

[1]Biophotonics@Tyndall, Tyndall National Institute, Lee Maltings Complex, Cork T12 R5CP, Ireland
[2]Packaging Systems Group, Tyndall National Institute, Lee Maltings Complex, Cork T12 R5CP, Ireland
[3]Institute for Integrated Micro and Nano Systems, School of Engineering, University of Edinburgh, Edinburgh, UK
[4]School of Physics, University College Cork, College Road, Cork, Ireland
*dario.angelone@tyndall.ie

Received 23 March 2025; revised 9 May 2025; accepted 25 May 2025; posted 27 May 2025; published 20 June 2025

We present a chip-on-tip fluorescence lifetime imaging micro-camera on a size scale compatible with endoscopic applications. The micro-camera has an external diameter of 4 mm and comprises a miniaturized 128 × 120 SPAD array detector, integrated imaging optics, and an optical fiber for excitation light delivery. The spatial performance is characterized by imaging a resolution test target showing that the integrated system is able to resolve features of <30 μm. The temporal response is measured at a range of wavelengths, yielding a mean pixel impulse response width of < 1 ns. Benchmarking against a time-correlated single-photon counting system also shows good agreement with the micro-camera. Finally, fluorescence lifetime images of unlabeled *ex vivo* animal tissue samples are presented as examples.

Published by Optica Publishing Group under the terms of the Creative Commons Attribution 4.0 License. Further distribution of this work must maintain attribution to the author(s) and the published article's title, journal citation, and DOI.

https://doi.org/10.1364/OL.561838

Fluorescence lifetime measurements have the potential to be a powerful diagnostic tool; changes in tissue fluorescence lifetime can be indicative of a disease, meaning such measurements can be used to differentiate between healthy and diseased tissues [1,2]. Recently, fluorescence lifetime imaging (FLIm) has shown promise for label-free intraoperative tumor margin assessment in *ex vivo* human tissue samples [2,3].

In vivo FLIm probes often employ point scanning; in [4], a hybrid rotating probe uses FLIm and optical coherence tomography to image intravascular plaques, and in [5], a point scanning FLIm probe was employed in the oral cavity with machine learning used to generate a probabilistic heat-map of cancer. Recently, a fiber-bundle-based scanning FLIm endomicroscope has been reported, and its ability to differentiate cancerous regions demonstrated *ex vivo* [6]. However, manual scanning of such probes can be time consuming, and automated scanning systems require finely tuned mechanical motion.

Wide-field FLIm has the benefit of capturing lifetime information from the entire field of view (FoV) at the same time, reducing motion artifacts and potentially increasing system throughput and effective pixel rate [7]. Wide-field *in vivo* FLIm has been demonstrated with probes using a gradient index (GRIN) lens to image onto a fiber bundle and a gated intensified charge-coupled device (ICCD) camera for detection at the other end [8,9]. However, the flexibility of these probes is limited by the minimum bend radius of the fiber bundles, and light propagation along the fibers increases attenuation and dispersion. In addition, single-use disposable chip-on-tip endoscopes have become standard in white-light endoscopy. This trend is partly due to the miniaturization and reduction in cost of CMOS camera technology, as well as the avoidance of a sterilization process with single-use scopes [10–12]; therefore, the development of such endoscopes with wide-field FLIm capability is of interest for the long-term application of FLIm in surgery.

The use of SPAD cameras for wide-field FLIm has been demonstrated using a 0.5 megapixel time-gated SPAD camera [13], and they have also been applied for light-sheet FLIm [7,14]. There are now commercially available SPAD cameras with FLIm capability; the FLIMera camera from HORIBA has time-correlated single-photon counting (TCSPC) capability and the SPAD 512^2 from Pi Imaging Technology uses time-gating. These cameras are designed for use with benchtop microscopes and are therefore too large for endoscopic applications.

The miniaturization of SPAD arrays, fabricated with standard CMOS processes, makes their use for a chip-on-tip FLIm endoscope feasible. Low-cost SPAD detectors for LiDAR are widely available; with sufficient market demand, SPAD imagers could follow a similar trend. A 128 × 120 SPAD array with dimensions of 1.4 nm × 1.4 nm was presented in [15]. This detector has been used for FLIm of biological samples in benchtop [15,16] as well as handheld systems [17,18] and used for FLIm-based explosive detection [19]. A handheld system (23 mm × 23 mm × 28 mm) with this detector has also been used for combined lifetime and distance measurement (FLImDAR) [20].

In this Letter, we present a chip-on-tip FLIm micro-camera utilizing the miniaturized SPAD array mentioned above and

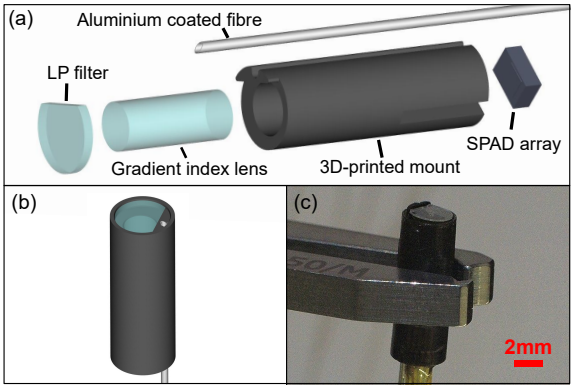


Fig. 1. (a) Exploded view of the FLIm micro-camera design. The SPAD array, lens, and long-pass filter are all housed in a custom 3D-printed mount. Excitation light is delivered via an aluminum-coated fiber. The mount has a groove along one side to guide the optical fiber. (b) 3D model of the assembled FLIm micro-camera including a 3D-printed outer casing, which holds the fiber in place. (c) Photograph of the assembled FLIm micro-camera having an external diameter of 4 mm.

including integrated imaging optics and excitation light delivery. With an external diameter of 4 mm and a rigid length of 10 mm, this is, to the authors' best knowledge, the first chip-on-tip FLIm micro-camera on a size scale compatible with endoscopic applications. This addresses key challenges in photonics packaging, stray light suppression, electrical interfacing, and compact optical design to enable time-resolved fluorescence imaging at clinically relevant scales. The temporal and spatial performance of this demonstrator system are characterized, and example images of *ex vivo* animal tissue samples are presented.

FLIm micro-camera system. The FLIm micro-camera includes integration of the detector, imaging optics, and excitation light. A custom 3D-printed mount was designed to house the detector, lens, and filter. The mount also has a groove along one side to guide an optical fiber, which delivers the excitation light. These elements are housed within a 3D-printed outer casing, which holds the fiber in place. The packaged FLIm micro-camera has a diameter of 4 mm and a rigid length of 10 mm, a ~40× decrease in the cross-sectional footprint compared to the smallest system previously reported using this detector [20], facilitating wide-field FLIm in narrow spaces. A 3D model and a photograph of the FLIm micro-camera are presented in Fig. 1.

The detector has been described elsewhere [12,15]. Briefly, the miniaturized SPAD array has an active area of ~ 1 mm^2 with 128 × 120 pixels. In fabrication, layout constraints on a wafer shared with other projects led to a physical footprint of 2.0 mm × 1.4 mm, slightly larger than the functional design. Time resolution is achieved by gating the in-pixel counting electronics. Each pixel has independent counting circuitry, which is enabled and disabled using a reference clock generated on-chip by a ring oscillator (RO). The width and position of each time gate are therefore in multiples of the RO period, 370 ps.

A GRIN lens with a diameter of 2 mm and a length of 5.1 mm (GRINTECH, Germany) was used for imaging with a 0.3 mm thick 500 nm long-pass filter (Everix, USA) mounted in front. Excitation light was delivered by an optical fiber. Early tests with a standard fiber showed light leaking from the fiber and reaching the detector through the 3D-printed holder. This was overcome by using a 300 μm core aluminum-coated fiber with a coating diameter of 430 μm and an NA of 0.22 (AS300/330 USMA 430, heracle, Germany). As the fiber is positioned adjacent to the imaging optics, initial tests showed that the excitation beam was significantly shifted to one side relative to the camera's FoV, and a similar effect was observed in [9]; this was overcome here by polishing the fiber tip at an angle, causing a deflection of the beam exiting the fiber [21,22]. A range of polishing angles were tested and an angle of 35° was found to be the most suitable.

The micro-camera requires five electronic connections: 1) 18.5 V SPAD bias voltage, 2) 2.8 V power supply, 3) Ground, 4) Data I/O, and 5) Clock. The chip is controlled with a custom MATLAB (R2021b MathWorks) graphical user interface (GUI) via a field-programmable gate array (FPGA) module (XEM7310-A200, Opal Kelly, USA). The chip was connected to a custom flexible PCB with gold wire bonds, and five micro-coaxial cables were soldered to the other end of the PCB, enabling connection to the FPGA. The cable length here was 50 cm, but the detector has previously been operated with a cable >1 m long [17]. The clocks for the FPGA and detector were synchronized with the laser sync signal via a picosecond delayer (Micro Photon Devices, Italy), which allows conversion to a TTL signal and adjustment of the laser pulse arrival time relative to the system clock.

Three different laser sources were used, a 375 nm pulsed laser diode (LDH-D-C-375, PicoQuant, Germany), a 405 nm pulsed laser diode (BDL-405-SMN-F, Becker & Hickl, Germany), and a pulsed supercontinuum laser (SuperK FIANIUM FIR-20 PP, UK). All sources were operated at a repetition rate of 20 MHz and provide a similar NIM sync signal that can be connected to the picosecond delayer, allowing the sources to be swapped relatively simply and quickly.

Spatial characterization. The spatial resolution of the system was characterized by capturing intensity images of a USAF resolution target illuminated from behind with diffuse white light. A series of images were acquired of groups 2–4 on the target. The modulation transfer function (MTF) of the system was obtained at a range of spatial frequencies from the contrast for each element. An example intensity image of the target is shown in Fig. 2(a). The pixel values across the horizontal and vertical parts of group 4, element 2, are plotted in Fig. 2(b); this element has a spatial frequency of 17.96lp/mm and a linewidth of 27.8 μm. The minimum contrast for this element was found to be 28.4%. The mean and minimum contrast from group 2, element 2, to group 4, element 6, inclusive are plotted in Fig. 2(c).

The contrast for each element was evaluated in the central region of the image, but there is some defocusing visible at the edges; this is likely due to the field curvature from the lens, causing a decrease in performance at the edges of the image. In spite of this, the image quality appears good across much of the FoV. A single lens was used in this design for ease of integration and to minimize potential losses and reflections, which can occur at each optical interface. Future designs could incorporate a more sophisticated lens to improve performance and tailor the FoV to a specific application, finding a balance between throughput and resolution. The detector has a defective pixel region in the top left corner caused by a race condition between the read and reset signals as has previously been reported in [15]; nevertheless, the vast majority of the imaged area remains usable.

Temporal characterization. The impulse response function (IRF) of the system was evaluated by measuring pulses from the SuperK laser scattered by a ground glass diffuser (DG05-600,

4232 Vol. 50, No. 13 / 1 July 2025 / Optics Letters Letter

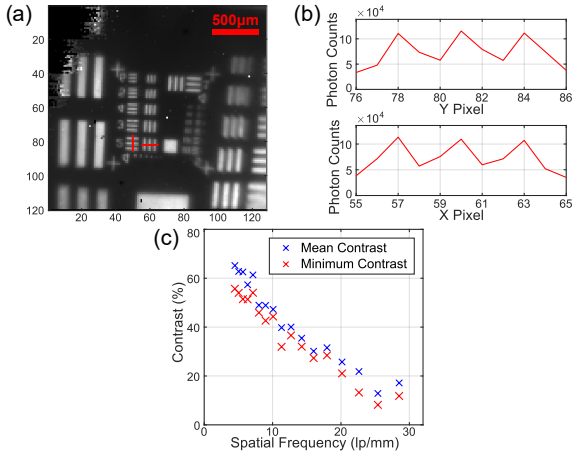


Fig. 2. (a) Intensity image captured using the micro-camera of a resolution test target illuminated from behind with diffuse white light. The camera has a FoV of 2.3 mm × 2.2 mm and a working distance of 4 mm. (b) Plots of the pixel values across the horizontal and vertical parts of group 4, element 2, on the target. This element has a spatial frequency of 17.96 lp/mm and a linewidth of 27.8 µm. (c) Scatterplot of the micro-camera MTF obtained by imaging groups 2–4 on the target.

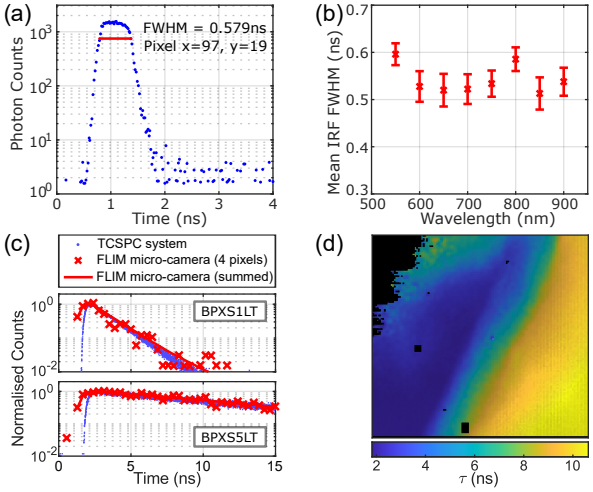


Fig. 3. (a) Response at 550 nm for an individual pixel on the camera; the FWHM was estimated by linear interpolation and is indicated by the red line. (b) Mean pixel response between 550 nm and 900 nm. The error bars show the standard deviation. (c) Fluorescence decay curves from two test targets measured with the FLIm micro-camera and a TCSPC system. The data for a 4-pixel group on the micro-camera is presented as well as the curve obtained by summing over all pixels. (d) Lifetime image of BPXS1LT (left) and BPXS5LT (right) acquired with the micro-camera.

Thorlabs, Germany). The laser was used with the monochromator described in [23]. The IRF was measured over a typical fluorescence emission wavelength range, from 550 nm to 900 nm in steps of 50 nm. Characterization at this range is important as the timing response of SPADs is wavelength dependent [24]. For these measurements, the sync signal was shifted in steps of 20 ps using the picosecond delayer, enabling a finer measurement of the IRF than is possible with on-chip gating alone. The IRF width (FWHM) was estimated for each pixel at each wavelength using linear interpolation. An example pixel IRF at 550 nm is shown in Fig. 3(a). The mean IRF width was calculated for each wavelength and plotted in Fig. 3(b). The mean IRF width across all wavelengths was 0.54 ns.

The SuperK has a pulse width of 30 ps–60 ps over the measured wavelength range, far narrower than the minimum time bin width of the detector; therefore, the measured IRF above approximates the micro-camera response to an infinitely short light pulse. For fluorescence imaging, the two pulsed laser diodes were used for excitation. These lasers have a wider pulse width of <100 ps, which is not taken into account in the IRF measured above. However, we can estimate a mean system IRF width ($FWHM_{sys}$) of < 1 ns when using these lasers from Eq. (1):

$$FWHM_{sys} = \sqrt{FWHM_{camera}^2 + FWHM_{laser}^2}, \quad (1)$$

where $FWHM_{camera}$ is the response of the micro-camera and $FWHM_{laser}$ is the temporal width of the excitation laser.

The micro-camera was also benchmarked against a system using a TCSPC module and a hybrid photomultiplier detector (PicoHarp 300 and PMA Hybrid 50, PicoQuant). For this system, emission was filtered using a 500 nm long-pass filter (FELH0500, Thorlabs). Benchmarking was performed by measuring two fluorescence lifetime test targets (BPXS1LT and BPXS5LT, BioPixS, Ireland) with both systems using the 405 nm laser for excitation. With the micro-camera, counts were acquired over 120 time bins with an acquisition time of ~ 75 s per measurement. The decay curves obtained are presented in Fig. 3(c) and show good agreement between the systems. A lifetime image of the two test targets next to each other was captured with the micro-camera and is presented in Fig. 3(d). For imaging, pixels were binned into groups of four to improve photon statistics, and a mono-exponential decay was fit to the tail of the measured counts between 90% and 20% of the peak value. A photograph of the test targets is shown in Fig. S1 in Supplement 1.

Tissue imaging. *Ex vivo* sheep lung and intestine samples were acquired from a local butcher (D.P Murphy & Sons – Middleton, Ireland) and stored in refrigerated conditions (<5°) overnight. The following afternoon, a sample was cut from each organ and measured with the micro-camera. For these measurements, the 375 nm pulsed laser diode was used with 0.29 mW average power. This wavelength is often used to excite key fluorophores such as NADH and FAD [7]. Counts were acquired over 50 time bins and fitting was performed as before. The acquisition time for each tissue image was approximately 30 s. The fluorescence intensity and lifetime images of the samples are presented in Fig. 4 along with the lifetime distributions. The lifetime images have been upscaled to the original image dimensions and pixel values interpolated (bilinear) for display only. The brightness of each pixel in the lifetime images is scaled by the intensity to highlight regions with a strong fluorescence signal. Defective pixels were excluded from the lifetime distributions and mean calculations by a manually drawn binary mask. The raw lifetime maps and binary mask are presented in Fig. S2 in Supplement 1. The intestine sample was cut open and the inside imaged. The lung image shows the inside of a larger bronchiole in the sample, where the two curved bright features are internal ridges of the bronchiole, likely primarily made up of cartilage.

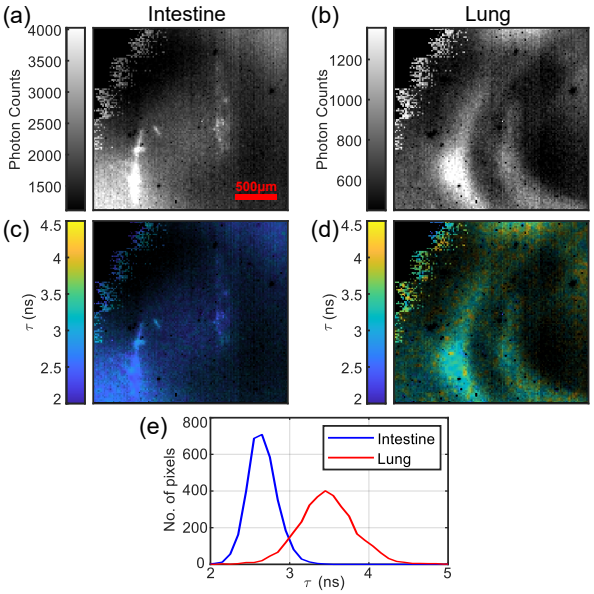


Fig. 4. (a), (b) Fluorescence intensity and (c), (d) lifetime images of *ex vivo* sheep lung and intestine samples. (e) Lifetime distributions for the two samples. The defective pixels in the top left corner are excluded by a binary mask. The intestine sample had a mean lifetime of 2.7 ± 0.2 ns (standard deviation), and the lung sample had a mean lifetime of 3.5 ± 0.4 ns.

More sophisticated fitting models may be implemented to improve the precision of the lifetime measurements, such as fitting to a multi-exponential model and/or reconvolution of the IRF with the decay model. However, there is still a clear contrast between the two samples; the intestine sample had a mean lifetime of 2.7 ± 0.2 ns (standard deviation), whereas the lung sample had a longer mean lifetime of 3.5 ± 0.4 ns.

Discussion and conclusion. The size of the FLIm micro-camera is compatible with imaging of segmental bronchi (second to fourth generation), which have a diameter in the range of 5 mm–8 mm [25]. With appropriate packaging, the system could either be deployed through the working channel of a larger scope or as an independent scope with intensity imaging used for navigation. For this design, 3D-printing the micro-camera body was convenient and effective for prototype development. However, future designs, using machined metal parts, e.g., with a high-tolerance packaging process, would improve stray light blocking. This would reduce noise and potentially remove the need to use a metal-coated fiber.

The method of gate-sweeping to acquire photon histograms also increases the acquisition time, as the data is read out from the detector as each gate is measured. However, faster acquisition times can be achieved by acquiring fewer gates or by using rapid lifetime determination (RLD) for near video-rate estimation of lifetimes. This has been demonstrated using this detector in a larger form factor handheld system to capture FLIm images of plant and animal samples at a frame rate of ∼ 1 Hz [17].

The ability of the system to acquire lifetime images of unlabeled tissues shows great promise for the future application of such detectors for *in vivo* FLIm. Further advances in miniaturized SPAD arrays with improved sensitivity, timing resolution, and readout time support this further. The demonstration here, of the first chip-on-tip FLIm micro-camera on a size scale compatible with endoscopic applications, combines advanced 3D SPAD integration, miniature optics, and high-speed data handling in a compact form factor. This is a critical step in bringing FLIm systems to the tip of an endoscope, thus opening new areas of exploration for intraoperative diagnostics and surgical guidance through improved imaging capabilities.

Funding. H2020 Marie Skłodowska-Curie Actions (PHAST ETN, 86018); Irish Research eLibrary (22/RP-2TF/10293, 12/RC/2276 P2); Engineering and Physical Sciences Research Council (EP/K03197X/1).

Acknowledgment. We would like thank GRINTECH and Dr. Bernhard Messerschmidt for providing the lens used in the micro-camera. Open access funding provided by Irish Research eLibrary.

Disclosures. RKH is a co-founder of Singular Photonics, a SPAD image sensor company. SKVS and SAE have equity ownership in the biophotonics phantoms and standards company BioPixS Ltd.

Data availability. All data and code used for analysis in this Letter are available in Ref. [26].

Supplemental document. See Supplement 1 for supporting content.

REFERENCES

1. L. Marcu, Ann. Biomed. Eng. **40**, 304 (2012).
2. A. Alfonso-Garcia, J. Bec, B. Weyers, *et al.*, J Biophotonics **14**, e202000472 (2021).
3. M. Wang, F. Tang, X. Pan, *et al.*, BBA Clin **8**, 7 (2017).
4. M. W. Lee, J. Woo Song, W. J. Kang, *et al.*, Sci. Rep. **8**, 14561 (2018).
5. M. Marsden, T. Fukazawa, Y.-C. Deng, *et al.*, Biomed. Opt. Express **11**, 5166 (2020).
6. S. Fernandes, E. Williams, N. Finlayson, *et al.*, Transl. Lung. Cancer Res. **13**, 355 (2024).
7. K. Samimi, D. E. Desa, W. Lin, *et al.*, J. Biomed. Opt. **28**, 066502 (2023).
8. Y. H. Sun, N. Hatami, M. Yee, *et al.*, J. Biomed. Opt. **15**, 056022 (2010).
9. H. Sparks, S. Warren, J. Guedes, *et al.*, J. Biophotonics **8**, 168 (2015).
10. S. T. Sørensen, W. Messina, L. Niemitz, *et al.*, Biomed. Opt. Express **16**, 12 (2025).
11. M. R. Gaab, World Neurosurg. **79**, S14.e11 (2013).
12. T. Al Abbas, O. Almer, S. W. Hutchings, *et al.*, in *IEEE Symposium on VLSI Circuits, Digest of Technical Papers* (2019), paper C260.
13. V. Zickus, M. L. Wu, K. Morimoto, *et al.*, Sci. Rep. **10**, 20986 (2020).
14. J. Nedbal, F. Mattioli Della Rocca, I. T. Ivanova, *et al.*, Sci. Rep. **14**, 7247 (2024).
15. A. T. Erdogan, T. A. Abbas, N. Finlayson, *et al.*, IEEE J. Solid-State Circuits **57**, 1649 (2022).
16. D. Angelone, L. Li, C. Devoy, *et al.*, Sensors and Actuators B: Chemical **431**, 137441 (2025).
17. A. B. Matheson, A. T. Erdogan, S. Borrowman, *et al.*, Opt. Express **31**, 22766 (2023).
18. D. Angelone, S. Konugolu Venkata Sekar, W. Messina, *et al.*, Proc. SPIE **12368**, 1236807 (2023).
19. A. B. Matheson, R. Henderson, R. N. Gillanders, *et al.*, Opt. Lett. **48**, 6015 (2023).
20. A. B. Matheson, C. Hopkinson, M. G. Tanner, *et al.*, Sci. Rep. **14**, 13285 (2024).
21. J. J. Davenport, M. Hickey, J. P. Phillips, *et al.*, Opt. Eng. **55**, 026120 (2016).
22. R. N. Bunch, J. P. Caughey, and M. Douglas, *Applications of Optical Engineering: Proceedings of OE/Midwest '90*, Vol. 1396 (SPIE, 1991), pp. 411–416.
23. S. K. Venkata Sekar, A. Dalla Mora, I. Bargigia, *et al.*, IEEE J. Sel. Top. Quantum Electron. **22**, 406 (2016).
24. I. Rech, G. Acconcia, F. Ceccarelli, *et al.*, Opt. Express **31**, 33963 (2023).
25. C. Beigelman-Aubry, P. Y. Brillet, and P. A. Grenier, Radiol. Clin. North Am. **47**, 185 (2009).
26. D. Angelone and S. K. Venkata Sekar, "Dataset: chip-on-tip fluorescence lifetime imaging micro-camera towards endoscopic applications," Zenodo (2025), https://doi.org/10.5281/zenodo.15375004.

Paper IV

Development of solid-state fluorescence lifetime standards for clinical applications using dyed epoxy resins

Dario Angelone, Keela Hughes, Hasti Yavari, Sara Eugenia Garduño Gómez, Brian C. Wilson, Stefan Andersson-Engels, Katarzyna Komolibus, and Sanathana Konugolu Venkata Sekar.

Journal of Biomedical Optics **-**, (Accepted 30th December 2025).

Development of solid-state fluorescence lifetime standards for clinical applications using dyed epoxy resins

Dario Angelone[a,*], Keela Hughes[a,b], Hasti Yavari[a], Sara Eugenia Garduño Gómez[c], Brian C. Wilson[d], Stefan Andersson-Engels[a,b], Katarzyna Komolibus[a], Sanathana Konugolu Venkata Sekar[a,b,c,*]

[a]Biophotonics@Tyndall, Tyndall National Institute, Lee Maltings Complex, Cork T12 R5CP, Ireland
[b]School of Physics, University College Cork, College Road, Cork, Ireland
[c]BioPixS Ltd. (Biophotonics Standards), Lee Maltings Complex, Cork T12 R5CP, Ireland
[d]Princess Margaret Cancer Centre, University Health Network, Toronto, ON M5G 1L7, Ontario, Canada

Abstract.

Significance: Fluorescence lifetime imaging (FLIm) offers label-free contrast based on intrinsic tissue properties, making it a promising tool for clinical diagnostics and intraoperative guidance. However, the lack of robust, reproducible standards for system validation limits cross-platform comparability, impedes quality assurance, and hinders clinical translation.

Aim: To develop and characterize a set of stable solid-state fluorescence lifetime standards using dyed epoxy resins, with the goal of enabling reliable calibration, benchmarking, and validation of FLIm systems in both research and clinical environments.

Approach: A series of solid standards incorporating different dyes were fabricated to span a range of lifetimes from sub-nanosecond to over 3.5 ns. These materials were evaluated for fluorescence lifetime, emission intensity, photostability under UV exposure, and fabrication repeatability. The influence of dye concentration and microstructural uniformity was assessed using a confocal microscope. The standards were also applied to validate a chip-on-tip FLIm micro-camera designed for endoscopic imaging.

Results: The dyed epoxy standards demonstrated consistent and reproducible lifetimes, good photostability, and scalable fabrication. Confocal imaging revealed some microstructural heterogeneity, while bulk measurements remained robust. The standards enabled effective validation of the FLIm micro-camera, including spatial and temporal resolution assessment, and highlighted platform-dependent biases in lifetime estimation.

Conclusions: Dyed epoxy materials show strong potential as practical, scalable tools for FLIm system calibration and quality assurance. These standards may support cross-platform validation and benchmarking of emerging FLIm technologies, and could contribute to the development of future regulatory frameworks for clinical adoption.

Keywords: fluorescence lifetime imaging, standardisation, phantoms, calibration.

*D. Angelone, dario.angelone@tyndall.ie, S. Konugolu Venkata Sekar, sanathana.konugolu@tyndall.ie

1 Introduction

Fluorescence lifetime imaging (FLIm) has potential as a powerful diagnostic tool due to its ability to provide contrast based on the intrinsic decay time of fluorophores, independent of the fluorophore concentration or the excitation intensity used.[1–4] Unlike fluorescence intensity measurements, which can be influenced by photobleaching, scattering, or absorption, fluorescence lifetime (FLT) measurements can offer a higher biochemical specificity. This makes FLIm particularly

valuable in biomedical applications, where subtle changes in tissue composition or metabolic state can be detected through lifetime variations.[2,4,5]

Recent studies have demonstrated the clinical potential of FLIm for label-free intraoperative assessment of tumour margins in various tissues, including the brain,[6,7] oral cavity,[8,9] and breast.[10,11] Beyond intraoperative oncology, FLIm has also been explored for dermatological diagnostics,[12] and for probing subcellular lipid heterogeneity in metabolic studies.[13] These applications highlight the growing interest in translating FLIm from research settings to clinical environments. This is reflected in the large number of novel systems for *in vivo* FLIm which have been reported in recent years.[14] In addition to stand-alone FLIm systems, multimodal approaches have been explored to combine fluorescence lifetime imaging with complementary techniques such as Raman[15–17] and optical coherence tomography[18,19] for enhanced tissue characterization.

The development of diagnostic imaging systems more generally has led to the use of tissue-simulating objects, commonly known as "phantoms".[20,21] These phantoms serve multiple critical purposes, including initial system design testing, optimizing signal-to-noise ratios in existing systems, performing routine quality control, and comparing performance between different systems. Phantoms can be fabricated from solid or liquid materials that mimic a range of tissue optical properties as well as anthropomorphic features, enabling realistic evaluation of various system performance.[22,23] For established systems in routine clinical use with regulatory approval, bodies such as the American College of Radiology (ACR), the American Association of Physicists in Medicine (AAPM), and the Canadian Organization of Medical Physicists (COMP) typically recommend or require specific phantoms for validating system performance and ensuring uniformity across institutions and over time.[20]

Given the rapid rate at which new FLIm systems are being developed and the vast amounts of tissue lifetime data being acquired both *in vivo* and *ex vivo*, there is an increased need for standardisation and cross-platform validation. A major barrier to clinical translation remains the lack of robust, reproducible standards for system calibration and validation.[24,25] Currently, system validation often relies on liquid dye solutions with known lifetimes, such as Rhodamine 6G or Erythrosine B, measured under controlled conditions.[26,27] While effective in laboratory settings, this approach is impractical for routine or on-site calibration, particularly in clinical workflows, and is sensitive to environmental factors such as oxygen quenching and dye aggregation. Biological

samples such as Convallaria are often used for qualitative FLIM demonstrations; however, their autofluorescence properties can vary between specimens and degrade over time, making them unsuitable as reproducible calibration standards. Commercial fluorescent plastic slides, available from suppliers such as Thorlabs, are designed to provide broad absorption and emission coverage for alignment and qualitative checks. However, they are not developed for use as lifetime standards. There are FLIM standards available from BioPixS,[28] but the specific dyes used are not disclosed. As a result, these materials are ill-suited for rigorous calibration or cross-platform validation.

To address these limitations, several studies have focused on improving the accuracy and reproducibility of FLIm calibration; Talbot et al.[29] identified systematic errors in fluorescence lifetime fitting using the Delta Function Convolution Method, particularly when the reference dye has a longer lifetime than the sample, and proposed a correction model to mitigate these biases. Complementing this, Margineanu[25] provided a comprehensive experimental framework for calibrating time-domain FLIm systems, emphasizing the importance of acquiring accurate instrument response functions (IRF) and using well-characterized reference dyes. Both studies also noted that discrepancies in lifetime measurements across platforms can arise due to differences in photon collection geometry and reabsorption effects, further underscoring the importance of physical standards that can reveal and help correct such biases. Building on this, Freymüller et al.[30] developed a microstructured phantom incorporating fluorescent beads embedded at known depths within a scattering medium. This design enables depth-resolved calibration and is particularly suited for characterising axial resolution in multiphoton and microendoscopic systems lacking z-stage control. However, the phantom's short shelf-life and complex fabrication process limit its scalability for routine use or widespread deployment.

In this work, we present a complementary approach by developing and characterising a set of solid-state fluorescence lifetime standards using dyed epoxy resins. These standards are designed to be photostable, reproducible, and easy to handle, making them suitable for both research and clinical environments. We fabricate and characterise a range of such materials incorporating different dyes, targeting a spread of lifetimes relevant to biomedical FLIm. The materials are evaluated in terms of their fluorescence lifetime, intensity, photostability, and fabrication repeatability. We also explore the effect of dye quantity and assess the microstructure of the materials using confocal fluorescence lifetime imaging microscopy (FLIM). Finally, we demonstrate the utility of these

standards by applying them to validate a novel chip-on-tip FLIm micro-camera system developed for endoscopic applications.[31]

2 Materials and methods

2.1 FLT standards fabrication process

The solid-state fluorescence lifetime standards were fabricated using Poly-optic® 1490 Clear Casting Resin, a water-clear urethane resin consisting of a base (Part A) and a curer (Part B). The two-part resin was mixed by weight at a 100A:90B ratio, with varying masses of fluorescent dyes added to achieve a range of target lifetimes. In this study, four Smooth-On Ignite™ dyes (Smooth-On, Inc., USA) have been used; purple (PMS purple), yellow (PMS 809C), magenta (PMS 813C), and orange (PMS 805C). The Smooth-On Ignite™ dyes were selected for their strong visible fluorescence and lifetimes spanning the sub-nanosecond to multi-nanosecond range. Other dyes from the same range were screened, and four were chosen to cover a clinically relevant lifetime span. The Poly-optic® 1490 resin was selected for its optical clarity and stable curing properties. The wide commercial availability of these components also facilitates reproducible standard fabrication internationally. Solid standards containing each dye were fabricated. The dye quantity added for each standard material is as follows: 119 mg for the purple standards, 219 mg for yellow, 90 mg for magenta, and 160 mg for the orange standards. An epoxy sheet containing no dye was also fabricated and measured to assess the fluorescence of the undyed epoxy and its potential influence on the standard material performance.

The fabrication process is illustrated in Fig. 1. First, the selected dye was weighed and thoroughly mixed with Part A to ensure uniform dispersion and degassed under vacuum to eliminate air bubbles, which could otherwise scatter light and distort fluorescence measurements. Part B was then added, and the mixture was stirred again to achieve homogeneity. The resulting solution was degassed again. Finally, the mixture was poured into moulds and left to cure undisturbed at room temperature for 16 to 24 hours. This process yielded optically clear solid sheets with reproducible fluorescence characteristics. The dyes were selected to span a range of lifetimes, enabling evaluation of FLIm system accuracy across the range of lifetimes covered. The standard sheets can then be cut to a desired planar geometry. For this work, three types of standard tools were explored as illustrated in Fig. 2; (i) a homogeneous slide (ii) a square slide with a chrome USAF resolution test

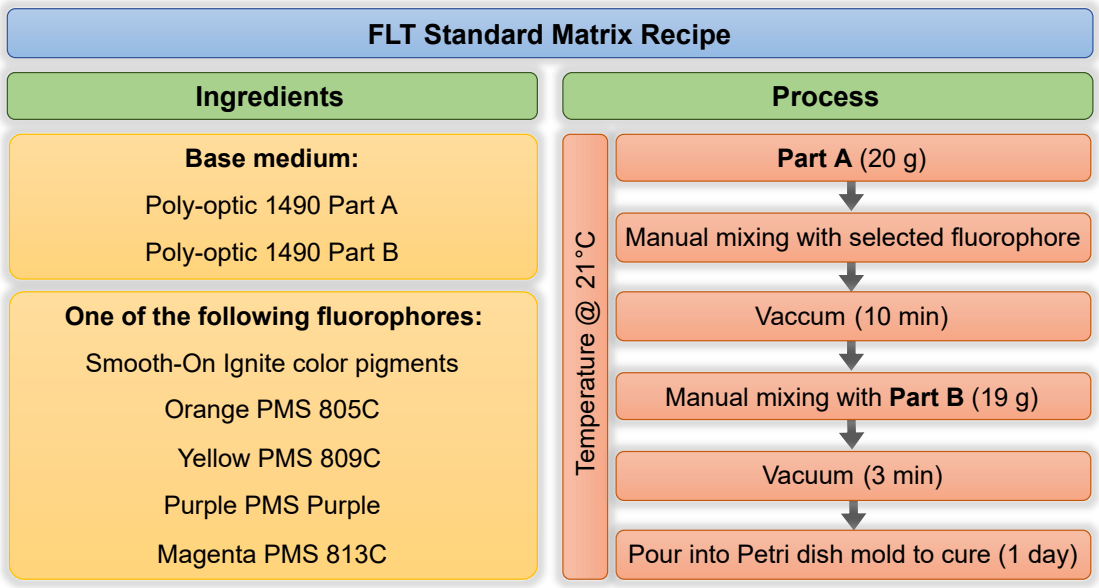


Fig 1 Overview of the solid fluorescence lifetime standard recipe including all ingredients and the fabrication process steps.

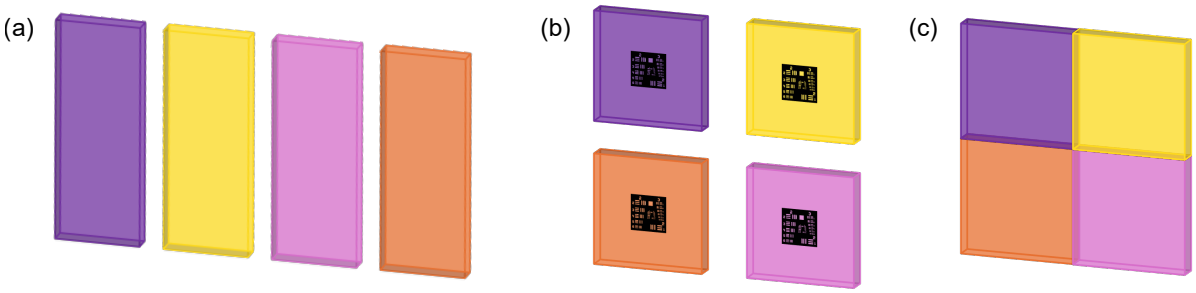


Fig 2 Solid fluorescence lifetime standard tools created (not drawn to scale); 4 standard materials have been tested with a range of lifetimes. The standard sheets can be cut to a desired planar geometry. For this work, use of the standard materials in three forms was explored; (a) as a homogeneous slide cut to 17 mm × 45 mm (b) a square slide cut to 22 mm × 22 mm with a chrome USAF resolution test target glued to the surface for combined system evaluation of fluorescence lifetime measurements and spatial resolution, or (c) each material fixed together in a quadrant pattern for system lifetime imaging demonstration with multiple lifetimes in the same field of view.

target glued to the surface for combined system evaluation of fluorescence lifetime measurements and spatial resolution (herein referred to as FLT-USAF targets), and (iii) one of each material fixed together for lifetime imaging demonstrations with multiple lifetimes in the same field of view.

2.2 Material characterisation

2.2.1 Absorption and emission spectra

The absorption and emission spectra of the dyed epoxy standards were measured to characterise their spectral properties. Spectra were acquired using a fluorescence spectrometer (Cary Eclipse, Agilent, USA) with excitation and emission wavelengths scanned across the visible range.

2.2.2 Fluorescence lifetime system

A home-built FLT system was used for characterization of the standard materials. This system employs a TCSPC-based single-photon counting architecture similar to that of our well-validated time-domain diffuse optical spectroscopy system.[32,33] Measurements were performed using a 405 nm picosecond laser diode (BDL-405-SMN-F, Becker&Hickl) as an excitation source pulsed at a repetition rate of 20 MHz. The materials were excited with a collimated laser beam; fluorescence emission was collected perpendicular to the excitation beam and filtered using a long pass filter with a cut-off wavelength of 500 nm (FELH0500, Thorlabs, Germany). The laser power was adjusted using a variable reflective neutral density filter (NDM4/M, Thorlabs, Germany) positioned in the laser beam path before the sample and mounted at an angle to reduce back-reflections. Fluorescence decay curves were recorded using a hybrid photomultiplier detector (PMA Hybrid 50, PicoQuant, Germany) and a time-to-digital converter (TDC, Picoharp 300, Picoquant, Germany). A photodiode connected to a power meter (S120VC and PM100D, Thorlabs, Germany) was placed after the sample in the excitation beam path for monitoring of the excitation laser power used for each sample.

For FLT measurements, the laser power was adjusted until a count rate of 10^5 counts per second (cps) ±5 % was seen at the hybrid detector. Photon counts were then acquired for one second. The sample was then removed from the excitation beam path and the laser power recorded from the power meter.

The system IRF was recorded by removing the long pass filter from the detection path and measuring the laser pulse scattered by a frosted glass microscope slide. The FLT of each sample was found by fitting a monoexponential decay model convolved with the system IRF. Fitting was performed from 80 % of the max counts on the rising edge of the measured decay curve to 1 % on the falling tail. The code used for data acquisition and fitting is available on GitHub.[34] The relative

fluorescence intensity of each sample was estimated from the inverse of the excitation laser power required to achieve a count rate of 10^5 cps. This is a proxy measurement rather than a direct one but gives a useful indication of the relative brightness of the fluorescent materials.

2.2.3 Bulk FLT characterisation

For each sheet of standard material fabricated, three homogeneous slides of 17 mm × 45 mm were cut. The three slides were then measured three times each with the system described above and the mean, standard deviation, and coefficient of variation of these measurements calculated. The fluorescence lifetime and intensity of the dyes were then compared to assess their suitability for use as solid lifetime standards.

2.2.4 Repeatability

The repeatability of the solid standard fabrication process was assessed by carrying out three fabrication repetitions of the orange standards with 160 mg of orange dye and evaluating the variability in the standard lifetimes across the different repetitions. Three homogenous slides were cut from each sheet, each slide was then measured three times and the results from each fabrication compared.

2.2.5 Microscopic inspection

The standard materials were inspected using a Leica TCS SP8 STED3X confocal and super-resolution microscope (Leica Microsystems, Germany) equipped with the FALCON (Fast Lifetime CONtrast) module for high-speed FLIM acquisition[35] and processed using LAS X software (Leica Microsystems, Germany) at the Advanced Optical Microscopy Facility in University health Network, Canada. Samples were excited at 488 nm using a 40 MHz pulsed white light laser with fluorescence emission from 500 nm to 785 nm detected with a Leica HyD GaAsP single molecule detector. Lifetime images of four homogenous slides, one for each dye, were acquired using a $20\times$ objective for microscopic inspection of the standard materials' lifetimes and morphologies.

2.2.6 Dye quantity

The influence of the dye quantity on the standard characteristics was also assessed. An additional three orange standards with different quantities of dye were fabricated, resulting in four different

quantities of dye added; 80 mg, 160 mg, 320 mg, and 640 mg. As above, three slides were cut from each sheet and measured for comparison. The lifetime and intensity of these samples was then measured with the system described in Sec. 2.2.2. One sample having each dye quantity was also imaged with the confocal system as described in Sec. 2.2.5 for comparison.

2.2.7 Stability

Photostability is an important factor for the reliability of potential standard materials. In order to investigate the stability of the materials studied here, the ageing process is simulated through prolonged UV exposure. Four homogeneous slides, one containing each dye, were placed under a high-power 365nm LED (M365LP1, Thorlabs, Germany). The light power density at the samples was measured as $1.35 \pm 0.05\,\mathrm{mW/cm^2}$. The materials were exposed for a total of 10 hours, and the cumulative UV dose was calculated from the measured irradiance and exposure time. Measurements were performed every hour during the 10-hour period. At each time point, three lifetime measurements and one intensity measurement were recorded per sample.

2.3 Case study: characterisation of a FLIm micro-camera

As a demonstration of the potential application of the FLT standards, they were used to characterise and validate the wide-field chip-on-tip FLIm micro-camera we have previously reported[31] which uses a custom miniaturised 128×120 SPAD array as the image sensor.[36] The micro-camera sensor has a defective pixel region which has previously been described;[36] the images presented here have been cropped to remove this defective region. For all micro-camera measurements, photon counts were acquired over 50 time-bins each with a width of 370 ps, and a total acquisition time of $\sim$30 s. The tail of the measured decay for each pixel was then fit to a mono-exponential model between 90 % and 20 % of the peak.

Fluorescence lifetime images of four uniform standards (one for each dye colour) were captured with the micro-camera. The lifetimes measured for each material by the micro-camera were then compared with the bulk values measured with the system described in Sec. 2.2.2. Lifetime and intensity images of the orange FLT-USAF target were acquired. The intensity image was used to assess the spatial resolution of the system, and the lifetime measured from this target is compared with orange uniform standard. A lifetime image of the quadrant standard was also captured

with the micro-camera to demonstrate the system's ability to resolve different lifetimes spatially in the same field of view.

3 Results and discussion

3.1 FLT standard design and application

Fig. 3 presents photographs of the range of FLT standard tools developed using the dyed epoxy materials. These include homogeneous slides, FLT-USAF targets for combined spatial and temporal resolution assessment, and quadrant standards for multi-lifetime imaging. These tools enable flexible and application-specific validation of FLIm systems.

3.2 Fluorescence lifetime and intensity of standard materials

Table 1 summarizes the measured fluorescence lifetimes and relative intensities of the four dyed epoxy standards (purple, yellow, magenta, and orange), along with an undyed control. The absorption and emission spectra for the standards, along with example decay plots and fits are presented in Fig. 4. The results show a clear separation in lifetime values across the different dyes, ranging from 0.80 ns for the purple standard to 3.61 ns for the orange. The undyed epoxy exhibited a low intensity and a lifetime similar to the orange standard, suggesting that the epoxy matrix itself may contribute a weak background signal.

However, the background fluorescence from the undyed epoxy was found to be more than an order of magnitude weaker than any of the dyed materials, and approximately two orders of magnitude weaker than the yellow and orange standards. This indicates that the contribution of

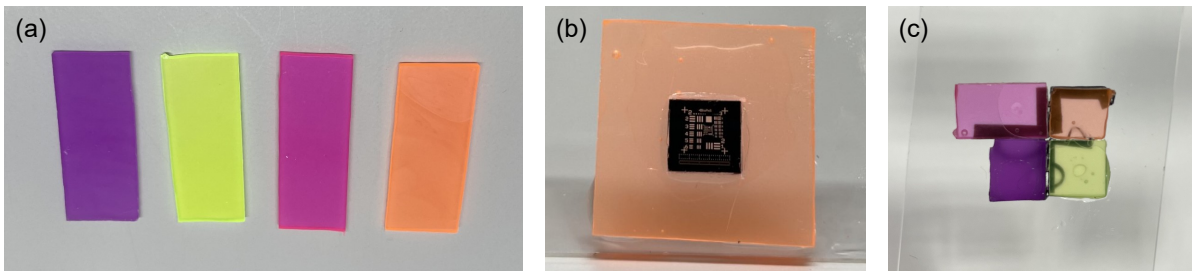


Fig 3 Photographs of the solid-state fluorescence lifetime (FLT) standard tools fabricated using dyed epoxy resins. Three distinct formats were developed to support a range of FLIm system validation tasks: (a) homogeneous slides for bulk lifetime measurements, (b) FLT-USAF targets for simultaneous assessment of spatial resolution and fluorescence lifetime accuracy, and (c) quadrant standards composed of four different dyed materials arranged in a single field of view to enable multi-lifetime imaging demonstrations.

Table 1 Measured fluorescence lifetimes and relative intensities of the four dyed epoxy standards (purple, yellow, magenta, and orange), along with an undyed control. The mean, standard deviation (SD) and coefficient of variation (CV) are presented for each.

Dye	Lifetime			Intensity		
	Mean (ns)	SD (ns)	CV (%)	Mean (AU)	SD (AU)	CV (%)
Purple	0.80	0.01	1.25	0.24	0.02	8.33
Yellow	2.43	0.01	0.41	2.48	0.05	2.02
Magenta	2.56	0.05	1.95	0.50	0.01	2.00
Orange	3.61	0.02	0.55	2.29	0.01	0.44
None	3.59	0.12	2.24	0.02	0.003	15.00

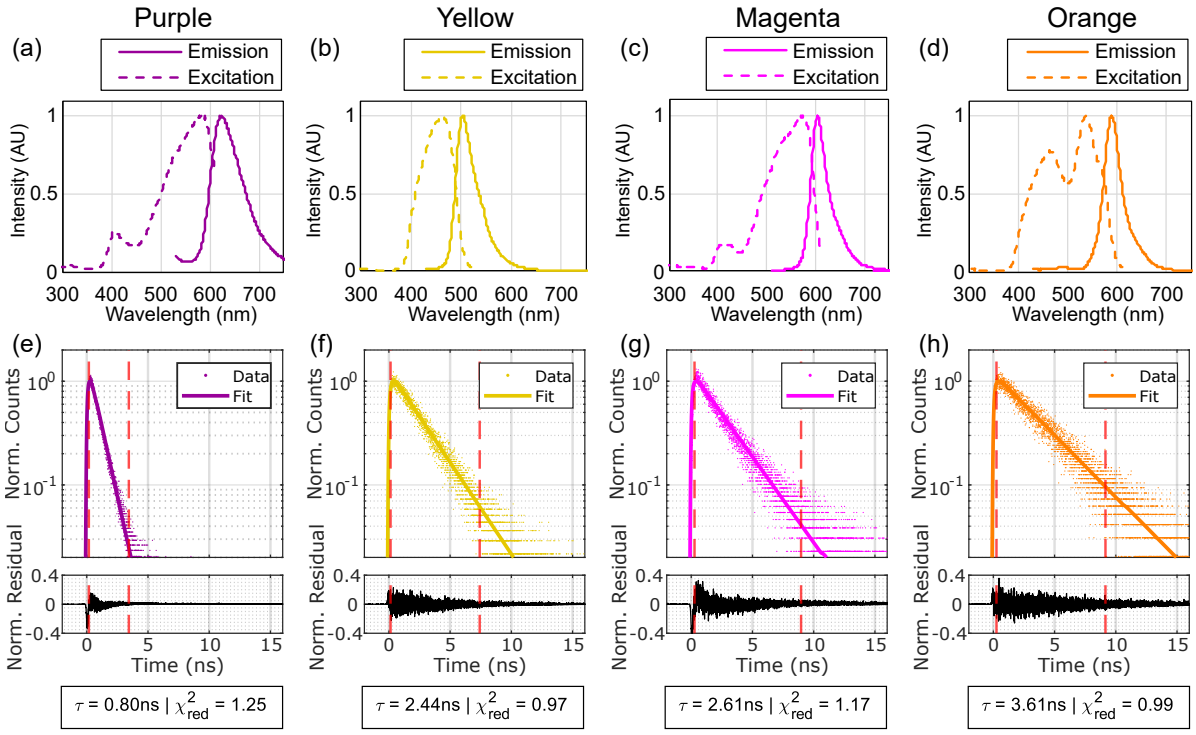


Fig 4 (a–d) Normalised absorption and emission spectra of the dyed epoxy standards (purple, yellow, magenta, and orange). (e–h) Example plots of the normalised measured decay curves, fit, and normalised residuals for the solid standards fabricated with each dye and measured with the home-built FLT system. The fitted lifetime (τ), and the goodness-of-fit (χ^2_{red}) are also presented for each curve.The dotted red lines in each plot indicate the range of time bins over which fitting was performed.

the epoxy matrix to the overall signal is minimal, particularly for the brighter dyes, and should not significantly affect the accuracy of lifetime measurements.

Among the dyed materials, the purple standard had the lowest intensity, but it remains valuable due to its sub-nanosecond lifetime which is distinct from the other dyes tested. This makes it a

useful reference for validating FLIm systems operating in the sub-nanosecond regime, despite its lower brightness.The development of a solid FLT standard with a similarly short lifetime but with enhanced brightness represents a promising direction for future work.

All materials exhibited absorption in the 400 nm to 500 nm range (as seen in Fig. 4a–d), making them suitable for excitation with common sources in this range. The magenta and purple dyes did have lower absorption in this range, consistent with their reduced fluorescence intensity under 405 nm excitation. All dyes except yellow also absorbed in the 500 nm to 600 nm range, indicating potential for use with longer-wavelength excitation. However, all four of the dyes showed weak fluorescence when excited in the 300 nm to 400 nm range, which limits their compatibility with FLIm systems using UV excitation (e.g., 355 nm or 375 nm) targeting endogenous fluorescence from molecules such as NAD(P)H. This spectral gap highlights an area for future development to broaden the standards' utility in clinical FLIm applications.

3.3 Photostability under UV exposure

The photostability of the standards was evaluated by exposing them to continuous UV illumination over a 10-hour period. Measurements were performed at each hour; the corresponding cumulative UV dose was calculated and plotted against the measured lifetime and intensity in Fig. 5; the values of these plots are presented in Table S1. The fluorescence lifetimes and intensity of the purple, yellow, and orange dyes remained relatively stable throughout the exposure, with minimal drift.

In contrast, the magenta material exhibited a more pronounced change in both fluorescence lifetime and intensity over the exposure period. This suggests that the magenta dye may be more susceptible to photodegradation under prolonged UV illumination. Additionally, the magenta standard exhibits a lifetime that is very similar to that of the yellow dye, but with significantly lower fluorescence intensity.

These trends are quantified in Table 2, which summarizes the minimum and maximum values observed for each dye, along with the corresponding percentage changes in both lifetime and intensity. Notably, the magenta intensity measurement after one hour appears to be an outlier, potentially due to sample positioning or other user-dependent factors during measurement. If this

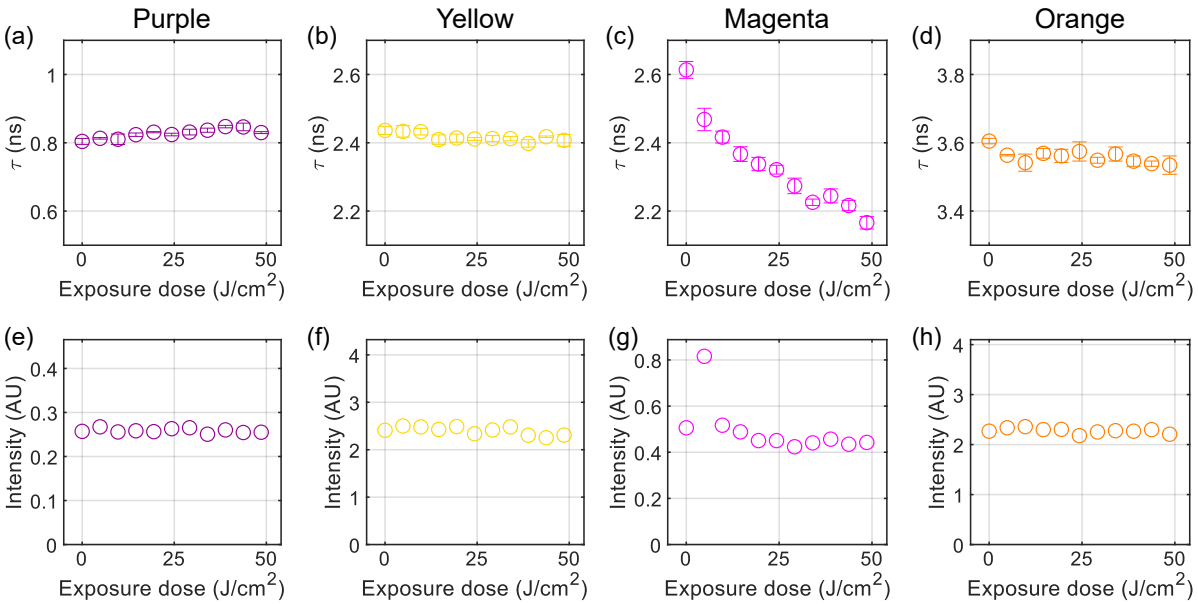


Fig 5 Photostability assessment of the FLT standards under continuous UV illumination over 10 hours. Measurements were taken every hour, and the cumulative UV dose is shown on the x-axes. (a–d) Fluorescence lifetime of each standard material over the exposure period. Error bars indicate the standard deviation from three measurements at each time point. (e–h) Corresponding fluorescence intensity measurements over the same period. The intensity of each standard was only measured once at each time point. The purple, yellow, and orange standards exhibited minimal changes in both lifetime and intensity, indicating good photostability and suitability for long-term use. In contrast, the magenta standard showed a noticeable decline in both parameters, suggesting susceptibility to photodegradation.

Table 2 Summary of the maximum variation in fluorescence lifetime and intensity observed for each dye during 10 hours of continuous UV exposure. The maximum variation represents the difference between the lowest and highest values recorded for each dye over the 10-hour exposure period.

Dye	**Lifetime**			**Intensity**		
	Min (ns)	**Max (ns)**	**Change (%)**	**Min (AU)**	**Max (AU)**	**Change (%)**
Purple	0.80	0.85	5.39%	0.25	0.27	6.68%
Yellow	2.40	2.44	1.59%	2.25	2.50	11.00%
Magenta	2.17	2.61	20.65%	0.42	0.82	92.50%
Orange	3.53	3.60	1.99%	2.18	2.36	8.25%

data point is excluded, the percentage variation in magenta intensity is reduced to 22.03 %, indicating a less severe degradation than initially observed but still more than twice as large as the other three dyes. Given its reduced photostability, lifetime redundancy with the yellow dye, and weaker signal, the magenta material may be less suitable for continued development as a reference standard.

These findings have important implications for the practical use of FLT standards in clinical

and research environments. The stability of the purple, yellow, and orange dyes under prolonged UV exposure supports their suitability for repeated use in calibration protocols, including routine system checks and longitudinal studies. In contrast, the observed variability in the magenta standard highlights the need for careful dye selection and further optimization to ensure long-term reliability. Overall, photostable standards are essential for maintaining consistency in fluorescence lifetime measurements across time and platforms.

3.4 Fabrication repeatability

To assess the repeatability of the fabrication process, three independent batches of the orange standard were produced using identical protocols. Table 3 shows the mean lifetime and intensity values for each batch. The results demonstrate excellent consistency in lifetime measurements (standard deviation $\leq$0.03 ns), indicating that the fabrication process is robust and reproducible. Some variation in intensity was observed, which may be attributed to slight differences in dye dispersion or curing conditions.

3.5 Microscopic inspection

Confocal FLIM microscopy was used to inspect the homogeneity of the standards at the microscale. Fig. 6 shows lifetime images of each dye captured using a $20\times$ objective. The images reveal a sparse or heterogeneous fluorescence distribution. This may be due to incomplete dissolution of the dye in the epoxy matrix or the presence of insoluble scattering particles in the dye powder. Further optimization of the mixing and filtering process may improve the uniformity of the standards.

The mean lifetimes and standard deviations extracted from the confocal images were 0.92 ± 1.25 ns for the purple standard, 2.03 ± 0.80 ns for the yellow, 2.32 ± 1.11 ns for the magenta, and 2.97 ± 1.11 ns

Table 3 Summary of mean lifetime and normalized intensity for the orange standards across three fabrication repetitions. The mean, standard deviation (SD) and coefficient of variation (CV) are presented for each fabrication.

Fabrication no.	**Lifetime**			**Intensity**		
	Mean (ns)	SD (ns)	CV (%)	Mean (AU)	SD (AU)	CV (%)
1	3.70	0.03	0.81	3.06	0.06	1.96
2	3.62	0.02	0.55	2.31	0.35	15.15
3	3.61	0.02	0.55	2.29	0.15	6.55

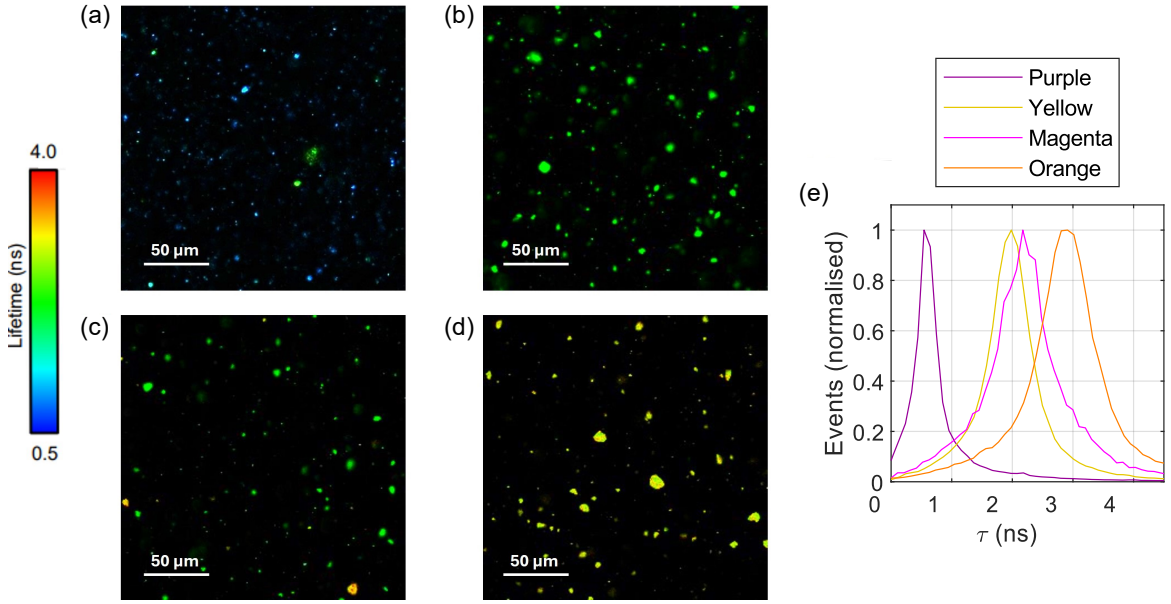


Fig 6 Lifetime images of the (a) purple, (b) yellow, (c) magenta, and (d) orange standards captured with a confocal FLIM microscope using 488 nm excitation, detection between 500 nm to 785 nm, and a 20× objective. (e) The lifetime histograms obtained from each of these images. The mean lifetimes and standard deviations from these distributions are 0.92 ± 1.25 ns for the purple standard, 2.03 ± 0.80 ns for the yellow standard, 2.32 ± 1.11 ns for the magenta standard, and 2.97 ± 1.11 ns for the orange standard.

for the orange. Apart from the purple standard, these values are consistently lower than the corresponding bulk lifetimes reported in Table 1.

One factor that may explain the discrepancy is the role of reabsorption and re-emission. In bulk measurements, secondary fluorescence generated by reabsorption of emitted photons and their subsequent re-emission can contribute to the detected signal, effectively extending the measured lifetime. In contrast, the confocal system spatially filters the emission through a pinhole, rejecting fluorescence generated outside the focal volume. As a result, secondary emission occurring away from the confocal spot is unlikely to be detected, and the measured lifetime is not artificially extended. This spatial filtering effect could explain why the confocal measurements yield consistently shorter lifetimes. These findings are consistent with prior reports that highlight platform-dependent biases in fluorescence lifetime estimation due to differences in photon collection geometry and reabsorption effects.[25,29]

3.6 Effect of dye quantity

The influence of dye quantity on fluorescence lifetime and intensity was investigated using orange standards fabricated with increasing dye quantities. As shown in Fig. 7, the fluorescence intensity increases with dye quantity as expected. However, the bulk TCSPC system measured a pronounced rise in lifetime at higher dye loads, whereas the lifetimes measured with the confocal FLIM system remained consistent. The confocal FLIM images of the four standards and their corresponding lifetime distributions can be seen in Fig. S1. The data plotted graphically in Fig. 7 is shown in Table S2. This divergence supports the interpretation that reabsorption and re-emission processes at elevated dye densities contribute to extended apparent lifetimes in bulk measurements, while the spatial filtering inherent to confocal imaging suppresses these secondary emissions.

This effect has previously been reported for other fluorophores, such as phthalocyanines,[37] and these results confirm its relevance for solid-state standards. While higher dye concentrations can enhance signal strength, they also introduce a concentration-dependent lifetime shift for non-confocal systems, which should be considered when designing standards for absolute calibration. For future development, it would be valuable to investigate at what fluorophore concentrations the measured lifetimes converge between bulk and confocal systems, as this could provide insight into the impact of reabsorption and re-emission effects.

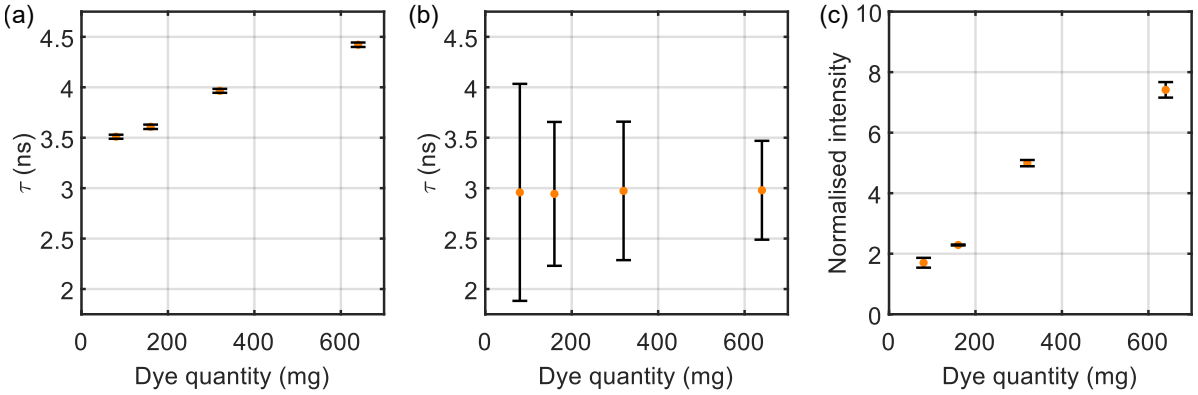


Fig 7 Influence of dye concentration on the fluorescence properties of the orange epoxy standard. Mean fluorescence lifetimes of orange standards with increasing dye concentration measured with the bulk system described in Sec. 2.2.2 (a), and measured with the Leica confocal system (b). (c) Corresponding fluorescence intensities, which increase with dye concentration. Error bars indicate the standard deviation.

3.7 Case study: FLIm micro-camera validation

To demonstrate the practical utility of the standards, they were used to validate a wide-field chip-on-tip FLIm micro-camera system. Fig. 8 shows lifetime histograms and images acquired using the micro-camera. The micro-camera was clearly able to differentiate the different standard material based on lifetime with the exception of the yellow and magenta materials, which have been noted to have already been seen to have very similar lifetimes.

The measured lifetimes for each dye were in good agreement with the bulk values obtained from the TCSPC system, although the micro-camera measured slightly longer lifetimes for the yellow and orange standards. This discrepancy is unlikely to be caused by differences in the instrument response function, as such an effect would impact all dyes similarly. Instead, it may also be attributed to reabsorption and re-emission processes, which are more pronounced for the brightest dyes (yellow and orange). Wide-field imaging systems such as the micro-camera collect fluorescence from a larger volume with no spatial filtering, increasing the likelihood of detecting secondary photons that extend the apparent decay time.

The quadrant reference standard enabled simultaneous imaging of multiple lifetimes in a single field of view, while the FLT-USAF target provided a means to assess both spatial resolution and lifetime fidelity. In the previous publication on the micro-camera, the spatial performance was characterised using a standard USAF resolution target and a diffuse white light source from behind, the minimum contrast achieved for Group 4, Element 2 was 28.4 %.[31] In this work, using the fluo-

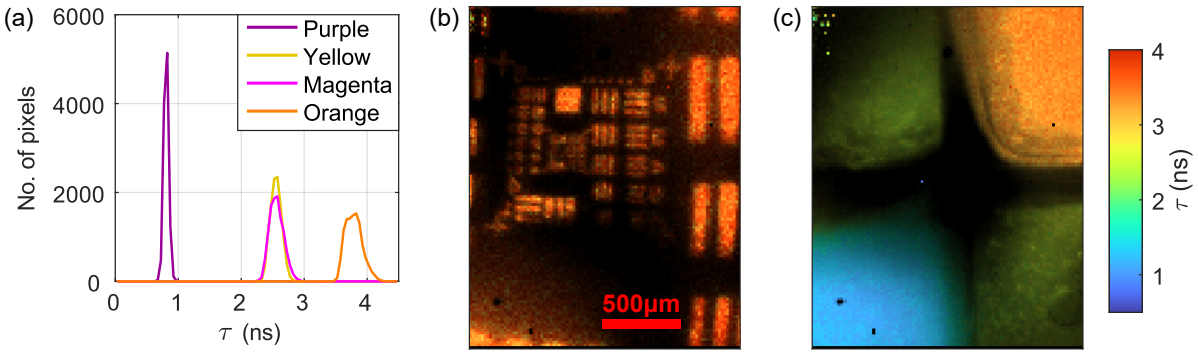


Fig 8 (a) Lifetime histograms from images acquired of each of the uniform standard materials using the microcamera. The mean lifetime measured with the micro-camera was 0.81 ± 0.06 ns for the purple standard, 2.56 ± 0.10 ns for the yellow, 2.57 ± 0.13 ns for the magenta, and 3.80 ± 0.16 ns for the orange. The uncertainty is the standard deviation for each measurement. Lifetime images of (b) the orange FLT-USAF standard and (c) the quadrant lifetime standard captured with the micro-camera with pixel brightness scaled by the intensity. The mean lifetime obtained from the USAF standard was 3.72 ± 0.26 ns. The quadrant standard is in the same orientation as shown in Fig. 3c.

rescent resolution target and delivering excitation through the optical fibre, the minimum contrast for the same element was reduced to 12.2 %. This reduction in contrast may be attributed to several factors. First, the fluorescence emission is inherently weaker and more spatially diffuse than direct back-illumination with white light, leading to lower signal-to-noise ratios at fine spatial scales. Second, the excitation geometry, delivering light via optical fibre, introduces uneven illumination which can impact the spatial resolution. These factors combined likely contribute to the reduced contrast observed in the fluorescent imaging configuration. Despite this, the FLT-USAF target still enabled clear resolution of spatial features and provided a valuable tool for assessing the combined spatial and temporal performance of the FLIm system under realistic imaging conditions.

3.8 Limitations and future prospects

While the dyed epoxy standards developed here provide robust fluorescence lifetime references, they do not replicate the optical scattering and absorption properties of biological tissues. Such phantoms would allow for more accurate benchmarking of FLIm systems under conditions that mimic *in vivo* imaging. Future work may explore integrating scattering agents and absorbers with the dyed epoxy standards to create hybrid phantoms that combine fluorescence lifetime calibration with tissue-mimicking optical properties.

As mentioned in Sec. 3.2, the current standards exhibited weak fluorescence when excited in the 300 nm to 400 nm range, which limits their compatibility with FLIm systems employing UV excitation for endogenous fluorophore detection. Future work should explore alternative dyes with enhanced UV absorption to broaden the applicability of the standards.

In addition to hardware validation, the development of standardized analysis protocols for FLIm data is a critical need for ensuring reproducibility and comparability across studies. Recent efforts from Georgakoudi et al.[38] have sought to establish consensus guidelines for fluorescence-based metabolic imaging, emphasizing the need for standardised acquisition, calibration, and reporting protocols to enhance reproducibility and comparability across systems. Although our work does not directly address this aspect, the reproducible and well-characterized standards presented here could play a supporting role in the development of such protocols by providing a consistent reference for evaluating and calibrating measurement and analysis pipelines.

4 Conclusions

This work aimed to address the lack of robust, reproducible standards for fluorescence lifetime imaging (FLIm) system validation. To do this, a set of solid-state fluorescence lifetime standards have been developed using dyed epoxy resins, targeting a range of lifetimes relevant to biomedical FLIm.

The fabricated standards exhibited lifetimes spanning from sub-nanosecond to over 3.5 ns, with good photostability and reproducibility across fabrication batches. We demonstrated their suitability for system benchmarking through bulk lifetime measurements, photostability testing, and microscopic inspection. While some heterogeneity in dye distribution was observed at the microscale, the standards provided consistent bulk measurements and proved effective for validation of a miniaturised chip-on-tip FLIm micro-camera.

In addition to lifetime and intensity characterisation, absorption and emission spectra were measured for each material. All dyes showed absorption in the 400 nm to 500 nm range, with most also absorbing in the 500 nm to 600 nm range, supporting their compatibility with a range of visible excitation sources. However, the lack of absorption below 400 nm limits their use with FLIm systems employing 355 nm or 375 nm excitation, which are commonly used for probing endogenous fluorescence. Addressing this spectral limitation will be an important focus for future material development.

These findings support the use of dyed epoxy resins as scalable, application-specific reference standards for FLIm system validation. They may facilitate the development of benchmarking protocols for emerging FLIm-based diagnostic tools and support future regulatory frameworks for clinical FLIm instrumentation. Future work will focus on improving material homogeneity, expanding the range of available lifetimes and excitation compatibility, and developing protocols for system benchmarking in both clinical and research settings.

Disclosures

SKVS and SAE are co-founders with equity ownership in the spin-off company BioPixS Ltd. BioPixS's vision is to develop next-generation phantoms and standards in biophotonics. The authors clarify that the phantoms developed in this study are research prototypes, distinct from the

FLIM phantoms commercially available from BioPixS Ltd. The other authors declare no conflicts of interest.

Code, Data, and Materials Availability

All data and code used for analysis in this manuscript is publicly available on Zenodo.[39]

Acknowledgments

This manuscript was prepared with the assistance of Microsoft Copilot to support language refinement, summarisation, and grammar. All scientific content, data interpretation, and conclusions were developed and verified by the authors. We gratefully acknowledge funding from the EU H2020 MSCA-ITN project "Photonics for Healthcare: multiscale cancer diagnosis and therapy" (PHAST-ETN), grant agreement no. 86018; Taighde Éireann – Research Ireland (22/RP-2TF/10293 and 12/RC/2276 P2). Partially funded by the European Union (ERC, NOBIAS, 101164780). Views and opinions expressed are however those of the author(s) only and do not necessarily reflect those of the European Union or the European Research Council. Neither the European Union nor the granting authority can be held responsible for them.

References

1 A. Alfonso-Garcia, J. Bec, B. Weyers, *et al.*, "Mesoscopic fluorescence lifetime imaging: Fundamental principles, clinical applications and future directions," *Journal of Biophotonics* **14**, e202000472 (2021). Publisher: John Wiley & Sons, Ltd.

2 L. Marcu, "Fluorescence Lifetime Techniques in Medical Applications," *Annals of Biomedical Engineering* **40**, 304–331 (2012).

3 W. Becker, "Fluorescence lifetime imaging – techniques and applications," *Journal of Microscopy* **247**(2), 119–136 (2012).

4 R. Datta, T. M. Heaster, J. T. Sharick, *et al.*, "Fluorescence lifetime imaging microscopy: fundamentals and advances in instrumentation, analysis, and applications," *Journal of Biomedical Optics* **25**, 1 (2020). Publisher: SPIE-Intl Soc Optical Eng.

5 V. I. Shcheslavskiy, M. V. Shirmanova, K. S. Yashin, *et al.*, "Fluorescence Lifetime Imaging Techniques—A Review on Principles, Applications and Clinical Relevance," *Journal of Biophotonics* , e202400450 (2025).

6 A. Alfonso-Garcia, J. Bec, S. Sridharan Weaver, *et al.*, "Real-time augmented reality for delineation of surgical margins during neurosurgery using autofluorescence lifetime contrast," *Journal of Biophotonics* **13**(1), e201900108 (2020).

7 S. Noble Anbunesan, A. Alfonso-Garcia, X. Zhou, *et al.*, "Intraoperative detection of IDH-mutant glioma using fluorescence lifetime imaging," *Journal of Biophotonics* **16**(4), e202200291 (2023).

8 B. W. Weyers, M. Marsden, T. Sun, *et al.*, "Fluorescence lifetime imaging for intraoperative cancer delineation in transoral robotic surgery," *Translational Biophotonics* **1**(1-2), e201900017 (2019).

9 M. Marsden, T. Fukazawa, Y.-C. Deng, *et al.*, "FLImBrush: dynamic visualization of intraoperative free-hand fiber-based fluorescence lifetime imaging," *Biomedical Optics Express* **11**, 5166–5180 (2020). Publisher: Optica Publishing Group.

10 J. E. Phipps, D. Gorpas, J. Unger, *et al.*, "Automated detection of breast cancer in resected specimens with fluorescence lifetime imaging," *Physics in Medicine & Biology* **63**, 015003 (2017).

11 J. Unger, C. Hebisch, J. E. Phipps, *et al.*, "Real-time diagnosis and visualization of tumor margins in excised breast specimens using fluorescence lifetime imaging and machine learning," *Biomedical Optics Express* **11**, 1216–1230 (2020).

12 J. James, R. Inci, N. Neittaanmäki, *et al.*, "Exploring MPM-FLIM for diagnostics of porokeratosis – a pilot study *ex vivo*," *Biomedical Optics Express* **16**, 2243–2253 (2025).

13 J. Wang, M. Taki, Y. Ohba, *et al.*, "Fluorescence Lifetime Imaging of Lipid Heterogeneity in the Inner Mitochondrial Membrane with a Super-photostable Environment-Sensitive Probe," *Angewandte Chemie International Edition* **63**(28), e202404328 (2024).

14 R. Datta, A. Gillette, M. Stefely, *et al.*, "Recent innovations in fluorescence lifetime imaging microscopy for biology and medicine," *Journal of Biomedical Optics* **26**(7), 070603 (2021).

15 S. Dochow, D. Ma, I. Latka, *et al.*, "Combined fiber probe for fluorescence lifetime and Raman spectroscopy," *Analytical and bioanalytical chemistry* **407**, 8291 (2015). Publisher: NIH Public Access.

16 S. Dochow, H. Fatakdawala, J. E. Phipps, *et al.*, "Comparing Raman and fluorescence lifetime spectroscopy from human atherosclerotic lesions using a bimodal probe," *Journal of Biophotonics* **9**(9), 958–966 (2016).

17 J. L. Lagarto, V. Shcheslavskiy, F. S. Pavone, *et al.*, "Simultaneous fluorescence lifetime and Raman fiber-based mapping of tissues," *Optics Letters* **45**, 2247–2250 (2020).

18 C. Li, J. Bec, X. Zhou, *et al.*, "Dual-modality fluorescence lifetime imaging-optical coherence tomography intravascular catheter system with freeform catheter optics," *Journal of Biomedical Optics* **27**, 076005 (2022). Publisher: SPIE.

19 J. Bec, X. Zhou, M. Villiger, *et al.*, "Dual modality intravascular catheter system combining pulse-sampling fluorescence lifetime imaging and polarization-sensitive optical coherence tomography," *Biomedical Optics Express* **15**, 2114–2132 (2024). Publisher: Optica Publishing Group.

20 B. W. Pogue and M. S. Patterson, "Review of tissue simulating phantoms for optical spectroscopy, imaging and dosimetry," *Journal of Biomedical Optics* **11**, 041102 (2006).

21 S. K. V. Sekar, A. Pacheco, P. Martella, *et al.*, "Solid phantom recipe for diffuse optics in biophotonics applications: a step towards anatomically correct 3D tissue phantoms," *Biomedical Optics Express* **10**, 2090–2100 (2019).

22 M. D. Ghauri, S. Šušnjar, C. N. Guadagno, *et al.*, "Hybrid heterogeneous phantoms for biomedical applications: a demonstration to dosimetry validation," *Biomedical Optics Express* **15**, 863–874 (2024).

23 G. Dumlupinar, S. K. V. Sekar, C. N. Guadagno, *et al.*, "Solid optical tissue phantom tools based on upconverting nanoparticles for biomedical applications," *Journal of Biomedical Optics* **28**, 036004 (2023).

24 N. Boens, W. Qin, N. Basarić, *et al.*, "Fluorescence Lifetime Standards for Time and Frequency Domain Fluorescence Spectroscopy," *Analytical Chemistry* **79**, 2137–2149 (2007).

25 A. Margineanu, "Calibration approaches for fluorescence lifetime applications using time-domain measurements," *Methods in Microscopy* **2**, 61–71 (2025).

26 A. S. Kristoffersen, S. R. Erga, B. Hamre, *et al.*, "Testing Fluorescence Lifetime Standards using Two-Photon Excitation and Time-Domain Instrumentation: Rhodamine B, Coumarin 6 and Lucifer Yellow," *Journal of Fluorescence* **24**(4), 1015–1024 (2014).

27 A. S. Kristoffersen, S. R. Erga, B. Hamre, *et al.*, "Testing Fluorescence Lifetime Standards using Two-Photon Excitation and Time-Domain Instrumentation: Fluorescein, Quinine Sulfate and Green Fluorescent Protein," *Journal of Fluorescence* **28**, 1065–1073 (2018).

28 "High Resolution Fluorescence Lifetime Test Targets." BioPixS Online Store - https://store.biopixstandards.com/product/high-resolution-fluorescence-lifetime-test-targets/.

29 C. B. Talbot, J. Lagarto, S. Warren, *et al.*, "Correction Approach for Delta Function Convolution Model Fitting of Fluorescence Decay Data in the Case of a Monoexponential Reference Fluorophore," *Journal of Fluorescence* **25**, 1169–1182 (2015).

30 C. Freymüller, S. Ströbl, M. Aumiller, *et al.*, "Development of a microstructured tissue phantom with adaptable optical properties for use with microscopes and fluorescence lifetime imaging systems," *Lasers in Surgery and Medicine* **54**(7), 1010–1026 (2022).

31 D. Angelone, N. Nudds, A. Matheson, *et al.*, "Chip-on-tip FLIm micro-camera towards endoscopic applications," *Optics Letters* , 4230–4233 (2025).

32 S. Konugolu Venkata Sekar, A. Dalla Mora, I. Bargigia, *et al.*, "Broadband (600–1350 nm) Time-Resolved Diffuse Optical Spectrometer for Clinical Use," *IEEE Journal of Selected Topics in Quantum Electronics* **22**, 406–414 (2016).

33 S. K. Kothuri, D. MacMahon, P. Lanka, *et al.*, "Broadband time domain diffuse optical characterization of human cadaver bone from 500 to 1100 nm," *Scientific Reports* **15**, 25931 (2025).

34 K. Hughes and S. Konugolu Venkata Sekar, "FLIM_keela," (2025). GitHub repository: https://github.com/konugolu/FLIM_Keela.

35 L. A. J. Alvarez, B. Widzgoeski, G. Ossato, *et al.*, "Application Note: SP8 FALCON: a novel concept in fluorescence lifetime imaging enabling video-rate confocal FLIM," *Nature Methods* **16** (2019).

36 A. T. Erdogan, T. A. Abbas, N. Finlayson, *et al.*, "A High Dynamic Range 128 x 120 3-D Stacked CMOS SPAD Image Sensor SoC for Fluorescence Microendoscopy," *IEEE Journal of Solid-State Circuits* **57**(6), 1649–1660 (2022).

37 S. Dhami, A. J. D. Mello, G. Rumbles, *et al.*, "Phthalocyanine Fluorescence at High Concentration: Dimers or Reabsorption Effect?," *Photochemistry and Photobiology* **61**(4), 341–346 (1995).

38 I. Georgakoudi, M. C. Skala, K. P. Quinn, *et al.*, "Consensus guidelines for cellular label-free optical metabolic imaging: ensuring accuracy and reproducibility in metabolic profiling," *Journal of Biomedical Optics* **30**(S2), S23901 (2025).

39 D. Angelone and S. Konugolu Venkata Sekar, "Dataset: Development of solid-state fluorescence lifetime standards for clinical applications using dyed epoxy resins," (2025).

Appendix

Supplementary information for the papers.

Supporting Information:

Metabolic imaging of tumor tissue samples using planar fluorescence lifetime-based pH sensors and a SPAD array imager

Dario Angelone[a,*], Liang Li[b], Ciaran Devoy[c], Andrew B. Matheson[d], Ahmet T. Erdogan[d], Robert K. Henderson[d], Mark Tangney[c], Dmitri B. Papkovsky[b], Stefan Andersson-Engels[a,e], Sanathana Konugolu Venkata Sekar[a,*]

[a]*Biophotonics, Tyndall National Institute, Lee Maltings Complex, Cork, T12 R5CP, Ireland*
[b]*School of Biochemistry and Cell Biology, University College Cork, Pharmacy Building, College Road, Cork, Ireland*
[c]*Cancer Research @UCC, University College Cork, Cork, Ireland*
[d]*Institute for Integrated Micro and Nano Systems, School of Engineering, University of Edinburgh, Edinburgh, United Kingdom*
[e]*Department of Physics, University College Cork, College Road, Cork, Ireland*

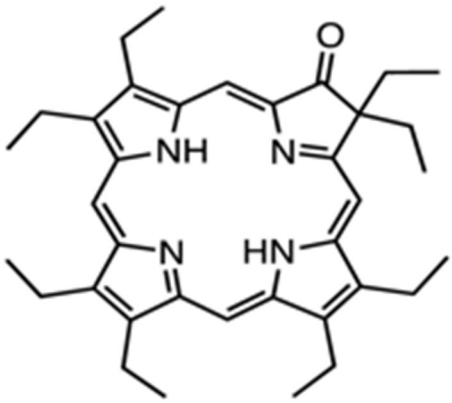


Figure S1. The chemical structure of the protonable fluorescent dye, octaethylporphin-ketone (OEPK).

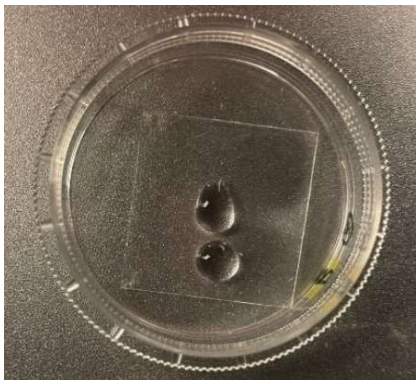


Figure S2. An optochemical sensor with standard solutions having pH 6.5 (top) and pH 5.5 (bottom) measured for initial assessment of the imaging capabilities of the sensor.

[*]Corresponding authors, *email:* dario.angelone@tyndall.ie, sanathana.konugolu@tyndall.ie

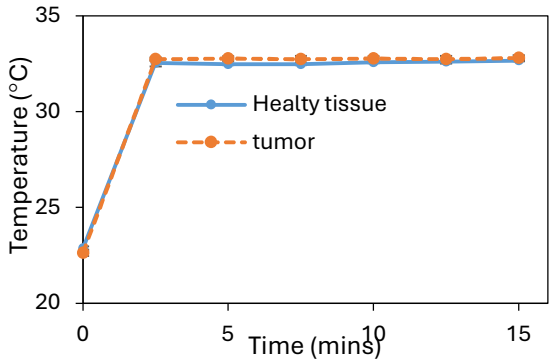


Figure S3. Temperature of tissue samples on the heating plate were monitored with a contactless IR thermometer DT8803 (Duratool). After initial equilibration (<2 min), temperature of the tissue samples stabilizes at approximately 33°C. FLIM measurements were performed at least 3 minutes after samples were placed on the plate, therefore sample temperature had stabilized during these measurements.

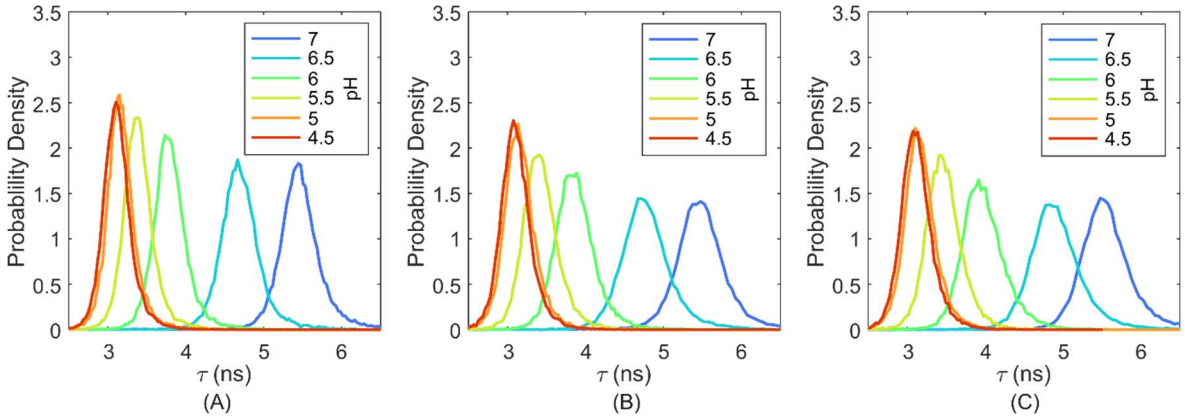


Figure S4. Lifetime distributions obtained from the calibration measurements. The sensor fluorescence lifetime was measured while in contact with a range of pH standard solutions from pH 4.5 to pH 7. This was repeated using new sensors (A), used sensors which received no pretreatment (B), and used sensors that had been pretreated with foetal bovine serum (C). There is very little difference observed between the distributions from each calibration.

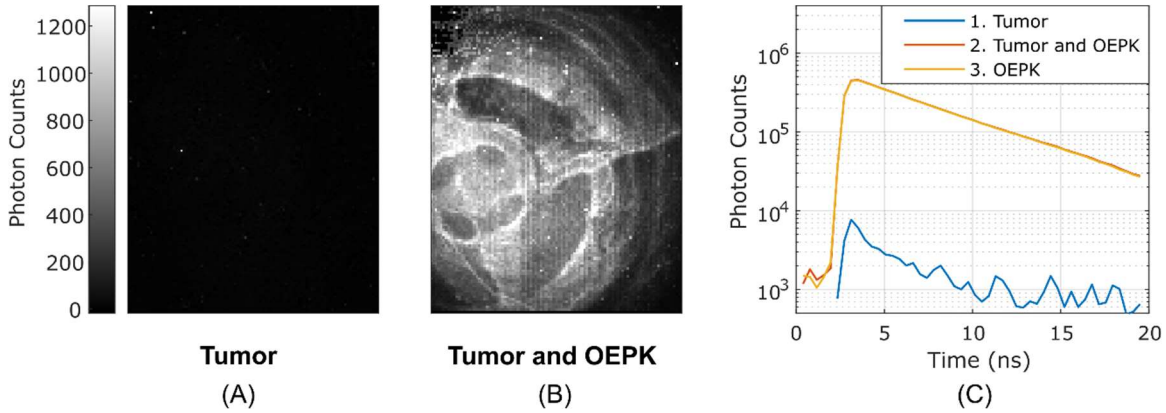


Figure S5. Fluorescence intensity images of a mouse tumor sample (A) and the same sample with an OEPK pH sensor placed on top. A plot of the time resolved fluorescence decay curves summed across all pixels (C). Curve 3 was obtained by subtracting curve 1 from curve 2. The fluorescent signal from the tumor itself is observed to be significantly weaker than that of the OEPK sensor. Subtraction of the tumor autofluorescence decay curve from the combined fluorescence shows a negligible impact.

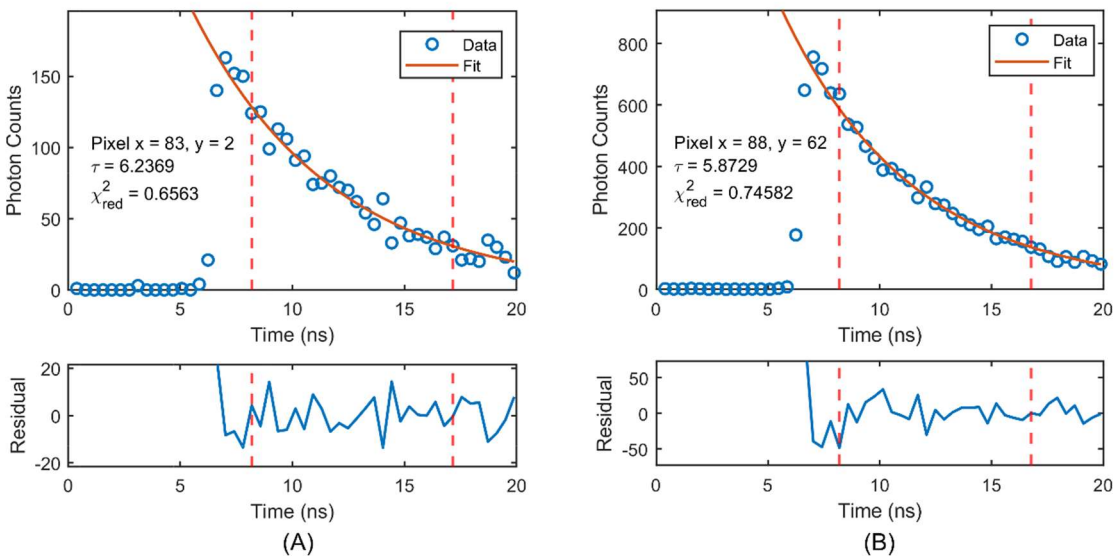


Figure S6. Two examples of photon counts obtained by individual pixels on the SPAD array along with a plot of the fit. The reduced chi squared values are also displayed as a measure of the goodness-of-fit along with a plot of the residuals. The dotted red lines indicate the range of time bins over which fitting was performed. These two examples are taken from the measurement of the tumour sample presented in Figure 4. In order to give representative plots, (A) shows a pixel from the 10th percentile of peak photon counts (low counts) while (B) shows a pixel from the 90th percentile (high counts).

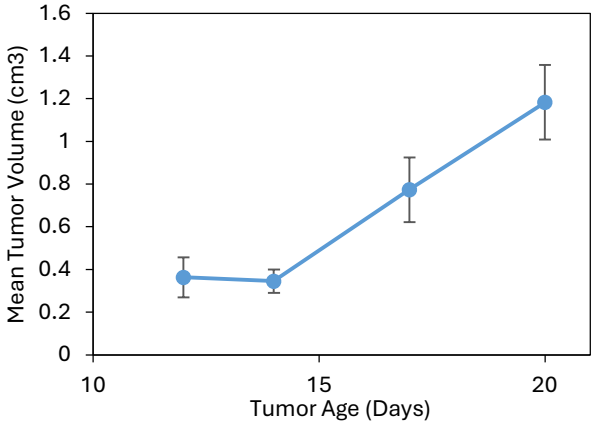


Figure S7. Mean tumour volumes for the groups of mice from each measurement day. Tumours volumes were recorded the evening before the FLIM measurements were performed. The error bars indicate the standard deviation of each group.

Supporting Information:

Chip-on-tip fluorescence lifetime imaging micro-camera towards endoscopic applications

Dario Angelone[1,*], Noreen Nudds[2], Andrew B. Matheson[3], Ahmet T. Erdogan[3], Walter Messina[1], Ray Burke[1], Robert K. Henderson[3], Stefan Andersson-Engels[1,4], Sanathana Konugolu Venkata Sekar[1,4,*]

[1]Biophotonics, Tyndall National Institute, Lee Maltings Complex, Cork, T12 R5CP, Ireland
[2]Packaging Systems Group, Tyndall National Institute, Lee Maltings Complex, Cork T12 R5CP, Ireland
[3]Institute for Integrated Micro and Nano Systems, School of Engineering, University of Edinburgh, Edinburgh, United Kingdom
[4]Department of Physics, University College Cork, College Road, Cork, Ireland

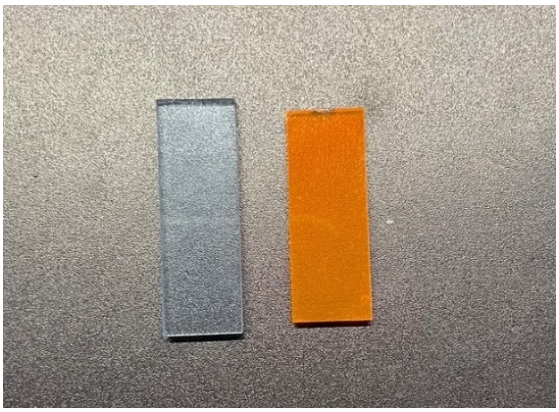


Fig S1: A photograph of the two BioPixS lifetime test targets (BPXS1LT left and BPXS5LT right) used for benchmarking the FLIm micro-camera system against a traditional TCSPC system. The two standards were placed next to each other and imaged with the micro-camera to produce Fig. 3d.

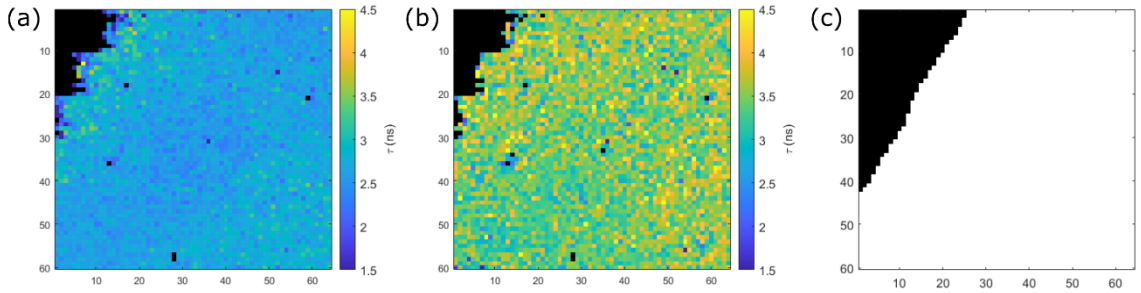


Fig. S2: The raw lifetime maps of ex vivo sheep (a) intestine and (b) lung captured using the FLIm micro-camera. To produce the lifetime images in Fig. 4, these maps were upscaled to the original image resolution and interpolated (bilinear), and the pixel brightness was then scaled by the intensity. (c) The binary exclusion mask applied to the lifetime maps before generating the lifetime distributions in Fig. 4e and before calculation of the mean lifetimes. This mask was manually drawn to exclude the defective pixels in the top left corner of the detector.

Supporting Information:

Development of solid-state fluorescence lifetime standards for clinical applications using dyed epoxy resins

Dario Angelone[a,*], Keela Hughes[a,b], Hasti Yavari[a], Sara Eugenia Garduño Gómez[c], Brian C. Wilson[d], Stefan Andersson-Engels[a,b], Katarzyna Komolibus[a], Sanathana Konugolu Venkata Sekar[a,b,*]

[a]*Biophotonics, Tyndall National Institute, Lee Maltings Complex, Cork, T12 R5CP, Ireland*
[b]*School of Physics, University College Cork, College Road, Cork, Ireland*
[c]*BioPixS Ltd. (Biophotonics Standards), Lee Maltings Complex, Cork T12 R5CP, Ireland*
[d]*Princess Margaret Cancer Centre, University Health Network, Toronto, ON M5G 1L7, Ontario, Canada*

Table S1. Lifetimes (***τ***) and intensities (***I***) of the dye materials under prolonged UV exposure measured with the TCSPC-based system described in Sec. 2.2.2. These results are plotted in Fig. 5.

Time (hr)	Dose (J/cm²)	Purple		Yellow		Magenta		Orange	
		τ (ns)	I (AU)	τ (ns)	I (AU)	τ (ns)	I (AU)	τ (ns)	I (AU)
0	0.00	0.80 ± 0.01	0.26	2.44 ± 0.01	2.41	2.61 ± 0.02	0.51	3.60 ± 0.01	2.27
1	4.86	0.81 ± 0.00	0.27	2.43 ± 0.02	2.50	2.46 ± 0.03	0.82	3.56 ± 0.00	2.34
2	9.72	0.81 ± 0.02	0.26	2.43 ± 0.01	2.48	2.42 ± 0.02	0.52	3.54 ± 0.03	2.36
3	14.58	0.82 ± 0.01	0.26	2.41 ± 0.01	2.43	2.37 ± 0.02	0.49	3.57 ± 0.01	2.30
4	19.44	0.83 ± 0.00	0.26	2.41 ± 0.01	2.49	2.34 ± 0.02	0.45	3.56 ± 0.02	2.30
5	24.30	0.82 ± 0.00	0.26	2.41 ± 0.00	2.34	2.32 ± 0.01	0.45	3.57 ± 0.03	2.18
6	29.16	0.83 ± 0.01	0.27	2.41 ± 0.01	2.42	2.27 ± 0.02	0.42	3.55 ± 0.01	2.25
7	34.02	0.84 ± 0.01	0.25	2.41 ± 0.01	2.48	2.23 ± 0.01	0.44	3.57 ± 0.02	2.28
8	38.88	0.85 ± 0.00	0.26	2.40 ± 0.01	2.30	2.24 ± 0.02	0.46	3.55 ± 0.01	2.27
9	43.74	0.85 ± 0.01	0.25	2.42 ± 0.00	2.25	2.21 ± 0.01	0.43	3.54 ± 0.01	2.30
10	48.60	0.83 ± 0.00	0.26	2.41 ± 0.02	2.31	2.16 ± 0.02	0.44	3.53 ± 0.03	2.21

Table S2 Mean fluorescence lifetimes and intensities of orange standards fabricated with varying dye quantities, along with their standard deviations (SD). Bulk measurements were acquired using the custom TCSPC-based system (Sec. 2.2.2), and confocal lifetimes were obtained with a Leica confocal microscope (Sec. 2.2.5). Corresponding confocal images are shown in Fig. S1. Data are plotted graphically in Fig. 7.

Dye Quantity (mg)	Bulk Lifetime (ns)		Confocal Lifetime (ns)		Intensity (AU)	
	Mean	SD	Mean	SD	Mean	SD
80	3.51	0.02	2.96	1.08	1.70	0.16
160	3.61	0.02	2.94	0.71	2.29	0.02
320	3.96	0.02	2.97	0.69	4.99	0.10
640	4.42	0.02	2.98	0.49	7.41	0.26

*Corresponding authors, *email:* dario.angelone@tyndall.ie, sanathana.konugolu@tyndall.ie

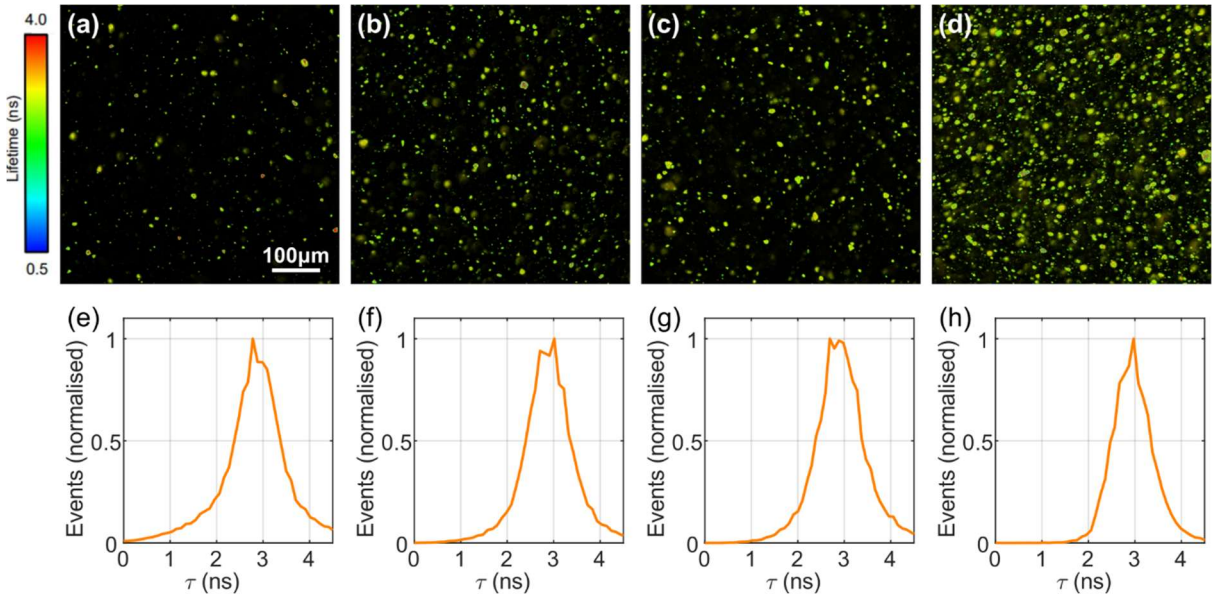


Figure S1. Lifetime images of orange standards with (a) 80 mg, (b) 160 mg, (c) 320 mg, and (d) 640 mg. Images captured with a confocal FLIM system using 488 nm excitation, detection between 500 nm and 785 nm. Corresponding lifetime distributions.